MOLECULAR SIMULATION ON CEMENTITIOUS MATERIALS: FROM COMPUTATIONAL CHEMISTRY METHOD TO APPLICATION

EDITED BY: Dongshuai Hou, Hongyan Ma and Jinrui Zhang
PUBLISHED IN: Frontiers in Materials

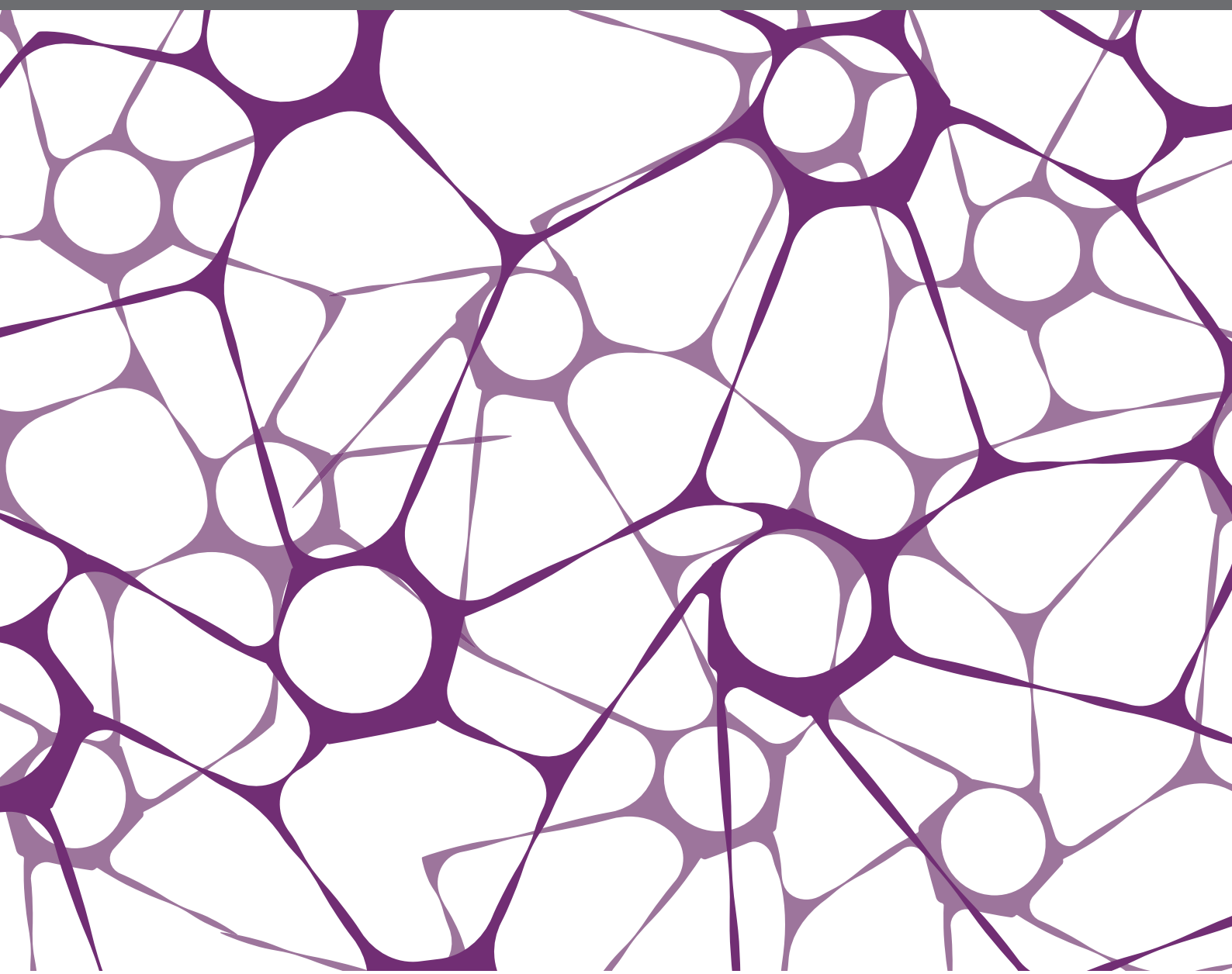

frontiers Research Topics

Frontiers eBook Copyright Statement

The copyright in the text of individual articles in this eBook is the property of their respective authors or their respective institutions or funders. The copyright in graphics and images within each article may be subject to copyright of other parties. In both cases this is subject to a license granted to Frontiers.

The compilation of articles constituting this eBook is the property of Frontiers.

Each article within this eBook, and the eBook itself, are published under the most recent version of the Creative Commons CC-BY licence. The version current at the date of publication of this eBook is CC-BY 4.0. If the CC-BY licence is updated, the licence granted by Frontiers is automatically updated to the new version.

When exercising any right under the CC-BY licence, Frontiers must be attributed as the original publisher of the article or eBook, as applicable.

Authors have the responsibility of ensuring that any graphics or other materials which are the property of others may be included in the CC-BY licence, but this should be checked before relying on the CC-BY licence to reproduce those materials. Any copyright notices relating to those materials must be complied with.

Copyright and source acknowledgement notices may not be removed and must be displayed in any copy, derivative work or partial copy which includes the elements in question.

All copyright, and all rights therein, are protected by national and international copyright laws. The above represents a summary only. For further information please read Frontiers' Conditions for Website Use and Copyright Statement, and the applicable CC-BY licence.

ISSN 1664-8714
ISBN 978-2-88974-302-5
DOI 10.3389/978-2-88974-302-5

About Frontiers

Frontiers is more than just an open-access publisher of scholarly articles: it is a pioneering approach to the world of academia, radically improving the way scholarly research is managed. The grand vision of Frontiers is a world where all people have an equal opportunity to seek, share and generate knowledge. Frontiers provides immediate and permanent online open access to all its publications, but this alone is not enough to realize our grand goals.

Frontiers Journal Series

The Frontiers Journal Series is a multi-tier and interdisciplinary set of open-access, online journals, promising a paradigm shift from the current review, selection and dissemination processes in academic publishing. All Frontiers journals are driven by researchers for researchers; therefore, they constitute a service to the scholarly community. At the same time, the Frontiers Journal Series operates on a revolutionary invention, the tiered publishing system, initially addressing specific communities of scholars, and gradually climbing up to broader public understanding, thus serving the interests of the lay society, too.

Dedication to Quality

Each Frontiers article is a landmark of the highest quality, thanks to genuinely collaborative interactions between authors and review editors, who include some of the world's best academicians. Research must be certified by peers before entering a stream of knowledge that may eventually reach the public - and shape society; therefore, Frontiers only applies the most rigorous and unbiased reviews.
Frontiers revolutionizes research publishing by freely delivering the most outstanding research, evaluated with no bias from both the academic and social point of view. By applying the most advanced information technologies, Frontiers is catapulting scholarly publishing into a new generation.

What are Frontiers Research Topics?

Frontiers Research Topics are very popular trademarks of the Frontiers Journals Series: they are collections of at least ten articles, all centered on a particular subject. With their unique mix of varied contributions from Original Research to Review Articles, Frontiers Research Topics unify the most influential researchers, the latest key findings and historical advances in a hot research area! Find out more on how to host your own Frontiers Research Topic or contribute to one as an author by contacting the Frontiers Editorial Office: frontiersin.org/about/contact

MOLECULAR SIMULATION ON CEMENTITIOUS MATERIALS: FROM COMPUTATIONAL CHEMISTRY METHOD TO APPLICATION

Topic Editors:
Dongshuai Hou, Qingdao University of Technology, China
Hongyan Ma, Missouri University of Science and Technology, United States
Jinrui Zhang, Tianjin University, China

Citation: Hou, D., Ma, H., Zhang, J., eds. (2022). Molecular Simulation on Cementitious Materials: From Computational Chemistry Method to Application. Lausanne: Frontiers Media SA. doi: 10.3389/978-2-88974-302-5

Table of Contents

frontiers in Materials

EDITORIAL
published: 20 December 2021
doi: 10.3389/fmats.2021.810850

Editorial: Molecular Simulation on Cementitious Materials: From Computational Chemistry Method to Application

Hongyan Ma[1]*, *Dongshuai Hou*[2] and *Jinrui Zhang*[3]

[1]Department of Civil, Architectural and Environmental Engineering, Missouri University of Science and Technology, Rolla, MO, United States, [2]Department of Civil Engineering, Qingdao University of Technology, Qingdao, China, [3]State Key Laboratory of Hydraulic Engineering Simulation and Safety, Tianjin University, Tianjin, China

Keywords: molecular dynamics, reactive force field, Monte Carlo method, first principles, calcium silicate hydrate

Editorial on the Research Topic

Molecular Simulation on Cementitious Materials: From Computational Chemistry Method to Application

The use of molecular simulation has made great progress over recent years in the field of cement chemistry. The progress includes, but is not limited to, deriving a series of accurate force fields, decoding the realistic structure of calcium-silicate-hydrate (C-S-H), unraveling the interfacial reactivity and chemistry of cement minerals, and studying interactions between cement hydrates and organic/inorganic additives (e.g., cellulose) or corrosive substances (e.g., chloride ions) (Mishra et al., 2017; Pellenq et al., 2009; Zhang, et al., 2021). Molecular simulation can be used as a powerful tool to yield a profound scientific understanding of cementitious materials and their behaviors across several length scales (as shown in **Figure 1**). Based on the understanding of intrinsic mechanisms, molecular simulation can complement experimental studies to offer more explicit and efficient guides for the design of cementitious materials.

It is our great pleasure to present this research topic on *Molecular Simulation on Cementitious Materials: From Computational Chemistry Method to Application*. The collection of 11 articles in this research topic further discovers the nanoscale nature of cementitious material and guides applications of nanotechnologies in cement-based materials. We expect that these studies will advance cement chemistry and concrete technology through the application of modern computational methodologies alone, or in conjunction with experimental techniques. These studies will also push forward development of eco-efficient cementitious materials along the three directions pointed out by Scrivener et al. (2018): enhancing usage of supplementary cementitious materials (SCMs); developing alternative cements; and enhancing the efficiency of cement (production and application).

So far, utilization of SCMs is still the most effective way to improve the eco-efficiency of cement and concrete. The most popular SCMs are normally from industrial waste streams (e.g., coal fly ash and ground granulated blast-furnace slag), which contain amorphous alumina apart from amorphous silica. Thus, when such SCMs are used to replace part of cement in the binder phase of concrete, the formed C-S-H gel often involves Al-uptake, forming calcium-aluminosilicate-hydrate (C-A-S-H) gel. To better understand the effect of Al-uptake, Zhang et al. used reactive force field molecular dynamics to reproduce the Al-induced cross-linking effect on the aluminosilicate chains in the C-A-S-H gel, which is a major hydrate phase of cement with SCMs. The chemical and fracture processes coupled in this study demonstrated the significant

OPEN ACCESS

Edited and reviewed by:
John L. Provis,
The University of Sheffield,
United Kingdom

***Correspondence:**
Hongyan Ma
mahon@mst.edu

Specialty section:
This article was submitted to Structural Materials, a section of the journal Frontiers in Materials

Received: *08 November 2021*
Accepted: *29 November 2021*
Published: *20 December 2021*

Citation:
Ma H, Hou D and Zhang J (2021) Editorial: Molecular Simulation on Cementitious Materials: From Computational Chemistry Method to Application. Front. Mater. 8:810850. doi: 10.3389/fmats.2021.810850

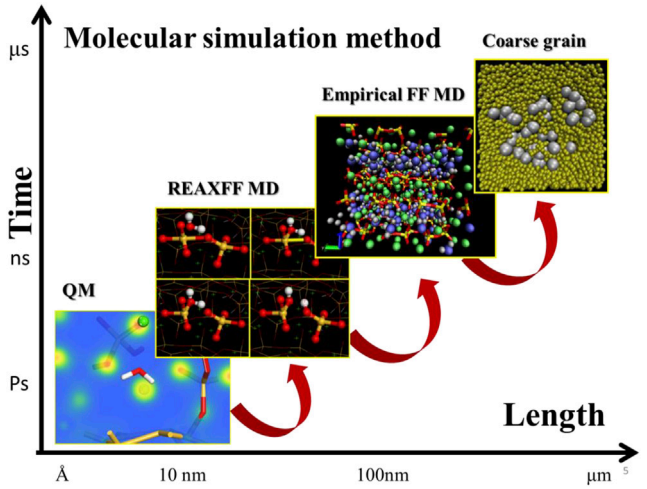

FIGURE 1 | Molecular simulation of cement-based materials at several length scales.

improvement of mechanical properties due to the incorporation of cross-linking aluminate structures.

When it comes to alternative binders, this research topic involves computational studies about alkali-activated materials, carbonation-hardening binders, and magnesium phosphate cement (MPC). Li et al. simulated a series of geopolymers using reactive force field molecular dynamics and Monte Carlo method. They found that the structure and mechanical properties of sodium aluminosilicate hydrate (N-A-S-H) gel is greatly dependent on sodium content: with Na/Al ratio rising, the aluminosilicate skeleton is transformed from an integral network to partially destroyed branch structures, reducing the stiffness and cohesive force of the gel. Wan et al. investigated the intrinsic mechanism for sodium dissolution (i.e., leaching) from the N-A-S-H gels of geopolymers. This study showed that sodium dissociation promotes a hydrolytic reaction, exacerbating the non-conservation of charge of the N-A-S-H system, and in the long term reduces the stability of the aluminosilicate skeleton. This finding is consistent with existing knowledge (Hou et al., 2014).

Carbonation-hardening binders have been attracting increasing attention because of their direct involvement of CO_2 mineralization. It has been known that nanotechnology can effectively improve the carbonation reactivity and, thus, the mechanical properties, of carbonation-hardening binders. Tao et al. presented first-principles calculations for screening potential dopants for increasing the carbonation reactivity of γ-Ca_2SiO_4 crystals. It is found that the carbonation reactivity is related to the reactive site distribution and the binding strength of γ-Ca_2SiO_4; and Ba, P, and F elements can potentially decrease the overall binding strength, which benefits the dissolution and carbonation reactions. MPC is a widely studied alternative binder for niche functional applications (e.g., fast repair, metal protection, fire retardant, etc.) (Ma et al., 2014). Similar to carbonation-hardening binders, the hardening process of MPC relies on reactions between a base oxide and an acidic component, which is completely different from traditional cements and alkali-activated materials. Li et al. proposed an experimental-computational approach to study the mechanical properties of magnesium potassium phosphate hexahydrate–the basic binding phase in MPC.

To improve the efficiency of cement utilization, a commonly considered approach is to use nano-reinforcement/modifier for improving the mechanical and/or durability properties of cement-based materials. Zhou et al. used reactive molecular simulation to investigate the effect of an emerging two-dimensional (2D) material—2D-silica–that is intentionally intercalated into the interlayer defective sites of C-S-H. This work may shed new light on the interaction mechanisms between 2D-materials and inorganic hosts, and provide solutions to modifying concrete against its high brittleness. Cement efficiency can also be improved by increasing strength and durability of concrete, since improved strength and durability imply needs of smaller volume of material in the construction stage and the whole life-cycle, respectively. Wang et al. advanced a well-known type of high-strength concrete (i.e., reactive powder concrete), and proved theoretically and experimentally that a well-selected delay (of start of steam curing after molding) can benefit the development of microstructure and strength. Realizing that high-strength concrete requires improved cracking resistance, Yue et al. proposed a methodology to optimize high-strength concrete mix proportion towards better cracking resistance using artificial neural network and genetic algorithm. To better understand the durability of concrete so as to improve it, Xu et al. simulated the coupled penetration of sulfate ions and chloride ions into concrete, say, in marine service environment; and Liu et al. developed a meso-scale five-phase model to decode the complexity of the microstructure, as well as to describe the transport and distribution of water in recycled aggregate incorporated concrete. In addition, to a large extent, the true quality of concrete (no matter how well it is designed) is determined by its workability (how well it can be manipulated in the fresh state). To better understand the nature of workability, Li et al. simulated the slump and J-ring tests of highly flowable concrete using discrete element method.

The Guest Editorial team is confident that the successful application of computational methods will facilitate the fundamental research and technology development of cementitious materials.

AUTHOR CONTRIBUTIONS

All authors listed have made a substantial, direct, and intellectual contribution to the work and approved it for publication.

REFERENCES

Hou, D., Ma, H., Li, Z., and Jin, Z. (2014). Molecular Simulation of "Hydrolytic Weakening": A Case Study on Silica. *Acta Materialia* 80, 264–277. doi:10.1016/j.actamat.2014.07.059

Ma, H., Xu, B., and Li, Z. (2014). Magnesium Potassium Phosphate Cement Paste: Degree of Reaction, Porosity and Pore Structure. *Cement Concrete Res.* 65, 96–104. doi:10.1016/j.cemconres.2014.07.012

Mishra, R. K., Mohamed, A. K., Geissbühler, D., Manzano, H., Jamil, T., Shahsavari, R., et al. (2017). *Cemff*: A Force Field Database for Cementitious Materials Including Validations, Applications and Opportunities. *Cement Concrete Res.* 102, 68–89. doi:10.1016/j.cemconres.2017.09.003

Pellenq, R. J.-M., Kushima, A., Shahsavari, R., Van Vliet, K. J., Buehler, M. J., Yip, S., et al. (2009). A Realistic Molecular Model of Cement Hydrates. *Proc. Natl. Acad. Sci.* 106 (38), 16102–16107. doi:10.1073/pnas.0902180106

Scrivener, K. L., John, V. M., and Gartner, E. M. (2018). Eco-efficient Cements: Potential Economically Viable Solutions for a low-CO2 Cement-Based Materials Industry. *Cement Concrete Res.* 114, 2–26. doi:10.1016/j.cemconres.2018.03.015

Zhang, W., Hou, D., and Ma, H. (2021). Multi-scale Study Water and Ions Transport in the Cement-Based Materials:from Molecular Dynamics to Random Walk. *Microporous Mesoporous Mater.* 325, 111330. doi:10.1016/j.micromeso.2021.111330

Conflict of Interest: The authors declare that the research was conducted in the absence of any commercial or financial relationships that could be construed as a potential conflict of interest.

Publisher's Note: All claims expressed in this article are solely those of the authors and do not necessarily represent those of their affiliated organizations, or those of the publisher, the editors and the reviewers. Any product that may be evaluated in this article, or claim that may be made by its manufacturer, is not guaranteed or endorsed by the publisher.

Copyright © 2021 Ma, Hou and Zhang. This is an open-access article distributed under the terms of the Creative Commons Attribution License (CC BY). The use, distribution or reproduction in other forums is permitted, provided the original author(s) and the copyright owner(s) are credited and that the original publication in this journal is cited, in accordance with accepted academic practice. No use, distribution or reproduction is permitted which does not comply with these terms.

frontiers in Materials

ORIGINAL RESEARCH
published: 14 January 2020
doi: 10.3389/fmats.2019.00344

Experimental-Computational Approach to Investigate Nanoindentation of Magnesium Potassium Phosphate Hexahydrate (MKP) With X-CT Technique and Finite Element Analysis

*Yue Li, Guosheng Zhang and Zigeng Wang**

Key Laboratory of Urban Security and Disaster Engineering of Ministry of Education, Beijing Key Laboratory of Earthquake Engineering and Structural Retrofit, Beijing University of Technology, Beijing, China

OPEN ACCESS

Edited by:
Dongshuai Hou, Qingdao University of Technology, China

Reviewed by:
Yunsheng Zhang, Southeast University, China
Zeyu Lu, University of Macau, China

***Correspondence:**
Zigeng Wang
zigengw@bjut.edu.cn

Specialty section:
This article was submitted to Computational Materials Science, a section of the journal Frontiers in Materials

Received: *09 November 2019*
Accepted: *18 December 2019*
Published: *14 January 2020*

Citation:
Li Y, Zhang G and Wang Z (2020) Experimental-Computational Approach to Investigate Nanoindentation of Magnesium Potassium Phosphate Hexahydrate (MKP) With X-CT Technique and Finite Element Analysis. Front. Mater. 6:344. doi: 10.3389/fmats.2019.00344

The magnesium phosphate cement (MPC) is a carbon-free cementitious material, widely used in solidification of nuclear waste, heavy metals, and repair and reinforcement. The magnesium potassium phosphate hexahydrate ($MgKPO_4 \cdot 6H_2O$, MKP) is the main hydration product of MPC, seriously affecting the mechanical properties of the MPC. Therefore, this paper presented an experimental-computational approach to investigate the mechanical properties of the MKP through nanoindentation with X-ray Computed Tomography (X-CT) technique and finite element analysis. Firstly, the micro-mechanical properties and structural distribution characteristics of the MKP were tested based on the nanoindentation and the X-CT technique, respectively. Then, the 3D structure grid model of the MKP was obtained based on X-CT data, imported into the ABAQUS software for the finite element simulation. Besides, considering the effect of porosity and pore distribution on the damage, the modified MKP constitutive relation was proposed and input into the X-CT nanoindentation model and the RAP nanoindentation model, respectively. It was found that those two models can effectively describe the mechanical and deformation characteristics of the MKP, which verified the correctness of the modified constitutive relationship of MKP. Finally, the influence of pore distribution on the nanoindentation results was predicted based on the RAP nanoindentation model.

Keywords: X-ray computed tomography, random aggregate placement method, damage factor, modified constitutive relation, pore distribution

INTRODUCTION

The production of widely used Portland cement consumes a lot of energy and emits a large amount of carbon dioxide, causing serious environmental pollution. Green building materials are urgently needed in today's world to avoid the deterioration of ecosystems and the intensification of global warming. Magnesium phosphate cement (MPC) is a carbon-free cement that does not emit carbon dioxide during the production process (Walling and Provis, 2016). MPC is considered as a new

type of environmentally friendly cement (Haque and Chen, 2019). Additionally, it is believed as a cementitious material formed by acid-base chemical reaction between water, magnesium oxide, and phosphate. The main chemical reaction equation of potassium MPC is shown in Equation (1):

$$MgO + KH_2PO_4 + 5H_2O \rightarrow MgKPO_4 \cdot 6H_2O$$

where potassium hexahydrate hexahydrate (MKP) is the main hydration product of the MPC (Vinokurov et al., 2018a).

Furthermore, MPC is widely used in solidification of nuclear waste, heavy metals and repair and reinforcement due to its advantages of fast hardening, early high strength, and high viscosity (Li et al., 2017; He et al., 2019; Mestres et al., 2019; Zhenghua et al., 2019), which attracts many scholars to do enormous research on hydration mechanism, durability, and mechanical properties (Ma et al., 2014; Li et al., 2015, 2016).

Liquid radioactive waste (LRW) containing elements such as uranium and thorium is the product of nuclear industry activities which has great harm to the environment and human health. Long-term controlled storage or disposal of LRW is one of the key links in the safe management of radioactive waste (Stefanovsky et al., 2017). Solidification/stabilization (S/S) is the mixing of LRW and binder, thus fixing the LRW in the binder for long-term safe disposal. The S/S is a very effective technique for handling large amounts of the LRW and the MPC is one of the most promising materials for solidifying the radioactive waste (Vinokurov et al., 2019). Four different leaching tests were conducted to determine the effect of the MPC on solidifying heavy metal-containing waste liquid. The results showed that the MPC could successfully solidify the solution containing Cd, Cr, Cu, N, Pb, or Zn (Buj et al., 2010). The radioactive waste containing metal uranium is incompatible with conventional ordinary Portland cement (OPC)-based encapsulation matrices. The reason is that the high alkaline environment and high free water content in the OPC result in volume change of the system and hydrogen generation. Since the MPC has lower pH value and less free water content, it can encapsulate the radioactive waste containing active metals such as uranium (Covill et al., 2011). In addition, the researchers found that the MPC can solidify radioactive waste within actinide and rare earth elements. The method of the MPC curing the LRW has the advantages of simple technology and high physical and chemical stability (Vinokurov et al., 2009, 2018b).

Heavy metals such as Zn, Pb, Cd, As contaminate soils, which are also increasingly serious environmental problems. Heavy metals not only pose a threat to the human health and the environment, but also deteriorate the mechanical properties of the soil, limit the reuse of contaminated sites, and even pose a safety threat to engineering in the polluted areas (Du et al., 2014). As mentioned above, the S/S technique is an effective and economical remediation technology. It mixes the binder MPC with contaminated soil to physically fix or chemically bind harmful contaminants, thus preventing heavy metals from migrating to the environment and enhancing the strength of the soil (Wang Y.S. et al., 2018; Xu et al., 2018). Aiming at the environmental problem of high lead content in soil polluted by lead-acid batteries, researchers found that the MPC could effectively fix lead in soil and convert lead in polluted areas into less mobile contaminant binding forms at an acceptable cost, effectively increasing the strength of polluted soil (Zhang et al., 2015). The factors affecting the solidification effect of the MPC are metal concentration in soil and water-binder ratio of the MPC, curing age and dosage (Wang P. et al., 2017, 2018). In addition, municipal solid waste incineration (MSWI) fly ash pollution is highly toxic, threatening human living environment and health. The MPC can also effectively reduce the toxic pollution of the MSWI fly ash (Fan et al., 2018).

Energy demand and resource extraction activities are one of the major environmental concerns of modern society. The MPC has a good repair and reinforcement effect on concrete structures due to its characteristics of fast hardening and early high strength. The MPC can be injected into cracks from old buildings or bonded with CFRP to reinforce damaged structures, thus delaying the demolition of old buildings and the construction of new buildings, reducing energy, and resource consumption (Li et al., 2017). In addition, the MPC can be produced from industrial by-products, which has a positive impact on the environment and sustainability (Maldonado-Alameda et al., 2017). For example, boron-containing magnesium oxide (B-MgO) was a byproduct of the production of Li_2CO_3 from salt lakes. B-MgO can be used as raw materials to produce MPC (Tan et al., 2014; Formosa et al., 2015). The MPC even can upcycle construction wood waste into rapidshaping cement-bonded particleboards, reducing environmental burden and increasing economic value (Wang L. et al., 2017).

In summary, the mechanical properties of the MPC have an important influence on the solidification of heavy metal contaminated soil and the repair and reinforcement of engineering structures. The main hydration product MKP determines the mechanical properties of the MPC. However, most researches only focus on the application and macro-mechanical properties of the MPC, which do not involve the mechanical properties of the MKP. Therefore, in this paper, the micro-mechanical properties and structural characteristics of the MKP are studied in detail.

Nanoindentation technique and X-ray Computed Tomography (X-CT) technique are the state of the art technologies, which can measure the micro-mechanical properties and 3D structure distribution characteristics of materials. The micro-mechanical properties and creep behavior of cement paste were attained by the nanoindentation technique. The factors affecting the test results of nanoindentation and the contact creep function of various phases in cement paste were determined (Liang et al., 2017a,b; Wei et al., 2017). CT technology was used for *in-situ* monitoring of water and ion intrusion into cement paste and the erosion process was visualized in three dimensions (Yang et al., 2015, 2018). Based on the CT images, pore-scale modeling and micromechanical modeling of cement paste could be obtained (Zhang and Jivkov, 2016; Zhang, 2017). The combination of X-CT and finite element method can more accurately simulate the properties of the materials (Skarzynski and Tejchman, 2016).

Therefore, based on nanoindentation and X-CT techniques, the micro-mechanical properties and structural distribution characteristics of the MKP were investigated. The nanoindentation model of the MKP was established based on the X-CT and the random aggregate placement method. From the perspective of damage factor, the modified constitutive relation of the MKP considering porosity and pore distribution was proposed. Firstly, the 3D microstructure distribution characteristics of the MKP were obtained based on the X-CT technique. The MKP was tested by the nanoindentation to attain the elastic modulus and the indentation load-displacement curves. Then based on the X-CT images, the MKP 3D structure grid model was obtained and imported into ABAQUS software as the nanoindentation model. In addition, the influence equation of pores on the damage factor in MKP constitutive was proposed. The effect of porosity and pore distribution on the MKP damage was studied in detail and the modified MKP constitutive relation considering porosity and pore distribution was verified. Finally, based on the random aggregate placement method (RAP), the RAP nanoindentation model of the MKP was established and the effect of pore distribution on the nanoindentation results was predicted.

MATERIALS AND METHODS

Materials and Specimen Preparation

The experimental material in this research was magnesium potassium phosphate hexahydrate ($MgKPO_4{\cdot}6H_2O$, MKP). The MKP granules were obtained from a pharmaceutical reagent factory in Xuzhou City, Jiangsu Province, China, with a purity of over 99%.

The elastic modulus and internal structure of MKP were tested by nanoindentation and X-CT techniques, respectively. Before the nanoindentation test, the specimens needed to be pretreated: the mass ratio of MKP particles to epoxy resin is 1/10, and these two materials were stirred for 5 min, then the epoxy resin hardened after 6 h as the specimens for the nanoindentation test. Since the nanoindentation test requires high flatness on the surface of specimens, it is necessary to perform smooth pretreatment on the test piece (Zhao et al., 2005; Zheng et al., 2008; Han et al., 2012). The surfaces of the specimens were polished in the order of 400–4,000 mesh sandpaper, canvas, and silk. The surface roughness of the polished specimens was tested by an atomic force microscope to ensure that the roughness was <100 nm. After smoothing the MKP, the testing region was marked and then the structure distribution characteristics of the region was obtained by X-CT.

Methods

X-CT Test

X-ray Computed Tomography (X-CT) technique is one of the most advanced non-destructive testing techniques, which can obtain the internal structure of materials. The density difference between the MKP and the pores leads to the difference of X-ray absorption coefficient and gray value in the X-CT images. Therefore, the two materials can be distinguished according to the gray value division (Sun et al., 2014). The X-ray projections were obtained with an exposure time of 0.32 s at an accelerating voltage of 150 kV and 140 μA beam current using a tungsten target.

Nanoindentation Test

In nanoindentation test, the elastic modulus of the specimens was measured by nanoindentation instrument manufactured by Agilent Company, USA with the Berkovich indenter (a positive triangular pyramid with an angle of 65.35° between the center line and the side). The appropriate loading depth and indentation spacing should be selected for nanoindentation test (Al-Amoudi, 2002; Němeček et al., 2009; Wang et al., 2009; Chen et al., 2010). Since in this study the nanoindentation test was simulated, a larger indentation depth was required to match the X-CT resolution and obtain a sufficient number of finite element meshes. The maximum indentation depth of the nanoindentation instrument used in this study is 20 μm. Hence, the indentation depth was set to 20 μm and the indentation point spacing was set to 200 μm.

Figure 1A displays a typical Scanning Electron Microscope (SEM) image of the nanoindentation. However, the indentation area includes not only the matrix MKP but also the pores, shown in **Figure 1B**. Therefore, the material properties, volume fractions and distribution characteristics of the matrix and pores both affect the test results of the nanoindentation test. The nanoindentation process can be divided into three stages: first, the elastic deformation of the specimen occurred at the loading stage, followed by the plastic deformation with the increase of the load. Then the constant loading stage appeared when the maximum indentation depth was reached. Finally, the unloading stage took place, reflecting the elastic recovery of the indentation points. The typical load-displacement curve of the nanoindentation is shown in **Figure 1C**. The curve consists of three parts: the loading stage, the constant loading and the unloading stage. The loading time of the loading stage was 1,000 s. When the indentation depth reached 20 μm, the constant loading kept for 100 s, followed by the unloading stage for 300 s. The contact stiffness S is fitted by the upper elastic part of the unloading curve. According to the Oliver-Pharr principle (Oliver and Pharr, 2011), the elastic modulus of the indentation point can be calculated by Equation (1).

$$E = \frac{1-\nu^2}{\frac{2\gamma}{S}\sqrt{\frac{A}{\pi}} - \frac{1-\nu_i^2}{E_i}} \tag{1}$$

where E and ν indicate the elastic modulus and Poisson's ratio of tested material, γ is a correction factor ($\gamma = 1.034$), S is the contact stiffness, A is the contact area, ν_i and E_i denote the parameters of indenter ($\nu_i = 0.07$, $E_i = 1{,}141$ GPa).

Random Aggregate Placement Method

In the mesoscopic numerical analysis of cement-based materials, it is important to study the numerical morphology and gradation of aggregates, pores and other phases, which directly affect the mechanical properties of the materials (Wang et al., 2016).

In order to improve the accuracy of numerical simulation in material mesomechanics, a 3D random concave-convex

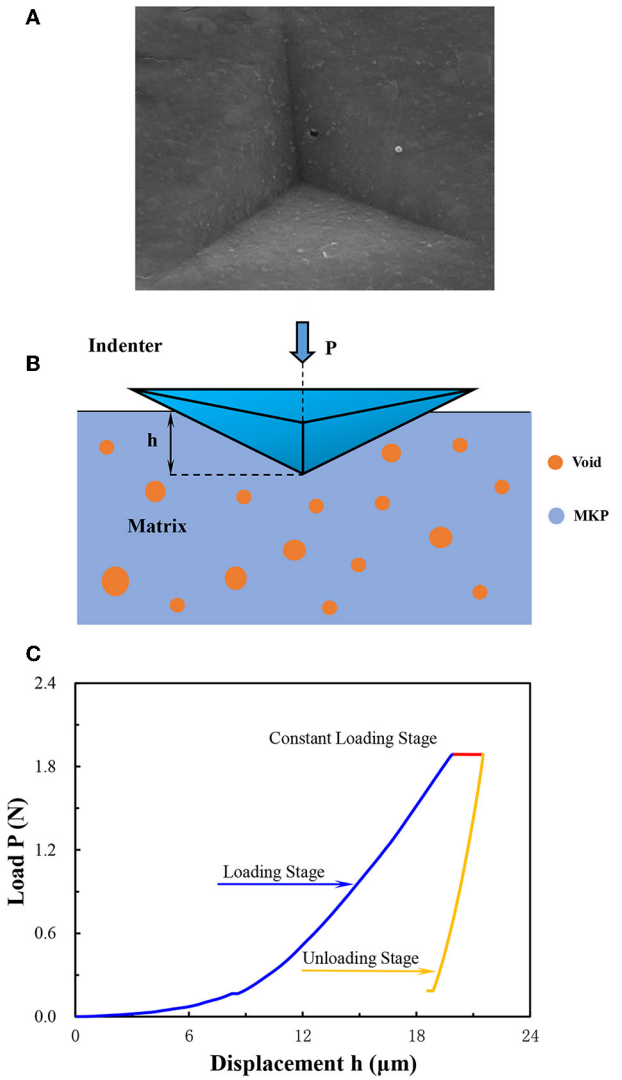

FIGURE 1 | (A) A typical SEM image of the nanoindentation; **(B)** The schematic diagram of nanoindentation; **(C)** The typical load-displacement curve of nanoindentation.

aggregate modeling method with grid pre-generated was proposed (Wang B. et al., 2018). Before placing the aggregate, grid partition was needed to record all node information and unit information in the model. In the three-dimensional polar coordinate system, the position of any point in space could be determined by three parameters r, θ, φ. It is impossible to use infinite number of spherical aggregate surface nodes in the numerical modeling. It is found through trial calculation that the spherical aggregate established by the following method could meet the calculation requirements: take r as the aggregate radius and take a point, respectively, at every 45° in the direction of θ and φ, forming an approximate spherical area composed of 26 points in the space. The three-dimensional spherical aggregate had a total of 26 nodes and the surface was divided into 48 triangular regions. The generation of the concave-convex aggregate could be achieved when the apex of each aggregate fluctuates randomly with respect to its initial position. After the single concave-convex aggregate was generated, the aggregate library could be generated according to the required gradation.

The flow path of placing aggregate was as follows (Wang B. et al., 2017): firstly, the aggregates to be placed were sorted according to the radius from large to small. Secondly, the central point of the non-throwing unit was selected to place aggregate based on whether there was a geometric boundary point inside the aggregate. If there were any, the placing failed. Thirdly, if the interior of the aggregate did not contain the geometric boundary point and the outer boundary element point of the delivered aggregate, the delivery was successful. Fourthly, when the delivery failed, the aggregate was rotated to continue judging and the position was reselected after a certain number of rotations. If all the delivery failed in the center position of all the non-throwing areas, the aggregate failed to be delivered. In order to prevent the delivery process from entering an infinite loop, the failed aggregate was stored in the specified set. Fifthly, the aggregate information was updated after delivering successfully. In this study, when the random aggregate placement method was adopted to establish the MKP nanoindentation model, the pores were regarded as the aggregates and put into the MKP matrix.

THE RESULTS OF EXPERIMENTS AND RANDOM AGGREGATE PLACEMENT

The Results of X-CT

A total of 15 indentation area on the MKP specimens was scanned by X-CT. Three hundred and twenty two-dimensional CT slices with the resolution of 1,000 × 1,000 pixels were obtained by each X-CT scan and the spatial resolution was 0.5 μm voxel. Then the images were processed by the AVIZO software to gain the structural distribution characteristics and volume fraction of each phase in each indentation area. Subsequently, the tetrahedral mesh generated by AVIZO software was imported into ABAQUS software as the X-CT nanoindentation model of the MKP.

The X-CT images of the MKP was imported into the AVIZO software. Based on the difference of gray value between the MKP and pores, the slices were divided into two phases. Determining the threshold value of the phases was the premise to correctly distinguish MKP from pore. Therefore, a MKP particle with the size of about 3 mm was tested by mercury intrusion porosimeter (MIP) and X-CT, respectively. The porosity of the MKP particle was 28.43% from the MIP. Then the threshold of the X-CT slices of the particle was debugged. It was found that when the parts with the gray range of 0–149 and 149–207 were adopted to divide the pores and the MKP, the voxel number of the MKP and the pores were 5.33E8 and 2.12E8. So, that is to say, the porosity of the MKP particle is 2.12E8 ÷ (2.12E8 + 5.33E8) = 28.46%, which was almost consistent with the test result. Therefore, the gray threshold of distinguishing the MKP from pore was 149. For example, the gray value 149 was used as the threshold to divide the MKP and pores, when the X-CT data of the P_{14} indentation point region was processed. The 160th slice of the P_{14} indentation

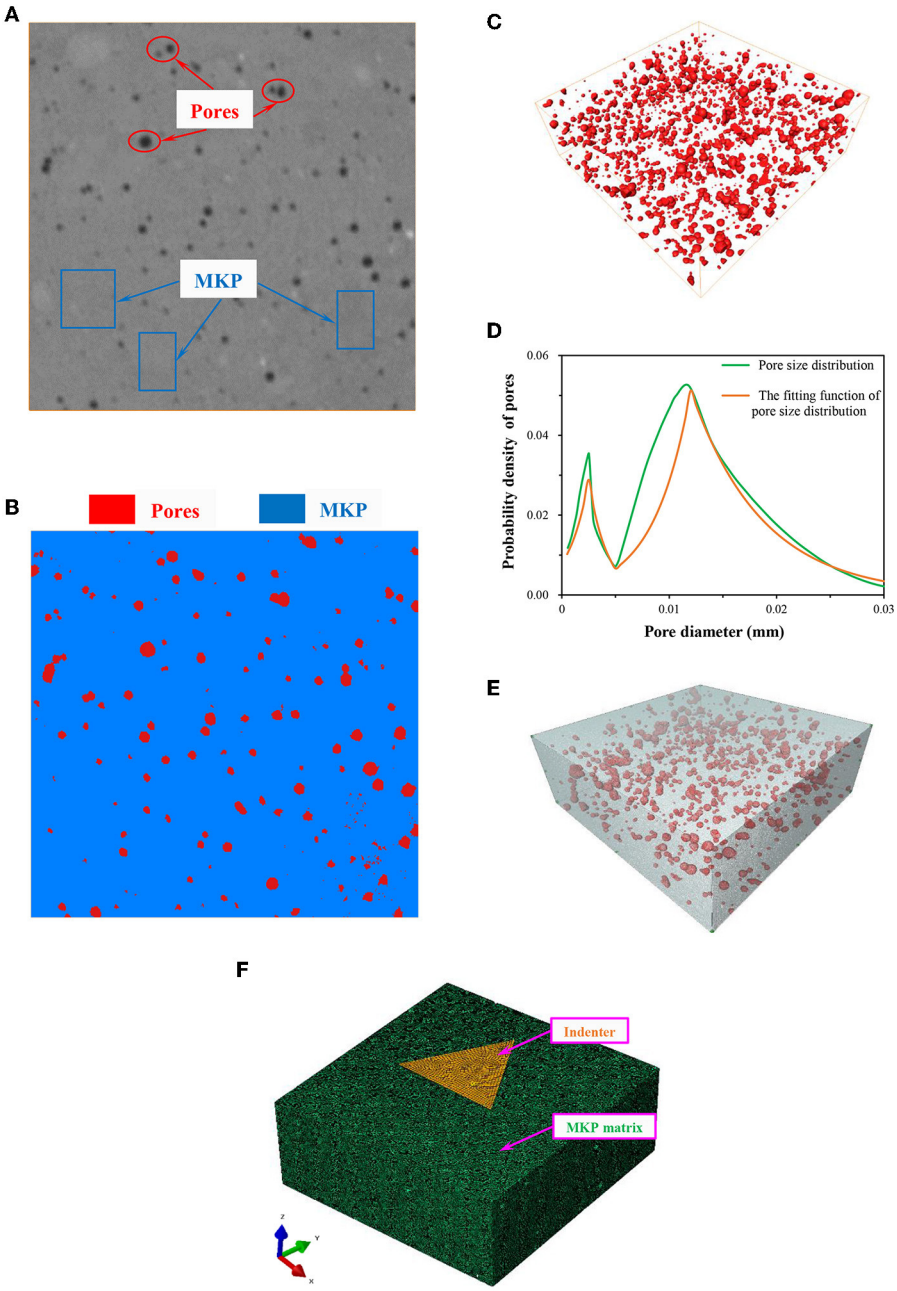

FIGURE 2 | The modeling process of P_{14} indentation point based on X-CT **(A)** the 160th slice of the P_{14} indentation point; **(B)** the result of the threshold segmentation of the 160th slice; **(C)** the distribution characteristics of the pores; **(D)** the pore size distribution curve; **(E)** the tetrahedral meshes based on the X-CT model; **(F)** The X-CT nanoindentation model of the MKP.

point is shown in **Figure 2A**. The dark gray area was the pores and the light gray area was the MKP. **Figure 2B** displays the result of the threshold segmentation of the 160th slice, where the red part indicates pores and the blue part represents the MKP. The distribution characteristics of the pores in the P_{14} indentation point are shown in **Figure 2C** and the green curve in **Figure 2D** denotes the statistical pore size distribution. The yellow curve in **Figure 2D** displays the pore distribution function curve, which will be discussed in detail in section The Effect of Porosity on the Damage Factor. Additionally, the voxel number of the two phases was 2.9412E8 and 2.528E7, respectively. In other words, the volume fractions of the MKP and pores after the threshold segmentation were $2.9412E8 \div (2.9412E8 + 2.528E7) = 92.1\%$ and $2.528E7 \div (2.9412E8 + 2.528E7) = 7.9\%$, respectively.

TABLE 1 | The porosity of 15 indentation points (%).

	P_{i1}	P_{i2}	P_{i3}	P_{i4}	P_{i5}
P_{1j}	10.8	5.1	22.6	7.9	9.8
P_{2j}	12.6	18.5	14.3	20.7	12.4
P_{3j}	3.4	15.9	6.6	9.1	16.5

TABLE 2 | The elastic modulus (GPa) and peak loads (N) of nanoindentation points.

	P_{i1}	P_{i2}	P_{i3}	P_{i4}	P_{i5}
P_{1j}	22.52, 1.91	25.26, 2.19	17.66, 1.57	23.88, 2.04	22.98, 1.96
P_{2j}	21.71, 1.85	19.24, 1.67	20.98, 1.78	18.38, 1.61	21.80, 1.85
P_{3j}	26.14, 2.23	20.30, 1.74	24.51, 2.12	23.31, 1.99	20.05, 1.72

Similarly, the porosity of each indentation point region could be obtained. There were 15 indentation points numbered P_{11}-P_{35}, as shown in **Table 1**.

Finally, the tetrahedral meshes were generated based on the X-CT model, as shown in **Figure 2E**, in which the gray portion indicates the MKP and the red portion represents the pores. The tetrahedral mesh model was imported into the finite element software ABAQUS and then the pore set was deleted. The remaining MKP set was used as the compressive matrix of the nanoindentation model. A triangular pyramid model with a height of 30 μm was established by CAD and imported into the finite element software ABAQUS as the indenter of the nanoindentation model. The X-CT nanoindentation model of the MKP was obtained by assembling the MKP matrix with the triangular pyramid indenter, as shown in **Figure 2F**, where the green part represents the MKP matrix and the yellow part denotes the triangular pyramid indenter. When the indenter was assembled with the MKP substrate, the upper surface of the triangular pyramid indenter was parallel to the upper surface of the MKP substrate, in which the central axes of the indenter and the MKP substrate were coincident. Additional details on the X-CT nanoindentation model were discussed in section Simulation Based on X-CT Results.

The Results of Nanoindentation

In this study, 15 marked areas were selected on the MKP specimens for nanoindentation test and the indentation points were numbered P_{11}-P_{35} with the elastic modulus and the peak loads shown in **Table 2**. There are two data at each indentation point, the elastic modulus and the peak loads, respectively. For example, the data "22.52, 1.91" for the indentation point P_{11} indicates that the elastic modulus and the peak load at the indentation point P_{11} are 22.52 GPa and 1.91 N, respectively. It can be seen that the elastic modulus of all the indentation points are in the range of 17.66–26.14 GPa. The average elastic modulus of the indentation points is 21.91 GPa. Besides, the peak loads fluctuate in the range of 1.57–2.23 N and the average peak load is 1.88 N. The fluctuations of the elastic modulus and the peak loads are mainly caused by the difference in volume fraction and distribution characteristics of the matrix and pores in each indentation area.

The Results of Random Aggregate Placement

First, a matrix part of 500 × 500 × 160 μm was built in ABAQUS and was meshed with the grid unit size of 1.5 μm and the element type of linear hexahedral elements C3D8R. Then, based on the random aggregate placement method (RAP), the RAP nanoindentation model of the P_{14} indentation point was established. The pores were randomly placed in the matrix part and the porosity was set to 7.9%. Thus, the RAP nanoindentation model corresponding to the X-CT nanoindentation model was obtained. As shown in **Figure 3A**, the blue part indicates the MKP set and the white part represents the pores set. Subsequently, the pore set was deleted and the remaining MKP matrix was assembled with the triangular pyramid indenter. Hence, the RAP nanoindentation model of the P_{14} indentation point was displayed in **Figure 3B**, where the blue part denotes the MKP matrix and the yellow part indicates the triangular pyramid indenter. When the indenter was assembled with the MKP substrate, the upper surface of the triangular pyramid indenter was parallel to the upper surface of the MKP substrate, in which the central axes of the indenter and the MKP substrate were coincident. Additional details on the model were discussed in section Simulation Based on the Random Aggregate Placement Method (RAP). Similarly, the RAP nanoindentation models of other indentation points were obtained.

SIMULATION BASED ON X-CT RESULTS

In section Simulation Based on X-CT Results, the nanoindentation test of the MKP was simulated based on the X-CT nanoindentation model. Firstly, the input parameters and boundary conditions of the X-CT model were determined. Secondly, considering the effect of pores on damage, the modified MKP constitutive relation was proposed and input into the X-CT nanoindentation model. Then, the equations of influence of porosity and pore distribution on the damage factor were proposed. Finally, the correctness of the modified damage factor equation was verified with the average relative error of 3.2% by comparing the numerical results with the experimental results.

The X-CT Nanoindentation Model

The Input Parameters and Boundary Condition

Since the elastic modulus of the diamond indenter was much larger than the elastic modulus of the MKP, the deformation of the indenter during the indentation process was negligible. Consequently, the indenter in the nanoindentation model was set as a rigid body without deformation and was meshed with the mesh size of 5 μm. During the contact between the indenter and the MKP, the contact surface was assumed to be smooth. Material properties were the extremely critical input parameters for the finite element model. Material parameters were not required for the indenter as a rigid body. The material properties of the MKP were verified in the previous paper: the density was 1.864 g/cm^3, the elastic modulus was 37.3 GPa, the Poisson's ratio was 0.2,

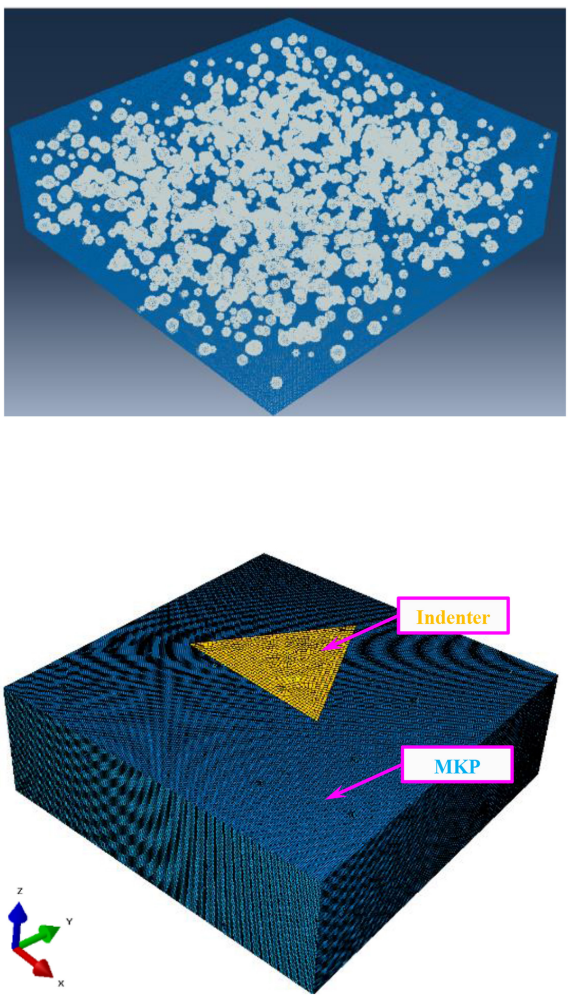

FIGURE 3 | The modeling process of P_{14} indentation point based on RAP **(A)** the distribution characteristics of the pores; **(B)** the RAP nanoindentation model of the MKP.

and the compressive strength and tensile strength were 75.6 and 11.3 MPa, respectively (Li et al., 2018a). The above MKP material parameters were input into the nanoindentation model.

In the X-CT nanoindentation model, the six degrees of freedom of all nodes on the bottom surface of the MKP substrate were limited to zero, indicating that it was completely fixed, while the nodes of the other five surfaces were not limited. Five degrees of freedom of the indenter was restricted except Z direction, so they could only move in the directions of loading and unloading. Besides, the tip of the rigid indenter was regarded as a reference point applied with a displacement of about 20 μm. The model was solved by ABAQUS dynamic analysis with the total running time of 1.4×10^{-6}. The loading time-amplitude conformed to the following rules. When the time was between 0 s and 10^{-6}, the indenter was in the loading stage with the displacement from 0 to 20 μm. When the time was in the range of 10^{-6} to 1.1×10^{-6}, the indenter was in the constant loading without movement. During the period of 1.1×10^{-6} to 1.4×10^{-6}, the indenter was in the unloading phase with the displacement reducing from 20 to 16.2 μm. The relationship between amplitude and time is as follows:

when $t \leq 10^{-6}$,

$$A = t \times 10^{6} \tag{2}$$

when $10^{-6} < t < 1.1 \times 10^{-6}$,

$$A = 1 \tag{3}$$

when $1.1 \times 10^{-6} < t < 1.4 \times 10^{-6}$,

$$A = -2.1\left(t - 10^{-6}\right)^{2} \times 10^{12} + 1 \tag{4}$$

where A is the amplitude, t represents time.

The Constitutive Relation of the MKP

The MKP constitutive relation was plastic damage model and determined in previous studies (Li et al., 2018a) as follows:

$$\varepsilon_c = \left(700 + 172\sqrt{f_c}\right) \times 10^{-6} \tag{5}$$

when $\varepsilon < 0.4\varepsilon_c$,

$$\sigma/f_c = 1.08\varepsilon/\varepsilon_c \tag{6}$$

when $0.4\varepsilon_c \leq \varepsilon \leq \varepsilon_c$,

$$\sigma/f_c = 1.46\varepsilon/\varepsilon_c - 0.08(\varepsilon/\varepsilon_c)^2 - 0.54(\varepsilon/\varepsilon_c)^3 \tag{7}$$

when $\varepsilon > \varepsilon_c$,

$$\sigma/f_c = \frac{\varepsilon/\varepsilon_c}{2.4(\varepsilon/\varepsilon_c - 1)^2 + \varepsilon/\varepsilon_c} \tag{8}$$

where subscript c indicates "compressive," ε_c is the corresponding peak compressive strain, f_c denotes the compressive strength of the MKP, namely 75.6 MPa.

$$\varepsilon_t = f_t^{0.65} \times 65 \times 10^{-6} \tag{9}$$

when $\varepsilon \leq \varepsilon_t$,

$$\sigma/f_t = \varepsilon/\varepsilon_t \tag{10}$$

when $\varepsilon > \varepsilon_t$,

$$\sigma/f_t = \frac{\varepsilon/\varepsilon_t}{15.3(\varepsilon/\varepsilon_t - 1)^{1.7} + \varepsilon/\varepsilon_t} \tag{11}$$

where subscript t indicates "tensile," ε_t is the corresponding peak tensile strain, f_t denotes the peak tensile strength of the MKP, namely 11.3 MPa.

Damage Factor of the MKP and Simulation Results

According to the literature (Birtel and Mark, 2006), the classical damage factor can be calculated from Equations (12)–(14):

$$d = 1 - \frac{\sigma E^{-1}}{\varepsilon^{pl}(1/b - 1) + \sigma E^{-1}} \tag{12}$$

$$\varepsilon^{in} = \varepsilon - \sigma E^{-1} \tag{13}$$

$$\varepsilon^{pl} = b\varepsilon^{in} \tag{14}$$

where d indicates the damage factor of the MKP, σ is the stress, E represents the elastic modulus, ε^{in} and ε^{pl} denote the inelastic strain and the plastic strain, b is the constant ($b_c = 0.7$, $b_t = 0.1$), subscript c and t indicate "compressive" and "tensile," respectively.

Since the elastic modulus of MKP is 37,300 MPa, the compressive and tensile damage factor of the MKP are expressed as:

$$d_c = 1 - \frac{\sigma/37300}{0.3\varepsilon^{in} + \sigma/37300} \tag{15}$$

$$d_t = 1 - \frac{\sigma/37300}{0.9\varepsilon^{in} + \sigma/37300} \tag{16}$$

where the relationship between σ and ε can be calculated from Equations (6)–(11) in section The Constitutive Relation of the MKP. Thus, the curve of the classical damage factor is shown as the blue curves in **Figure 4**.

The above boundary conditions, MKP material parameters, constitutive relations and damage factors were input into the X-CT nanoindentation model of the P_{14} indentation point. Then the simulated load-displacement curve based on the classical damage factor were expressed as the red curve in **Figure 5**, in which the simulated peak load is 2.25 N. The blue curve in **Figure 5** indicates the test load-displacement curve with a peak load of 2.04 N. The relative difference was used to compare the simulated peak loads with the experimental peak loads, defined as

$$R = \frac{|L_E - L_S|}{L_E} \times 100 \tag{17}$$

where L_E indicates the experimental peak load, L_S is the simulated peak load. It can be seen that the relative error of the peak load of the classical simulation is 10.3% and the classical simulated load-displacement curve is above the experimental curve. The poor simulation result was because the classical simulation did not consider the damage contributed by the pores. Since the matrix in the nanoindentation model contained two phases: the MKP and pores, the pores inevitably affected the simulation results, so the influence coefficient of the pores on the damage factor was introduced as χ. Then the modified damage factor considering the influence of the pores was expressed as

$$d_c = \chi\left(1 - \frac{\sigma/37300}{0.3\varepsilon^{in} + \sigma/37300}\right) \tag{18}$$

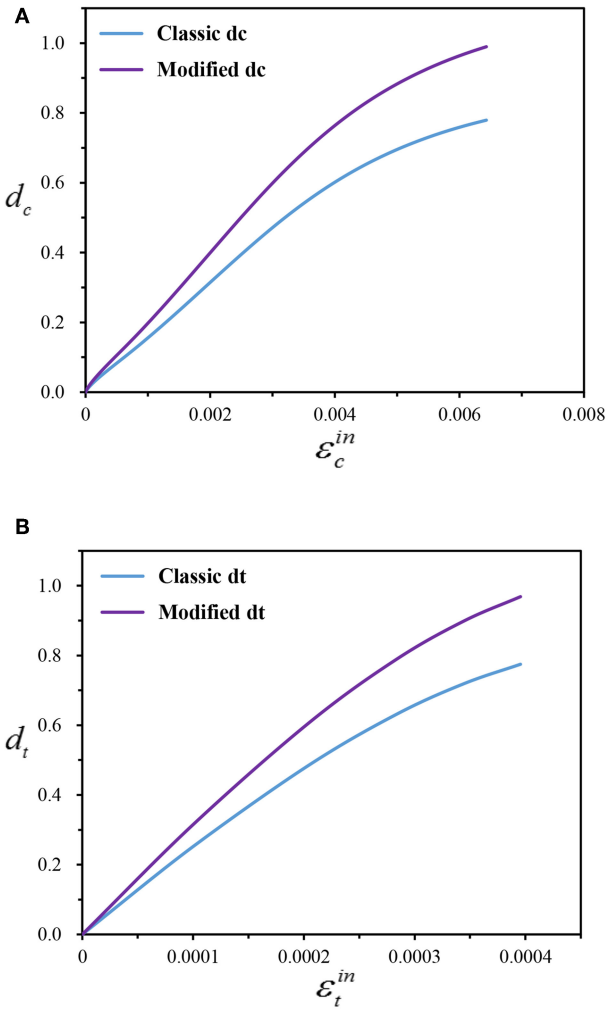

FIGURE 4 | The curves of compressive and tensile damage factors: **(A)** the compressive factor **(B)** the tensile factor.

$$d_t = \chi\left(1 - \frac{\sigma/37300}{0.9\varepsilon^{in} + \sigma/37300}\right) \tag{19}$$

The influence coefficient of P_{14} indentation point was debugged. It was found that the simulation result with the influence coefficient χ 1.262 was the closest to the experimental result. The modified damage factor with the influence coefficient of 1.262 is shown as the purple curve in **Figure 4** and the yellow curve of **Figure 5** displays the modified simulated load-displacement curve. The modified simulated peak load was 2.11 N with the relative error of only 3.4%. The modified simulation accuracy was greatly improved, indicating that it was necessary to consider the influence of pores on the damage. The modified simulated nephogram is shown in **Figure 6**.

Figure 6A shows the simulated stress nephogram of the model at the time 10^{-6}. It can be seen that the shape of the indentation area is a triangular pyramid and the mesh deformity in contact with the three edges of the indenter is severe due to the stress

concentration. The stress at the bottom of the indentation area is larger and the upward stress decreases gradually. As a result of the extrusion of the indenter, the upper end of the indentation region produces a crowding effect. The stress distribution of the middle section in the X direction is displayed in **Figure 6B** at time 0 and 10^{-6}, respectively. It can be seen that the stress in the lower part of the indenter is larger and gradually decreases toward the far side. The stress nephogram shows an elliptic shape and extends outward in layers. During the loading process, the pores in the lower region of the indenter were squeezed and seriously deformed, such as the red marked pores being extruded from the initial quasi-circular into a long strip. In addition, the existence of pores may result in stress concentrations, just as the sudden increase of stress around the pore marked with yellow. Moreover, pores may affect the path of stress transfer. For instance the pink marked pore hindered the development of stress. **Figure 6C** is the distribution of the compressive damage of the model when the time is 10^{-6}. It is observed that the element damage in the larger area around the indenter is serious, that is to say, the pressing of the indenter greatly affects the stress state of the surrounding area. **Figure 6D** displays the distribution of the compressive damage in the middle section of the Y direction at time 0 and 10^{-6}, respectively. It can also be seen that the loading of the indenter leads to severe distortion of the pores, such as the green marked pores being significantly flattened. In addition, the development of damage may be affected by the pores, such as the damage transmission path in pink marked area was affected by the pores.

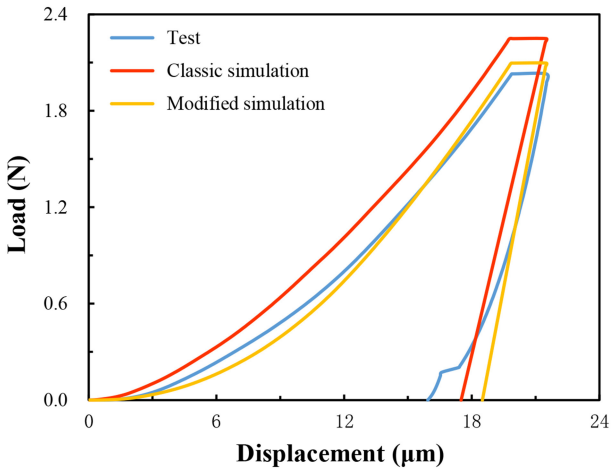

FIGURE 5 | Comparison of the load-displacement curves of P_{14} indentation point between experimental results and simulation results.

It was the same as the process of debugging the influence coefficient of P14 indentation point with the influence coefficient of 1.262 in the fourth paragraph of this subsection. The influence coefficient of the porosity of the other indentation point model on the damage factor was debugged, thereby making the simulation results most consistent with the experimental results. Thus, the optimal influence coefficient values and the optimal simulated peak loads of each indentation point were obtained as shown in **Table 3**. There are two data at each indentation point, the optimal influence coefficient values and the optimal simulated peak loads, respectively. For example, the data "1.248, 1.84" for the indentation point P_{11} indicates that the optimal influence coefficient value and the optimal simulated peak load at the indentation point P_{11} are 1.248 and 1.84 N, respectively. The average relative error of the peak load simulated by the X-CT nanoindentation model was 3.8%, which indicates that the accuracy of the model was greatly improved after debugging the optimal influence coefficient.

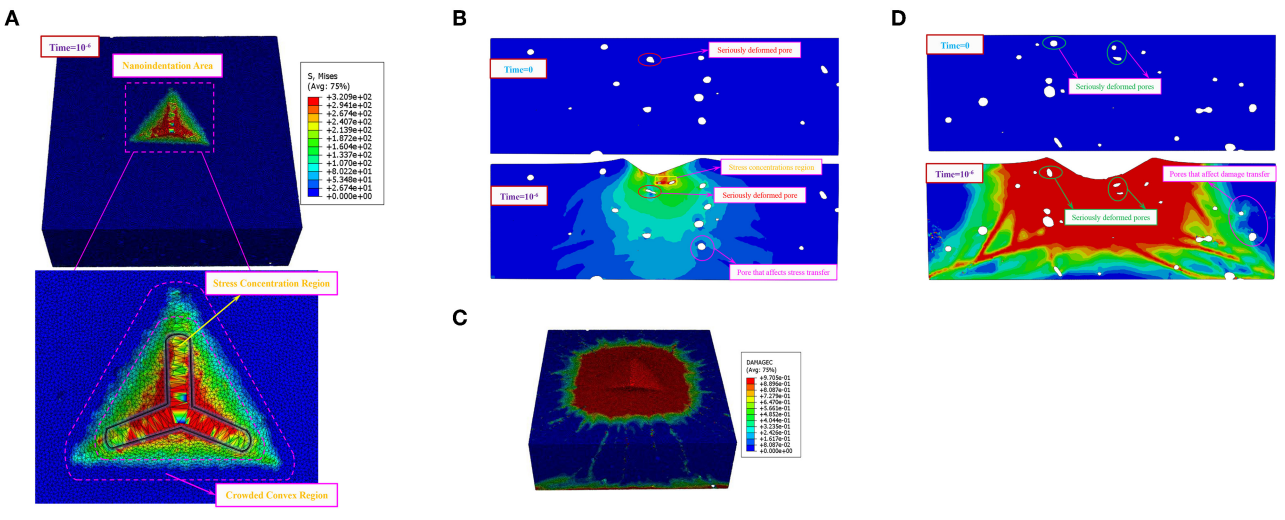

FIGURE 6 | The modified simulated nephogram of P_{14} **(A)** the stress distribution of the model **(B)** the stress distribution of the middle section in the X direction **(C)** the distribution of the compressive damage of the model **(D)** the compressive damage distribution of the middle section in the Y direction.

TABLE 3 | Optimal influence coefficient χ and simulated peak loads (N) for each indentation point.

	P_{i1}	P_{i2}	P_{i3}	P_{i4}
P_{1j}	1.248, 1.84	1.061, 2.31	1.537, 1.63	1.262, 2.11
P_{2j}	1.381, 1.93	1.266, 1.74	1.335, 1.85	1.415, 1.71
P_{3j}	0.966, 2.27	1.413, 1.70	1.150, 2.05	1.220, 2.04

The Effect of Porosity and Pore Distribution on the Damage Factor

The influence of pores on the damage factor came from two aspects: on the one hand, the larger the porosity was, the greater the damage factor was. On the other hand, under the same porosity, different pore distributions led to differences in damage factors. Therefore, the total influence coefficient χ of pores on the damage factor was a comprehensive reflection of the influence of porosity and pore distribution. Then, the influence coefficient of porosity and pore distribution on the damage factor were defined as β and λ, respectively. Thus, the relationship of the three coefficients was assumed to be:

$$\chi = \beta\lambda \tag{20}$$

Considering the influence of porosity and pore size on the damage factor, the modified MKP damage factor is expressed as follows:

$$d_c = \chi \times \left(1 - \frac{\sigma/37300}{0.3\varepsilon^{in} + \sigma/37300}\right) = \beta\lambda \times \left(1 - \frac{\sigma/37300}{0.3\varepsilon^{in} + \sigma/37300}\right) \tag{21}$$

$$d_t = \chi \times \left(1 - \frac{\sigma/37300}{0.9\varepsilon^{in} + \sigma/37300}\right) = \beta\lambda \times \left(1 - \frac{\sigma/37300}{0.9\varepsilon^{in} + \sigma/37300}\right) \tag{22}$$

After obtaining the total pore influence coefficient of 12 indentation points, the effects of porosity and pore distribution on the damage factors were further discussed.

The Effect of Pore Size Distribution on the Damage Factor

The strength of the material was affected not only by the porosity, but also by the pore distribution. The pore structure of the material was complex and the pore size reflected the dominant characteristics of the pore structure (Hou et al., 2019). Therefore, the pore size was selected as an important factor affecting the damage factor. Considering the distribution and contribution of pore size, the effect of pore distribution on the damage factor was defined as λ.

First, the actual pore size distribution of the material was complex. Previous studies indicated that the pore distribution functions of cement-based materials and rock masses were similar, which all had an exponential function distribution (Ju et al., 2008). It was also assumed that the pore size distribution of MKP conformed to the exponential function distribution, as shown in Equation (23):

$$p(D) = E\exp\left(-\frac{D}{F}\right) \tag{23}$$

where D indicates the pore size (mm), E and F represent the parameter of the exponential function. The values of the parameters E and F can be solved by fitting the hole structure results based on the X-CT statistics.

Secondly, gray correlation analysis was a good method to reflect the correlation between various factors, which could be used to study the influence of pore size on strength. The correlation value had a power function relation with pore size. The larger the pore size was, the lower the strength of the material was Zhang and Zhang (2007), Li et al. (2018b). In addition, the influence coefficient was zero when the pore size was zero. Therefore, the influence function of pore size was assumed to be:

$$\lambda(D) = GD^H \tag{24}$$

where $\lambda(D)$ is the influence coefficient associated with the pore size, G and H denote the parameter of the influence function. By fitting the relationship between the strength and the test results of pore structure with gray correlation analysis, the values of the parameters G and H can be determined.

Combining the MKP pore distribution function with the pore size influence function, the influence coefficient of the pore size distribution on the damage factor was obtained as follows:

$$\lambda = \frac{\int_{d_{\min}}^{d_{\max}} \lambda(D)\, p(D)\mathrm{d}D}{\int_{d_{\min}}^{d_{\max}} p(D)\mathrm{d}D} \tag{25}$$

where λ is the influence coefficient depending on the pore size distribution, $D_{\min}$ and $D_{\max}$ indicate the minimum diameter and the maximum diameter (mm) of the pores, respectively.

Due to the complexity of the integration process, the Equation (25) was substituted by the Equation (26) for the sake of simplicity:

$$\lambda = \frac{\sum_{i=1}^{n} c_i\lambda_i}{c} \tag{26}$$

where c_i and λ_i represent the porosity and the influence coefficient of the *i-th* interval when the pore size range is divided into n intervals. c_i is related to the pore size distribution, namely, $c_i = \sum_{D_i}^{D_{i+1}} p(D)\mathrm{d}D$. The value of λ_i is the influence coefficient of the pore median of the *i-th* interval. c indicates the total porosity, namely, $c = \sum_{i=1}^{n} c_i$. The smaller the interval is, the closer the Equation (26) is based on the Equation (25).

The Effect of Porosity on the Damage Factor

According to the porosity results based on X-CT statistics, the porosity of the MKP nanoindentation area was between 3 and 23%. Therefore, the maximum porosity in this study was

TABLE 4 | Simulation result after considering the pores influence.

Indentation point	Total porosity (%)	Grading porosity (%)									Test peak load (*N*)	Influence coefficient χ	Simulation result of X-CT (*N*)	Error (%)
		0.0005–0.0025 (mm)	0.0025–0.005 (mm)	0.005–0.0085 (mm)	0.0085–0.012 (mm)	0.012–0.0145 (mm)	0.0145–0.017 (mm)	0.017–0.02 (mm)	0.02–0.024 (mm)	0.024–0.03 (mm)				
P_{14}	7.9	0.66	0.47	0.62	1.74	1.48	1.02	0.81	0.64	0.46	2.04	1.26	2.11	3.4
P_{15}	9.8	1.86	2.06	0.95	1.57	1.37	0.98	0.62	0.21	0.12	1.96	1.18	1.90	3.1
P_{25}	12.4	0.68	0.93	1.12	2.48	2.05	1.80	1.61	1.02	0.73	1.85	1.40	1.89	2.4
P_{35}	16.5	2.15	2.48	1.82	3.14	2.54	1.98	1.32	0.68	0.41	1.72	1.37	1.79	4.2

considered as 30%. According to the pore distribution curve of P_{14} in **Figure 2D**, the pore distribution function of the P_{14} indentation point was fitted as shown in the Equation (27). The yellow curve in **Figure 2D** displays the pore distribution function curve.

$$p(D) = \begin{cases} 0.0079e^{518D}, & 0.0005 < D < 0.0025 \\ 0.125e^{-587D}, & 0.0025 < D < 0.005 \\ 0.00154e^{292D}, & 0.005 < D < 0.012 \\ 0.31e^{-150D}, & 0.012 < D < 0.03 \end{cases} \quad (27)$$

According to the Equation (27), the pore size range was divided into nine intervals, as listed in **Table 4**. The grading porosity indicates the percentage of the pore volume fraction in this interval. The regression values of the parameters G and H in Equation (21) were 2.4 and 0.18, respectively, by fitting the relationship between the load and the pore distribution of each indentation point. The parameters λ_1, λ_2, λ_3, λ_4, λ_5, λ_6, λ_7, λ_8, and λ_9 were determined as 0.745, 0.878, 0.976, 1.052, 1.102, 1.137, 1.170, 1.207, and 1.253, respectively, according to the Equation (26). Thus, the influence coefficient λ of the pore distribution was 1.06. Because the total pore influence coefficient χ of P_{14} was 1.262, the influence coefficient β of porosity on damage was 1.191 according to the Equation (21). Similarly, the influence coefficient of the porosity of each indentation point could be obtained as **Table 3**. **Figure 7** displays the scatter plot about the coefficient β and the porosity. Then the relationship between the porosity and the influence coefficient β was gained by fitting the scatter plot:

$$\beta = \frac{17c+1}{9c+1} \quad (28)$$

where c denotes the porosity, R^2 represents the correlation coefficient of the fitted equation. The R^2-value is 0.98, which means that the fitted curve has high accuracy.

Considering the influence of porosity and pore size on the damage factor, the modified MKP damage factor is expressed as follows:

$$d_c = \beta\lambda \times \left(1 - \frac{\sigma/37300}{0.3\varepsilon^{in} + \sigma/37300}\right) = \frac{17c+1}{9c+1} \times \frac{\sum_{i=1}^{n} c_i\lambda_i}{c} \times \left(1 - \frac{\sigma/37300}{0.3\varepsilon^{in} + \sigma/37300}\right) \quad (29)$$

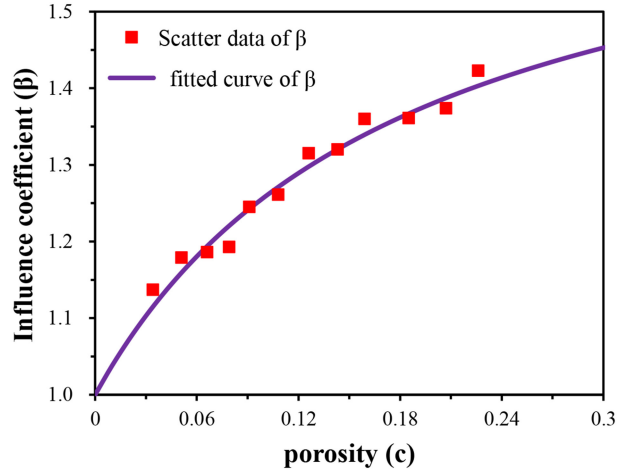

FIGURE 7 | The scatter plot about the coefficient β and the porosity.

$$d_t = \beta\lambda \times \left(1 - \frac{\sigma/37300}{0.9\varepsilon^{in} + \sigma/37300}\right) = \frac{17c+1}{9c+1} \times \frac{\sum_{i=1}^{n} c_i\lambda_i}{c} \times \left(1 - \frac{\sigma/37300}{0.9\varepsilon^{in} + \sigma/37300}\right) \quad (30)$$

Verification of the Modified Damage Factor Equation

The damage factors calculated by Equations (29) and (30) were input into the X-CT nanoindentation model and the three indentation points of P_{15}, P_{25}, and P_{35} were simulated, respectively, to verify the accuracy of the modified damage factor equation. **Table 4** shows some input parameters and simulation results. The simulated peak loads of the three indentation points were 1.90, 1.89, and 1.79 N with the relative errors of 3.1, 2.4, and 4.2%, respectively. The average relative error was 3.2%. Thus, the assumptions that the relationship between the influence coefficient β and λ, the MKP pores conforms to the exponential distribution and the influence function of the pore size distribution were correct. That is, the modified damage factor equation considering the pores influence was valid.

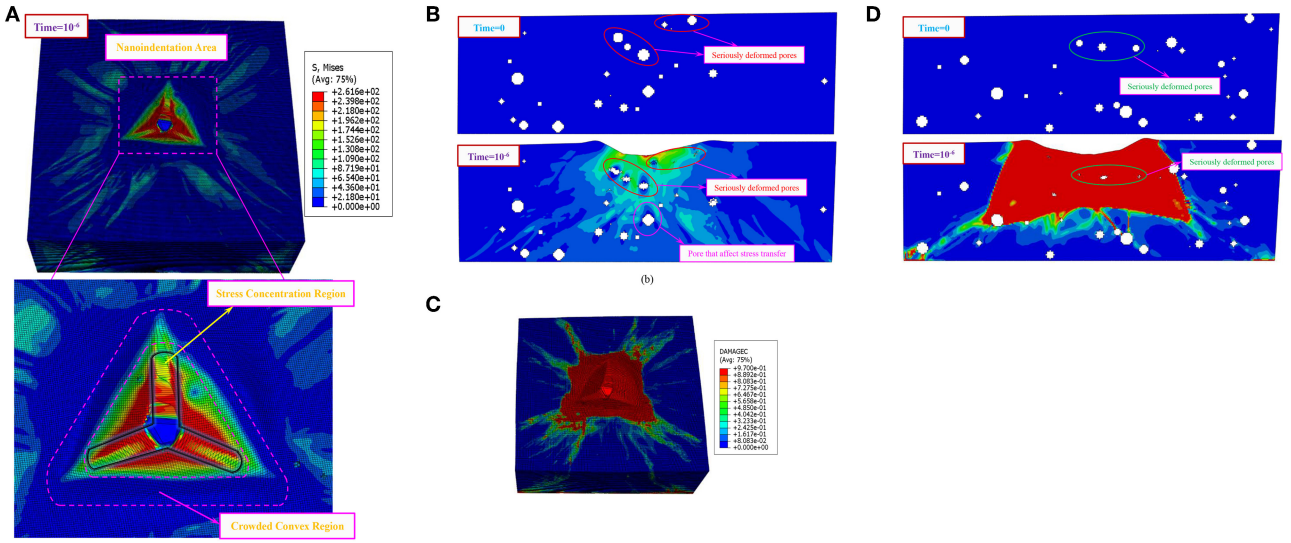

FIGURE 8 | The simulated nephogram of P_{14} by the RAP model **(A)** the stress distribution of the model **(B)** the stress distribution of the middle section in the X direction **(C)** the distribution of the compressive damage of the model **(D)** the compressive damage distribution of the middle section in the Y direction.

TABLE 5 | The simulation results of the RAP nanoindentation model.

Indentation point	Total porosity (%)	Test peak load (*N*)	Simulation result of RAP (*N*)	Error (%)
P_{14}	7.9	2.04	2.17	6.4
P_{15}	9.8	1.96	1.86	5.1
P_{25}	12.4	1.85	1.98	6.9
P_{35}	16.5	1.72	1.82	5.7

SIMULATION BASED ON THE RANDOM AGGREGATE PLACEMENT METHOD (RAP)

Verification of the RAP Nanoindentation Model

The nanoindentation test of P_{14} was simulated based on the random aggregate placement method (RAP). The relevant parameter settings for the RAP nanoindentation model were identical to those of the X-CT nanoindentation model in section The X-CT Nanoindentation Model. The MKP material properties were the same as those of the X-CT model: the MKP density was 1.864 g/cm^3, the elastic modulus was 37.3 GPa, the Poisson's ratio was 0.2, and the compressive strength and tensile strength were 75.6 and 11.3 MPa, respectively. Besides, the same boundary conditions were set: the bottom of the matrix was fixed and the indenter could only move in the Z direction. Additionally, the modified damage factor considering the pores were input into the RAP model. Finally, the simulated peak load of P_{14} by the RAP model was 2.17 N with the relative error of 6.4%. The simulated nephogram of the RAP model is displayed in **Figure 8**.

It can be seen that the RAP nanoindentation model also exhibited stress concentration, severe mesh deformity and crowding effect. In addition, the pores in the lower region of the indenter were seriously deformed and the pores affected the transmission of stress and damage. That is to say, the simulation results of the RAP nanoindentation model were consistent with those of the X-CT model. According to the above steps, the simulation results of P_{15}, P_{25}, P_{35} were obtained by the RAP model, listed in **Table 5**. It was calculated that the average relative error of the peak load of was 5.9%, which verified the validity of the RAP nanoindentation model.

Prediction of Nanoindentation Test

The pore distribution certainly affected the results of the nanoindentation test, but it was difficult to find the indentation points with the same porosity in the X-CT model to study the effect of the pore distribution on the results alone. Therefore, the RAP model can be used to study the effect of pore distribution by controlling both porosity and pore distribution characteristics. The effect of the pore distribution on the total influence coefficient and peak load was predicted with the same porosity of 9% and the influence function $k(D) = 2.45D^{0.18}$. Firstly, the pore distribution was in the range of 0.0005–0.03 mm. Then, the pore distribution dominated by small pores, medium pores and large pores were, respectively, set, listed in **Table 6**. Subsequently, according to Equations (29) and (30), the total influence coefficient and peak load prediction results are exhibited in **Table 6** and **Figure 9** displays the simulated displacement-load curve. It can be seen that at the same porosity, with the increase of the distribution of the large pore size, the total influence coefficient of MKP increased, the peak load decreased and the load-displacement curve as a whole was lower.

TABLE 6 | The prediction of the effect of pore distribution.

Total porosity (%)	Grading porosity (%)									Influence coefficient χ	Simulation result of RAP (N)
	0.0005–0.0025 (mm)	0.0025–0.005 (mm)	0.005–0.0085 (mm)	0.0085–0.012 (mm)	0.012–0.0145 (mm)	0.0145–0.017 (mm)	0.017–0.02 (mm)	0.02–0.024 (mm)	0.024–0.03 (mm)		
9	2.16	1.81	1.49	1.17	0.87	0.68	0.45	0.27	0.11	1.18	2.09
9	0.32	0.63	1.17	2.07	1.62	1.35	0.99	0.59	0.27	1.33	1.87
9	0.11	0.27	0.45	0.68	0.87	1.17	1.49	1.81	2.16	1.43	1.73

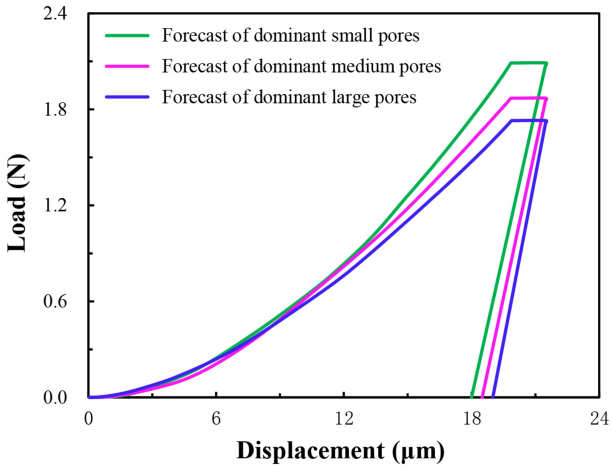

FIGURE 9 | The simulated displacement-load curve.

It indicated that the effect of pore size on peak load should not be neglected.

CONCLUSIONS

In this study, the micro-mechanical properties and structural distribution characteristics of the MKP were investigated by nanoindentation and X-CT techniques. The MKP nanoindentation model was established based on X-CT and random aggregate placement method. The constitutive relationship of the MKP was modified considering the effects of porosity and pore distribution. The influence of pore distribution on the results was predicted by RAP model. The conclusions are as follows:

1. The elastic modulus of the indentation points of the MKP are in the range of 17.66–26.14 GPa with the average elastic modulus of 21.91 GPa while the peak loads of the indentation points fluctuate in the range of 1.57–2.23 N and the average peak load is 1.88 N.
2. The nanoindentation plastic damage model based on X-CT method can effectively describe the mechanical and deformation characteristics of the MKP.
3. The average relative error of simulated peak load is only 3.2% based on the X-CT model, which indicates that the hypothesis of the relationship between the influence coefficients β and λ, the MKP pores conforming to the exponential distribution and the influence function of pore size distribution are correct. That is, from the perspective of the damage factor, the modified mkp constitutive relation considering porosity and pore distribution is effective.
4. The mechanical and deformation characteristics of the MKP can also be described effectively by the RAP model, which verifies the valid of the modified constitutive relation of the MKP again.

DATA AVAILABILITY STATEMENT

The raw data supporting the conclusions of this article will be made available by the authors, without undue reservation, to any qualified researcher.

AUTHOR CONTRIBUTIONS

YL provided the research direction and funding equipment support. GZ was responsible for testing, simulating, and writing papers. ZW provided the detailed research ideas and suggestions for the research.

FUNDING

Beijing Municipal Project for Training Tens of Millions of Talent (No. 2018A37).

ACKNOWLEDGMENTS

The authors would like to acknowledge the financial support of National Natural Science Foundation of China (No. 51678011) and Beijing Municipal Project for Training Tens of Millions of Talent (No. 2018A37). Meanwhile, the authors would like to acknowledge the Avizo software package supported by Beijing Institute for Scientific and Engineering Computing, Beijing University of Technology.

REFERENCES

Al-Amoudi, O. S. B. (2002). Attack on plain and blended cements exposed to aggressive sulfate environments. *Cement Concrete Compos*. 24, 305–316. doi: 10.1016/S0958-9465(01)00082-8

Birtel, V., and Mark, P. (2006). *Parameterised Finite Element Modelling of RC Beam Shear Failure*. Boston, MA: ABAQUS, Inc.

Buj, I., Torras, J., Rovira, M., and de Pablo, J. (2010). Leaching behaviour of magnesium phosphate cements containing high quantities of heavy metals. *J. Hazard Mater*. 175, 789–794. doi: 10.1016/j.jhazmat.2009.10.077

Chen, J. J., Sorelli, L., Vandamme, M., and Ulm, F.-J. (2010). A Coupled nanoindentation/SEM-EDS study on low water/cement ratio portland cement paste: evidence for C-S-H/Ca(OH)2 nanocomposites. *J. Am. Ceram. Soc*. 93, 1484–1493. doi: 10.1111/j.1551-2916.2009.03599.x

Covill, A., Hyatt, N. C., Hill, J., and Collier, N. C. (2011). Development of magnesium phosphate cements for encapsulation of radioactive waste. *Adv. Appl. Ceram*. 110, 151–156. doi: 10.1179/1743676110Y.0000000008

Du, Y.-J., Jiang, N. J., Liu, S., Jin, F., Singh, D. N., Puppala, A., et al. (2014). Engineering properties and microstructural characteristics of cement-stabilized zinc-contaminated kaolin. *Can. Geotech. J*. 51, 289–302. doi: 10.1139/cgj-2013-0177

Fan, C., Wang, B., and Zhang, T. (2018). Review on cement stabilization/solidification of municipal solid waste incineration fly ash. *Adv. Mater. Sci. Eng*. 2018, 1–7. doi: 10.1155/2018/5120649

Formosa, J., Lacasta, A. M., Navarro, A., del Valle-Zermeño, R., Niubó, M., and Rosell, J. R. (2015). Magnesium phosphate cements formulated with a low-grade MgO by-product: physico-mechanical and durability aspects. *Constr. Build. Mater*. 91, 150–157. doi: 10.1016/j.conbuildmat.2015.05.071

Han, J., Pan, G., and Sun, W. (2012). Elastic modulus change investigation of cement paste before and after carbonation using nanoindentation technique. *Proc. Eng*. 27, 341–347. doi: 10.1016/j.proeng.2011.12.461

Haque, M. A., and Chen, B. (2019). Research progresses on magnesium phosphate cement: a review. *Constr. Build. Mater*. 211, 885–898. doi: 10.1016/j.conbuildmat.2019.03.304

He, Y., Lai, Z., Yan, T., He, X., Lu, Z., Lv, S., et al. (2019). Effect of Cd2+ on early hydration process of magnesium phosphate cement and its leaching toxicity properties. *Constr. Build. Mater*. 209, 32–40. doi: 10.1016/j.conbuildmat.2019.03.075

Hou, D., Li, D., Hua, P., Jiang, J., and Zhang, G. (2019). Statistical modelling of compressive strength controlled by porosity and pore size distribution for cementitious materials. *Cement Concrete Compos*. 96, 11–20. doi: 10.1016/j.cemconcomp.2018.10.012

Ju, Y., Yang, Y., Song, Z., and Xu, W. (2008). A statistical model for porous structure of rocks. *Sci. China Ser. E Technol. Sci*. 51, 2040–2058. doi: 10.1007/s11431-008-0111-z

Li, D., Li, Z., Lv, C., Zhang, G., and Yin, Y. (2018a). A predictive model of the effective tensile and compressive strengths of concrete considering porosity and pore size. *Constr. Build. Mater*. 170, 520–526. doi: 10.1016/j.conbuildmat.2018.03.028

Li, Y., Bai, W., and Shi, T. (2017). A study of the bonding performance of magnesium phosphate cement on mortar and concrete. *Constr. Build. Mater*. 142, 459–468. doi: 10.1016/j.conbuildmat.2017.03.090

Li, Y., Li, Y., Shi, T., and Li, J. (2015). Experimental study on mechanical properties and fracture toughness of magnesium phosphate cement. *Constr. Build. Mater*. 96, 346–352. doi: 10.1016/j.conbuildmat.2015.08.012

Li, Y., Shi, T., and Li, J. (2016). Effects of fly ash and quartz sand on water-resistance and salt-resistance of magnesium phosphate cement. *Constr. Build. Mater*. 105, 384–390. doi: 10.1016/j.conbuildmat.2015.12.154

Li, Y., Zhang, G., Wang, Z., and Guan, Z. (2018b). Experimental-computational approach to investigate compressive strength of magnesium phosphate cement with nanoindentation and finite element analysis. *Constr. Build. Mater*. 190, 414–426. doi: 10.1016/j.conbuildmat.2018.09.145

Liang, S., Wei, Y., and Gao, X. (2017a). Strain-rate sensitivity of cement paste by microindentation continuous stiffness measurement: implication to isotache approach for creep modeling. *Cement Concrete Res*. 100, 84–95. doi: 10.1016/j.cemconres.2017.05.023

Liang, S., Wei, Y., and Wu, Z. (2017b). Multiscale modeling elastic properties of cement-based materials considering imperfect interface effect. *Constr. Build. Mater*. 154, 567–579. doi: 10.1016/j.conbuildmat.2017.07.196

Ma, H., Xu, B., and Li, Z. (2014). Magnesium potassium phosphate cement paste: Degree of reaction, porosity and pore structure. *Cement Concrete Res*. 65, 96–104. doi: 10.1016/j.cemconres.2014.07.012

Maldonado-Alameda, A., Lacasta, A. M., Giro-Paloma, J., Chimenos, J. M., and Formosa, J. (2017). Physical, thermal and mechanical study of MPC formulated with LG-MgO incorporating phase change materials as admixture. *IOP Conf. Ser. Mater. Sci. Eng*. 251:012024. doi: 10.1088/1757-899X/251/1/012024

Mestres, G., Fernandez-Yague, M. A., Pastorino, D., Montufar, E. B., Canal, C., Manzanares-Céspedes, M. C., et al. (2019). *In vivo* efficiency of antimicrobial inorganic bone grafts in osteomyelitis treatments. *Mater. Sci. Eng C* 97, 84–95. doi: 10.1016/j.msec.2018.11.064

Němeček, J., Šmilauer, V., and Kopecký, L. (2009). Characterization of alkali-activated fly-ash by nanoindentation. *Nanotechnol. Constr*. 3, 337–343. doi: 10.1007/978-3-642-00980-8_45

Oliver, W. C., and Pharr, G. M. (2011). An improved technique for determining hardness and elastic modulus using load and displacement sensing indentation experiments. *J. Mater. Res*. 7, 1564–1583. doi: 10.1557/JMR.1992.1564

Skarzynski, Ł., and Tejchman, J. (2016). Experimental investigations of fracture process in concrete by means of X-ray micro-computed tomography. *Strain* 52, 26–45. doi: 10.1111/str.12168

Stefanovsky, S., Yudintsev, S. V., Vinokurov, S. E., and Myasoedov, B. F. (2017). Chemical-technological and mineralogical-geochemical aspects of the radioactive waste management. *Geochem. Int*. 54, 1136–1155. doi: 10.1134/S001670291613019X

Sun, X., Dai, Q., and Ng, K. (2014). Computational investigation of pore permeability and connectivity from transmission X-ray microscope images of a cement paste specimen. *Constr. Build. Mater*. 68, 240–251. doi: 10.1016/j.conbuildmat.2014.06.049

Tan, Y., Yu, H., Li, Y., Wu, C., Dong, J., and Wen, J. (2014). Magnesium potassium phosphate cement prepared by the byproduct of magnesium oxide after producing Li2CO3 from salt lakes. *Ceram. Int*. 40, 13543–13551. doi: 10.1016/j.ceramint.2014.05.063

Vinokurov, S. E., Kulikova, S. A., Krupskaya, V., Danilov, S. S., Gromyak, I. N., Myasoedov, B. F., et al. (2018a). Investigation of the leaching behavior of components of the magnesium potassium phosphate matrix after high salt radioactive waste immobilization. *J. Radioanal. Nucl. Chem*. 315, 481–486. doi: 10.1007/s10967-018-5698-3

Vinokurov, S. E., Kulikova, S. A., Myasoedov, B. F. (2018b). Magnesium potassium phosphate compound for immobilization of radioactive waste containing actinide and rare earth elements. *Materials* 11:E976. doi: 10.3390/ma11060976

Vinokurov, S. E., Kulikova, S. A., and Myasoedov, B. F. (2019). Solidification of high level waste using magnesium potassium phosphate compound. *Nucl. Eng. Technol*. 51, 755–760. doi: 10.1016/j.net.2018.12.009

Vinokurov, S. E., Kulyako, Y. M., Slyuntchev, O. M., Rovny, S. I., and Myasoedov, B. F. (2009). Low-temperature immobilization of actinides and other components of high-level waste in magnesium potassium phosphate matrices. *J. Nucl. Mater*. 385, 189–192. doi: 10.1016/j.jnucmat.2008.09.053

Walling, S. A., and Provis, J. L. (2016). Magnesia-based cements: a journey of 150 years, and cements for the future? *Chem. Rev*. 116, 4170–4204. doi: 10.1021/acs.chemrev.5b00463

Wang, B., Wang, H., Zhang, Z., and Zhou, M. (2018). Study on mesoscopic modeling method for three-dimensional random concave-convex concrete aggregate. *Chin. J. Appl. Mech*. 35, 1072–1076. doi: 10.11776/cjam.35.05.B062

Wang, B., Wang, H., Zhang, Z.-Q., and Zhou, M.-J. (2017). Mesoscopic modeling method of concrete aggregates with arbitrary shapes based on mesh generation. *Chin. J. Comput. Mech*. 34, 591–596. doi: 10.7511/jslx201705009

Wang, L., Yu, I. K. M., Tsang, D. C. W., Li, S., and Poon, C. S. (2017). Mixture design and reaction sequence for recycling construction wood waste into rapid-shaping magnesia–phosphate cement particleboard. *Ind. Eng. Chem. Res*. 56, 6645–6654. doi: 10.1021/acs.iecr.7b01175

Wang, P., Xue, Q., Li, J.-S., Zhang, T. T., Wang, S.-Y., Le, Z.-Z., et al. (2018). Factors affecting the leaching behaviours of magnesium phosphate cement-stabilised/solidified Pb-contaminated soil, part 1: water-to-solid ratio and Pb concentration. *Int. J. Environ. Pollut*. 63, 89–103. doi: 10.1504/IJEP.2018.093027

Wang, P., Xue, Q., Yang, Z., Li, J., Zhang, T., and Huang, Q. (2017). Factors affecting the leaching behaviors of magnesium phosphate cement-stabilized/solidified Pb-contaminated soil, part II: dosage and curing age. *Environ. Progr. Sustain. Energy* 36, 1351–1357. doi: 10.1002/ep.12588

Wang, X., Zhang, M., and Jivkov, A. P. (2016). Computational technology for analysis of 3D meso-structure effects on damage and failure of concrete. *Int. J. Solids Struct*. 80, 310–333. doi: 10.1016/j.ijsolstr.2015.11.018

Wang, X. H., Jacobsen, S., He, J., Zhang, Z. L., Lee, S. F., and Lein, H. L. (2009). Application of nanoindentation testing to study of the interfacial transition zone in steel fiber reinforced mortar. *Cement Concrete Res*. 39, 701–715. doi: 10.1016/j.cemconres.2009.05.002

Wang, Y. S., Dai, J. G., Wang, L., Tsang, D. C. W., and Poon, C. S. (2018). Influence of lead on stabilization/solidification by ordinary Portland cement and magnesium phosphate cement. *Chemosphere* 190, 90–96. doi: 10.1016/j.chemosphere.2017.09.114

Wei, Y., Liang, S., and Gao, X. (2017). Indentation creep of cementitious materials: experimental investigation from nano to micro length scales. *Constr. Build. Mater*. 143, 222–233. doi: 10.1016/j.conbuildmat.2017.03.126

Xu, S., Wu, X., Cai, Y., Ding, Y., and Wang, Z. (2018). Strength and leaching characteristics of magnesium phosphate cement-solidified zinc- contaminated soil under the effect of acid rain. *Soil Sediment Contam. Int. J.* 27, 161–174. doi: 10.1080/15320383.2018.1438364

Yang, L., Zhang, Y., Liu, Z., Zhao, P., and Liu, C. (2015). *In-situ* tracking of water transport in cement paste using X-ray computed tomography combined with CsCl enhancing. *Mater. Lett*. 160, 381–383. doi: 10.1016/j.matlet.2015.08.011

Yang, Y., Zhang, Y., She, W., Wu, Z., Liu, Z., and Ding, Y. (2018). Nondestructive monitoring the deterioration process of cement paste exposed to sodium sulfate solution by X-ray computed tomography. *Constr. Build. Mater*. 186, 182–190. doi: 10.1016/j.conbuildmat.2018.07.145

Zhang, M. (2017). Pore-scale modelling of relative permeability of cementitious materials using X-ray computed microtomography images. *Cement Concrete Res*. 95, 18–29. doi: 10.1016/j.cemconres.2017.02.005

Zhang, M., and Jivkov, A. P. (2016). Micromechanical modelling of deformation and fracture of hydrating cement paste using X-ray computed tomography characterisation. *Compos. Part B Eng*. 88, 64–72. doi: 10.1016/j.compositesb.2015.11.007

Zhang, Y., and Zhang, X. (2007). Grey correlation analysis between strength of slag cement and particle fractions of slag powder. *Cement Concr. Compos*. 29, 498–504. doi: 10.1016/j.cemconcomp.2007.02.004

Zhang, Z., Guo, G., Teng, Y., Wang, J., Rhee, J. S., Wang, S., et al. (2015). Screening and assessment of solidification/stabilization amendments suitable for soils of lead-acid battery contaminated site. *J. Hazard Mater*. 288, 140–146. doi: 10.1016/j.jhazmat.2015.02.015

Zhao, Q., Sun, W., Zheng, K., and Jiang, G. (2005). Comparison for elastic modulus of cement, ground granulated blast-furnace slag and fly ash particles. *J. Chin. Ceram. Soc*. 33:837. doi: 10.14062/j.issn.0454-5648.2005.07.009

Zheng, K., Sun, W., Lin, W., and Zhao, Q. (2008). Effects of blast furnace slag on micro-mechanical properties of interface transition zone. *J. Nanjing Univ. Aero. Astr*. 40, 407–411. doi: 10.16356/j.1005-2615.2008.03.021

Zhenghua, Q., Liu, X.-Y., Qiao, Y.-B., Wang, S., Qin, Q., Shi, L.-Q., et al. (2019). Effect of fluorine on stabilization/solidification of radioactive fluoride liquid waste in magnesium potassium phosphate cement. *J. Radioanaly. Nucl. Chem*. 319, 393–399. doi: 10.1007/s10967-018-6339-6

Conflict of Interest: The authors declare that the research was conducted in the absence of any commercial or financial relationships that could be construed as a potential conflict of interest.

Copyright © 2020 Li, Zhang and Wang. This is an open-access article distributed under the terms of the Creative Commons Attribution License (CC BY). The use, distribution or reproduction in other forums is permitted, provided the original author(s) and the copyright owner(s) are credited and that the original publication in this journal is cited, in accordance with accepted academic practice. No use, distribution or reproduction is permitted which does not comply with these terms.

frontiers in Materials

ORIGINAL RESEARCH
published: 24 March 2020
doi: 10.3389/fmats.2020.00056

Insight Into the Leaching of Sodium Alumino-Silicate Hydrate (N-A-S-H) Gel: A Molecular Dynamics Study

Hongyan Wan[1], *Liqun Yuan*[2] *and Yu Zhang*[1]*

[1] School of Materials Science and Engineering, Southeast University, Nanjing, China, [2] School of Architecture and Civil Engineering, Liaocheng University, Liaocheng, China

This paper provides an intrinsic mechanism for alkali dissolution from the gels of geopolymers at the nanoscale, via a molecular dynamics (MD) investigation on N-A-S-H gel, the predominant binding phase in geopolymers. Sodium plays roles in balancing the charges of [AlO_4] tetrahedrons, and its absence causes local structures to show a negative charge, resulting in locally mutual repulsion between tetrahedrons. Also, sodium dissociation promotes a hydrolytic reaction, exacerbating the non-conservation of charge of the N-A-S-H system, further swelling the structure. The above evolution weakens the alumino-silicate skeleton and reduces the stability of silicate and aluminate species, which in turn promotes sodium dissociation. In the long term, it increases the potential of structure depolymerization and even peeling off. Based on previously reported experiments and our computational results, it is likely that leaching starts from the N-A-S-H substrate surface, and the gel peels off layer by layer in the above manner, resulting in microscopic holes and fissures. In addition, leaching also leads to the degradation of the mechanical properties of the surface gel, including Young's modulus, tensile strength, and ductility, which considerably increases the possibility of surface gel peeling. Additionally, sodium is able to connect [AlO_4] and [SiO_4] tetrahedrons by the electrostatic force with tetrahedral oxygen, which transfers stress and contributes to uniform stress dispersion.

Keywords: geopolymer, leaching, molecular dynamics, N-A-S-H gel, alkalis

OPEN ACCESS

Edited by:
Dongshuai Hou, Qingdao University of Technology, China

Reviewed by:
Zuhua Zhang, Hunan University, China
*Jianguo Li, Bioinformatics Institute (A*STAR), Singapore*

***Correspondence:**
Yu Zhang
tgyuzhang@outlook.com

Specialty section:
This article was submitted to Computational Materials Science, a section of the journal Frontiers in Materials

Received: *28 December 2019*
Accepted: *21 February 2020*
Published: *24 March 2020*

Citation:
Wan H, Yuan L and Zhang Y (2020) Insight Into the Leaching of Sodium Alumino-Silicate Hydrate (N-A-S-H) Gel: A Molecular Dynamics Study. Front. Mater. 7:56. doi: 10.3389/fmats.2020.00056

INTRODUCTION

Sodium alumino-silicate hydrate (N-A-S-H) gel is the primary binding phase in geopolymers, and determines the durability and mechanical properties of these materials. With respect to the geopolymer, it is an alkali-activated material and is considered to be an alternative to conventional Portland cement (PC). Using industrial by-products as a precursor, developing geopolymers can reduce carbon oxide emissions and energy consumption as compared to PC materials (Habert et al., 2011; Singh et al., 2015). Importantly, it also shows mechanical properties comparable to PC and even much better durability (Shi et al., 2011; Provis et al., 2015; Arbi et al., 2016; Zhang et al., 2018d). The geopolymer can be prepared by mixing fly ash or metakaolin with an alkaline solution and curing at an elevated temperature (around 60∼80°C). Generally, the molecular structure of the reaction product is described as a three-dimensional alumino-silicate network constructed by [SiO_4] and [AlO_4] tetrahedrons interlinked by bridging oxygen, with alkali ions (Na^+ or K^+) loosely bound to [AlO_4] tetrahedrons and compensating for the negative charge of four-coordinated aluminum

(Duxson et al., 2005, 2007; Provis and Van Deventer, 2007). This reaction product is called sodium (or potassium) alumino-silicate hydrate [N(K)-A-S-H] gel.

Leaching generally occurs with geopolymers, especially when exposed to flowing fresh water or weak acids, as these remove sodium from the geopolymer paste. Leaching begins with aqueous sodium in the pore solution, which can be seen as sodium transporting inside the pore structure of the geopolymer before being discharged from the material. Consequently the reduced sodium concentration in the pore solution results in solid sodium dissolving from the gel. These two processes promote each other. Leaching is closely associated with various types of material degradation. From a macro perspective, the results caused by leaching are typically a decrease in pH value in the pore solution (Zhang et al., 2013, 2014), a decline in the quality of geopolymer specimens (Zhang et al., 2016), coarsening of pore structure (Yao et al., 2016), and degradation of mechanical properties (e.g., compressive strength, tensile strength, and Young's modulus) (Yao et al., 2016; Zhang et al., 2016). The degradation can be explained by the weakening of AlO_4's tetrahedral structure whose net negative charge is normally balanced by alkalis, which was characterized by both a molecular dynamics simulation (Sadat et al., 2016a) and ^{29}Si and ^{27}Al MAS-NMR and FTIR analysis (Longhi et al., 2019). It also matches well with the experimental results of the detection of aluminate species in water soaked geopolymer specimens (Zhang et al., 2016), which means the dealumination of the gel and thus dissolution of the gel.

The leaching can be divided into two processes which are the movement of aqueous alkalis in the pore solution and the extraction of alkalis from the gels. With respect to the former, previous works have shown that the transportation of free alkalis in the pore solution (resulting from excess, weakly-bonded or unreacted alkalis) is influenced by pore structure, where a looser and less tortuous pore network promotes movement of alkali cations (Lloyd et al., 2010; Zhang et al., 2018d). At present, a majority of the relevant published papers focus on the mix proportion of geopolymer materials and the curing environment used in order to reach denser pore structures and less free alkali in the materials. The aim of which is to create low leaching potentials, by methods, such as the selection of activators and the addition of supplementary cementitious materials (e.g., slag, metakaolin, and calcium aluminate cements) (Kani et al., 2012; Zhang et al., 2013, 2014; Yao et al., 2016; Longhi et al., 2020).

It is worth noting that leaching has a special manifestation that is efflorescence. It happens when geopolymer materials are in contact with damp soil at their base, from which water is drawn through the material by capillary action carrying alkalis with it which evaporate from the concrete surface, leaving the alkalis deposited on the surface where they react with atmospheric CO_2, resulting in the formation of white carbonate deposits on the surface known as efflorescence. Obviously, the influencing factors for efflorescence are carbonization in addition to alkali transport. It seems that the deleterious effect of efflorescence on the geopolymer is greater than that of leaching only (Yao et al., 2016). Zhang et al. (2018d) reported subflorescence which is efflorescence taking place under the surface of a material, forming sodium carbonate crystallization pressure under the material surface, generating greater material damage.

The above-mentioned hazards can be attributed to the continued dissolution of sodium from the gel. Therefore, studies related to the extraction of alkalis from gels is necessary, including investigating the roles sodium plays in the gel and the reasons for sodium dissolution. Solid phase sodium may not be involved in alumino-silicate skeleton formation (Škvára et al., 2012). In the results of a ^{23}Na MAS NMR (Duxson et al., 2005), there was no evidence of resonances resulting from sodium associating with non-bridging oxygen, which suggests that the interaction between solid sodium and the oxygen in the skeleton is very weak, and at the very least is not an ionic bond. Therefore, the dissolution of solid sodium can be attributed to the relatively weak binding of alkalis in the structure (Bortnovsky et al., 2008; Škvára et al., 2008; Szklorzová and Bílek, 2008). Some have attempted to utilize potassium hydroxide instead of sodium hydroxide as the alkali activator, due to the stronger electrostatic interaction between potassium and the alumino-silicate skeleton (Duxson et al., 2006; Longhi et al., 2020). By means of molecular dynamics, the computation results conducted by Zhang et al. (2018a) indicate that it is impossible for sodium to escape from inside the dense alumino-silicate network, but only from several nanometer-thick surface layers, where the binding energy is much lower. Additionally, they also reported the stabilizing effect of hydroxyls on the sodium in the gel (Zhang et al., 2018b).

However, there is still an absence of knowledge about the process by which alkalis are extracted from gels. To our knowledge, there are very few papers on this dedicated topic. This is due to the fact that relevant research involves the atomic scale, so the results obtained from experiments alone are scarce and some of them are obtained through indirect inference. Molecular dynamics (MD) has the potential to give such explanations. With force field parameters derived from first-principle theory computation, MD is able to provide a quantitative intrinsic illustration on the structure, reactivity, dynamics, and energy of the system on the molecular level.

Leaching begins from the surface of the gel. This paper simulated the leaching of a surface N-A-S-H gel with a volume of $2 \times 2 \times 2$ nm to reveal the effect of alkali dissociation on N-A-S-H gels and to give the mechanisms of the process of alkali dissociation from the gel. By means of reactive molecular dynamics, a model lacking sodium was constructed and the relevant evolutions of structure, dynamics, and mechanical properties were investigated.

METHODOLOGY

Model Construction

The N-A-S-H model can be constructed by the following procedures. At the beginning silicon, aluminum, sodium, and oxygen atoms, according to the chemical composition shown in **Table 1**, were randomly assigned in the simulation box with a size of $20 \times 20 \times 20$ Å, with each atom separated by at least 2.2 Å. A periodic boundary was imposed in all three directions. Verlet algorithms were utilized to calculate the atomic trajectory. The structure was subjected to an NVT ensemble

TABLE 1 | Chemical composition of the N-A-S-H model.

Si/Al	SiO_2 (wt. %)	Al_2O_3 (wt. %)	Na_2O (wt. %)	H_2O (wt. %)	Skeletal density (g/cm^3)	Gel density (g/cm^3)
2	55.32	24.16	14.64	6.78	2.56	2.71

at 300 K for 50 ps and a subsequent NPT ensemble where the temperature was raised up to 4,000 K and then cooled down to 300 K at a healing/cooling rate of 5 K/ps. Then, the structure was subjected to an NPT ensemble at 300 K and 0 atm for structural equilibrium. Pressure was applied on all directions (i.e., x, y, and z directions). Finally, the Grand Canonical Monte Carlo (GCMC) method (Bonnaud et al., 2012), performed on LAMMPS, was performed for 300 million steps to adsorb water molecules into the structure until saturation.

The obtained N-A-S-H model is shown in **Figure 1**. The structure of N-A-S-H consists of a three-dimensional alumino-silicate skeleton filled with sodium and water molecules. Silicon and aluminum species are predominantly tetrahedral as listed in **Table 2**, and the Q4 ([SiO_4] or [AlO_4] tetrahedron with four tetrahedrons connected around it) percentage is 79%. The structure of the N-A-S-H model obtained matches with published results of MAS-NMR (Duxson et al., 2005; Singh et al., 2005; Bernal et al., 2013). Furthermore, a similar N-A-S-H model obtained by the same modeling approach has been presented in previously published articles and attained ideal modeling results related to the transport, structure, dynamics and mechanical properties of N-A-S-H (Sadat et al., 2016b; Zhang et al., 2018a,b).

In order to simulate the effect of leaching on the N-A-S-H gel, sodium atoms were deleted randomly from the structure. For a gel with a volume of 2 × 2 × 2 nm containing just a few dozens of sodium atoms, complete dissolution is possible when it is exposed to flowing water or acid. Thus, the leaching ratio was set as 0, 25, 50, 75, and 100%.

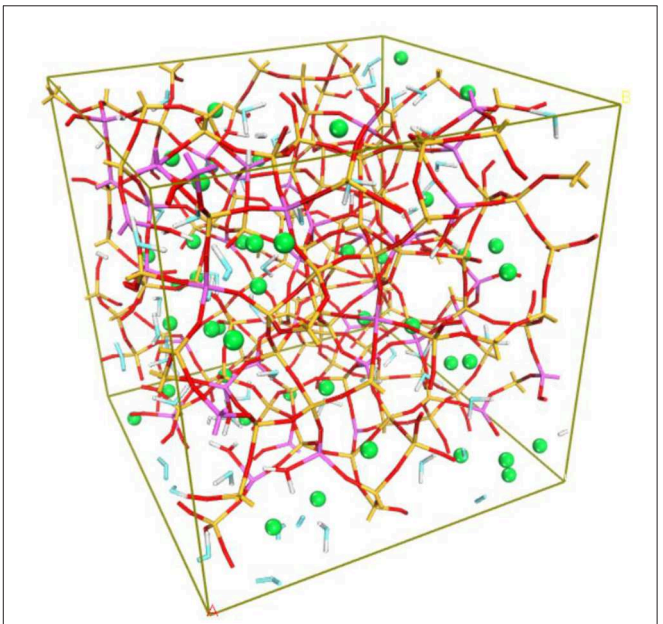

FIGURE 1 | N-A-S-H gel model. Yellow-red sticks represent the Si-O bond; purple-red sticks stand for the Al-O bond; red-white sticks are the hydroxyls attached to Si or Al; blue-white sticks are the OH of water molecules; green balls represent Na.

TABLE 2 | Coordination number (CN) of Al and Si in the N-A-S-H model.

CN	3	4	5
Al	3.90%	94.63%	1.48%
Si	–	100%	–

Reactive Force Field and Simulation Procedure

Reactive force field (ReaxFF) was applied in this simulation to model the chemical reactions and dynamics of sodium, aluminum, silicon, oxygen, and hydrogen species in the N-A-S-H gel. ReaxFF utilizes a bond order scheme to simulate chemical reactions. The interaction is determined by instantaneous interatomic distance, which is updated continuously to model chemical reactions. ReaxFF consists of bonded potential, including bond stretching energy, bond bending energy, bond torsion energy, and non-bonded potentials, including van der Waals and Coulombic potential. The bonded interaction is determined by the bond orders, so that all partial energy contributions of bonded interaction can reduce to zero smoothly as the bond breaks. The calculation of Coulombic potential is derived from the classical Coulomb force formula. The cutoff distance for long-range interaction is set as 10 Å.

The parameters of these species as described by ReaxFF are directly available in Bai et al. (2012). In previously published papers, ReaxFF has been confirmed to be accurate when modeling glass and crystal systems with species of sodium, aluminum, silicon, such as silica glass (Hou et al., 2014), calcium silicate hydrate (Hou et al., 2019; Lu et al., 2020), calcium alumino-silicate hydrate (Wan et al., 2017; Hou et al., 2018a) and Tobermorite (Hou and Li, 2014), as well as N-A-S-H gels (Sadat et al., 2016b; Hou et al., 2018b, 2020; Zhang et al., 2018a,b, 2020) that are similar to the model in this paper.

The time step was 0.25 fs. Temperature and pressure were monitored and adjusted at regular intervals using the Nose-Hoover thermostat (Hoover, 1985) and Berendsen Barostat (Hoover, 1986) algorithms, respectively. The computational procedure was performed on LAMMPS, a molecular dynamics simulator. After leaching the N-A-S-H gel was relaxed on NPT and NVT ensembles for 100 ps. It turns out that structure equilibrium took only 40 ps. Then an NVT run of 100 ps was followed for structure analysis. Finally, a tensile test was

conducted using a tensile strain rate of 0.08/ps under an NPT ensemble, which took 15 ps. As the model was elongated in the x direction, the pressure in the y and z directions was set as zero to reflect the Poisson effect. One frame of atomic trajectory was outputted every 1,000 steps for the analysis of structure and mechanical properties. The modeling of each leaching ratio was repeated three times, and the results were the same. The small amount of error is one of the advantages of simulation over experiments.

RESULTS AND DISCUSSIONS

Structure Expansion of Surface Gel

Leaching leads to an expansion of the N-A-S-H structure. As plotted in **Figure 2**, the simulation box size shows an exponential increase as the leaching ratio increases, and the volume increases from around 7,916.28 to 8,257.27 $Å^2$ from the beginning to the complete dissociation of sodium. Generally, the leaching process is started from the exposed surface of N-A-S-H gel, because there are fewer electrostatic and geometric restrictions on sodium from the alumino-silicate skeleton (Zhang et al., 2018a). Under the influence of leaching, the gel of the surface swells, causing mismatches with internal deformation and generating internal stress, leading to a potential for cracking and peeling. The gel system has a considerably large specific surface area, and impacts caused by linear expansion of only 2% cannot be underestimated.

Sodium is loosely bound to aluminate tetrahedrons and plays a role in maintaining the charge neutrality of aluminate tetrahedrons in the N-A-S-H structure (Duxson et al., 2005). An absence of sodium leads local structures to show a negative charge, which results in mutual repulsion between [SiO_4] or [AlO_4] tetrahedrons in those local locations and eventually causes swelling of the overall structure.

Radial distribution functions (RDF) were utilized to characterize the interatomic spatial correlation to reflect the evolution of local structure caused by leaching. The RDFs of Si-Al and Si-Si are shown in **Figure 3**. The first peak of the RDF profiles represents the Si-O-Al bond and Si-O-Si bond. In **Figure 3A**, under the influence of leaching, the distance between Si and Al in the Si-O-Al bond increases from 3.12 to 3.27 Å, which is attributed to an increase in the Si-O-Al angle caused by the repulsion between [SiO_4] and [AlO_4] tetrahedrons. It explains the observation from the FTIR spectra (Zhang et al., 2016) that the asymmetric stretching vibration band of Si-O-Al was shifted to a higher wavenumber after the leaching of the geopolymer sample. Essentially, this is due to the imbalance of charge caused by the lack of sodium, and confirms the conclusion that the important role of sodium is in maintaining the charge neutrality of aluminate tetrahedrons. The stretching of the alumino-silicate skeleton is one of the explanations for structure expansion. However, such a local structure evolution does not occur for the Si-O-Si bond. It seems that leaching may not influence the silicate skeleton directly.

ReaxFF utilizes a bond order scheme to determine the variation of interatomic interactions to accurately simulate chemical reactions. During the relaxation, a hydrolysis reaction can be observed as shown in **Figure 4A**. The oxygen species in the alumino-silicate skeleton attracts hydrogen atoms from nearby water molecules and occupies their electron, resulting in a hydrolytic reaction and the formation of Si/Al-OH and free OH^-. This is because the sodium distributed among the alumino-silicate skeleton interacts with the oxygen species in the structure, such as non-bridging oxygen, and shares their charge. But the

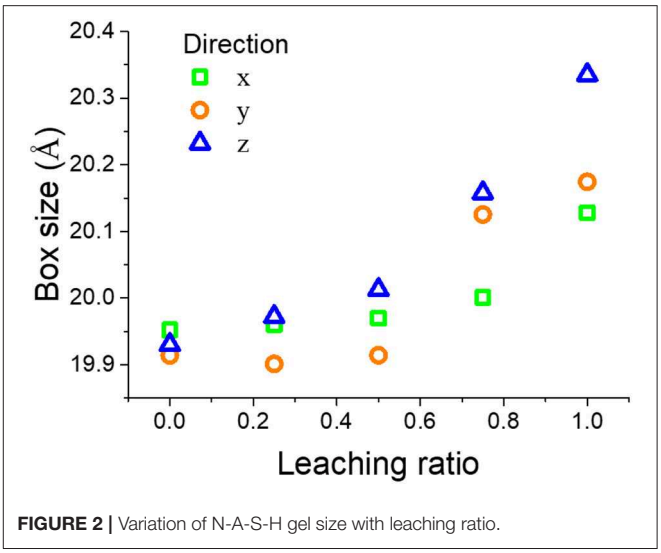

FIGURE 2 | Variation of N-A-S-H gel size with leaching ratio.

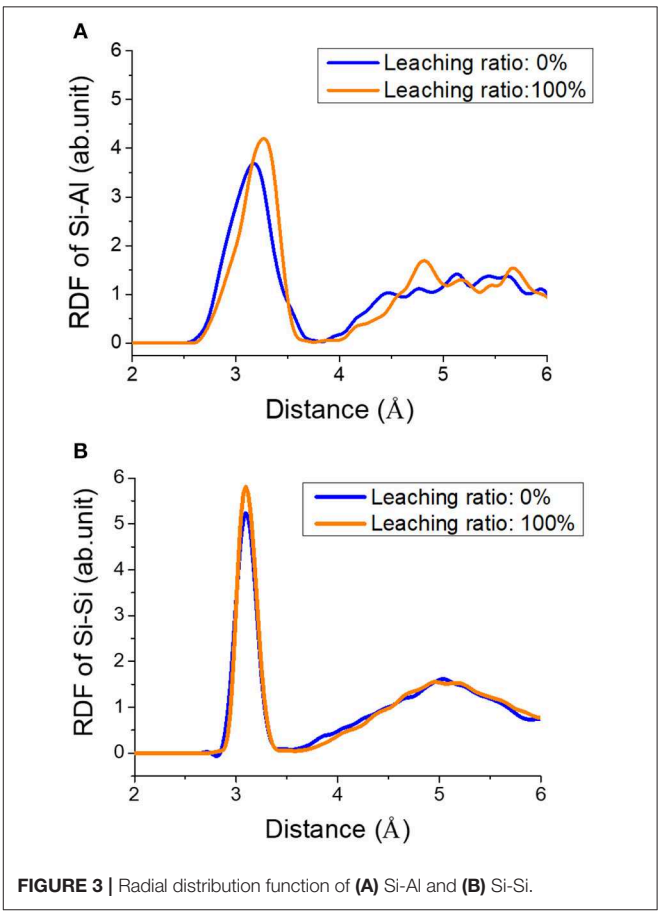

FIGURE 3 | Radial distribution function of **(A)** Si-Al and **(B)** Si-Si.

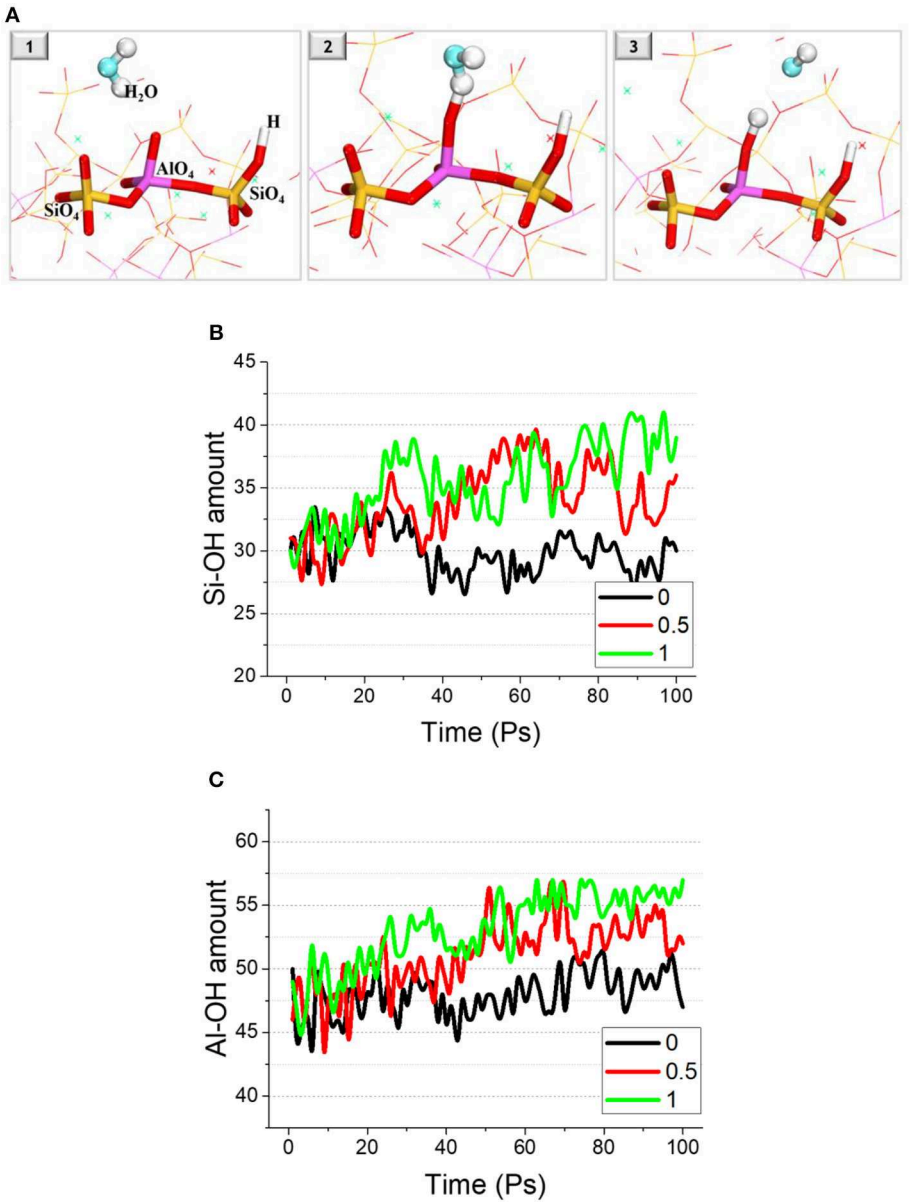

FIGURE 4 | (A) Snapshot of the hydrolysis reaction process, in which yellow-red sticks represent the Si-O bond; purple-red sticks stands for the Al-O bond; red-white sticks are the hydroxyls attached to Si or Al. The amount of **(B)** Si-O and **(C)** Al-O bonds as a function of time.

absence of sodium caused by leaching makes the originally stable oxygen species active again.

Figure 4 shows the variation in the amount of hydroxyls attached to the alumino-silicate skeleton (Si-OH and Al-OH), with or without the influence of leaching. For the reference sample (no leaching), the hydroxyl amount fluctuates but remains almost unchanged. By contrast, the amount of Si-OH and Al-OH increases with relaxation time for the samples with leaching. At 100 ps, the amount of Si-OH and Al-OH in the sample after 100% leaching has increased by around 8 times, and the increased amount for the sample after 50% leaching is around 4 and 5 times.

It should be noted that the formation of hydroxyls in the N-A-S-H structure produced by the hydrolytic reaction mentioned above further swells the N-A-S-H structure. This is because that newly formed negatively-charged hydroxyls increase the level of non-conservation of charge for the N-A-S-H system. However, due to the tendency toward charge neutral, a part of the hydrolytic reaction proceeds in the reverse direction, which gives a reason for the large fluctuation in the amount of hydroxyls in the structure over time. Ultimately, there are still some hydroxyls formed in the structure, which exacerbates the volume expansion of the N-A-S-H gel.

Furthermore, it has been reported (Zhang et al., 2018b) that hydrolytic reactions can also directly weaken the N-A-S-H structure. The stability of Al-O bonds is significantly reduced by the chemical reaction between water and aluminate tetrahedrons. But the stability of sodium is slightly improved, as a result of the restriction of newly formed OH^-.

Alumino-Silicate Skeleton Weakening

Leaching not only swells the N-A-S-H structure as mentioned above, but also weakens parts of the alumino-silicate skeleton, including the weakening of Si-O and Al-O bonds and reducing the degree of polymerization of the N-A-S-H gel. A time-correlated function (TCF), as determined by Equation (1), was applied to the system to estimate the stability of Si-O and Al-O bonds by counting the number of related bonds broken as functions of relaxation time.

$$C(t) = \frac{< \delta b(t)\, \delta b(0) >}{< \delta b(0)\, \delta b(0) >} \quad (1)$$

where $\delta b(t)$ is equal to $b(t) - < b >$, and b(t) is a binary operator. If the chemical bond remains bonded, the value is one, otherwise it is zero; <b> is the average value of b during the whole simulation process.

The TCF profiles of Al-O and Si-O bonds are depicted in **Figure 5**. As simulation time goes, the TCF value begins to decay from 1, which indicates the breaking of chemical bonds. A reduced value of <0.01 after 90 ps for the scenario without leaching shows the extreme stability of Al-O and Si-O bonds. As the leaching ratio increases, the rate of decline increases and the reduced value reaches around 0.02, indicating that the weakening of Al-O and Si-O bonds is caused by leaching.

Under the influence of leaching, when compared with Si-O bonds, there is a steeper downward gradient in the TCF profiles of Al-O bonds, implying that Al-O bonds are weakened more seriously by leaching. Sodium plays roles in maintaining the charge balance of aluminate tetrahedrons, and its absence has a direct effect on it. However, for the silicate tetrahedrons, they are only indirectly affected by structural expansion and the hydrolytic reaction mentioned in section Structure Expansion of Surface Gel, thus the stability of Si-O bonds shows a relatively slight decline.

In this stable environment, leaching may have little effect on the stability of Si/Al-O bonds, because a reduced value of 0.02 for the TCF profile after 90 ps is still very small. A decreased value up to 0.4 has also been obtained for the stable H-bond in the cement system when studied via an MD method (Zhang et al., 2018c). However, the effect of leaching only becomes apparent once the environment deteriorates, such as after structure deformation caused by loading or temperature variation.

Polymerization of N-A-S-H gel is characterized by the connectivity factor Q_n. It varies with the leaching ratio as shown in **Figure 6**. For a pristine sample (no leaching), Q_4 is predominant and accounts for 79% of the sample, and is followed by Q_3 at 19%, and also there is a little Q_2 structure. This means that the N-A-S-H gel is mostly constructed of a three-dimensional alumino-silciate network, and also contains some two-dimensional branch structures and a small number of chain structures. As the leaching ratio increases, the Q_4 percentage gradually declines from 79 to 73%, which is replaced by Q_3 and Q_2 structures, implying that three-dimensional

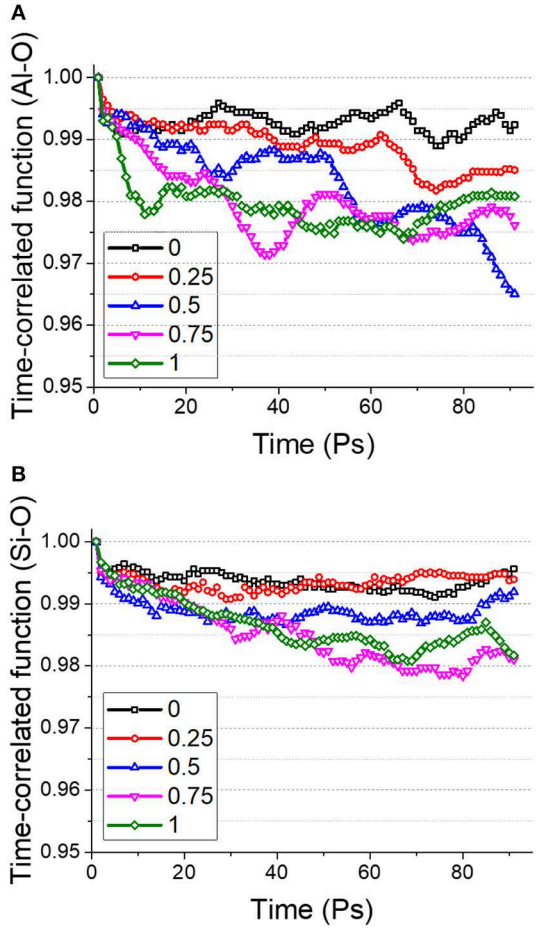

FIGURE 5 | Time-correlated function of **(A)** Al-O and **(B)** Si-O bonds.

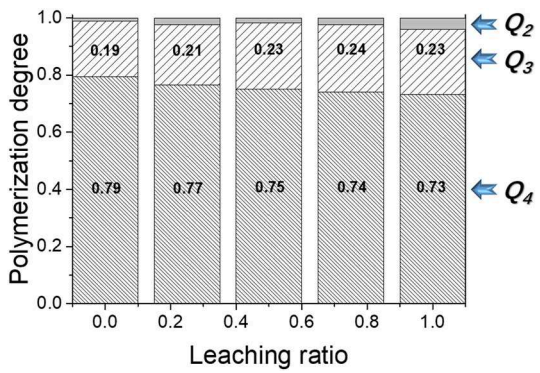

FIGURE 6 | The degree of polymerization evolution with leaching ratio. Q_n is the polymerization factor, where n can be 0, 1, 2, 3, or, 4, representing the number of bridging oxygens for a given Si/Al tetrahedron. Q_0 means monomer, Q_1 stands for dimer, Q_2 represents a chain structure, and Q_3 and Q_4 are branch structure and network structure, respectively.

network structure is gradually transformed into branch and chain structures. It shows that leaching not only weakens the alumino-silicate skeleton, but also breaks a small amount of the alumino-silicate skeleton.

Under the influence of leaching, the alumino-silicate skeleton of N-A-S-H gel is weakened to some extent, and even fractured, leaching to the decrease in the stability of the overall structure. Herein, the dynamics of the structure is estimated by mean square displacement (MSD), as determined by the following equation. The mobility of the solid species Si, Al, and Na, of the N-A-S-H gel is investigated as follows:

$$\mathrm{MSD}\,(\mathrm{t}) = < |r_i\,(t) - r_i(0)|^2 > \qquad (2)$$

where $r_i(t)$ is the position of atom i at time t.

MSD profiles of Al, Si, and Na at different leaching ratios are depicted in **Figure 7**. The MSD profiles increase with fluctuation as relaxation time increases, and this means a slight displacement of the atoms accompanied with vibrations. For the cases without leaching, the MSD of Si and Al at 100 ps is just 0.005 and 0.02 $Å^2$, respectively, meaning that the displacement of both types of atoms is <0.14 Å during 100 ps, which is the typical nature of a solid.

By contrast, the MSD of Na is around 50 times more than that of Si and Al, and exhibits a glassy nature like that of physically binding water in cement hydrates (Youssef et al., 2011). Moreover, it has been reported (Zhang et al., 2018a) that the mobility of the sodium depends on its position in the N-A-S-H gel. For ones located at the surface of the N-A-S-H substrate, their mobility is around 100 times more than that of those in the interior. It means surface sodium can be dissociated from the cavities among the alumino-silicate skeleton or exchanged with outside alkali ions, which underlies the dissociation of sodium from the N-A-S-H gel that is called leaching. The sodium species are the most unstable species in the structure.

With the leaching of sodium, the mobility and the amplitude of atomic vibrations increases for both Al and Si. It indicates a gradual decrease in the stability of the alumino-silicate skeleton of the N-A-S-H gel. Moreover, the increase in the MSD of Al is much more than that of Si, and the value it reaches is around 70% of that of the easily soluble Na (reference sample), which is also consistent with the above conclusion that leaching has a direct weakening effect on aluminate species. In previous work, it was demonstrated that the removal of alkalis induces the reduction of Q_4(Al) and Al(VI) species as observed by 29Si and 27Al MAS-NMR and FTIR analysis (Longhi et al., 2019). The weakening of the AlO_4 tetrahedral structure caused by sodium absence was also characterized by molecular dynamics simulation (Sadat et al., 2016a). Both of these explain the experimental results of the detection of aluminate species in the water soaked geopolymer specimens (Zhang et al., 2016), which means the dealumination of gel and thus dissolution of gel. The dissolution leads to the decrease in geopolymer quality and the coarsening of the pore structure. It also gives an explanation for the Mercury Intrusion Method (MIP) experiments (Yao et al., 2016) which showed an increase in nanopore volume in the geopolymer samples after leaching.

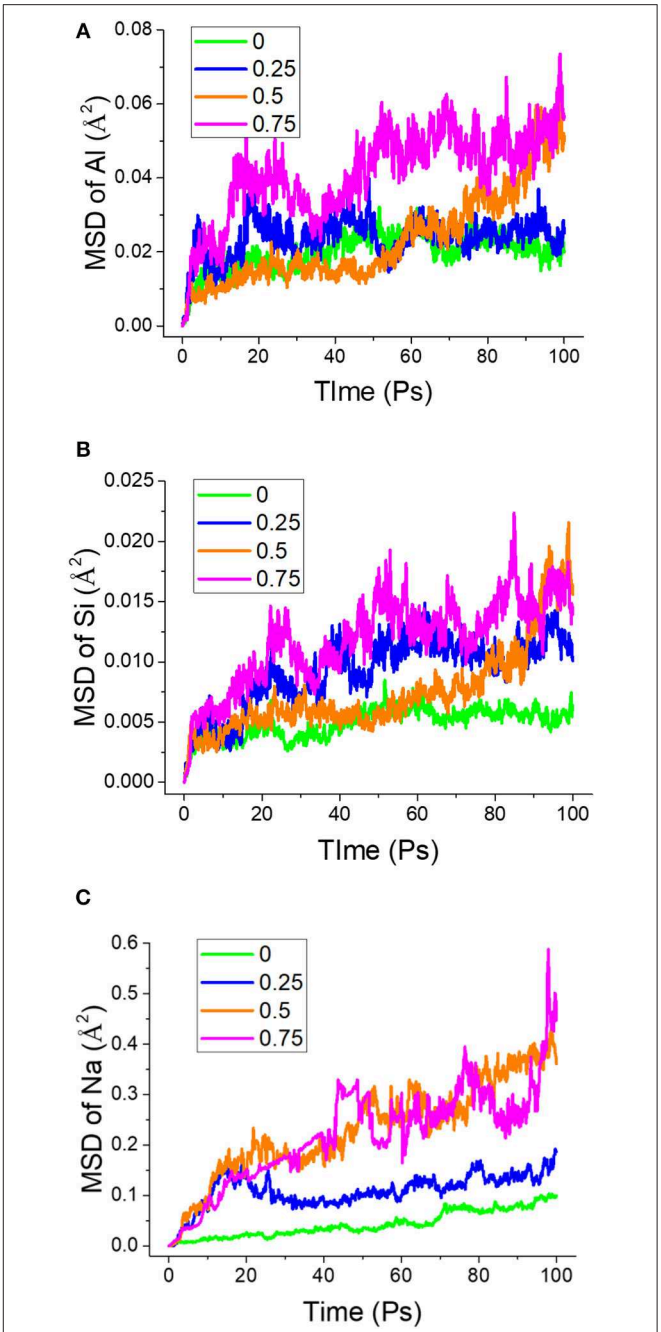

FIGURE 7 | Mean square displacement of **(A)** Al, **(B)** Si, and **(C)** Na under the influence of leaching.

Due to the degradation of the alumino-silicate skeleton, sodium distributed among the skeleton receives less restriction from the skeleton, resulting in the sodium transforming from a glassy state into a flowing state progressively with leaching, as illustrated in **Figure 7C**. It implies that the rate of sodium dissociating from the N-A-S-H gel is getting faster and faster. Also, it indicates that the dissociation of sodium accelerates the degradation of alumino-silicate skeleton, which in turn promotes

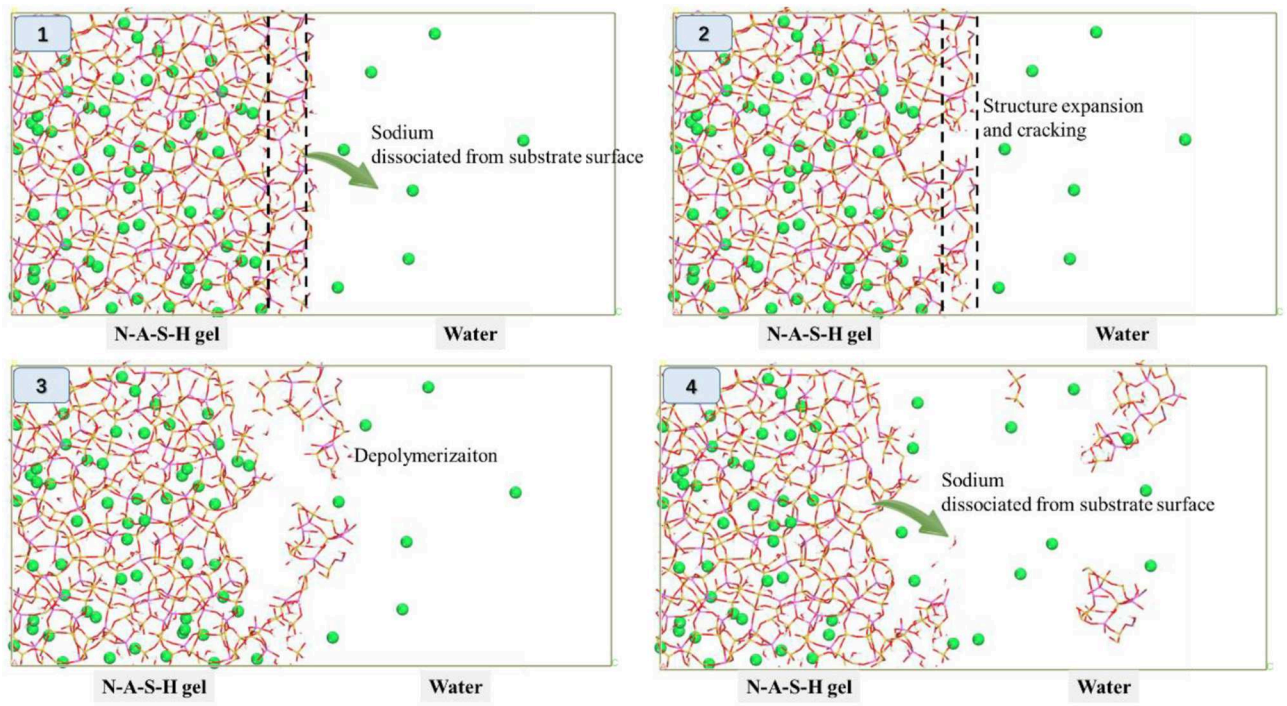

FIGURE 8 | Schematic diagram of leaching process. Green balls stand for sodium.

the dissociation of sodium. Therefore, the dissolution of surface sodium is an accelerated process.

According to the above discussion, the mechanism of leaching can be summarized in **Figure 8**. Loose in the alumino-silicate skeleton, sodium located at the surface of the N-A-S-H substrate is gradually dissociated and diffuses into the bulk water. It results in structure swelling and the weakening of the alumino-silicate skeleton, and then processes into the depolymerization of the skeleton and even the peeling and dissolution of the surface layer of the gel substrate. Subsequently, fresh internal N-A-S-H gel is exposed, and the sodium in its surface begins to diffuse into the bulk water. A new leaching process starts. In this way, the N-A-S-H gel can be depolymerized layer by layer, resulting in microscopic holes and fissures produced leading to the degradation of the macroscopic properties of the gel.

Mechanical Properties

Under the influence of leaching, the N-A-S-H gel is weakened and even dissolved. Herein, the mechanical properties of the N-A-S-H gel before and after leaching is investigated.

Figure 9A shows the stress-strain relations of the N-A-S-H gel during elongation. The curves increase linearly and step into a yield stage at around 60–80% of the peak value. The peak value decreases with the leaching ratio. Tensile strength and Young's modulus are plotted in **Figure 9B**, showing a roughly linear relationship with the leaching ratio. Approximately, the tensile strength and Young's modulus decline by respectively 0.45 and 2.55 GPa for every 25% sodium dissociation. This is caused by the deterioration in terms of the degree of polymerization of the N-A-S-H gel and the strength of Si-O and Al-O bonds as discussed in section Alumino-Silicate Skeleton Weakening.

Particularly, the reduction in Young's modulus of the surface gel can result in a mismatch of deformation between the surface and internal gel when it is loaded. Taking the sample with 100% leaching as an example, the linear deformation of the surface gel is 84.5% of the internal when they are subject to the same stress. For geopolymer materials with a considerably larger specific surface area, it significantly increases the potential for surface gel peeling.

For the post-peak stage, the curves drop at different rates. The curve for the case of 100% leaching drops sharply, and the strain at the breaking point is 0.71. The strain at the breaking point increases with the decrease of the leaching ratio. **Figure 9C** shows an approximately linear relationship between the leaching ratio and the strain at the breaking point. The strain at the breaking point for the sample with 100% leaching is around the 37% of the pristine sample, meaning a significant reduction in ductility of the structure after leaching.

In order to investigate the effect of leaching on the structure evolution during a tensile process, the amount of variation in Si-O-Si and Al-O-Si bonds during elongation is presented in **Figure 9D**. Before a strain of 0.1, the amount of chemical bonds remains stable, because this is the elastic stage at which the alumino-silicate skeleton can resist tensile strain by deformation only. For the strain between 0.1 and 0.2, the bond amounts decrease slightly but the variation is almost the same

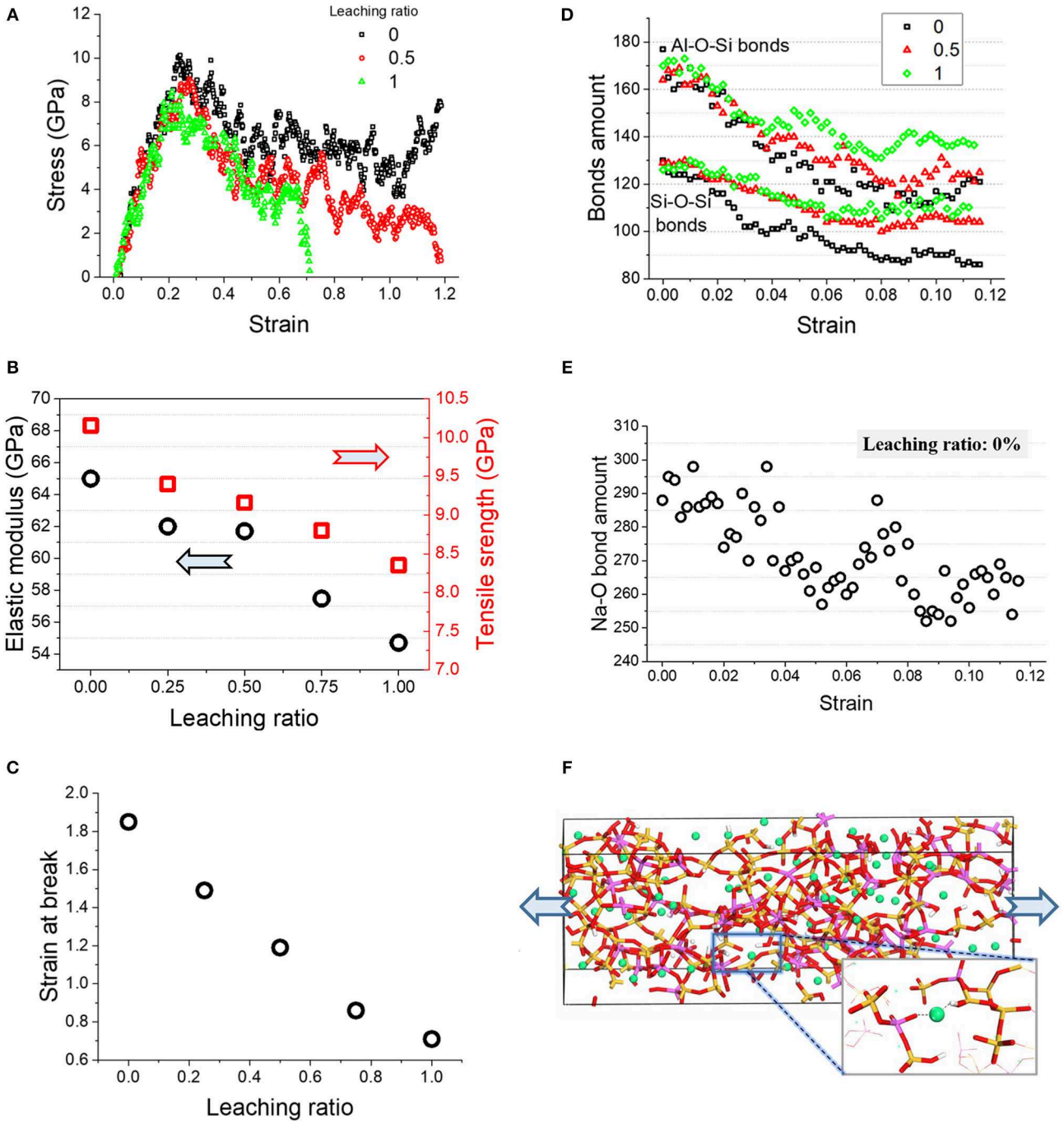

FIGURE 9 | (A) Stress-strain relation of N-A-S-H gels after leaching; **(B)** tensile strength and elastic modulus, and **(C)** strain at the breaking point of N-A-S-H; variations of **(D)** S-O-Si and Si-O-Al bonds and **(E)** Na-O bond variations as functions of tensile strain; **(F)** a snapshot of N-A-S-H gel without leaching at a tensile strain of 1.

for all samples. The above discussion is related to the pre-peak stage.

In the post-peak stage, as plotted in **Figure 9D**, the downward gradient of the bond amount increases, implying that the alumosilicate skeleton is broken to consume tensile energy. Meanwhile, the breakage of the skeleton also means the appearance of cracks, leading to a decrease in loading capacity.

Overall, the total amount of broken Si-O-Si and Al-O-Si bonds decreases as the leaching ratio increases, as illustrated in **Figure 9D**. For the N-A-S-H gel subject to mechanical tests, it elucidates that the lower the amount of leaching, the more energy is consumed.

The bridging effect of sodium underlies divergence of bond breakages between samples with different leaching ratios.

Figure 9E presents a snapshot of a N-A-S-H gel without leaching at a tensile strain of 1. Sodium plays roles in connecting the broken alumino-silicate skeleton through the electrostatic force between sodium and oxygen. The sodium distributed among the skeleton effectively transfers tensile stress, contributing to a uniform dispersion of tensile stress.

Moreover, the existence of Na-O bonds also increases the integrity of the structure. **Figure 9F** shows the variation of Na-O bonds with strain. The downward trend indicates the breakage of Na-O bonds under tension. But the broken Na-O bonds can be easily reformed by matching with surrounding tetrahedral oxygen. As a result, the breakage and regeneration of Na-O bonds occurs simultaneously, resulting in a large fluctuation in the amount of Na-O bonds. All of these processes contribute to an improvement of the fracture energy of the N-A-S-H gel.

The above results complement the mechanism of the leaching process shown in **Figure 8**. The deterioration of mechanical properties only occurs on the N-A-S-H substrate surface that is exposed to solution. When the external environment deteriorates, such as after exposure to temperature variation or external loading, it is more apparent that the dissolution and peeling of the surface layer of N-A-S-H substrate further accelerates sodium dissociation.

CONCLUSIONS

This paper simulated the leaching of a surface of a N-A-S-H gel with a volume of $2 \times 2 \times 2$ nm to reveal the mechanism of alkali dissolution from the gels of geopolymers at the nanoscale.

1. Sodium plays roles in balancing the charges of $[AlO_4]$ tetrahedrons, and its absence leads to local structures showing a negative charge, resulting in locally mutual repulsion between tetrahedrons, and eventually swelling the overall structure. Leaching may not affect silicate species directly.
2. Sodium absence makes the originally stable non-bridging oxygen active again, promoting hydrolytic reactions. Newly produced hydroxyls exacerbate non-conservation of charge of the N-A-S-H system, further swelling the structure.
3. Under the influence of leaching, the alumino-silicate skeleton of the N-A-S-H gel is weakened to some extent, and even fractured, leading to a decrease in the stability of the overall structure, which in turn promotes the dissociation of sodium.
4. The structure deterioration mentioned above leads to the degradation of mechanical properties of surface gel, including strength, Young's modulus, and ductility, which promotes the disaggregation of the surface gel. Sodium plays roles in connecting the skeleton by the electrostatic force with tetrahedral oxygen, which transfers stress and contributes to uniform stress dispersion.
5. Leaching starts from the gel surface, in which the gel swells and is weakened in the above manner, resulting in depolymerization and peeling. Then, a fresh internal N-A-S-H gel surface is exposed and a new leaching process begins. In this way, the gel peels off layer by layer, resulting in microscopic holes and fissures.

DATA AVAILABILITY STATEMENT

The raw data supporting the conclusions of this article will be made available by the authors, without undue reservation, to any qualified researcher.

AUTHOR CONTRIBUTIONS

HW: writing–original draft preparation. LY: supervision. YZ: conceptualization, methodology, software, visualization, and investigation.

FUNDING

This research was financially supported by the National Natural Science Foundation of China (51578143) and the National Key Research and Development Program of China (2018YFC0705400).

REFERENCES

Arbi, K., Nedeljković, M., Zuo, Y., and Ye, G. (2016). A review on the durability of alkali-activated fly ash/slag systems: advances, lssues, and perspectives. *Ind. Eng. Chem. Res.* 55:5439–5453. doi: 10.1021/acs.iecr.6b00559

Bai, C., Liu, L., and Sun, H. (2012). Molecular dynamics simulations of methanol to olefin reactions in HZSM-5 zeolite using a reaxff force field. *J. Phys. Chem.* 116, 7029–7039. doi: 10.1021/jp300221j

Bernal, S. A., Provis, J. L., Walkley, B., Nicolas, R. S., Gehman, J. D., Brice, D. G., et al. (2013). Gel nanostructure in alkali-activated binders based on slag and fly ash, and effects of accelerated carbonation. *Cem. Concr. Res.* 53, 127–144. doi: 10.1016/j.cemconres.2013.06.007

Bonnaud, P. A., Ji, Q., Coasne, B., Pellenq, R. J., and Van Vliet, K. J. (2012). Thermodynamics of water confined in porous calcium-silicate-hydrates. *Langmuir* 28, 11422–11432. doi: 10.1021/la301738p

Bortnovsky, O., Dědeček, J., TvaruŽková, Z., Sobalík, Z., and Šubrt, J. (2008). Metal ions as probes for characterization of geopolymer materials. *J. Am. Ceram. Soc.* 91, 3052–3057. doi: 10.1111/j.1551-2916.2008.02577.x

Duxson, P., Fernández-Jiménez, A., Provis, J. L., Lukey, G. C., Palomo, A., and Deventer, J. S. J. V. (2007). Geopolymer technology: the current state of the art. *J. Mater. Sci.* 42, 2917–2933. doi: 10.1007/s10853-006-0637-z

Duxson, P., Lukey, G., Separovic, F., and Van Deventer, J. (2005). Effect of alkali cations on aluminum incorporation in geopolymeric gels. *Ind. Eng. Chem. Res.* 44, 832–839. doi: 10.1021/ie0494216

Duxson, P., Provis, J., Lukey, G., Van Deventer, J., Separovic, F., and Gan, Z. (2006). 39K NMR of free potassium in geopolymers. *Ind. Eng. Chem. Res.* 45, 9208–9210. doi: 10.1021/ie060838g

Habert, G., Lacaillerie, J. B. D. E. D., and Roussel, N. (2011). An environmental evaluation of geopolymer based concrete production: reviewing current research trends. *J. Clean. Prod.* 19, 1229–1238. doi: 10.1016/j.jclepro.2011.03.012

Hoover, W. G. (1985). Canonical dynamics: equilibrium phase-space distributions. *Phys. Rev. A Gen. Phys.* 31, 1695–1697. doi: 10.1103/PhysRevA.31.1695

Hoover, W. G. (1986). Constant-pressure equations of motion. *Phys. Rev. A Gen. Phys.* 34, 2499–2500. doi: 10.1103/PhysRevA.34.2499

Hou, D., Li, T., and Wang, P. (2018a). Molecular dynamics study on the structure and dynamics of NaCl solution transport in the nanometer channel of CASH gel. *ACS Sustain. Chem. Eng.* 6, 9498–9509. doi: 10.1021/acssuschemeng.8b02126

Hou, D., and Li, Z. (2014). Molecular dynamics study of water and ions transport in nano-pore of layered structure: a case study of tobermorite. *Microporous Mesoporous Mater.* 195, 9–20. doi: 10.1016/j.micromeso.2014.04.011

Hou, D., Ma, H., Li, Z., and Jin, Z. (2014). Molecular simulation of "hydrolytic weakening": a case study on silica. *Acta Mater.* 80, 264–277. doi: 10.1016/j.actamat.2014.07.059

Hou, D., Yu, J., and Wang, P. (2019). Molecular dynamics modeling of the structure, dynamics, energetics and mechanical properties of cement-polymer nanocomposite. *Compos. B Eng.* 162, 433–444. doi: 10.1016/j.compositesb.2018.12.142

Hou, D., Zhang, J., Pan, W., Zhang, Y., and Zhang, Z. (2020). Nanoscale mechanism of ions immobilized by the geopolymer: a molecular dynamics study. *J. Nucl. Mater.* 528:151841. doi: 10.1016/j.jnucmat.2019.151841

Hou, D., Zhang, Y., Yang, T., Zhang, J., Pei, H., Zhang, J., et al. (2018b). Molecular structure, dynamics, and mechanical behavior of sodium aluminosilicate hydrate (NASH) gel at elevated temperature: a molecular dynamics study. *Phys. Chem. Chem. Phys.* 20, 20695–20711. doi: 10.1039/C8CP03411G

Kani, E. N., Allahverdi, A., and Provis, J. L. (2012). Efflorescence control in geopolymer binders based on natural pozzolan. *Cem. Concr. Compos.* 34, 25–33. doi: 10.1016/j.cemconcomp.2011.07.007

Lloyd, R. R., Provis, J. L., and Van Deventer, J. S. (2010). Pore solution composition and alkali diffusion in inorganic polymer cement. *Cem. Concr. Res.* 40, 1386–1392. doi: 10.1016/j.cemconres.2010.04.008

Longhi, M. A., Rodríguez, E. D., Walkley, B., Zhang, Z., and Kirchheim, A. P. (2020). Metakaolin-based geopolymers: relation between formulation, physicochemical properties and efflorescence formation. *Compos. B Eng.* 182:107671. doi: 10.1016/j.compositesb.2019.107671

Longhi, M. A., Walkley, B., Rodríguez, E. D., Kirchheim, A. P., Zhang, Z., and Wang, H. (2019). New selective dissolution process to quantify reaction extent and product stability in metakaolin-based geopolymers. *Compos. B Eng.* 176:107172. doi: 10.1016/j.compositesb.2019.107172

Lu, L., Zhang, Y., and Yin, B. (2020). Structure evolution of the interface between graphene oxide-reinforced calcium silicate hydrate gel particles exposed to high temperature. *Comput. Mater. Sci.* 173:109440. doi: 10.1016/j.commatsci.2019.109440

Provis, J., and Van Deventer, J. (2007). Geopolymerisation kinetics. 2. reaction kinetic modelling. *Chem. Eng. Sci.* 62, 2318–2329. doi: 10.1016/j.ces.2007.01.028

Provis, J. L., Palomo, A., and Shi, C. (2015). Advances in understanding alkali-activated materials. *Cem. Concr. Res.* 78, 110–125. doi: 10.1016/j.cemconres.2015.04.013

Sadat, M. R., Bringuier, S., Asaduzzaman, A., Muralidharan, K., and Zhang, L. (2016a). A molecular dynamics study of the role of molecular water on the structure and mechanics of amorphous geopolymer binders. *J. Chem. Phys.* 145, 1633–1503. doi: 10.1063/1.4964301

Sadat, M. R., Bringuier, S., Muralidharan, K., Runge, K., Asaduzzaman, A., and Zhang, L. (2016b). An atomistic characterization of the interplay between composition, structure and mechanical properties of amorphous geopolymer binders. *J. Noncryst. Solids* 434, 53–61. doi: 10.1016/j.jnoncrysol.2015.11.022

Shi, C., Jiménez, A. F., and Palomo, A. (2011). New cements for the 21st century: the pursuit of an alternative to Portland cement. *Cem. Concr. Res.* 41, 750–763. doi: 10.1016/j.cemconres.2011.03.016

Singh, B., Ishwarya, G., Gupta, M., and Bhattacharyya, S. (2015). Geopolymer concrete: a review of some recent developments. *Constr. Build. Mater.* 85, 78–90. doi: 10.1016/j.conbuildmat.2015.03.036

Singh, P. S., Trigg, M., Burgar, I., and Bastow, T. (2005). Geopolymer formation processes at room temperature studied by 29Si and 27Al MAS-NMR. *J. Mater. Sci. Eng. A* 396, 392–402. doi: 10.1016/j.msea.2005.02.002

Škvára, F., Pavlasová, S., Kopecký, L., Myšková, L., and Alberovská, L. (2008). "High temperature properties of fly ash-based geopolymers," in *Proceedings of the 3rd International Symposium on Non-Traditional Cement and Concrete,* 741–750.

Škvára, F., Šmilauer, V., Hlaváček, P., Kopecký, L., and Cilova, Z. (2012). A weak alkali bond in (N, K)–A–S–H gels: evidence from leaching and modeling. *Ceram. Silik.* 56, 374–382.

Szklorzová, H., and Bílek, V. (2008). "Influence of alkali ions in the activator on the performance of alkali-activated mortars,"in *Proceedings of the 3rd International Symposium on Non-traditional Cement and Concrete* (Brno, Czech Republic), 10–12.

Wan, X., Hou, D., Zhao, T., and Wang, L. (2017). Insights on molecular structure and micro-properties of alkali-activated slag materials: a reactive molecular dynamics study. *Constr. Build. Mater.* 139, 430–437. doi: 10.1016/j.conbuildmat.2017.02.049

Yao, X., Yang, T., and Zhang, Z. (2016). Compressive strength development and shrinkage of alkali-activated fly ash–slag blends associated with efflorescence. *Mater. Struc.* 49, 2907–2918. doi: 10.1617/s11527-015-0694-3

Youssef, M., Pellenq, R. J. M., and Yildiz, B. (2011). Glassy nature of water in an ultraconfining disordered material: the case of calcium–silicate–hydrate. *J. Am. Chem. Soc.* 133, 2499–2510. doi: 10.1021/ja107003a

Zhang, M., Zhao, M., Zhang, G., Mann, D., Lumsden, K., and Tao, M. (2016). Durability of red mud-fly ash based geopolymer and leaching behavior of heavy metals in sulfuric acid solutions and deionized water. *Constr. Build. Mater.* 124, 373–382. doi: 10.1016/j.conbuildmat.2016.07.108

Zhang, Y., Li, T., Hou, D., Zhang, J., and Jiang, J. (2018a). Insights on magnesium and sulfate ions' adsorption on the surface of sodium alumino-silicate hydrate (NASH) gel: a molecular dynamics study. *Phys. Chem. Chem. Phys.* 20:18297. doi: 10.1039/C8CP02469C

Zhang, Y., Wan, X., Hou, D., Zhao, T., and Cui, Y. (2018d). The effect of mechanical load on transport property and pore structure of alkali-activated slag concrete. *Constr. Build. Mater.* 189, 397–408. doi: 10.1016/j.conbuildmat.2018.09.009

Zhang, Y., Yang, T., Jia, Y., Hou, D., Li, H., Jiang, J., et al. (2018c). Molecular dynamics study on the weakening effect of moisture content on graphene oxide reinforced cement composite. *Chem. Phys. Lett.* 708, 177–182. doi: 10.1016/j.cplett.2018.08.023

Zhang, Y., Zhang, J., Jiang, J., Hou, D., and Zhang, J. (2018b). The effect of water molecules on the structure, dynamics, and mechanical properties of sodium aluminosilicate hydrate (NASH) gel: a molecular dynamics study. *Const. Build. Mater.* 193, 491–500. doi: 10.1016/j.conbuildmat.2018.10.221

Zhang, Y., Zhang, Q., Hou, D., and Zhang, J. (2020). Tuning interfacial structure and mechanical properties of graphene oxide sheets/polymer nanocomposites by controlling functional groups of polymer. *Appl. Surf. Sci.* 504:144152. doi: 10.1016/j.apsusc.2019.144152

Zhang, Z., Provis, J. L., Ma, X., Reid, A., and Wang, H. (2018). Efflorescence and subflorescence induced microstructural and mechanical evolution in fly ash-based geopolymers. *Cem. Concr. Compos.* 92, 165–177. doi: 10.1016/j.cemconcomp.2018.06.010

Zhang, Z., Provis, J. L., Reid, A., and Wang, H. (2014). Fly ash-based geopolymers: the relationship between composition, pore structure and efflorescence. *Cem. Concr. Res.* 64, 30–41. doi: 10.1016/j.cemconres.2014.06.004

Zhang, Z., Wang, H., Provis, J. L., and Reid, A. (2013). "Efflorescence: a critical challenge for geopolymer applications?" in *Concrete Institute of Australia's Biennial National Conference* (Gold Coast, QLD), 1–10. Available online at: http://www.ceramics-silikaty.cz/index.php?page=cs_detail_doi&id=250

Conflict of Interest: The authors declare that the research was conducted in the absence of any commercial or financial relationships that could be construed as a potential conflict of interest.

Copyright © 2020 Wan, Yuan and Zhang. This is an open-access article distributed under the terms of the Creative Commons Attribution License (CC BY). The use, distribution or reproduction in other forums is permitted, provided the original author(s) and the copyright owner(s) are credited and that the original publication in this journal is cited, in accordance with accepted academic practice. No use, distribution or reproduction is permitted which does not comply with these terms.

frontiers in Materials

ORIGINAL RESEARCH
published: 02 June 2020
doi: 10.3389/fmats.2020.00127

A Molecular Dynamics Study on the Structure, Interfaces, Mechanical Properties, and Mechanisms of a Calcium Silicate Hydrate/2D-Silica Nanocomposite

Yang Zhou[1,2], Haojie Zheng[1], Yuwen Qiu[1], Xixi Zou[1] and Jiale Huang[1]*

[1] School of Materials Science and Engineering, Southeast University, Nanjing, China, [2] State Key Laboratory of High Performance Civil Engineering Materials, Jiangsu Research Institute of Building Science Co., Nanjing, China

OPEN ACCESS

Edited by:
Dongshuai Hou, Qingdao University of Technology, China

Reviewed by:
Jinrui Zhang, Tianjin University, China
Asad Hanif, University of Macau, China
Ravichandar Babarao, RMIT University, Australia

***Correspondence:**
Yang Zhou
tomaszy@seu.edu.cn

Specialty section:
This article was submitted to Computational Materials Science, a section of the journal Frontiers in Materials

Received: *20 December 2019*
Accepted: *20 April 2020*
Published: *02 June 2020*

Citation:
Zhou Y, Zheng H, Qiu Y, Zou X and Huang J (2020) A Molecular Dynamics Study on the Structure, Interfaces, Mechanical Properties, and Mechanisms of a Calcium Silicate Hydrate/2D-Silica Nanocomposite. Front. Mater. 7:127. doi: 10.3389/fmats.2020.00127

The incorporation of nano-reinforcements is believed to be a promising method to create high performance nanocomposites, which are largely dependent on the interfacial connections. In this work, the newly emerging two-dimensional (2D) material, 2D-silica is intentionally intercalated into the interlayer defective sites of calcium silicate hydrate (C-S-H), which is the primary hydration product of ordinary portland cements. The reactive molecular simulation results indicate the nano-reinforcement can strongly interact with the inorganic matrix to form a high-ductility nanocomposite. The uniaxial tensile loading tests show the plastic stage of the C-S-H is considerably enhanced due to the intercalation of 2D-silica, which removes the intrinsic brittleness of cement-based materials at the nano-scale. It is observed that the dangling atoms at the edge of 2D-silica can react with non-bridging oxygen atoms of C-S-H, forming Si-O-Si bonds at interfaces. Those covalent bonds transform Q_1 and Q_2 in the C-S-H into high connectivity Q_3 and Q_4 species, which increases the integrity of the matrix and its resistance to crack propagation. During the tensile process, the elongation and breakage of those high-strength covalent bonds needs higher tensile stress and consumes higher energy, which leads to a strong plasticity and higher toughness. This work may shed new lights on the interaction mechanisms between 2D-materials and inorganic hosts, and provide solutions to modifying the brittleness of concrete.

Keywords: 2D-silica, calcium silicate hydrate, ductility, molecular dynamics study, mechanical property

INTRODUCTION

As the most widely used building material at present, nearly 30 billion tons concrete was consumed globally every year (Kim et al., 2018). The manufacturing of cement and concrete releases large amount of greenhouse gas and causes a huge adverse impact on the environment. To mitigate this effect, one path is using less concrete to achieve the same engineering requirements. Therefore, it is necessary to improve the various performance of concrete per unit mass, especially the tensile strength, which is a significant index of mechanical properties and has always been the inherent

defect of cementitious materials (Mehta and Monteiro, 2014; Monteiro et al., 2017). As the main component of ordinary cement hydration products, calcium silicate hydrate (C-S-H) provides the cohesion strength and determines the durability, volume stability, mechanical properties and other engineering properties of concrete (Richardson, 2008; Zhou et al., 2016, 2018b). The C-S-H is a porous gel with an unfixed composition (calcium to silicon ratio) ranging from 0.6 to 2.0 (Jennings, 2008). It shows an amorphous nano-structure, where 3–5 nm particles are packed arbitrarily and thus pores are present in the midst among particles (Jennings, 2008). Within a particle, it is suggested that atoms are arranged in long-range disorder and short-range order. The calcium sheets attract defective silicate sheets to constitute a skeleton of a layered C-S-H molecular structure, with free calcium ions and water molecules filled into the interlayer region (Cong and Kirkpatrick, 1996a; Bauchy et al., 2014). The occurrence of large numbers of pores and defects within the C-S-H nano-structure is believed to be a main factor which limits the mechanical performance of cement-based materials (Jennings, 2008; Richardson, 2008; Mehta and Monteiro, 2014).

Previous publications have proved that an incorporation of nanomaterials into pores and defects of C-S-H such as polymers [PEG (Zhou et al., 2019a), PVA (Zhou et al., 2019b)] and carbon materials [graphene (Hou et al., 2017), carbon nanotube (Konsta-Gdoutos et al., 2010)], can effectively improve the strength, stiffness, ductility, and toughness of C-S-H gels at nano-scale and even concrete at macro-scale. Besides, nano-silica is considered as one of the extremely promising high-tech superfine inorganic materials, due to the small particle size, large specific surface area, strong surface adsorption, high surface energy, excellent thermal electrical resistance. It is widely applied in diverse industries including catalyst carrier, petrochemical, rubber reinforcing agent, plastic filling agent, printing ink thickener and so on (Liong et al., 2008; Tang et al., 2012; Tang and Cheng, 2013). Recently, nano-silica has been used to modify cement-based material (Du et al., 2014; Yu et al., 2014). It is found that nano-silica can act as a nucleation site of cement hydration and participate the pozzolanic reaction to form C-S-H, which improves the release rate of cement hydration heat, shortens hydration induction period and thus improves the early strength of concrete (Madani et al., 2012; Yu et al., 2014). On the other hand, a two-dimensional version of nano-silica (2D-silica) has emerged with the thermal, dynamical, and mechanical stabilities of two-dimensional significantly stronger than the typical bulk silica (Huang et al., 2012; Büchner and Heyde, 2017; Gao et al., 2017). It is believed that 2D-silica can be a superior reinforcement phase into C-S-H due to its high compatibility with the matrix in terms of size and composition, potentially leading to a high performance nanocomposite. However, both experimental and theoretical studies on the C-S-H/2D-silica nanocomposites are still missing, and the interaction mechanisms between the guest and matrix remain unclear.

Molecular dynamics (MD), a force filed based numerical computation method, has recently been widely used to assist the understanding of experimental results, help explain the interaction mechanisms at different phase interfaces, and provide evidence for the composition, structure, and mechanical properties of nanocomposites at the molecular scale (Sanchez and Zhang, 2008; Sakhavand et al., 2013; Duque-Redondo et al., 2014; Hou et al., 2018a,b, 2020). With the aid of molecular dynamics, Pellenq et al. (2009) proposed a molecular model of C-S-H with a calcium to silicon molar ratio (C/S) of 1.7 and a density of 2.6 g/cm^3 (Monteiro et al., 2017), which conformed to the experimental data of nuclear magnetic resonance (NMR), X-ray diffraction (XRD), and small angle neutron scattering (SANS) (Cong and Kirkpatrick, 1996b; Janik et al., 2001; Allen et al., 2007). This model also accurately predict the strength and stiffness of C-S-H (Constantinides and Ulm, 2007; Ulm et al., 2007). Besides, the mechanical properties of C-S-H with different C/S ratios and its structural analogues jennite and tobermorite, calculated by MD simulations, also agreed well with the experimental results (Shahsavari et al., 2009; Manzano et al., 2013; Hou et al., 2014a,b). It implied that C-S-H exhibited an anisotropic feature when subjected to a uniaxial tensile process. C-S-H possessed the weakest tensile strength and ductility along the direction where calcium silicate sheets were aligned alternately due to the defects and pores in the interlayer region (Hou et al., 2014a). Furthermore, previous MD studies have also demonstrated that the intercalation of reinforcement phases could enhance the mechanical properties of C-S-H at the nano-scale, and the corresponding mechanisms have been elucidated. Zhou et al. (2018a) incorporated low-molecular weight polymers into the defects of C-S-H and found a significant increase in the ductility of C-S-H, which may be attributed to the bridging effect. Similarly, the addition of graphene oxide also strengthened the interlayer region of C-S-H by the formation of interfacial bonds in the study of Hou et al. (2017) Moreover, MD simulations also suggested that the stability of those interfacial bonds was highly affected by the polarity of functional groups, which determined the overall performance of the composite (Zhou et al., 2017b). However, the simulation of the mechanical behavior and mechanism of C-S-H/2D-silica nanocomposites is still lacking.

Therefore, in this work, in consideration of a high compositional and volumetric compatibility with the matrix, 2D-silica, a newly promising high-stiffness material was intercalated into the defective sites of C-S-H. With the aid of molecular dynamics, the composition, structure, and mechanical properties of C-S-H/2D-silca nanocomposites were evaluated, while the interfacial interactions between the matrix and reinforcement phase and mechanisms on the performance enhancement were investigated.

SIMULATION DETAILS

Reactive Force Fields

The reactive force field ReaxFF was employed to simulate the chemical reactions occurring in both model establishment and uniaxial loading test. The ReaxFF force field (C/O/H), developed by van Duin, was originally applied in the large scale reactive chemical systems of the hydrocarbons (van Duin et al., 2001), and then another updated version (Si/O/H) was utilized to describe an inorganic system (van Duin et al., 2003). Currently, it also has extensive applications in the study of nanocrystals, silica-water

interfaces, and calcium silicate hydrates (Ca/Si/O/H) (Manzano et al., 2012; Hou et al., 2015; Zhou et al., 2017a). Instead of predefining the connectivity between the atoms at a fixed state, such as ClayFF and CSHFF, the ReaxFF force field adopts a bond order-bond distance scheme. It can generate a smooth energy evolution curve, which enables the breakage and formation of chemical bonds to be captured (Schuetz and Frenklach, 2003). In the light of this philosophy, the reaction process can be tracked and the reaction can be unraveled. The fitting of quantum chemical calculations determines the parameters of ReaxFF (Ca/Si/O/H) and the specific values can be referred to previously published papers (van Duin et al., 2001; Chenoweth et al., 2008; Manzano et al., 2012).

Models

At first, an anhydrous C-S-H host model of around 44 × 44 × 44 Å was built following the procedures in Zhou et al. (2017b), and the C/S was set to be 1.3. As shown in **Figure 1**, the C-S-H model has a layered structure. Within a calcium silicate sheet (xy plane), and the defective chains of silicate tetrahedrons are arranged along y direction and the neighboring silicate chains are attracted by calcium sheets along x direction. The calcium silicate sheets are alternately aligned out of the xy plane along z direction. Obviously, several defects are present in the interlayer region of C-S-H.

Subsequently, a proper 2D-silica guest model was selected according to a previous density function theory study. Gao et al. (2017) put forward four possible structures of 2D-silica. Among those, δ-2D-silica, presented in **Figure 1**, is selected as the reinforcement phase to be intercalated into the interlayer region of C-S-H, due to its advantages over other structures (Gao et al., 2017). δ-2D-silica has the smallest layer thickness and high Young's modulus as well as a negative Poisson ratio. Different dosages of 2D-silica were intercalated into the defective sites of anhydrous C-S-H model to construct the C-S-H/2D-silica model.

Finally, a Grand Canonical Monte Carlo (GCMC) water adsorption method was employed to saturate the pure C-S-H model and C-S-H/2D-silica model. By GCMC simulations, water molecules can be imbibed into the anhydrous C-S-H, until reaching an equilibrium sate with a fictitious infinite reservoir, at chemical potential $\mu = 0$ eV and temperature $T = 298$ K (Bonnaud et al., 2012). In each GCMC simulation, water molecules are shifted, rotated, created or destructed in equal quantities. The equilibrium and production steps were 10^8 and $2*10^8$, respectively, in a run. The final pure C-S-H and C-S-H/2D-silica models have around 8,000 atoms, which can ensure the statistical reliability of the following structural analysis and uniaxial tensile tests.

Structural Analysis and Uniaxial Tension Tests

Reactive force field molecular dynamics simulations were implemented to investigate the composition and structure of pure C-S-H and C-S-H/2D-silica models. An isothermal–isobaric (NPT) ensemble was utilized, with an equilibrium time of 100 ps and a production time of 300 ps. The C-S-H and C-S-H/2D-silica models were subjected to uniaxial tensile loading through gradual elongation at a fixed rate of 0.08/ps along x, y, z direction, respectively. An isothermal–isobaric (NPT) ensemble was also used. The model was initially relaxed at 298 K and then coupled to zero external pressure in all three dimensions for 300 ps. Subsequently, while the uniaxial test was carried out, the pressure perpendicular to the loading direction was kept at zero, to remove the influence of artificial constraint for the deformation. The maximum strain was set to 0.8 Å/Å. The stress-strain relationships can be obtained by recording the internal stress along the loading direction as a function of the applied strain.

RESULTS AND DISCUSSION

Interactions between calcium silicate hydrate (C-S-H) and 2D-silica are presented from the following perspectives. First, the structure characteristics of pure C-S-H and C-S-H/2D-silica are investigated, respectively, and several structural parameters will be utilized to emphasize the influence of the intercalation of 2D-silica on the composition and structure of the matrix. Second, uniaxial tensile loading experiments are carried out and the effect of 2D-silica on the mechanical properties of the matrix is evaluated. At last, the interfacial reaction mechanisms are unraveled on the basis of the microstructural analysis as a function of the strain developments.

Structure

Calcium Silicate Hydrate

The pure calcium silicate hydrate, as presented in **Figure 1**, has a layered structure. The well-aligned calcium sheets attract the silicate sheets where silicate tetrahedrons connect with each other and are aligned in chains to form the skeleton. Between neighboring calcium silicate sheets, water molecules and calcium ions are distributed, forming the interlayer regions. In the light of different chemical environments, the calcium ions can be divided into two categories, the structural calcium ions and the interlayer calcium ions. The former represent those on the skeleton merely surrounded by silicate tetrahedron chains, attracting the oxygen atoms from silicate tetrahedrons (O_s) to achieve a specific coordination structure. The latter are those in the interlayer regions, distinct of enclosure of water molecules. Likewise, the calcium ions and the oxygen atoms from the water molecules (O_w) are attracted by electrostatic force.

In silicate chains, the presence of bridging oxygen atoms which connect with two silicon atoms, primarily contribute to the connectivity (**Figure 2**). An index of Q species is put forward to analyze the structural composition and connectivity of silicate chains in C-S-H. For a certain silicon atom, Q species is defined as the number of bridging oxygen atoms it forms covalent bonds with. As illustrated in **Figure 2**, Q_1 represents the silicon atoms attracting merely one bridging oxygen atom, while Q_2 for two bridging atoms. Besides, the increase of the parameter n indicates higher degree of polymerization of the silicate chains. Q_1 and Q_2 is only existing Q species in the pure C-S-H, as presented in **Table 1**, and the calculated percentages are consistent with the

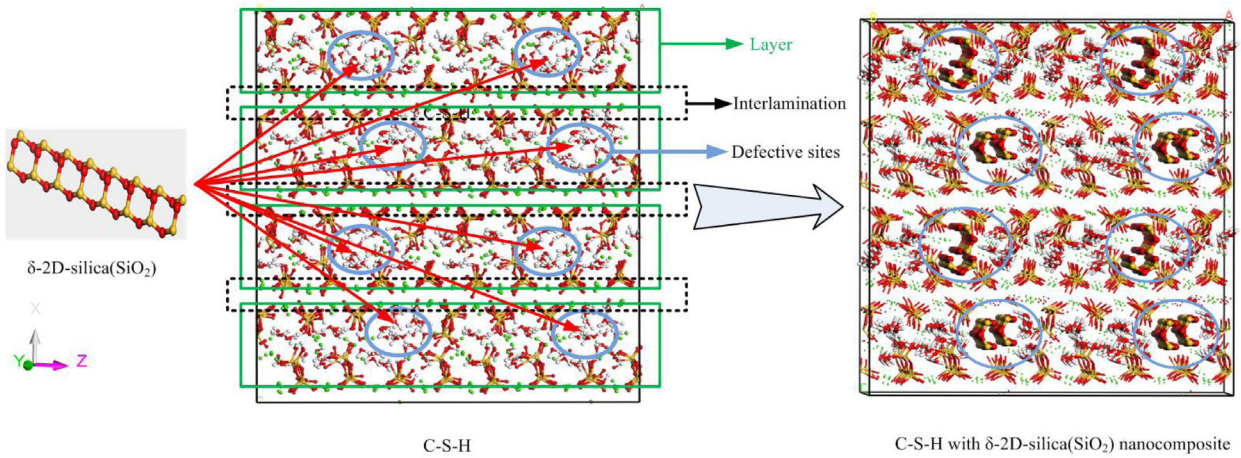

FIGURE 1 | The schematic illustration of the δ-2D-silica (red and yellow balls denote oxygen and silicon atoms, respectively) intercalation into the interlayer defective sites of C-S-H model (green balls indicate calcium ions, red and yellow sticks indicate silicate tetrahedrons, red and white sticks denote water molecules).

(Pellenq et al., 2009) Si NMR experiments (Cong and Kirkpatrick, 1996a). As mentioned above, the interaction between the calcium ions and oxygen atoms plays an important role on the internal cohesion of C-S-H. Therefore, radial distribution function (RDF) (Zhou et al., 2018a), another structural index is proposed to describe the coordination between the calcium ions and oxygen atoms. The result, as presented in **Figure 3A**, indicates the interaction at a distance ranging from 2 to 3 angstroms, abundant pairs of calcium ions and oxygen atoms are present, which represent the Ca-O coordination in C-S-H. Ca-O_s (oxygen from silicate tetrahedrons) pairs constitute the calcium octahedral sheets of C-S-H, while Ca-O_w (oxygen from water molecules) pairs represent the attraction between the intralayer and interlayer region.

Calcium Silicate Hydrate With 2D-Silica Intercalated

The pure C-S-H structure and C-S-H intercalated with 2D-silica structure are shown in **Figures 4A,B**, respectively. In the interlayer regions of pure C-S-H, interstices induced by the defective silicate tetrahedron chains are filled up by large quantities of water molecules, which decrease the density of C-S-H and may affect the mechanical properties. With 2D-silica intercalated, the deficiencies are physically filled up. Meanwhile, owing to the surface effect of 2D-silica, the reactive dangling atoms on the boundary of 2D-silica interact with the silicate tetrahedron chains and form considerable quantities of Si-O-Si bonds (**Figure 4C**). **Table 1** presents the distribution of Q species for pure C-S-H and C-S-H/2D-silica. It indicates that in pure C-S-H, with paucity of Q_3 and Q_4, Q_1 and Q_2 primarily dominate large fractions, respectively, 43.24 and 56.76%, which corresponds with the (Pellenq et al., 2009) Si NMR experimental values (Cong and Kirkpatrick, 1996a). In C-S-H/2D-silica, the occurrence of Q_3 and Q_4 species is observed. Q_3 denotes a silicon connected with three bridging oxygen atoms, which implies a cross-link between neighboring sheets, while Q_4 denotes a silicon network with all connecting oxygen atoms being bridged. The former is owing to the interaction between 2D-silica and the oxygen atoms in silicate tetrahedron chains. The latter, however, is confirmed to mainly derive from 2D-silica rather than C-S-H matrix, which will be explained in the next paragraph. As for Q_1 and Q_2, a drastic decrease of Q_1 is observed, along with a slight decrease of Q_2. The high reactivity of Q_1 is due to the fact that it is situated at the edge of the deficiencies, with a considerable quantity of non-bridging oxygen atoms surrounded. Thus, compared with Q_2, the polymerizations of Q_1 are susceptible to occur.

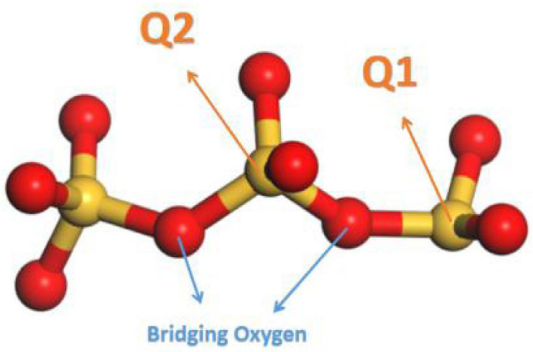

FIGURE 2 | Schematic illustrations of Q species (red balls denote oxygen atoms and yellow balls denote silicon atoms).

TABLE 1 | Q species distribution of pure C-S-H and C-S-H/2D-silica after structural relaxation.

Structure	Q_0 (%)	Q_1 (%)	Q_2 (%)	Q_3 (%)	Q_4 (%)
Pure C-S-H	0	43.24	56.76	0	0
C-S-H/10 wt.% 2D-silica	0.44	27.88	51.84	14.16	5.68
C-S-H/15 wt.% 2D-silica	0.31	22.41	49.21	18.40	9.67
C-S-H/20 wt.% 2D-silica	1.65	20.64	48.00	23.14	6.57

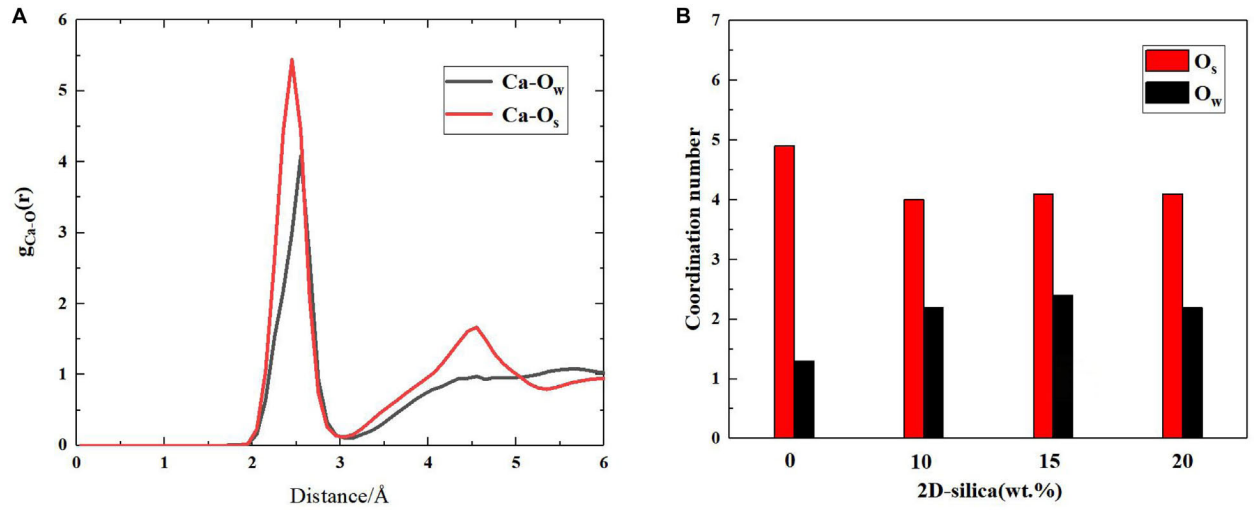

FIGURE 3 | (A) Radial distribution function between Ca and O_w (oxygen from water molecules), O_s (oxygen from silicate tetrahedrons); **(B)** The coordinated oxygen number of calcium ions on average.

Further analysis is conducted to distinguish the transformation details of Q species in the C-S-H matrix (**Table 2**). A decline of 121 is observed for Q_1, and an increase of 22, 26, 72, 8 for Q_0, Q_2, Q_3, and Q_4, respectively. The decline of Q_1 in the C-S-H matrix again confirms the active reactivity of Q_1 at the edge of the deficiencies. Thus, improvement of cohesion of the structure is achieved with further polymerization of Q_1. For Q_2, an increase is observed in the C-S-H matrix, yet the overall structure of C-S-H/2D-silica undergoes a decline of Q_2. This means that the decline of Q_2 primarily comes from 2D-silica. It is recognized that part of the surface silicon atoms in 2D-silica are Q_2, which interacts with non-bridging oxygen atoms from the C-S-H matrix and then transformed to Q_3 and Q_4. The increase of Q_3 in the C-S-H matrix originates from the polymerization of Q_1 and occupies the largest proportion of the loss Q_1 quantities, consistent with **Table 1** as demonstrated above. However, the quantity of generated Q_4 in the C-S-H matrix is relatively low. Combing **Tables 1** and **2**, it can be induced that Q_4 is primarily generated in 2D-silica. A possible explanation is the reorientation of Si-O bonds and transition of tetrahedron structure from δ-2D-silica to α-2D-silica (Madani et al., 2012). Apart from the polymerization, phenomenon of de-polymerization also takes place. The increase of Q_0 indicates that chemical reactions between C-S-H and 2D-silica will lead to a minor quantity of the breakage of Si-O bonds in the silicate tetrahedrons. It is concluded that the polymerization reactions of silicate tetrahedrons between C-S-H and 2D-silica reinforcements lead to an integrated nanocomposite with substantially higher connectivity than the matrix.

The interaction between calcium ions and oxygen atoms are also altered due to the intercalation of 2D-silica. As presented in **Figure 3B**, in pure C-S-H, the calculated coordination environment of a calcium ion is 4.9 O_s and 1.3 O_w on average. A total coordination number of around 6 was reported by a scanning transmission X-ray microscopy study (Orozco et al., 2017), which is consistent with the MD simulation results here. While in C-S-H/2D-silica nanocomposite, the coordination oxygen number of a calcium ion is 4.0 for O_s and 2.0 for O_w. As described earlier, the intercalated 2D-silica situates in the interlayer regions and reacts with O_s atoms, which lowers the number of O_s coordinating with the calcium ions. As a consequence, more O_w atoms will be attracted by calcium ions to maintain the stability of the coordination environment.

Mechanical Properties

The uniaxial tensile experiments for pure C-S-H along x, y, z directions are conducted and the corresponding stress-strain curves are presented in **Figure 5A**. It can be observed that along z direction, C-S-H exhibits the weakest mechanical performance, with a maximum tensile stress of merely 4.8 GPa. As the strain level reaches 45%, a complete breakdown occurs. While along y direction, C-S-H shows the best strength and ductility. After the tensile stress reaches 10.0 GPa at the end of the elastic stage, it maintains a plateau from 20 to 45%. Subsequently, the stress keeps decreasing along with the development of strain level. Along the x direction, the C-S-H exhibits a better mechanical performance than that along z direction, though relatively weaker than y direction. The different performances of C-S-H subjected to tensile loading along three directions are closely related to the structure of pure C-S-H. The out-of-plane stiffness and ductility of C-S-H is dramatically lower than ones of xy-plane. Here, the simulated results are consistent with the previous high pressure XRD results (Geng et al., 2017, 2018) and the detailed explanations will be illustrated in section Influence of the Tensile Direction. It should be noted a minor bump still appeared even after the stress reached zero. It is caused by the computation errors in molecular dynamics simulations. For example, some approximation methods may be employed when computing long-order electrostatic, in order force to decrease the overall computation cost, which may lead to errors.

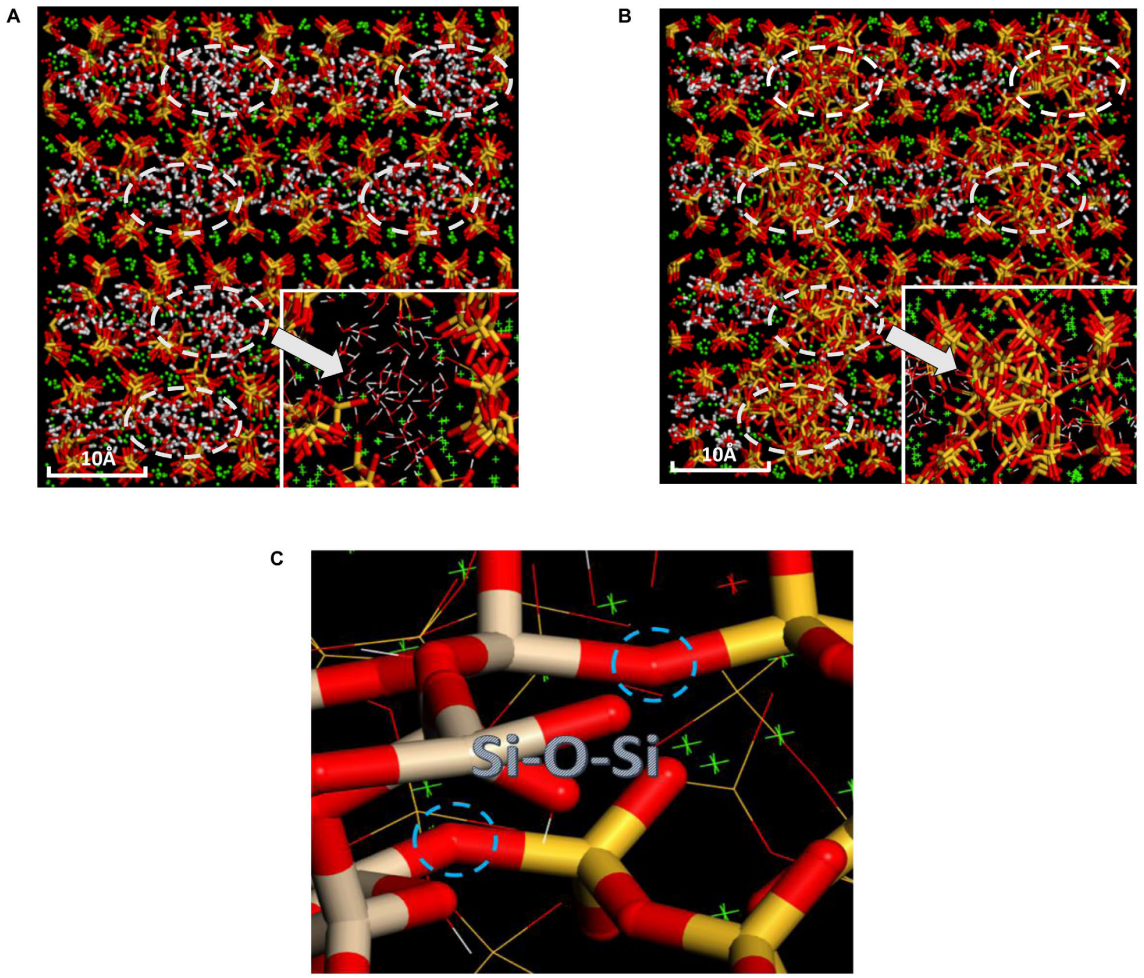

FIGURE 4 | Comparative snapshots of **(A)** pure C-S-H and **(B)** C-S-H/2D-silica structure; **(C)** Schematic illustration of the interfacial Si-O-Si bonds formed between C-S-H and intercalated 2D-silica (the right red and yellow sticks indicate silicate tetrahedrons from C-S-H, while the left red and gray sticks indicate those from 2D-silica).

The influence of 2D-silica reinforcement on the stress-strain relationships of C-S-H is shown in **Figures 5B–D**. Overall, the matrix performs a better mechanical performance along all three directions due to the incorporation of 2D-silica, while along z direction (the originally weakest one) the enhancement efficiency is the highest. It is observed in **Figure 5D** that the decline of stress of pure C-S-H begins when the strain level reaches 15% and the complete fracture occurs when the strain level reaches 45%. The maximum tensile strength is 4.8 GPa and afterward the stress drops rapidly, indicating a brittle fracture.

TABLE 2 | The number change of each Q species in the matrix of C-S-H after the intercalation of 20 wt.% 2D-silica.

	Q_0	Q_1	Q_2	Q_3	Q_4
Initial C-S-H	0	384	504	0	0
Final C-S-H	22	263	530	72	8
ΔQ of C-S-H	22	−121	26	72	8

After 2D-silica is intercalated, the ductility of the structure has been greatly improved, due to the elongation of yield stage. Especially for C-S-H/20 wt.% 2D-silica, the maximum tensile strength reaches 6.8 GPa and the C-S-H remains at the yield stage until the end of tensile process with no distinct fracture observed. The improvement in the ductility can be attributed to the filling of defective pores, and the strong interaction between intercalated 2D-silica and C-S-H matrix, which will be discussed in details in section Influence of the 2D-Silica Intercalated.

The mechanical properties (tensile strength and Young's modulus) of pure C-S-H and C-S-H/2D-silica with different dosages of reinforcements are presented in **Figures 6A,B**, respectively. As for tensile strength, it can be seen that intercalation of 2D-silica greatly improves the tensile strength along all three directions, while the increase of dosage of 2D-silica has a slight influence on the values. From **Figure 6B**, a distinct growth of Young's modulus can also be observed along each direction. Especially

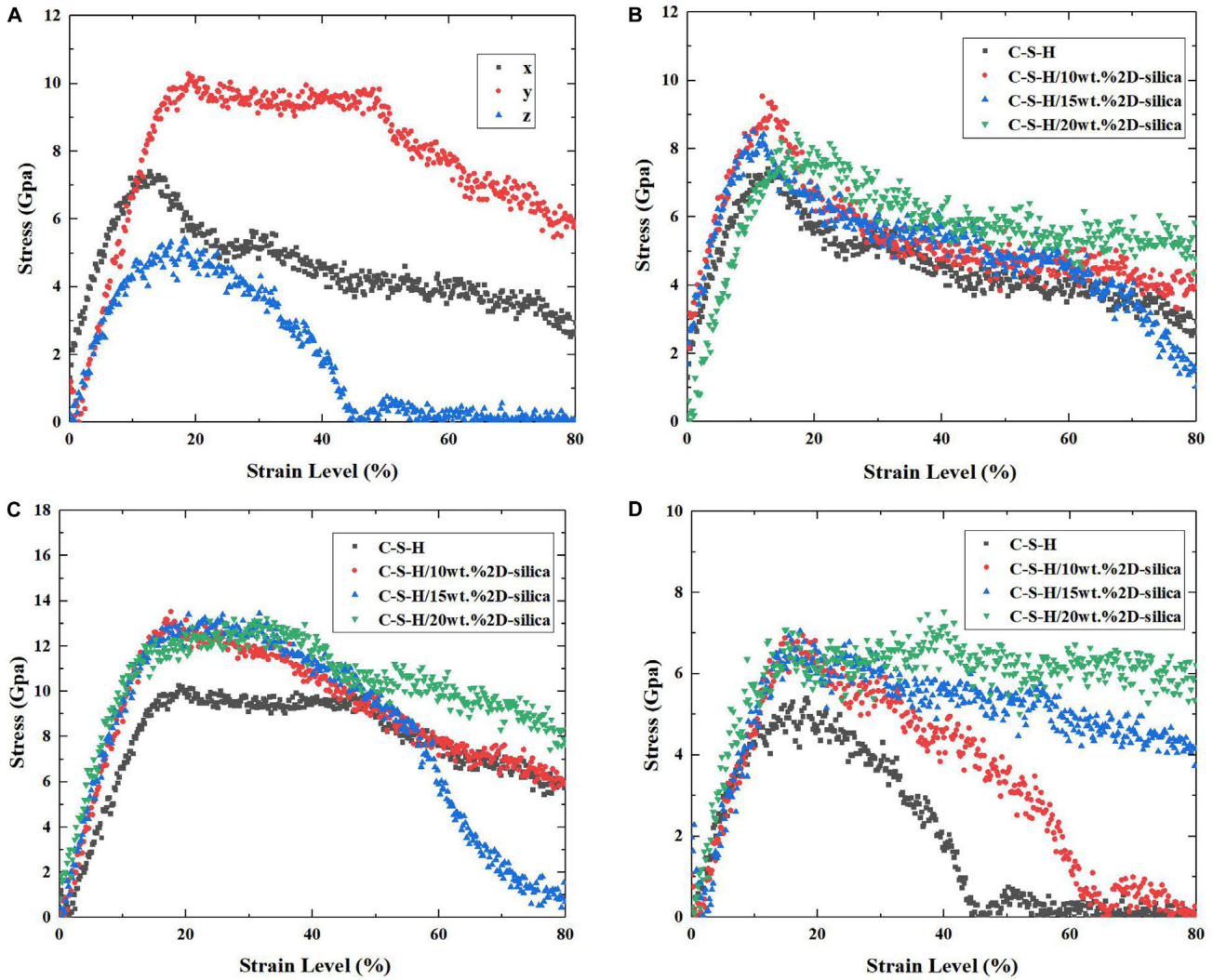

FIGURE 5 | (A) The stress–strain curves of pure C-S-H during the uniaxial tensile process along x, y, and z directions; The stress–strain curves of pure C-S-H and C-S-H/2D-silica with different dosages during the uniaxial tensile process along **(B)** x direction, **(C)** y direction, and **(D)** z direction.

along z direction, the values of Young's modulus seem to have a positive correlation with the dosage of 2D-silica. In conclusion, the intercalation of 2D-silica has the most remarkable improvement on the mechanical performance of the C-S-H matrix along z direction, while a slight influence along x direction.

Mechanism

Influence of the Tensile Direction

First, the mechanisms on the distinguished response of C-S-H matrix to uniaxial tensile process along x, y, and z direction are interpreted. According to the theory of Zhu et al. (2005), there exists two types of hydrolytic reactions in C-S-H model. On the other hand, during the tensile process, the internal tensile stress may reduce the activation energy of those hydrolytic reactions, leading to the dissociation of water molecules and further structural rearrangements. The two types of hydrolytic reaction can be illustrated by the following formulas, respectively:

$$Si - O \cdots Ca + H_2O \rightarrow Si - OH + Ca - OH \quad (1)$$

$$Si - O - Si + H_2O \rightarrow Si - OH + Si - OH \quad (2)$$

In formula (1), the Si-O. . .Ca ionic bonds are fairly weak so that they can be easily stretched until broken. The dangling Si-O bonds will attract the water molecules and cause dissociation of water molecules to hydrogen atoms and hydroxyl groups. Subsequently, the generated hydrogen atoms and hydroxyl groups react with the Si-O bonds and calcium ions, respectively, to form the same amount of Si-OH and Ca-OH (presented in **Figure 7**). In formula (2), the dissociation of water molecules is based on the breakage of Si-O-Si bonds into Si-O- and Si- groups, which indicates depolymerization of the silicate tetrahedrons.

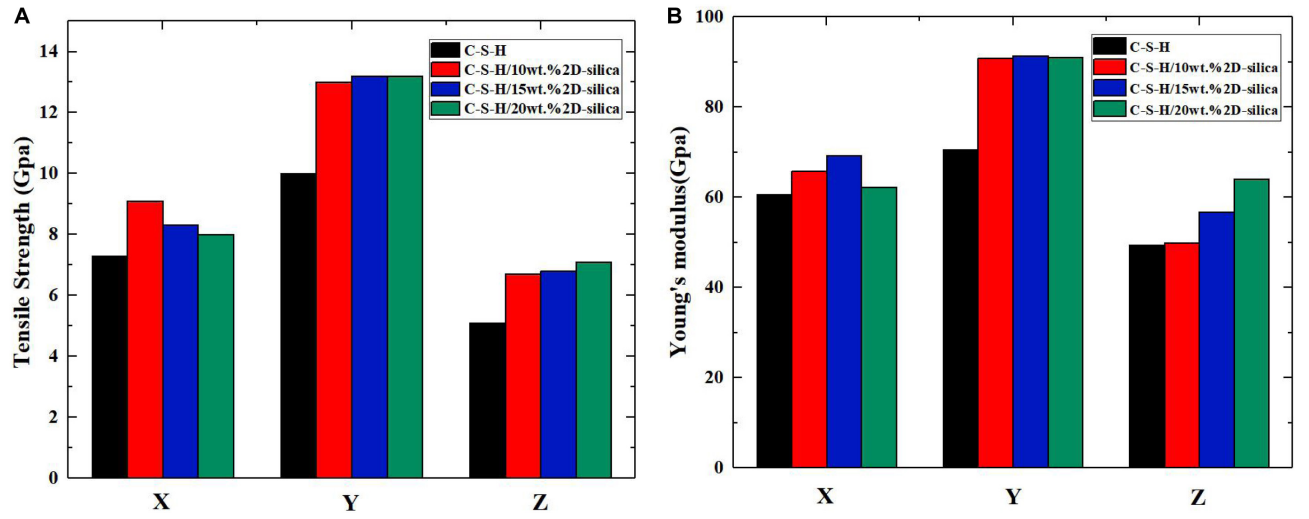

FIGURE 6 | The calculated mechanical properties of pure C-S-H and C-S-H/2D-silica with different dosages: **(A)** tensile strength; **(B)** Young's modulus.

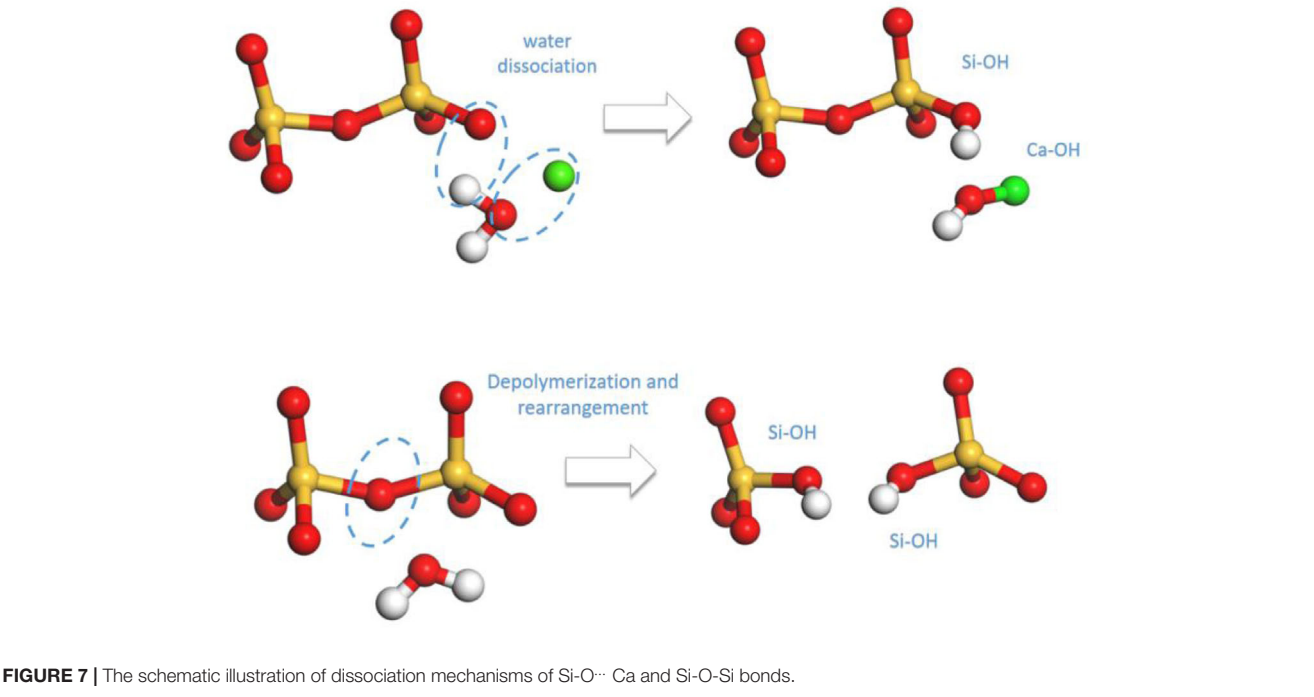

FIGURE 7 | The schematic illustration of dissociation mechanisms of Si-O··· Ca and Si-O-Si bonds.

The active non-bridging oxygen atoms in Si-O- will attract and dissociate the water molecules, forming double amount of Si-OH.

On the basis of the above reaction principles, the structural evolution mechanism of C-S-H during the tensile process can be unraveled by monitoring the number change of Ca-OH and Si-OH, as well as the distribution development of Q species. **Figures 8**, **9**, respectively, represent the number evolution of those indicators during the tensile process. As showed in **Figures 8A,C**, along x and z directions, the number of Ca-OH and Si-OH exhibits a synchronous increase, indicating merely the occurrence of reaction (1) during the tensile process. The plateau in the z direction (presented in **Figure 8C**) corresponds with the complete fracture of C-S-H when the strain reaches 0.45 Å/Å. Besides, according to **Figures 9A,C**, there is no distinct evolution of Q species along the x and z directions, which well proves that the silicate tetrahedron chains are not affected in the tensile process. Thus, it is the elongation and breakage of Si-O··· Ca bonds that are responsible for the strain development. Along the y direction, the evolution of the Ca-OH and Si-OH number follows another mode, with a rapid increase of Si-OH number and almost no change of Ca-OH number. It is caused by the mere occurrence of reaction (2). As for the evolution of Q species,

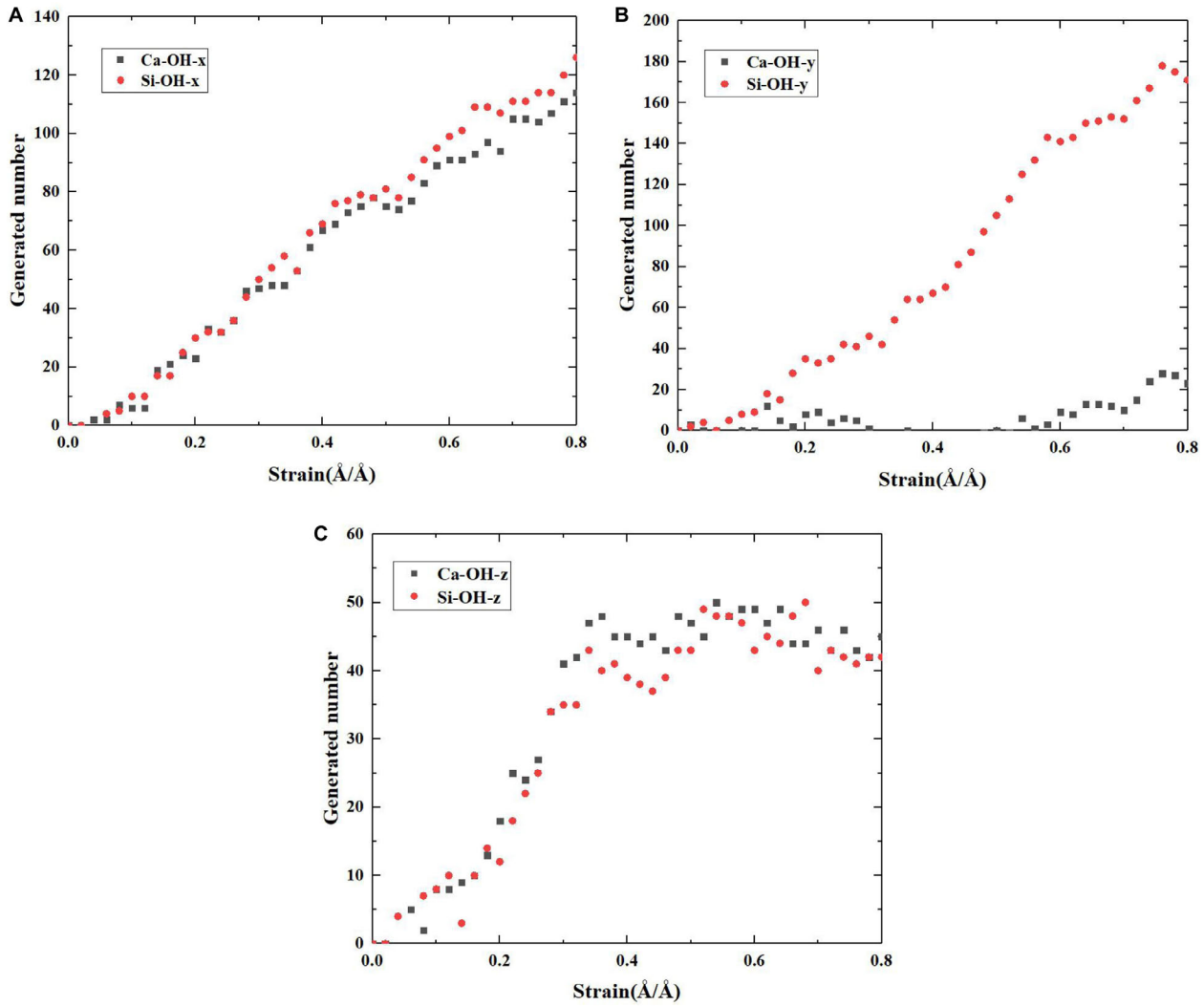

FIGURE 8 | The number evolution of generated Ca–OH, Si–OH along **(A)** x, **(B)** y, and **(C)** z direction.

as presented in **Figure 9B**, it indicates a decrease of Q_2 and an increase of Q_0 and Q_1, which also suggests a decomposition of Q_2 to form Q_0 and Q_1. Therefore, it is concluded that mainly the high-strength Si-O-Si bonds are stretched and broken during the tensile process along y direction. Since the Si-O-Si bond owns significantly higher bond energy than Si-O. . .Ca, C-S-H exhibits a higher performance along y direction (**Figure 5A**).

Influence of the 2D-Silica Intercalated

Since the intercalation of 2D-silica performs the highest enhancement efficiency on the mechanical properties of C-S-H along z direction, the detailed interaction mechanisms between the host and the reinforcement will be interpreted along this direction. Snapshots of pure C-S-H and C-S-H/2D-silica during the tensile process are presented in **Figure 10** which are arranged on the basis of different strain levels (0.1, 0.2, 0.3, 0.4, 0.5, and 0.6 Å/Å). The initial interlayer spacings are, respectively, 8.2 and 9.5 Å for C-S-H and C-S-H/2D-silica, indicating that the intercalation of 2D-silica has enlarged the interlayer spacing. The 2D-silica molecules act as bridges in the interlayer regions, connecting the neighboring calcium silicate sheets by the formation of large quantities of Si-O-Si bonds, which is caused by the strong interaction between the 2D-silica and C-S-H matrix, as shown in **Figure 4C**. As described earlier, during the tensile process along z direction, for pure C-S-H, the breakage of Si-O···Ca bonds is primarily responsible for the development of strain, generating the same amount of Ca-OH and Si-OH. However, for C-S-H/2D-silica, the presence of Si-O-Si bonds in the interlayer regions significantly changes the reaction mechanism during the tensile process.

With the development of the strain, the interlayer spacing of pure C-S-H is gradually enlarged, leading to distinct cracks when the strain reaches 0.3 Å/Å. On the contrary, the interlayer spacing of C-S-H/2D-silica increases continuously, with no soar of extension rate observed. The integrality of the C-S-H has not been affected owing to the formation of Si-O-Si bonds

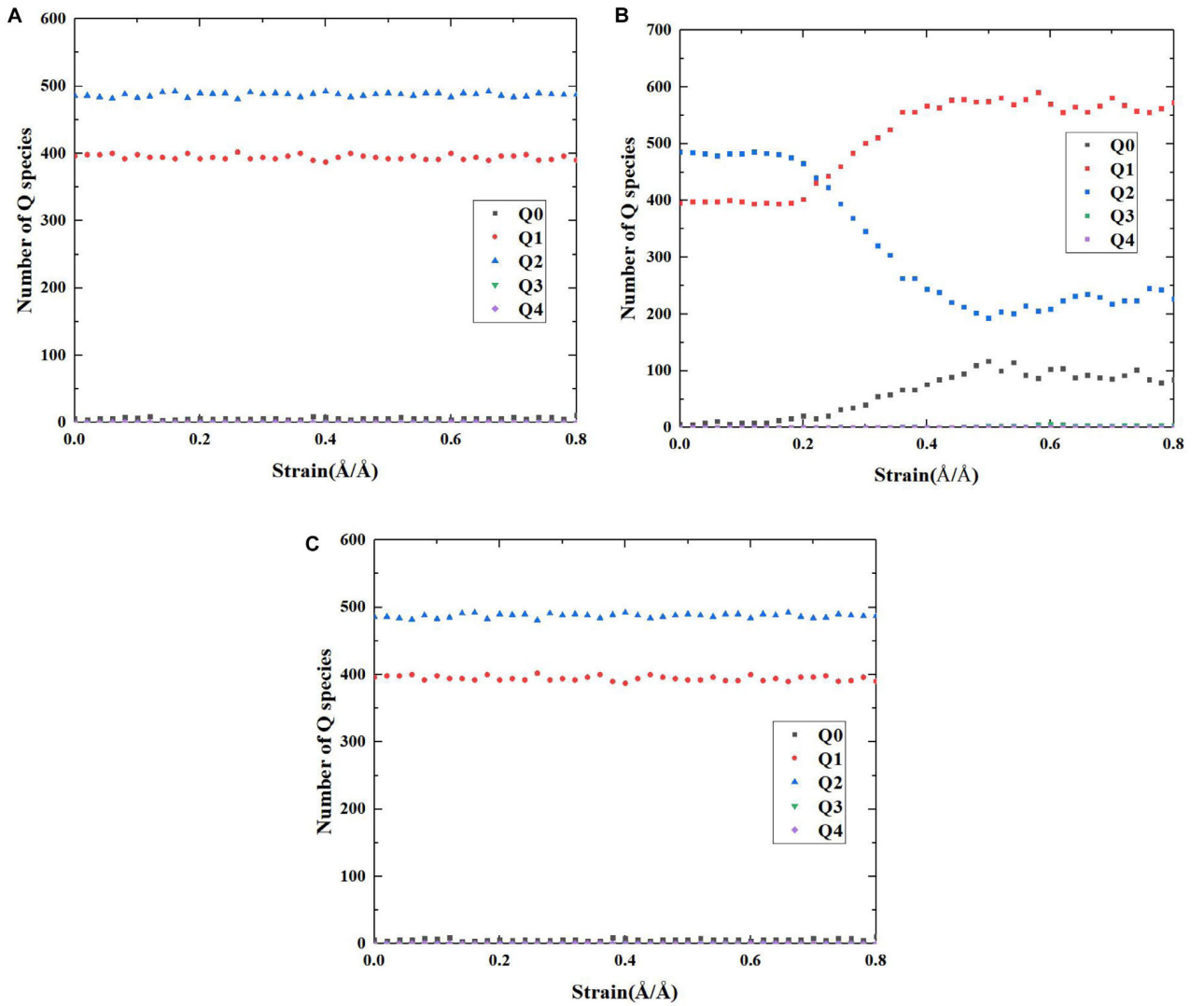

FIGURE 9 | The number evolution of each Q species of pure C-S-H as a function of strain during the tensile process along **(A)** x, **(B)** y, and **(C)** z direction.

between calcium silicate sheets. Yet for the regions deficient of layer connection, the expansion of interstices can be observed. When the strain reaches 0.4 Å/Å, pure C-S-H undergoes a complete fracture (interlayer spacing of 15.2 Å/Å), while C-S-H/2D-silica still remains intact (interlayer spacing of 12.1 Å/Å). When the strain continues to develop in C-S-H/2D-silica, considerable deformation and interstices can be observed. With the connection of the strong Si-O-Si bonds, ultimate rupture is not observed even though the strain reaches 0.8 Å/Å. It is owing to the high strength of Si-O-Si bonds that contributes to the elongation of yield stage, which is consistent with the plateau of stress as presented in **Figure 5D**.

Besides, it is worth noting that in Zhou's research about polymer-reinforced C-S-H (Zhou et al., 2018a), the formation of Si-O-C bonds between C-S-H and PEG, PVA, and PAA strengthens the connection of layers, which leads to similar effect of enhancement of strength and ductility. Thus, it is concluded that the interlayer bridging mechanism can effectively enhance the ductility of C-S-H matrix. In addition, in Zhou's research, even though the intercalation of PEG shows the best enhancement of ductility comparing with other polymers, the C-S-H structure still undergoes a complete fracture when the strain reaches 0.8 Å/Å. In the opposite, as presented in **Figures 5D**, **10**, the C-S-H/2D-silica structure still remains intact and retains a high level of tensile strength even the strain reaches 0.8 Å/Å. This proves that the strength of Si-O-Si bonds are higher than that of Si-O-C bonds, thus the breakage of bonds requires more activation energy. In other words, in terms of the enhancement efficiency, 2D-silica performs better than polymers. Besides, the enhancement effect shows a positive correlation with the amount of intercalation of 2D-silica (**Figures 5D**, **11**). The increase of amount of 2D-silica can effectively fill up the interstices and form more Si-O-Si bonds between layers which significantly enhance the connection.

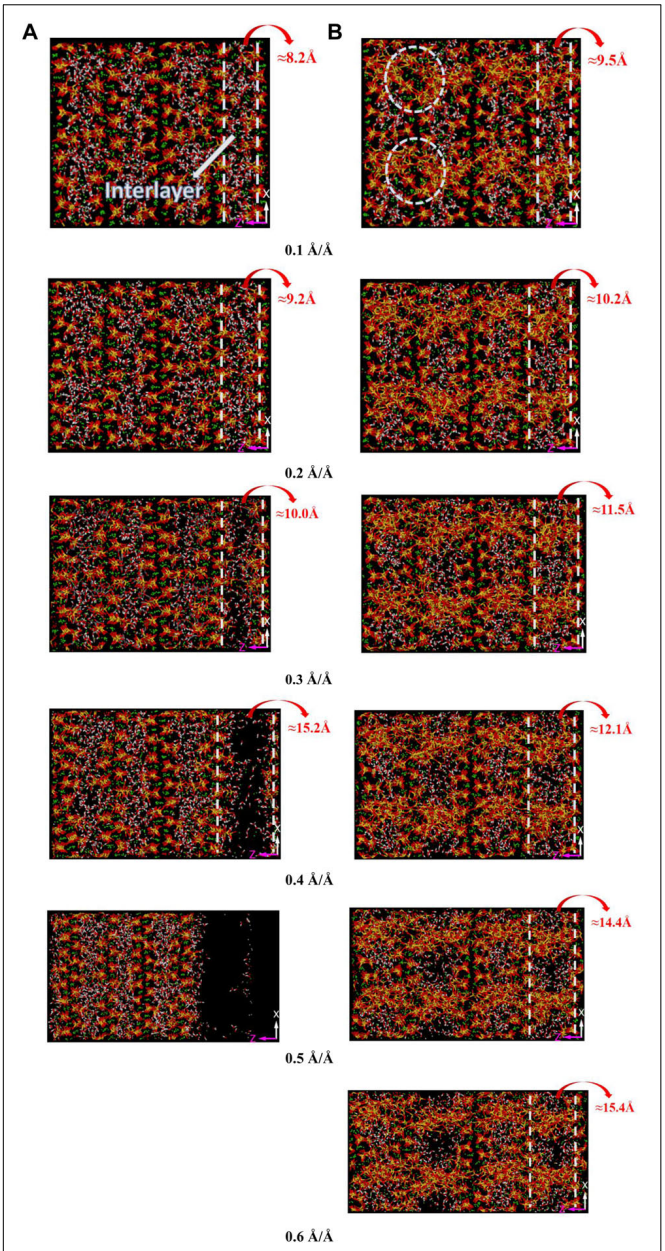

FIGURE 10 | The snapshots of **(A)** pure C-S-H and **(B)** C-S-H/20 wt.% 2D-silica during the tensile process along z direction at different strain levels.

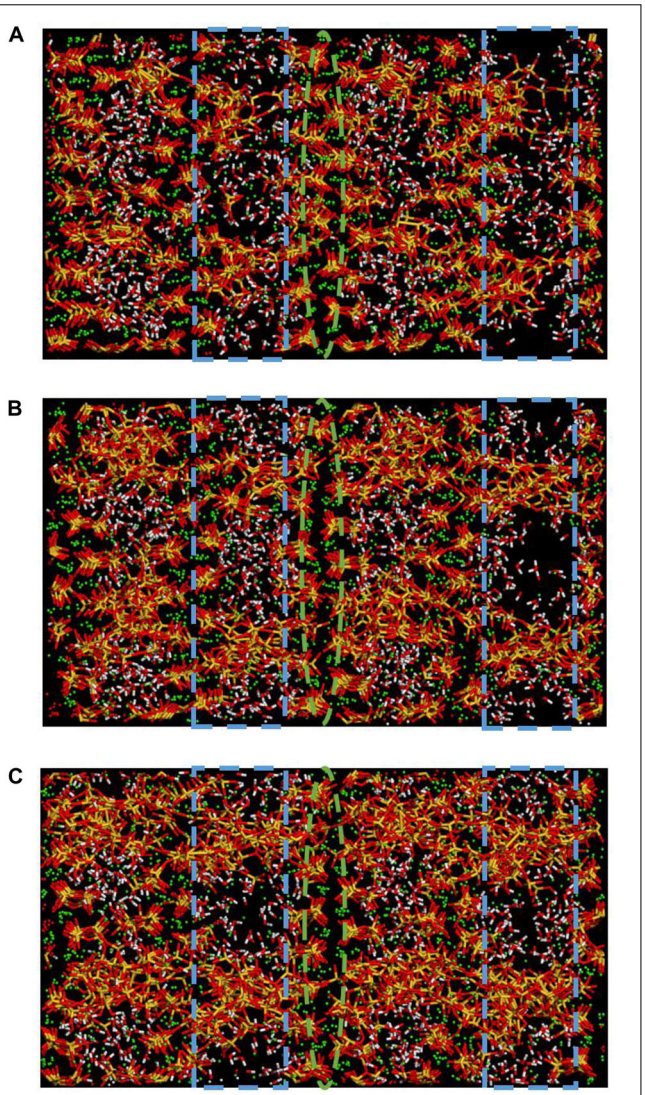

FIGURE 11 | Snapshots of **(A)** C-S-H/10 wt.% 2D-silica, **(B)** C-S-H/15 wt.% 2D-silica, **(C)** C-S-H/20 wt.% 2D-silica at the strain level of 0.5 Å/Å during the z direction tensile process.

Evolution of the number of generated Ca-OH and Si-OH of pure C-S-H and C-S-H/2D-silica during the tensile process along z direction are recorded and presented in **Figure 12**. And on the basis of the stress -strain curve in **Figure 5A**, the tensile process of pure C-S-H can be categorized into elastic stage, yield stage and ultimate fracture. In the elastic stage, the evolution of Ca-OH and Si-OH keeps a synchronous correlation, indicating the occurrence of reaction (1). With the development of the strain level, a distinct increase of the slope is observed, which is an indicator for the breakage of more Si-O. . .Ca bonds and can be considered as the beginning of the yield age (around 0.15 Å/Å). The number of generated Ca-OH and Si-OH keeps increasing until the ultimate fracture of C-S-H (0.4 Å/Å).

The number evolution of generated Ca-OH and Si-OH in C-S-H/2D-silica shows a similar tendency as the strain level is lower than 0.3 Å/Å. After that point, the number of hydroxyl groups keeps increasing and the rate of Si-OH surpasses that of Ca-OH, which is on account of the onset of reaction (2). From 0.3 to 0.8 Å/Å, both reaction (1) and (2) take place. The elongation and breakage of high-strength Si-O-Si bonds contribute to a higher stress level, which extends the yield stage compared with pure C-S-H. As shown in **Figure 5D**, the larger amount of 2D-silca is intercalated, the higher ultimate strain will be reached. For C-S-H with 20 wt.% 2D-silica intercalated, the stress still maintains as high as the yield stress until the end of the simulation. As presented in **Table 3**, the generated number of Ca-OH and Si-OH

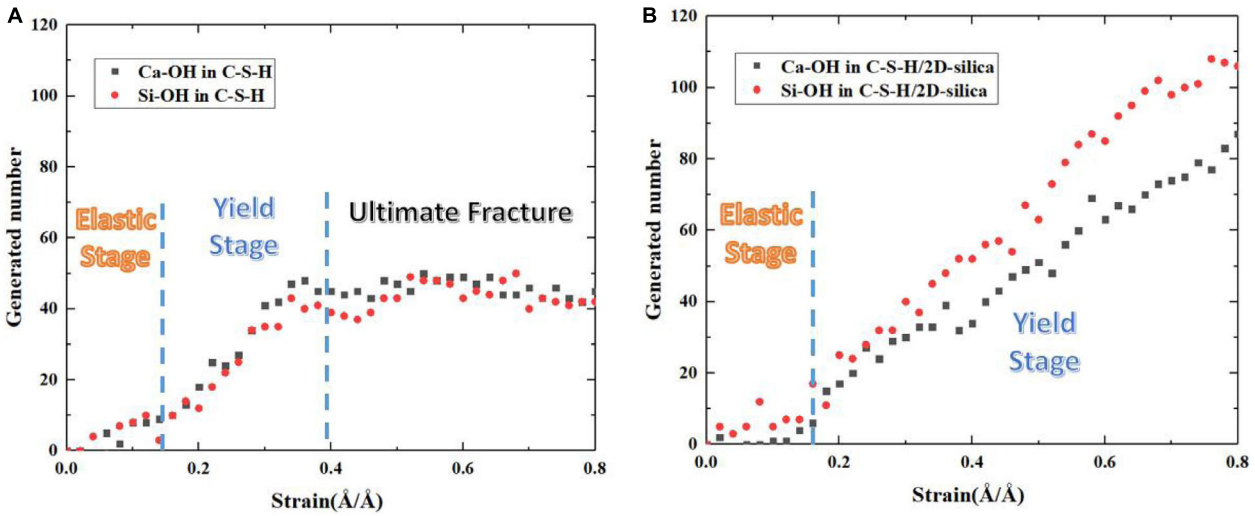

FIGURE 12 | The evolution of generated number of Ca–OH, Si–OH of **(A)** pure C-S-H and **(B)** C-S-H/2D-silica during tensile process along z direction.

TABLE 3 | Generated number of Ca-OH and Si-OH of pure C-S-H and C-S-H/2D-silica during the tensile process along z direction.

	Ca-OH				Si-OH			
	Starting number	Ending number	Generated number	Generated proportion (%)	Starting number	Ending number	Generated number	Generated proportion (%)
C-S-H	531	576	45	8.47	375	417	42	11.20
C-S-H/2D-silica	274	361	87	31.75	345	451	106	30.72

during the tensile process of pure C-S-H is, respectively, 45 and 42, which approximately agrees with the 1:1 correlation. While for C-S-H/2D-silica, the generated number is 87 and 106 for Ca-OH and Si-OH. From the perspective of energy dissipation, the occurrence of more chemical reactions takes in more energy, and thus increases the toughness of the matrix.

CONCLUSION

In this work, 2D-silica is selected as the nano-phase reinforcement and intercalated into the interlayer regions of a C-S-H matrix, modifying the structure and thus enhancing the mechanical performance. Molecular dynamic simulation is utilized to investigate the interactions between 2D-silica and C-S-H matrix and to unravel the interfacial mechanism.

The pure C-S-H has a layered structure with only Q_1 and Q_2 silicon atoms. As the 2D-silica reinforcement is incorporated into the C-S-H matrix, the dangling silicon atoms at the edge of 2D-silica strongly interact with the reactive non-bridging oxygen atoms at the defective sites, leading to formation of interfacial Si-O-Si bonds. Those covalent bonds transform Q_1 and Q_2 in the C-S-H into high connectivity Q_3 and Q_4 species, which increases the integrity of the matrix. The uniaxial tensile loading experiments are conducted on C-S-H and C-S-H/2D-silica models along x, y, and z direction, respectively. The results show that along z direction pure C-S-H performs the weakest mechanical performance due to large numbers of defects in the interlayer, while the intercalation of 2D-silica can dramatically improve the tensile strength and ductility along this direction. The enhancement efficiency of 2D-silica on the stiffness and toughness of C-S-H xy-plane is relatively lower, since the pure C-S-H model is originally strong in the intralayer region. The enhancement mechanisms are demonstrated as follows. During the tensile process of a pure C-S-H model along z direction, it is primarily the dissociation of Si-O. . .Ca ionic bonds in the interlayer region that contributes to the development of strain. This relatively weak interlayer cohesion causes a brittle fracture of the matrix. However, within a C-S-H/2D-silica model, the presence of interfacial Si-O-Si bonds also shares responsibility for the strain development. The elongation and breakage of those high-strength covalent bonds needs higher tensile stress and consumes higher energy, which leads to a longer plastic stage and higher toughness. The occurrence of Q_3 and Q_4 species in the nanocomposite leads to a high-connectivity net system, increasing the resistance of crack propagation.

This work may shed new lights on the interaction mechanisms between nano-reinforcements and an inorganic host. Geopolymers also include the silicate tetrahedra, hence, such a strengthening principle may also apply to geopolymers. The dangling atoms at the edge of 2D-silica can react with non-bridging oxygen atoms of geopolymers, forming Si-O-Si bonds at interfaces. Those covalent bonds transform Q_1 and Q_2 of geopolymers into high connectivity Q_3 and Q_4 species,

which increases the integrity of the matrix and its resistance to crack propagation.

Furthermore, this work provides solutions to modify the brittleness of concrete so as to achieve high performance construction materials. In this way, less cement is required for an equal bearing capacity, which promotes a low-carbon manufacturing and sustainable industry. However, the current study of 2D-silica reinforcement is still limited to a theoretical level, while further experimental research is needed to validate the simulation results.

DATA AVAILABILITY STATEMENT

The datasets generated for this study are available on request to the corresponding author.

AUTHOR CONTRIBUTIONS

YZ and JH contributed conception and design of the study. HZ, YQ, and XZ organized the database and wrote sections of the manuscript. YZ and HZ performed the statistical analysis. YZ, HZ, YQ, and XZ wrote the first draft of the manuscript. All authors contributed to manuscript revision, read and approved the submitted version.

ACKNOWLEDGMENTS

We acknowledge support from the National Natural Science Foundation of China (Grant Nos. 51908119, 6512009004A, and U1706222) and the Natural Science Foundation of Jiangsu Province (Grant No: BK20190367).

REFERENCES

Allen, A. J., Thomas, J. J., and Jennings, H. M. (2007). Composition and density of nanoscale calcium-silicate-hydrate in cement. *Nat. Mater.* 6, 311–316. doi: 10.1038/nmat1871

Bauchy, M., Qomi, M. J. A., Ulm, F. J., and Pellenq, R. J. M. (2014). Order and disorder in calcium-silicate-hydrate. *J. Chem. Phys.* 140:214503. doi: 10.1063/1.4878656

Bonnaud, P. A., Ji, Q., Coasne, B., Pellenq, R. J.-M., and Van Vliet, K. J. (2012). Thermodynamics of water confined in porous calcium-silicate-hydrates. *Langmuir* 28, 11422–11432. doi: 10.1021/la301738p

Büchner, C., and Heyde, M. (2017). Two-dimensional silica opens new perspectives. *Progr. Surf. Sci.* 92, 341–374. doi: 10.1016/j.progsurf.2017.09.001

Chenoweth, K., van Duin, A. C. T., and Goddard, W. A. III (2008). ReaxFF reactive force field for molecular dynamics simulations of hydrocarbon oxidation. *J. Phys. Chem. A* 112, 1040–1053. doi: 10.1021/jp709896w

Cong, X., and Kirkpatrick, J. R. (1996a). 29Si MAS NMR study of the structure of calcium silicate hydrate. *Adv. Cem. Based Mater.* 3, 144–156. doi: 10.3390/jfb10020025

Cong, X. D., and Kirkpatrick, R. J. (1996b). Si-29 and O-17 NMR investigation of the structure of some crystalline calcium silicate hydrates. *Adv. Cem. Based Mater.* 3, 133–143.

Constantinides, G., and Ulm, F.-J. (2007). The nanogranular nature of C-S-H. *J. Mech. Phys. Solids* 55, 64–90.

Du, H., Du, S., and Liu, X. (2014). Durability performances of concrete with nano-silica. *Constr. Build. Mater.* 73, 705–712. doi: 10.1016/j.conbuildmat.2014.10.014

Duque-Redondo, E., Manzano, H., Epelde-Elezcano, N., Martínez-Martínez, V., and López-Arbeloa, I. (2014). Molecular forces governing shear and tensile failure in clay-dye hybrid materials. *Chem. Mater.* 26, 4338–4345.

Gao, Z., Dong, X., Li, N., and Ren, J. (2017). Novel two-dimensional silicon dioxide with in-plane negative poisson's ratio. *Nano Lett.* 17, 772–777. doi: 10.1021/acs.nanolett.6b03921

Geng, G., Myers, R. J., Li, J., Maboudian, R., Carraro, C., Shapiro, D. A., et al. (2017). Aluminum-induced dreierketten chain cross-links increase the mechanical properties of nanocrystalline calcium aluminosilicate hydrate. *Sci. Rep.* 7:44032. doi: 10.1038/srep44032

Geng, G., Myers, R. J., Qomi, M. J. A., and Monteiro, P. J. M. (2018). Densification of the interlayer spacing governs the nanomechanical properties of calcium-silicate-hydrate. *Sci. Rep.* 7, 10986–10993. doi: 10.1038/s41598-017-11146-8

Hou, D., Li, T., and Wang, P. (2018a). Molecular Dynamics Study on the Structure and Dynamics of NaCl solution transport in the nanometer channel of CASH Gel. *ACS Sustain. Chem. Eng.* 6, 9498–9509.

Hou, D., Yu, J., Jin, Z., and Hanif, A. (2018b). Molecular dynamics study on calcium silicate hydrate subjected to tension loading and water attack: Structural evolution, dynamics degradation and reactivity mechanism. *Phys. Chem. Chem. Phys.* 20, 11130–11144. doi: 10.1039/c7cp08634b

Hou, D., Lu, Z., Li, X., Ma, H., and Li, Z. (2017). Reactive molecular dynamics and experimental study of graphene-cement composites: Structure, dynamics and reinforcement mechanisms. *Carbon N. Y.* 115, 188–208.

Hou, D., Ma, H., Zhu, Y., and Li, Z. (2014a). Calcium silicate hydrate from dry to saturated state: Structure, dynamics and mechanical properties. *Acta Mater.* 67, 81–94.

Hou, D., Zhu, Y., Lu, Y., and Li, Z. (2014b). Mechanical properties of calcium silicate hydrate (C-S-H) at nano-scale: A molecular dynamics study. *Mater. Chem. Phys.* 146, 503–511. doi: 10.3390/ma12172837

Hou, D., Zhang, J., Pan, W., Zhang, Y., and Zhang, Z. (2020). Nanoscale mechanism of ions immobilized by the geopolymer: A molecular dynamics study. *J. Nucl. Mater.* 528:151841. doi: 10.1016/j.jnucmat.2019.151841

Hou, D., Zhao, T., Ma, H., and Li, Z. (2015). Reactive molecular simulation on water confined in the Nanopores of the Calcium silicate hydrate gel: structure, reactivity, and mechanical properties. *J. Phys. Chem. C* 119, 1346–1358.

Huang, P. Y., Kurasch, S., Srivastava, A., Skakalova, V., Kotakoski, J., Krasheninnikov, A. V., et al. (2012). Direct imaging of a two-dimensional silica glass on graphene. *Nano Lett.* 12, 1081–1086. doi: 10.1021/nl204423x

Janik, J. A., Kurdowski, W., Podsiadly, R., and Samseth, J. (2001). Fractal structure of C-S-H and tobermorite phases. *ACTA Phys. Pol. A* 100, 529–537.

Jennings, H. M. (2008). Refinements to colloid model of C-S-H in cement: CM-II. *Cem. Concr. Res.* 38, 275–289. doi: 10.1016/j.cemconres.2007.10.006

Kim, Y., Hanif, A., Usman, M., Munir, M. J., Saleem, S. M., and Kim, S. (2018). Slag waste incorporation in high early strength concrete as cement replacement: Environmental impact and influence on hydration & durability attributes. *J. Clean. Prod.* 172, 3056–3065. doi: 10.1016/j.jclepro.2017.11.105

Konsta-Gdoutos, M. S., Metaxa, Z. S., and Shah, S. P. (2010). Highly dispersed carbon nanotube reinforced cement based materials. *Cem. Concr. Res.* 40, 1052–1059. doi: 10.1016/j.cemconres.2010.02.015

Liong, M., Lu, J., Kovochich, M., Xia, T., Ruehm, S. G., Nel, A. E., et al. (2008). Multifunctional inorganic nanoparticles for imaging, targeting, and drug delivery. *ACS Nano* 2, 889–896. doi: 10.1021/nn800072t

Madani, H., Bagheri, A., and Parhizkar, T. (2012). The pozzolanic reactivity of monodispersed nanosilica hydrosols and their influence on the hydration characteristics of Portland cement. *Cem. Concr. Res.* 42, 1563–1570.

Manzano, H., Masoero, E., Lopez-Arbeloa, I., and Jennings, H. M. (2013). Shear deformations in calcium silicate hydrates. *Soft Matter* 9:7333. doi: 10.1103/PhysRevLett.119.035502

Manzano, H., Moeini, S., Marinelli, F., van Duin, A. C. T., Ulm, F.-J., and Pellenq, R. J. M. (2012). Confined water dissociation in microporous defective silicates: Mechanism, dipole distribution, and impact on substrate properties. *J. Am. Chem. Soc.* 134, 2208–2215. doi: 10.1021/ja209152n

Mehta, P. K., and Monteiro, P. J. M. (2014). *Concrete Microstructure, Properties, and Materials*, 4th Edn. New York, NY: McGraw-Hill Companies, doi: 10.1036/0071462899

Monteiro, P. J. M., Miller, S. A., and Horvath, A. (2017). Towards sustainable concrete. *Nat. Mater.* 16, 688–689.

Orozco, C. A., Chun, B. W., Geng, G., Emwas, A. H., and Monteiro, P. J. M. (2017). Characterization of the bonds developed between calcium silicate hydrate and polycarboxylate-based superplasticizers with silyl functionalities. *Langmuir* 33, 3404–3412. doi: 10.1021/acs.langmuir.6b04368

Pellenq, R. J.-M., Kushima, A., Shahsavari, R., Van Vliet, K. J., Buehler, M. J., Yip, S., et al. (2009). A realistic molecular model of cement hydrates. *Proc. Natl. Acad. Sci. U. S. A.* 106, 16102–16107. doi: 10.1073/pnas.0902180106

Richardson, I. G. (2008). The calcium silicate hydrates. *Cem. Concr. Res.* 38, 137–158.

Sakhavand, N., Muthuramalingam, P., and Shahsavari, R. (2013). Toughness governs the rupture of the interfacial H-bond assemblies at a critical length scale in hybrid materials. *Langmuir* 29, 8154–8163. doi: 10.1021/la4014015

Sanchez, F., and Zhang, L. (2008). Molecular dynamics modeling of the interface between surface functionalized graphitic structures and calcium–silicate–hydrate: interaction energies, structure, and dynamics. *J. Colloid Interface Sci.* 323, 349–358. doi: 10.1016/j.jcis.2008.04.023

Schuetz, C. A., and Frenklach, M. (2003). Nucleation of soot: Molecular dynamics simulations of pyrene dimerization. *Proc. Combust. Inst.* 29, 2307–2314.

Shahsavari, R., Buehler, M. J., Pellenq, R. J. M., and Ulm, F. J. (2009). First-principles study of elastic constants and interlayer interactions of complex hydrated oxides: Case study of tobermorite and jennite. *J. Am. Ceram. Soc.* 92, 2323–2330.

Tang, F., Li, L., and Chen, D. (2012). Mesoporous silica nanoparticles: Synthesis, biocompatibility and drug delivery. *Adv. Mater.* 24, 1504–1534. doi: 10.1002/adma.201104763

Tang, L., and Cheng, J. (2013). Nonporous silica nanoparticles for nanomedicine application. *Nano Today* 8, 290–312. doi: 10.1016/j.nantod.2013.04.007

Ulm, F.-J., Vandamme, M., Bobko, C., and Ortega, J. A. (2007). Statistical indentation techniques for hydrated nanocomposites: Concrete, bone, and shale. *J. Am. Ceram. Soc.* 90, 2677–2692.

van Duin, A. C. T., Dasgupta, S., Lorant, F. A., and Goddard, A. W. (2001). ReaxFF: a reactive force field for hydrocarbonds. *J. Phys. Chem. A* 105, 9396–9409.

van Duin, A. C. T., Strachan, A., Stewman, S., Zhang, Q., Xu, X., and Goddard, W. A. (2003). ReaxFF(SiO) reactive force field for silicon and silicon oxide systems. *J. Phys. Chem. A* 107, 3803–3811.

Yu, R., Spiesz, P., and Brouwers, H. J. H. (2014). Effect of nano-silica on the hydration and microstructure development of Ultra-High Performance Concrete (UHPC) with a low binder amount. *Constr. Build. Mater.* 65, 140–150. doi: 10.1016/j.conbuildmat.2014.04.063

Zhou, Y., Hou, D., Geng, G., Feng, P., Yu, J., and Jiang, J. (2018a). Insights into the interfacial strengthening mechanisms of calcium-silicate-hydrate/polymer nanocomposites. *Phys. Chem. Chem. Phys.* 20, 8247–8266. doi: 10.1039/c8cp00328a

Zhou, Y., Hou, D., Jiang, J., Liu, L., She, W., Yu, J., et al. (2018b). Experimental and molecular dynamics studies on the transport and adsorption of chloride ions in the nano-pores of calcium silicate phase: The influence of calcium to silicate ratios. *Microporous Mesoporous Mater.* 255, 23–35.

Zhou, Y., Hou, D., Jiang, J., She, W., and Yu, J. (2017a). Reactive molecular simulation on the calcium silicate hydrates/polyethylene glycol composites. *Chem. Phys. Lett.* 687, 184–187.

Zhou, Y., Hou, D., Jiang, J., and Wang, P. (2016). Chloride ions transport and adsorption in the nano-pores of silicate calcium hydrate: Experimental and molecular dynamics studies. *Constr. Build. Mater.* 126, 991–1001.

Zhou, Y., Hou, D., Manzano, H., Orozco, C. A., Geng, G., Monteiro, P. J. M., et al. (2017b). Interfacial connection mechanisms in Calcium-Silicate-Hydrates/Polymer nanocomposites: a molecular dynamics study. *ACS Appl. Mater. Interfaces* 9, 41014–41025. doi: 10.1021/acsami.7b12795

Zhou, Y., Orozco, C. A., Duque-Redondo, E., Manzano, H., Geng, G., Feng, P., et al. (2019a). Modification of poly (ethylene glycol) on the microstructure and mechanical properties of calcium silicate hydrates. *Cem. Concr. Res.* 115, 20–30.

Zhou, Y., Tang, L., Liu, J., and Miao, C. (2019b). Interaction mechanisms between organic and inorganic phases in calcium silicate hydrates/poly(vinyl alcohol) composites. *Cem. Concr. Res.* 125:105891.

Zhu, T., Li, J., Lin, X., and Yip, S. (2005). Stress-dependent molecular pathways of silica-water reaction. *J. Mech. Phys. Solids* 53, 1597–1623.

Conflict of Interest: The authors declare that the research was conducted in the absence of any commercial or financial relationships that could be construed as a potential conflict of interest.

Copyright © 2020 Zhou, Zheng, Qiu, Zou and Huang. This is an open-access article distributed under the terms of the Creative Commons Attribution License (CC BY). The use, distribution or reproduction in other forums is permitted, provided the original author(s) and the copyright owner(s) are credited and that the original publication in this journal is cited, in accordance with accepted academic practice. No use, distribution or reproduction is permitted which does not comply with these terms.

frontiers in Materials

ORIGINAL RESEARCH
published: 23 June 2020
doi: 10.3389/fmats.2020.00069

Structure, Reactivity, and Mechanical Properties of Sustainable Geopolymer Material: A Reactive Molecular Dynamics Study

*Zhipeng Li[1,2], Jinglin Zhang[3] and Muhan Wang[4]**

[1] School of Transportation and Logistics Engineering, Shandong Jiaotong University, Jinan, China, [2] School of Civil Engineering, Shandong Jiaotong University, Jinan, China, [3] Collaborative Innovation Center of Engineering Construction and Safety in Shandong Blue Economic Zone, Qingdao, China, [4] School of Materials Science and Engineering, China University of Petroleum, Qingdao, China

Sodium aluminosilicate hydrate (NASH) gel, the primary binding phase in geopolymer, determines the mechanical properties and durability of environment-friendly construction materials. In this work, the models of NASH gel were obtained through a two-step procedure: the temperature quenching method and Grand Canonical Monte Carlo water adsorption. The reactive force field (ReaxFF) molecular dynamics were utilized to investigate the structure, reactivity, and mechanical performance of the NASH gel with Na/Al ratio ranging from 1 to 3. Q species, the connectivity factor, shows that the increase of sodium content in NASH gel leads to depolymerization of the aluminosilicate network and more non-bridging oxygen (NBO) atoms. The adsorbed water molecules dissociate near the NBO with high reactivity in defective aluminosilicate structure. The newly produced hydroxyls associate with the aluminate species, contributing to the formation of the pentahedron local structure. The sodium ions distributed in the cavity of the aluminosilicate skeleton have around 4 7 nearest neighbors. Furthermore, with an increase in sodium, the molecular structure of the aluminosilicate skeleton is transformed from an integrity network to partially destroyed branch structures, which gradually decrease the stiffness and cohesive force of NASH gel, characterized by the uniaxial tensile testing. During the large tensile deformation process, the ReaxFF MD correlates the mechanical response with the chemical reaction pathway. The aluminosilicate skeleton is stretched broken to resist the tensile loading and the hydrolytic reaction of water molecules near the stretched Si-O and Al-O bond further accelerates the degradation of NASH gel. Hopefully, this work can shed light on the material design for a high performance of sustainable geopolymer at the nanoscale.

Keywords: molecular dynamics, geopolymer, sodium aluminosilicate hydrate, mechanical properties, structure

OPEN ACCESS

Edited by:
Jinrui Zhang,
Tianjin University, China

Reviewed by:
Pavithra Parthasarathy,
University of Macau, China
Zhiyong Liu,
Southeast University, China

***Correspondence:**
Muhan Wang
hldwmh@gmail.com

Specialty section:
This article was submitted to Structural Materials, a section of the journal Frontiers in Materials

Received: *18 January 2020*
Accepted: *05 March 2020*
Published: *23 June 2020*

Citation:
Li Z, Zhang J and Wang M (2020) Structure, Reactivity, and Mechanical Properties of Sustainable Geopolymer Material: A Reactive Molecular Dynamics Study. Front. Mater. 7:69. doi: 10.3389/fmats.2020.00069

INTRODUCTION

Ordinary Portland cement (OPC) is ubiquitously utilized as the essential construction and building material worldwide (Li, 2011). Cement demand is estimated to increase from around 3.5 Gt in 2015 to nearly 4.4 Gt per year by 2050 (Luukkonen et al., 2018). The manufacturing of OPC is accompanied with CO_2 emissions such as the calcination of limestones at 1,450°C and the

energy consumed by the cement plant itself, which is supplied by coal combustion (Damtoft et al., 2008). In 2016, the production of OPC contributed to around 1.45 Gt CO_2, occupying approximately 8% of the global CO_2 release (Andrew, 2018). Even though great efforts have made to improve energy efficiency, the clean production of cement remains a difficult issue to solve, especially considering the increasing cement demand and the inevitable CO_2 emission reactions from cement production. Consequently, to reduce the carbon footprint, it is necessary to develop environment-friendly construction material to serve as an alternative and supplementary binder for OPC. Geopolymer, one type of alkali activated aluminosilicate cement, is used primarily as an environmentally beneficial alternative to OPC (Davidovits, 1991; Duxson et al., 2007a). Geopolymers use industrial byproducts as precursors, and therefore result in dramatically less CO_2 emissions per ton of concrete produced (Duxson et al., 2007a). The industrial byproducts utilized in geopolymer synthesis include fly ash and slag, which when combined with alkaline activators react to form a hardened binder possessing performance characteristics comparable to traditional Portland cement (Davidovits, 1982; Palomo et al., 1999; Van Jaarsveld et al., 2002; Bakharev, 2005). It is synthesized by dissolution of Al and Si in alkali medium, transportation, and polycondensation, forming a three-dimensional network structure. Due to their inorganic three-dimensional network structure, geopolymers show high efficiency of fireproofing, excellent thermal stability, and superior mechanical properties as compared with traditional OPC (Palomo and Glasser, 1992; Xu and Van Deventer, 2000; Barbosa and MacKenzie, 2003; Kriven et al., 2003). Geopolymers have therefore received great growing in recent years in the field of cleaner production of construction materials.

Sodium aluminosilicate hydrate (NASH) gel is a primary binding phase in geopolymers. According to most of the papers published so far (White et al., 2012; Parthasarathy et al., 2017), the mechanical properties, mass transport, ion exchange, and other physicochemical properties of NASH gels are controlled by the chemical composition and nanostructure, which have drawn attention from researchers in related fields. In order to determine the coordination state of aluminum and oxygen, and to explain the abnormal changes of physical properties from the perspective of structure, many experiments and simulations have been carried out (McKeown et al., 1984; Leonelli et al., 2001; Okuno et al., 2005; Sadat et al., 2016). Earlier spectroscopic studies on geopolymer paste show that the structure of NASH gel primarily consists of an alkali aluminosilicate hydrate gel framework (the alkali used commonly is Na) formed by disordered interlinked aluminosilicate tetrahedrons. Al and Si are both present in tetrahedral coordination connected by bridging oxygen (BO), and the negative charge associated with Al substitution for Si is balanced by the alkali cations (Barbosa et al., 2000; Duxson et al., 2005, 2007a,b; Singh et al., 2005). Compared with the bonding between Na and NBO, the interaction between charge compensating alkali cations (Na^+) and $[AlO_4]^-$ units are more ionic and weaker (Uchino et al., 1993). The Na/Al ratio in compositions indicates the change in internal structure. In the geopolymers with low sodium content, Na^+ is bound superficially to the $[AlO_4]^-$. When the Na/Al ratio is larger than 1, Na^+ may break the Si–O–Si linkage, associating it with part of the silicon in the form of SiO-(Na^+)-Si^- (Uchino et al., 1993). Using molecular dynamics, Xiang et al. (2013) studied the changes in the structure and mechanical properties of sodium aluminosilicate glass as a function of Al/Na ratios, and the results were in good agreement with experimental data. Zhang M. et al. (2018) studied the local structure and dynamics of sodium in NASH gel, demonstrated the loose connection between sodium and aluminate tetrahedron, and modeled the dissociation process of sodium, which is so-called leaching. Meanwhile, the ion immobilizing ability of NASH gel was studied by molecular dynamics, providing a fundamental understanding of the immobilization mechanism of geopolymer materials (Hou et al., 2019b). An empirical force field molecular dynamics method was also employed to investigate the structure, dynamics, energetics, and mechanical properties of calcium silicate hydrate (C-S-H) (Hou et al., 2019a, 2015b; Wang et al., 2019). Furthermore, reactive molecular dynamics were used to simulate the polymerization process and the molecular structure of geopolymer gels, and evaluated the influence of the simulation temperature and Si/Al ratio on the geopolymer (Zhang M. et al., 2018).

Typically, the properties of the materials subjected to loading will be greatly reduced largely due to the degradation of the chemical and physical structure. The aluminosilicate skeleton significantly influences the adsorption capability, reactivity, and hydrogen bond of the structural water molecules. The way of binding water in NASH gel is of particular importance, as it is closely related to strength and stiffness. In some cases, the internal damage of NASH gel is caused by the hydrolysis reaction of the silicate network, attacked by dissociated water molecules (Hou et al., 2014a, 2016a). Sadat et al. (2016) reported that exposure to water promotes the diffusion and dissociation of structural sodium, leading to destabilization of aluminate tetrahedrons and underling mechanical failure of the local structure. However, minute quantities of water could stabilize the sodium in NASH gel, which was attributed to the hydrolysis associated with aluminate tetrahedron and the formation of Na-OH (Zhang Y. et al., 2018). The attack of water molecules on chemical bonds promoted bond breaking in the loading test (Hou et al., 2014a; Zhang Y. et al., 2018). In addition, some studies have focused on the effects of chemical compositions (Hou et al., 2015a, 2016b, 2015c). To the best of our knowledge, the mechanical properties and weakening mechanisms have not been fully understood and the case of coupling with hydrolysis and depolymerization, in particular, has not been studied yet.

In this study, NASH gel with different compositions of the Na/Al ratio were characterized by molecular dynamics using a reactive force field (ReaxFF), which can perform a physical and chemical process in hydration, aiming to understand the structural role of sodium as a function of the chemical composition. The structural, mechanical, and chemical properties of NASH gel with different Na/Al ratios have been investigated. The influences of an existent form of water within NASH gel were also analyzed to obtain a better understanding of their behavior. The obtained results highlight that NASH gel

is weakened by the breakage of aluminosilicate chains and the penetration of water molecules, and show the mechanism of influence on its properties.

MATERIALS AND METHODS

Reactive Force Field

The ReaxFF, developed by van Duin et al. (2001), was used to simulate the chemical reaction between sodium aluminosilicate glass and water molecules for both atomic structure construction and uniaxial tensile testing. The ReaxFF provides an advanced description of the interaction between water and NASH surface. In addition, the ReaxFF has been widely used in silica glass (Hou et al., 2014a), C-S-H gel (Hou et al., 2015c), ordered crystal, and disordered glass (Hou et al., 2016b), discussing their structure evolution and tensile behavior under water penetration. The short-range interactions for the ReaxFF are determined by bond length-bond order scheme so that the bonds can be broken and formed with the potential energy transforming into a smooth state (Brenner et al., 2002). On the contrary, the long-range Coulombic interactions are determined by a seventh-order taper function, with an outer cutoff radius of 10 Å. The parameters of the force field for Na, Si, Al, O, and H can be obtained directly from previously published reference data (Cygan et al., 2004).

NASH Models With Different Na/Al Ratios

The LAMMPS package was used to construct three NASH gel models with Na/Al ratios of 1, 2, and 3 *via* two steps, respectively. First, a temperature quenching process was performed to build the NAS glass model. The water molecules were then inserted into the NAS glass model to obtain the NASH gel model. In order to obtain initial configuration with different Na/Al ratios, four types of atoms (Na, Si, Al, and O) were added in a cubic box with a side length of 20 Å to generate random coordinates. The density was adjusted to a typical value (see **Table 1**; Sadat et al., 2016). A time step of 0.1 fs was used for the simulation. The system was operated by a heating/cooling cycle process from 300 to 4,000 K under NPT ensemble at a rate of 10 K/ps, then the system was cooled from 4,000 to 300 K at the same rate. Finally, the system was further equilibrated at NVT ensemble with the temperature maintained at 300 K for 300 ps. The simulated equilibrium structure of the aluminosilicate chain with different Na/Al ratios are shown in **Figure 1**.

The Grand Canonical Monte Carlo (GCMC) method was utilized to adsorb water molecules into the NAS structure to obtain a NASH gel model (Bonnaud et al., 2012). The simulation process is analogous to the water adsorption in a microscopic porous structure such as C-S-H and silica glass (Hou et al., 2014a, 2015c). A two million step simulation was performed for the system equilibrium, followed by one million steps for data analysis. Water molecules can be inserted, deleted, displaced, and rotated in the constant volume system. After GCMC simulation, the NASH gel model saturated with water molecules will be obtained. The aluminosilicate skeletons with a Na/Al ratio of 1, 2, and 3 are shown in **Figure 1**. The composition of the NASH gel models is shown in **Table 1**.

Uniaxial Tension Test

A uniaxial tension test was utilized to detect the mechanical behavior of amorphous NASH gel. In order to reduce error and to ensure stability of the simulation system during stretching, the initial NASH models (20 × 20 × 20 Å) were expanded periodically (40 × 40 × 40 Å) and then used in a uniaxial tension test in the X direction. Moreover, there are 5,000 to 6,000 atoms in every supercell with a specific Na/Al ratio. It should be noted that a large number of atoms in simulation models can provide stable statistical results, especially for the reliable failure modes. To explore the failure mechanism of the NASH gel, the stress–strain relation and the change of molecular structure during loading were investigated.

To obtain the stress–strain relations, the supercell structures were subjected to uniaxial tensile loadings through gradual elongation at a strain rate of 0.08/ps. In the uniaxial tensile simulation process, NPT ensembles were defined for the system. When stretched along the X direction, the supercells were relaxed, coupled with zero external pressure in the x, y, and z dimensions at 300 K for 400 ps. Until the pressures reached equilibrium in three directions, the NASH gel would be elongated in the X direction. Furthermore, the pressure was zero in the Y and Z directions, respectively. Pressure evolution in the X direction was taken as the internal stress σ_{xx}. By setting the pressure to 0, which is perpendicular to the stretch direction, the normal direction can be relaxed toward the anisotropy without any restriction. The Poisson's ratio was considered in the setting, eliminating the artificial constraints of deformation.

RESULTS AND DISCUSSION

Structure Properties

After water adsorption, the molecular structures of the NASH gel were obtained. Water molecules penetrated into the cavity region of NAS glass and randomly distributed in the NASH gel. As shown in **Figure 2**, for gel with a Na/Al ratio of 1, two forms of the water molecules influencing the NAS glass can be found: chemical decomposition and physical adsorption. The water molecules adsorb and form physical bonds with NASH at first. Very small percentages of water molecules are decomposed to hydrogen and hydroxyl. The hydrogen forms a chemical bond with the oxygen of silicon–oxygen tetrahedron, and the hydroxyl forms a chemical bond with the aluminum. For chemical decomposition (see region I), a small number of water molecules (less than 7.2%) break the aluminosilicate skeleton by occupying the BO site, and construct aluminum hydroxyl or silicate hydroxyl. In the case of physical adsorption water (see region II), the hydroxyl in water molecules point to the aluminosilicate skeleton to form a hydrogen bond with its oxygen atoms, and these water molecules, called physical adsorption water, makes up more than 92.8% of the total. From the molecular structure of the static state, physical adsorption is the main existing form for water molecules in NASH gel, and the proportion of decomposition is very low. This conclusion agrees with previously published works (Hou et al., 2014a; Zhang Y. et al., 2018).

TABLE 1 | Compositions and densities of simulated NASH gel.

Na/Al ratio	Na_2O (wt. %)	Al_2O_3 (wt. %)	SiO_2 (wt. %)	H_2O (wt. %)	Total atoms in simulation cell	NAS density (g/cm^3)	NASH density (g/cm^3)
1	11.00	18.10	64.37	6.53	682	2.41	2.57
2	20.65	16.78	59.24	3.39	688	2.56	2.65
3	28.19	15.46	54.57	1.77	710	2.70	2.74

The three-dimensional network structure of the NASH gel with a Na/Al ratio of 1 is shown in **Figure 2**, which is the most representative feature. In the structure, silicon and aluminum atoms are interconnected by BO, and nearby sodium ions play a role in charge balance (Barbosa et al., 2000; Schmücker and MacKenzie, 2005). The coordination number (CN) of NASH gel, obtained using dynamic simulations, shows the local structure. In thermodynamic equilibrium state, as shown in **Table 2**, the CN of all the silicon in the gel with different Na/Al ratios is fourfold coordination, indicating that silicon in NASH gel exists in the form of tetrahedron. The aluminum coordination in the network structure is also predominantly tetrahedral (∼95.57, 94.14, and 96.51%), and some aluminum (∼2.16, 5.84, and 3.49%) with fivefold coordination, which is related to formation of Al-O_wH_w. Sodium diffuses in the cavity of the Si-Al framework, and exists in the form of $Na(H_2O)_n^+$ rather than Na^+, implying a loose interaction between sodium and the neighboring Si-O-Al bond. Sodium is located at a vacant region among the skeleton, showing multiple coordination forms. The results of MD simulation match well with previous experimental results (Barbosa et al., 2000; Duxson et al., 2005; De Silva et al., 2007; Walkley et al., 2018).

In NASH gel, Si and Al are predominantly tetrahedral, which can also be revealed by the angle distribution of the O-Si-O, Si-O-Si, and O-Al-O angle. As shown in **Figures 3A,B**, the angle distributions of Si-O-Si and O-Si-O are almost fully overlapped for different Na/Al ratio gels, indicating that the tetrahedral SiO_4 structure and the silicate skeleton is not sensitive to the Na/Al ratio. The O-Si-O angles are mainly distributed between 90° and 130°. The obvious peak located at around 110°, matches well with the experimental result of 109.7° measured by neutron diffraction (Mozzi and Warren, 1969). The simulated Si-O-Si angle distribution of the NASH gel ranges from 110° to 180°, and the average value is located at 144.0°, 143.4°, and 142.7°,

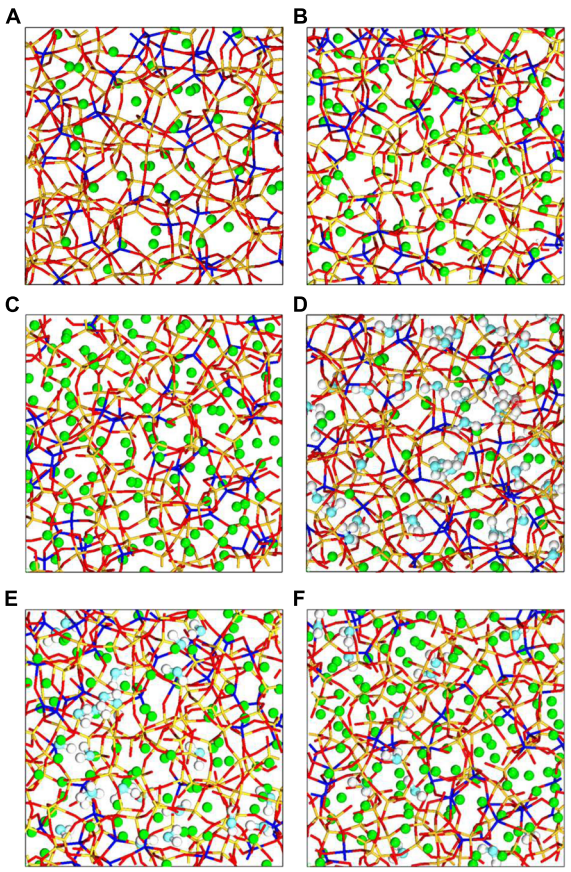

FIGURE 1 | Snapshot of the simulated NAS glass with Na/Al ratio **(A)** 1.0, **(B)** 2.0, **(C)** 3.0. The red (O atom) and yellow (Si atom) line represents the Si-O bond, the red and blue (Al atom) line represents the Al-O bond, and the green ball is sodium. Such markings are adopted in all of the following figures and the molecular structure of the NASH gel model with Na/Al ratio **(D)** 1.0, **(E)** 2.0, **(F)** 3.0. The light blue ball represents the O atom in water molecular or hydroxyl, the white ball represents the H atom. The balls have the same meaning in all following figures.

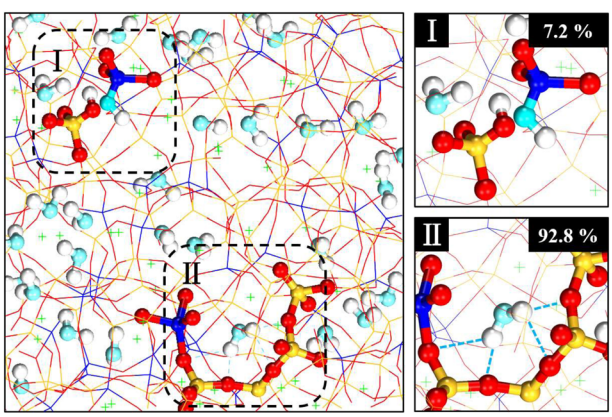

FIGURE 2 | Snapshot for the NASH gel with water penetration. The left-hand figure is the configuration of the NASH gel with a Na/Al ratio of 1. Region I and region II represent chemically dissociated water and physical adsorption water, respectively. Region I and region II are highlighted in the right-hand figures. The red ball is the BO atom in the aluminosilicate skeleton. The blue ball is the aluminum atom. The yellow ball is the silicon atom.

TABLE 2 | Coordination number (CN) of NASH gel model with different Na/Al ratios.

Na/Al ratio	CN (*n*)	4 (%)	5 (%)	6 (%)	7 (%)
1	Si-O_n	100	–	–	–
	Al-O_n	95.57	2.16	–	–
	Na-O_n	24.99	30.54	25.74	7.50
2	Si-O_n	100	–	–	–
	Al-O_n	94.14	5.84	–	–
	Na-O_n	10.76	29.85	41.02	14.33
3	Si-O_n	100	–	–	–
	Al-O_n	96.51	3.49	–	–
	Na-O_n	4.87	29.31	37.74	22.97

respectively. The simulation results are in agreement with the experimental results given by nuclear magnetic resonance, and X-ray diffractions are between 142° and 151° (Mauri et al., 2000). More significantly, the Si-O-Si angle peak value decreased slightly with the increase of the Na/Al ratio due to the change of sodium ions. However, **Figure 3C** shows that the angle distributions of O-Al-O are far broader than that of O-Si-O, and there are more obvious peaks located at different angles. It can be attributed to two possible factors: aluminum exists in multiple coordination configurations in the NASH gel, and the Al-O bond is relatively unstable in the aluminosilicate skeleton compared with the Si-O bond.

Mechanical Properties

Stress–Strain Relation for NASH Gel

Given the constitutive stress–strain relation, the stress–strain curve can reflect the mechanical properties of NASH gel in the process of uniaxial tension testing. Due to the isotropic structure of NASH, in the directions X, Y, and Z, they have the same stress–strain curves. **Figure 4** shows the constitutive relation between stress and strain with a strain rate of 0.08/ps along the X direction. Although the stress–strain curves have similar evolutionary

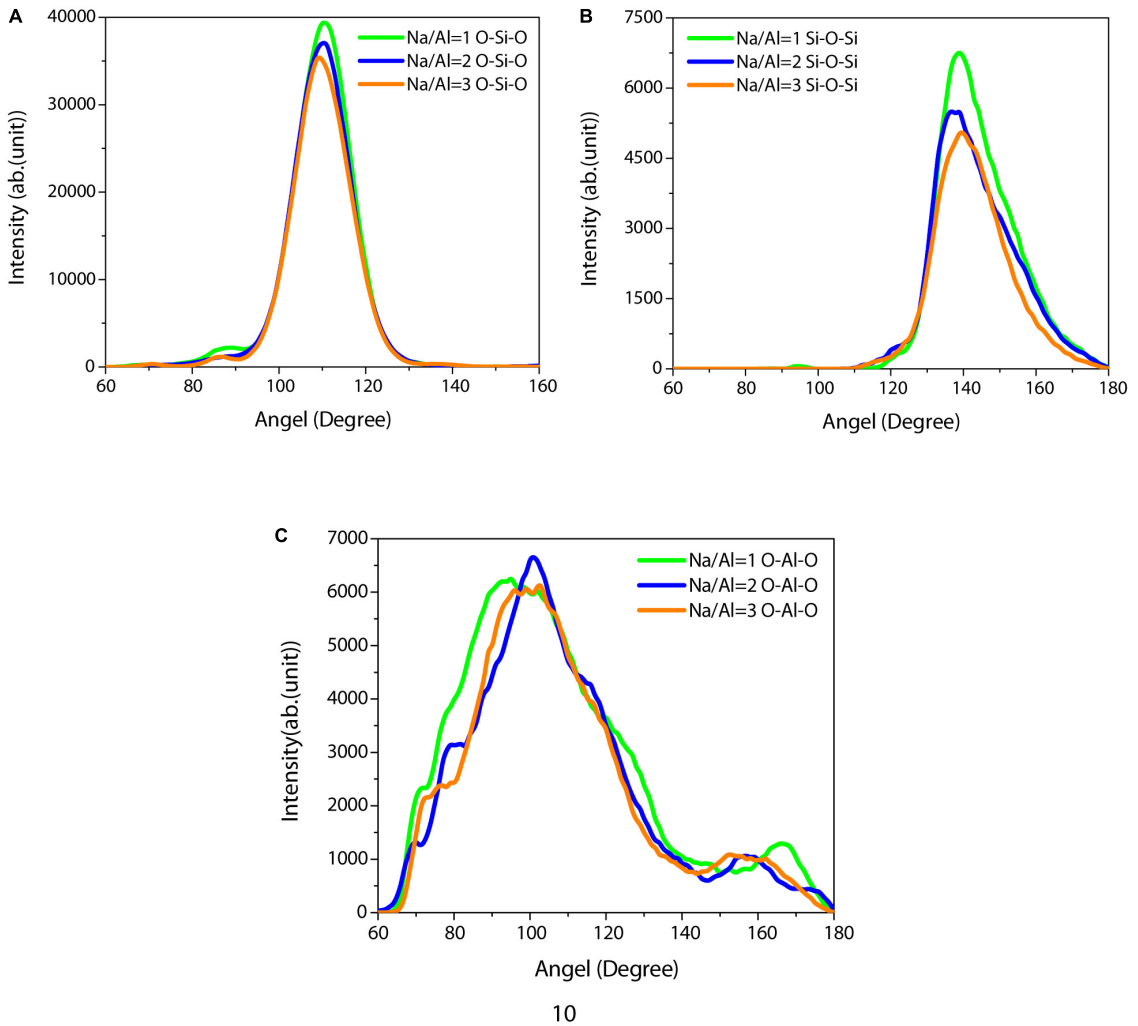

FIGURE 3 | (A) O-Si-O, **(B)** Si-O-Si, and **(C)** O-Al-O angle distribution of the NASH gel with a Na/Al ratio of 1, 2, and 3.

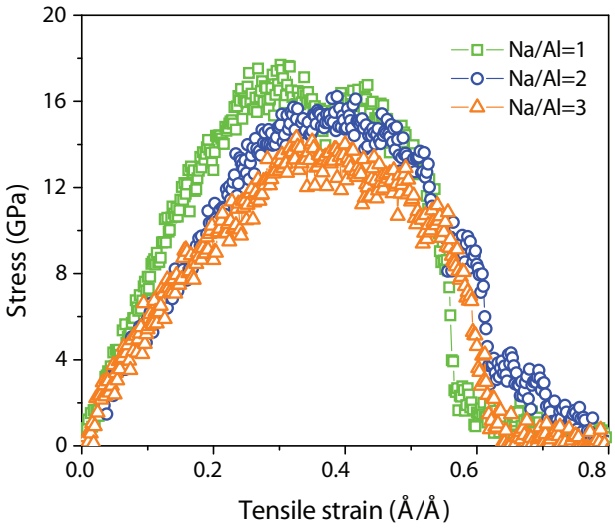

FIGURE 4 | Stress–strain relation for NASH gel with a ratio of 1, 2, and 3, stretched along the X direction with a strain rate of 0.08/ps.

trends, the intrinsic strength and failure strain of the specimen with a different Na/Al ratio is obviously different from others. The tensile strain, when the stress reaches the maximum value, is gradually decreased from 0.45 Å/Å to 0.3 Å/Å. The NASH gel with a lower Na/Al ratio is more easily stretched broken, and the yield strength of the NASH gel with a Na/Al ratio of 1, 2, and 3 is 17.7, 16.2, and 14.3 GPa, respectively. From the perspective of composition, the stress maximum value decreased as the Na/Al ratio increased. The number of sodium ions beyond that required, compensated for the negatively charged $[AlO4]^-$ units. Excess sodium ions with a positive charge can then attack the Si-O-Si and Si-O-Al bond (Irwin et al., 1988; Barbosa et al., 2000; Schmücker and MacKenzie, 2005), leading to aluminosilicate skeleton instability. It means that the increase of sodium content reduces the mechanical strength of the system. This result is consistent with the experimental result that the compressive strengths are decreased with increasing the Na/Al ratios when the Na/Al ratio is greater than 1 (Rowles and O'connor, 2003).

The stress–strain relations for different Na/Al ratios show the detailed mechanical performance during the process of tensile loading. The whole process can be divided into several stages. Taking the NASH gel with a Na/Al ratio of 1 as an example, the stress initially increases linearly in the elastic stage and subsequently slowly increases to a maximum value at a strain around 0.30 Å/Å. After the stress varies very slowly with strain from 0.3 to 0.45 Å/Å, there is a region with a dramatic drop in stress as the strain increases. Finally, the NASH gel was completely fractured at a strain of 0.8 Å/Å, corresponding to zero stress. It is obvious that the NASH gel is more prone to yield deformation as the Na/Al ratio increases. As the Na/Al ratio increase from 1 to 3 in the NASH gel, the tensile strength of the gel greatly decreases from 17.69 to 14.30 GPa accompanied by Young's modulus deduction from 71.84 to 47.46 GPa (see **Table 3**), and results in an obvious decrease of ultimate tensile strength of the NASH gel. For the specimens with different Na/Al ratios, the difference in the mechanical properties can be explained by different molecular structures and reactivity mechanisms.

TABLE 3 | Young's modulus of NASH gel models with different Na/Al ratios.

Na/Al	1	2	3
Young's modulus (GPa)	71.84	50.16	47.46
Tensile strength (GPa)	17.69	16.22	14.30

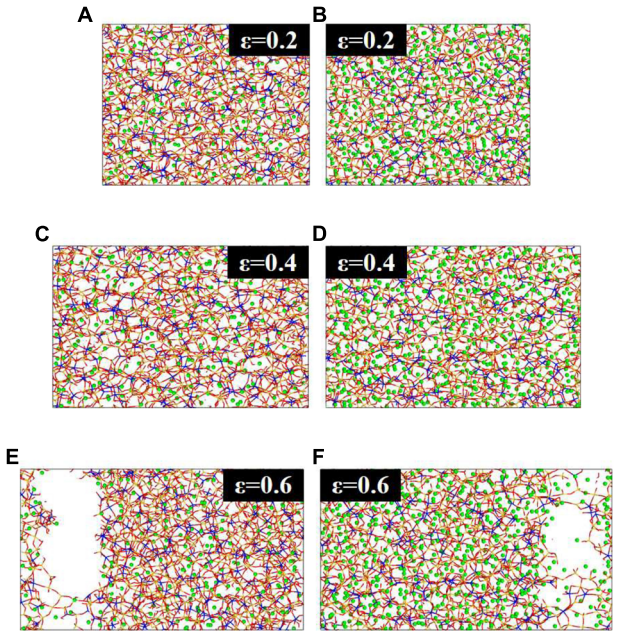

FIGURE 5 | Evolution of the structure during the tensile process with a Na/Al ratio of 1 and 3. From top to bottom, the strain state is 0.2 **(A,B)**, 0.4 **(C,D)**, and 0.6 **(E,F)** Å/Å, respectively.

Molecular Local Structure Evolution

The evolution of the structure during the tensile process from a strain of 0.2 Å/Å to 0.6 Å/Å is shown in **Figure 5**, a preliminary qualitative illustration of the damage process in the NASH gel. The aluminosilicate skeleton is stretched broken to resist the tensile loading. In the elastic region, Si-O and Al-O bonds in the aluminosilicate skeleton, subjected to tensile loading, are elongated. The Si-O-Si and Si-O-Al angles are stretched to bear the strain in the NASH gel system. In the subsequent yield region, the Si-O and Al-O bonds break down gradually, causing morphology transformation. As shown in **Figure 5**, the shape of the aluminosilicate skeleton changes at the strain of 0.4 Å/Å due to the bond breakage and reconnection. Small cracks have been created during the tensile process, but the local structure rearrangement slows down its propagation (Hou et al., 2014b, 2015c). In the failure stage of strain states 0.4 Å/Å to 0.6 Å/Å, the cracks created before continuing to grow and coalesce fast as strain increases in the area with the defective aluminosilicate skeleton, leading to the stress dropping rapidly (see **Figures 4**, **5**).

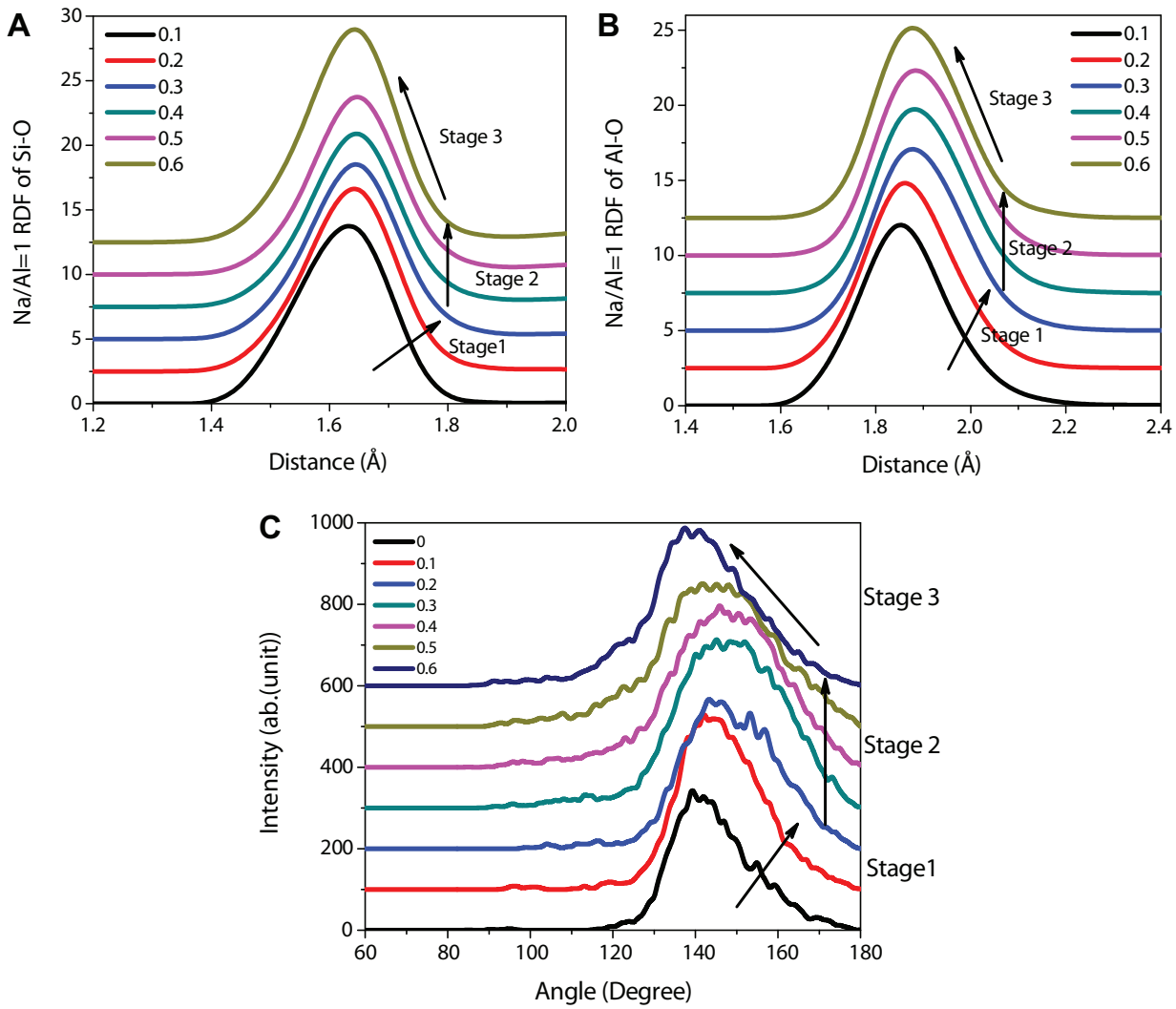

FIGURE 6 | Evolution of RDF for **(A)** Si-O, **(B)** Al-O stretched by loading with a rate of 0.08/ps, and **(C)** Si-O-Si angle distribution as a function of strain for the NASH gel with a Na/Al ratio of 1. Stage 1, 2, and 3 represent the elastic region, yield region, and failure region, respectively.

It should be noted that the increase of sodium ions at the end of the crack tips prevents the Si-O-Si and Si-O-Al bonds' reconnection, and further decreases the tensile properties of the gel structure. According to **Table 2**, the higher the Na/Al ratio, the more Na-O bonds and the less Al-O bonds form. The Na and Al are competitive, therefore, we can conclude that the aluminosilicate skeleton is unstable after an increase in the ratio of Na/Al.

TABLE 4 | Q species, bridging oxygen (BO), and non-bridging oxygen (NBO) of the NASH gel model with different Na/Al ratios.

Na/Al ratio	Q_4 (%)	Q_3 (%)	Q_2 (%)	BO (%)	NBO (%)
1	81.22	5.09	–	97.13	2.87
2	60.64	21.65	5.36	83.25	16.75
3	51.25	26.88	10.63	76.92	23.08

For the purpose of investigating the morphology evolution quantitatively, the RDF, angle distribution, and Q species changes have been calculated to depict the structural variation of the aluminosilicate skeleton during the tensile process. The RDFs of Si-O and Al-O as a function of strain for the NASH gel with a Na/Al ratio of 1 are shown in **Figures 6A,B**. Based on **Figures 6A,B**, the spectrums show similar peak emerging positions, indicating that the Si-O or Al-O were changed slightly during stretching. For the RDFs of Si-O, the peak positions of different strains are slightly different. In stage 1 (the elastic region), the Si-O peaks shift toward a lager distance with an increasing strain, which means the elastic elongation of the Si-O bonds. In stage 2 (the yield region), the peak positions of Si-O at different strains remain almost the same, implying that the continuous break and reconnection of a large number of Si-O bonds causes rearrangement of aluminosilicate chains. This is consistent with the conclusion obtained above from the evolution

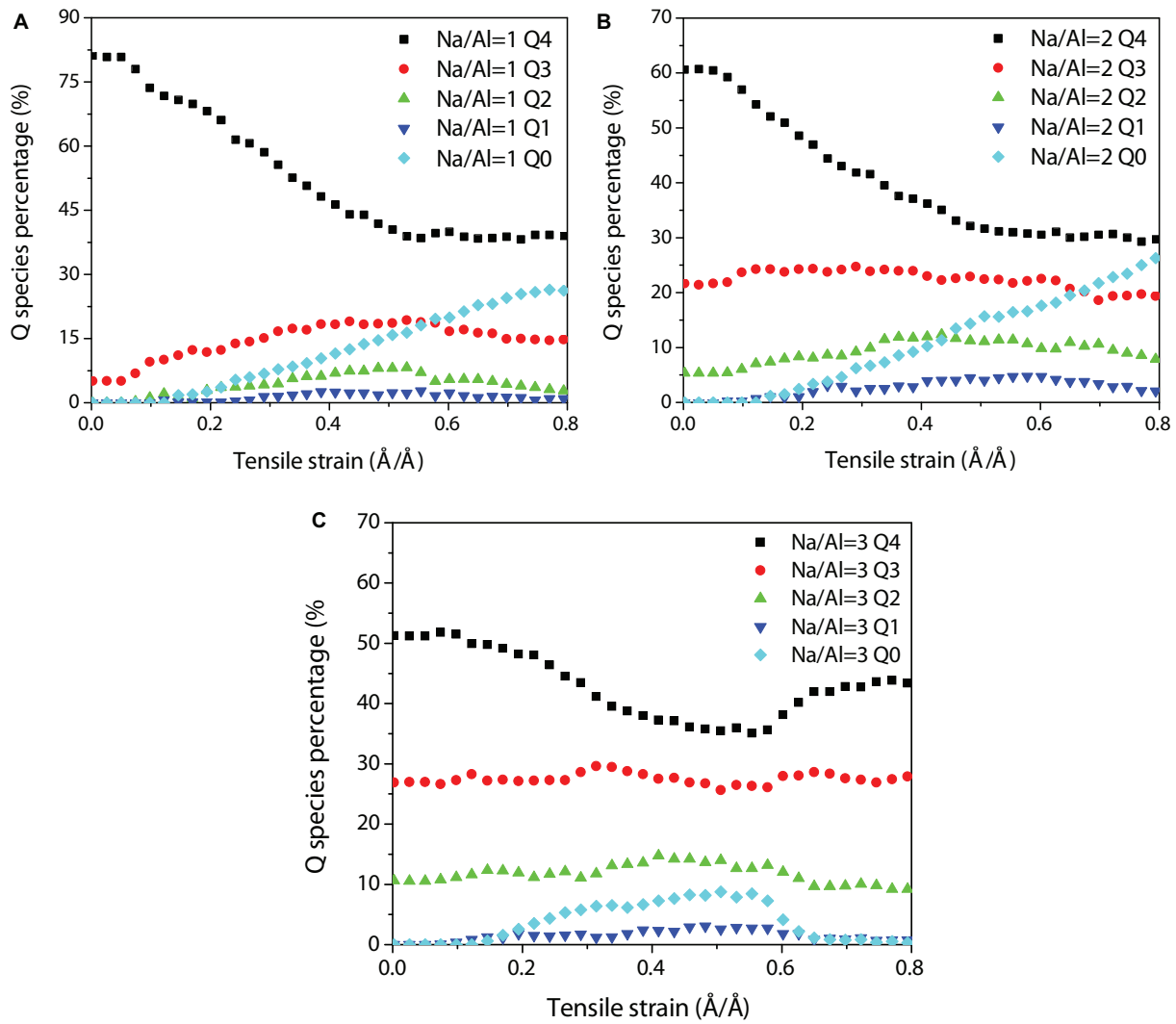

FIGURE 7 | Evolution of Q_n species (n = 0, 1, 2, 3, and 4) for the NASH gel with a Na/Al ratio of **(A)** 1, **(B)** 2, and **(C)** 3 during the tensile process at a strain rate of 0.08 ps.

of the structure during the tensile process (**Figure 5**). In stage 2 (the failure region), the Si-O distance observed in RDF, recovered close to that of the unstrained state (1.62 Å). The trends of RDFs for Al-O are the same, and further verifies the evolution of structure during the tensile process.

A similar evolution trend can be obtained in the angle distribution variation as a function of the strain. As shown in **Figure 6C**, the average value of the Si-O-Si angle is stretched from 139.2° to 150.7° in the elastic region. However, in the yield region, the angle remains basically unchanged and finally returns to the unstrained state. These are consistent with the trends of RDFs.

To depict the structural variation of the aluminosilicate skeleton, the change of Q_n percentages has been calculated. Q species play an important role in the quantitative analysis of the morphological evolution. A connectivity factor, Q_n (n = 0, 1, 2, 3, and 4), is a parameter that estimates the molecular skeleton connection, where n is the number of connected BO of central atoms (Si or Al). Q_0 is the monomer; Q_1 represents the dimmer structure (two connected BO of central atoms); Q_2 is the long chain; Q_3 is the branch structure; and Q_4 is the network structure (Feuston and Garofalini, 1990). When the system reaches the thermodynamic equilibrium state, the basic parameters of the Q species, BO, and NBO in different Na/Al ratio samples are shown in **Table 4**. It is basically consistent with the experimental results (Sadat et al., 2016). With a Na/Al ratio increase, the percentage of Q_4 species (from 81.22 to 51.25%) and BO are both decreased, implying that the network structure (aluminosilicate skeleton) depolymerizes, further resulting in a decrease of the mechanical properties. Furthermore, the aluminosilicate skeleton depolymerizes to branch structure, long chain, short chains, or monomers, so that the percentage of other phases, including Q_3, Q_2, and Q1 obviously increases as the sodium content increases.

During the tensile process, the Q species can depict the structural variation of the aluminosilicate skeleton quantitatively.

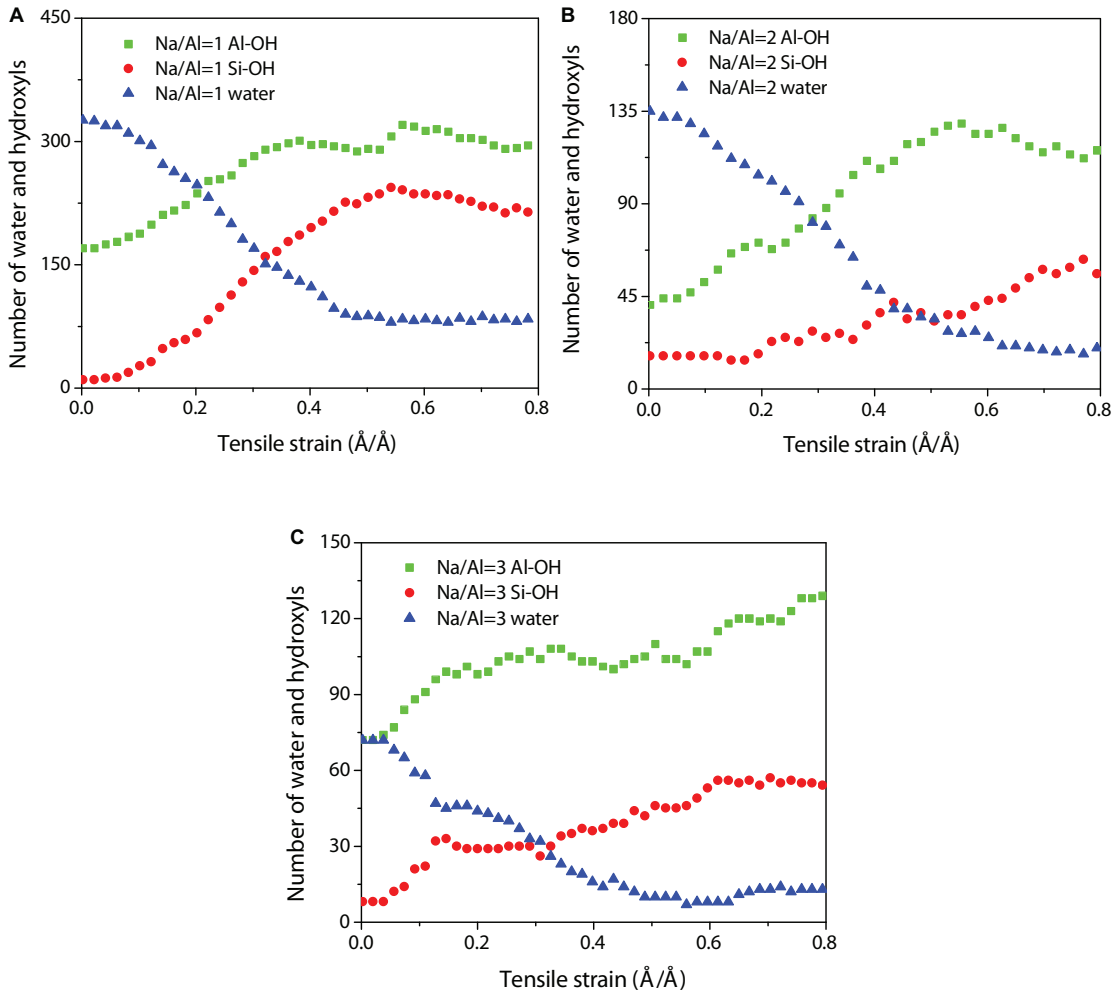

FIGURE 8 | Evolution of the number of water molecules and hydroxyl as functions of strain with a Na/Al ratio of **(A)** 1, **(B)** 2, and **(C)** 3.

At the beginning of the elastic stage, the aluminosilicate skeleton takes up the strain by changing the Si-O and Al-O bonds, and the Q_4 percentage remains unchanged at low strain levels for the NASH gel with all Na/Al ratios (**Figure 7**), implying that the structure only undergoes elastic deformation with no structural damage. As the strain increases, the Q_4 species starts to reduce at a strain of 0.06 Å/Å and continues to decrease from 81 to 39%. This means that some aluminosilicate skeletons were stretched broken, resulting in the morphological transformation from network structure to branch structure, long chain, short chains, or monomers. At the failure stage, the Q_4 species percentage decreases slightly and finally tends to become stable. Furthermore, the increase of the Q_3 and Q_2 species suggests that the network transforms to branch structures and long aluminosilicate chains. The Q_3 and Q_2 species continued to depolymerize to shorter chains and monomers, and the proportion of other Q species (Q_1, Q_0) also increased later. The tensile damage of the NASH gel structures is therefore mainly attributed to the depolymerization of the aluminosilicate network. The Q_4 species percentage increased partially in the NASH gel with a Na/Al ratio of 3 at the failure stage, suggesting that the increase of sodium content rearranges the structure by electrostatic attraction of Coulomb force.

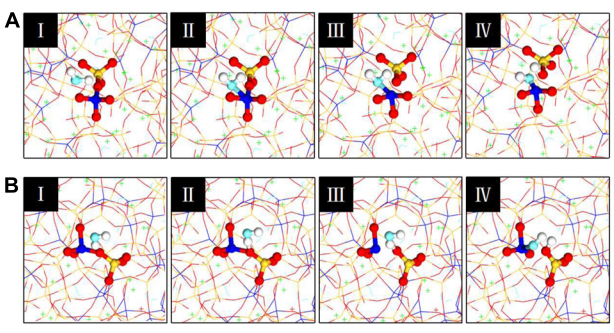

FIGURE 9 | Evolution of molecular structures for the chemical dissociation of water: **(A)** mechanism 1; **(B)** mechanism 2.

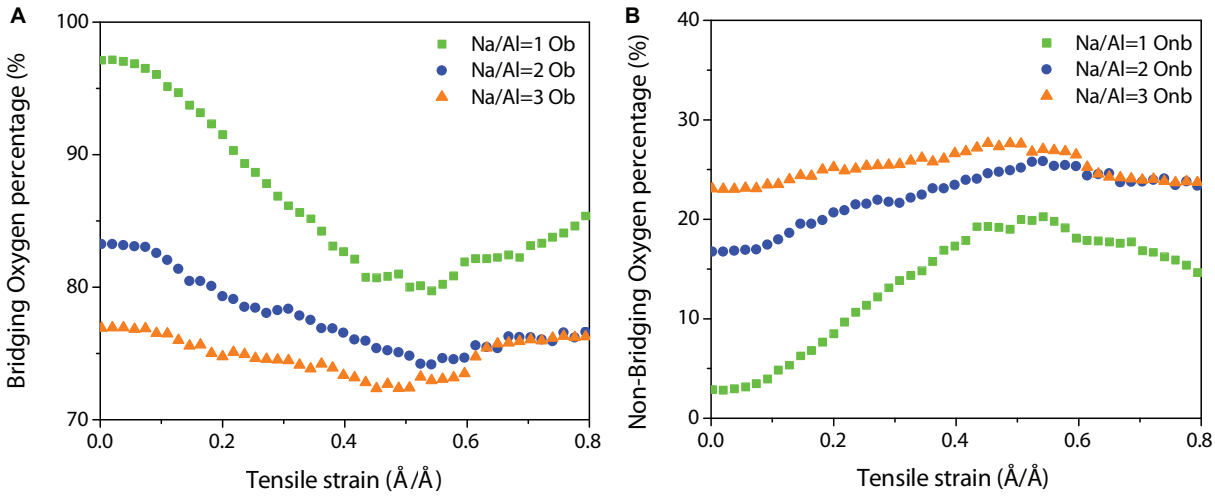

FIGURE 10 | Evolution of **(A)** bridging oxygen and **(B)** non-bridging oxygen as functions of strain.

Hydrolytic Reaction Under Tensile Loading

According to previous studies, water molecules play an important role in the depolymerization of the aluminosilicate network during the tensile process, and the chemical dissociations can be observed (Hou et al., 2014a, 2015c). Water molecules attack the Si-O-Si and Si-O-Al bonds form Si-OH and Al-OH groups, then further weakens the aluminosilicate skeleton during the tensile process. Therefore, the number of Si-OH, Al-OH groups, and water molecules were recorded as functions of strain to analyze the dissociation process quantitatively. The primary factor of the tensile process is the chemical effect. For the sample with a Na/Al ratio of 1 (**Figure 8A**), the number of water molecules decreases as the strain increases until reaching a strain of 0.5 Å/Å, and then it remains unchanged, implying that a large number of water molecules dissociate with the strain increase. The number of Si-OH and Al-OH groups increases co-instantaneous, and is close to a stable state at the strain of 0.5 Å/Å. This indicates that the hydrolysis reaction has gradually occurred in large quantities, especially after the strain is greater than 0.05 Å/Å. It is consistent with the theory that increasing the stress in the structure can reduce the energy barrier for activating the hydrolytic reaction (Zhu et al., 2005). For samples with different Na/Al ratios, the strain at which the number of water molecules starts to reduce with a Na/Al ratio increase (**Figures 8B,C**). In addition, at the same strain rate in the failure region, the number of water molecules of NASH gels with higher Na/Al ratios are significantly smaller than that of the lower sample. These are good validations of the inference that increasing the amount of sodium content accelerates the hydrolytic reaction and the silicate structure transformation, which can be interpreted by the attack on Si-O and Al-O bonds from sodium ions. Furthermore, the number of Al-OH groups increases significantly more than that of Si-OH as the Na/Al ratio increases. This is related to the poorer stability of Al-O bonds than Si-O bonds.

The hydrolytic reaction greatly affects the silicate structure transformation during the uniaxial tension process. The reaction mechanisms of water dissociation have been investigated, and there are two reaction mechanisms: the first mechanism of reaction started in the yield stage and is listed in the following sequence (**Figure 9A**): water diffuses and water molecule is adsorbed close to the neighboring aluminum atom; a bond forms between the aluminum atom and the oxygen atom of the water molecule; a five coordination aluminum structure is formed; the Al-O bond is broken and the aluminum structure restores to four coordination; the water molecule dissociation and proton transfers. In the dissociation process, water molecules lead to the formation of a five coordination aluminum structure, which is disadvantageous in terms of energy. Then the unstable structure separates from the BO. The stretched Si-O-Al bond was attacked by water molecules, and the separation of aluminosilicate network was accelerated. The other mechanism of water dissociation is illustrated in **Figure 9B**, the aluminosilicate skeleton was stretched broken by increasing the tensile strain. The sequence is displayed as follows: the water molecule diffuses close to the neighboring Si-O-Al bond or Si-O-Si bond; a bond is formed between the BO atom and the hydrogen atom of water molecules; the Al-O bond or Si-O bond is broken; water dissociation and proton transfers. However, it should be noted that Al-O bonds are more unstable and easily broken than Si-O bonds.

On the other hand, the dissociation process of water corresponds to the evolution of BO (**Figure 10A**) and NBO (**Figure 10B**) as functions of strain. During the tensile process, the percentage of BO decreases, and that of NBO increases as the Na/Al ratio increases from 1 to 3. It means that the aluminosilicate networks with a lower Na/Al ratios have a higher degree of polymerization, confirming the previous conclusion that an increase of sodium content leads to a decrease in the degree of polymerization and in the mechanical strength of system.

With an increase in the strain, the percentage change of BO and NBO shows nearly the opposite tendencies. At the beginning

of the elastic region, the percentage of BO and NBO is relatively stable, that is the process of crossing the energy barrier for activating the hydrolytic reaction (Hou et al., 2019c). And then the percentage of BO drops sharply and the percentage of NBO increases up to the tensile strain of around 0.4 Å/Å. With an increase of tensile strain before failure, the percentage of BO reduces slowly and fluctuates on a small-scale, which can also be found in the opposite trend of change for NBO. This is consistent with the analysis of the hydrolysis mechanism above. Thus, the hydrolytic reaction of water molecules near the stretched Si-O and Al-O bond further accelerates the NASH gel degradation to resist the tensile loading.

CONCLUSION

Based on the molecular dynamics by a ReaxFF, the structure, reactivity, and mechanical performance of the NASH gel with a Na/Al ratio ranging from 1 to 3 have been investigated. The conclusions can be drawn as follows.

(1) For NASH gels with different Na/Al ratios, Si and Al are predominantly tetrahedral, and the tetrahedral SiO_4 structure and silicate skeleton are not sensitive to the Na/Al ratio. The sodium ions distributed in the NASH gel have around 4 $\sim$ 7 nearest neighbors including oxygen atoms in the silicate/aluminate tetrahedron and hydroxyl. The adsorbed water molecules dissociate into the hydroxyl group near the defective aluminosilicate structure, contributing to the formation of an aluminate pentahedron.

(2) With the amount of sodium content increasing, the molecular structure of the aluminosilicate skeleton transforms from an integrity network to partially destroyed branch structures, decreasing the strength and cohesive force of the NASH gel, characterized by the uniaxial tensile testing. It means that the connection of the aluminosilicate skeleton becomes unstable and further affects the tensile properties of the structure, due to the attack on the Si-O-Si and Si-O-Al bond by sodium ions.

(3) The aluminosilicate skeleton is stretched broken to resist the tensile loading. A high degree of polymerization of the aluminosilicate skeleton network enhances the loading resistance. As the Na/Al ratio increases, the polymerization degree of the aluminosilicate skeleton gradually decreases, and the defective aluminosilicate chains produce more NBO.

(4) Water molecules play an important role in the depolymerization of the aluminosilicate network during the tensile process, and the chemical dissociations can be observed. The adsorption and dissociation are promoted by hydrophilic NBO, further forming Si-OH and Al-OH with the surrounding aluminosilicate skeleton. And the number of Al-OH changes more than that of Si-OH at high Na/Al ratios due to the increase of the sodium content.

DATA AVAILABILITY STATEMENT

All datasets generated for this study are included in the article/supplementary material.

AUTHOR CONTRIBUTIONS

ZL, JZ, and MW are the primary contributors in this work, performed this work, and reviewed the manuscript and approved it for publication.

FUNDING

Funding support for this study was provided by the National Natural Science Foundation of China (Grant Nos. 51678317, 51420105015, and 51909147), the China Ministry of Science and Technology (Grant No. 2015CB655100), the Natural Science Foundation of Shandong Province (Grant Nos. ZR2017JL024 and ZR2019MEM041), and The Fok Ying-Tong Education Foundation for Young Teachers in the Higher Education Institutions of China (Grant No. 161069).

REFERENCES

Andrew, R. M. (2018). Global CO2 emissions from cement production. *Earth Syst. Sci. Data* 10, 195–217. doi: 10.5194/essd-10-195-2018

Bakharev, T. (2005). Geopolymeric materials prepared using Class F fly ash and elevated temperature curing. *Cem. Concr. Res.* 35, 1224–1232. doi: 10.1016/j.cemconres.2004.06.031

Barbosa, V. F., and MacKenzie, K. J. (2003). Thermal behaviour of inorganic geopolymers and composites derived from sodium polysialate. *Mater. Res. Bull.* 38, 319–331. doi: 10.1016/s0025-5408(02)01022-x

Barbosa, V. F. F., Mackenzie, K. J. D., and Thaumaturgo, C. (2000). Synthesis and characterisation of materials based on inorganic polymers of alumina and silica: sodium polysialate polymers. *Int. J. Inorg. Mater.* 2, 309–317. doi: 10.1016/s1466-6049(00)00041-6

Bonnaud, P., Ji, Q., Coasne, B., Pellenq, R.-M., and Van Vliet, K. (2012). Thermodynamics of water confined in porous calcium-silicate-hydrates. *Langmuir* 28, 11422–11432. doi: 10.1021/la301738p

Brenner, D. W., Shenderova, O. A., Harrison, J. A., Stuart, S. J., Ni, B., and Sinnott, S. B. (2002). A second-generation reactive empirical bond order (REBO) potential energy expression for hydrocarbons. *J. Phys. Condens. Matter* 14, 783–802. doi: 10.1088/0953-8984/14/4/312

Cygan, R. T., Liang, J.-J., and Kalinichev, A. G. (2004). Molecular models of hydroxide, oxyhydroxide, and clay phases and the development of a general force field. *J. Phys. Chem. B* 108, 1255–1266. doi: 10.1021/jp0363287

Damtoft, J. S., Lukasik, J., Herfort, D., Sorrentino, D., and Gartner, E. M. (2008). Sustainable development and climate change initiatives. *Cem. Concr. Res.* 38, 115–127.

Davidovits, J. (1982). *Mineral Polymers and Methods of Making Them.* US Patent No 4472 1993.

Davidovits, J. (1991). Geopolymers. *J. Therm. Anal. Calorim.* 37, 1633–1656.

De Silva, P., Sagoe-Crenstil, K., and Sirivivatnanon, V. (2007). Kinetics of geopolymerization: role of Al2O3 and SiO2. *Cem. Concr. Res.* 37, 512–518. doi: 10.1016/j.cemconres.2007.01.003

Duin, A. C. T. V., Dasgupta, S., Lorant, F., and Goddard, W. A. (2001). ReaxFF: a reactive force field for hydrocarbon. *J. Phys. Chem. A* 105, 9396–9409.

Duxson, P., Fernández-Jiménez, A., Provis, J. L., Lukey, G. C., Palomo, A., and Deventer, J. S. J. V. (2007a). Geopolymer technology: the current state of the art. *J. Mater. Sci.* 42, 2917–2933. doi: 10.1007/s10853-006-0637-z

Duxson, P., Lukey, G. C., Separovic, F., and van Deventer, J. S. (2005). Effect of alkali cations on aluminum incorporation in geopolymeric gels. *Ind. Eng. Chem. Res* 44, 832–839. doi: 10.1021/ie0494216

Duxson, P., Provis, J. L., Lukey, G. C., and Deventer, J. S. J. V. (2007b). The role of inorganic polymer technology in the development of 'green concrete'. *Cem. Concr. Res.* 37, 1590–1597. doi: 10.1016/j.cemconres.2007.08.018

Duxson, P., Provis, J. L., Lukey, G. C., Mallicoat, S. W., Kriven, W. M., and van Deventer, J. S. (2005a). Understanding the relationship between geopolymer composition, microstructure and mechanical properties. *Colloids Surf. A Physicochem. Eng. Aspect* 269, 47–58. doi: 10.1016/j.colsurfa.2005.06.060

Duxson, P., Provis, J. L., Lukey, G. C., Separovic, F., and van Deventer, J. S. (2005b). 29Si NMR study of structural ordering in aluminosilicate geopolymer gels. *Langmuir* 21, 3028–3036. doi: 10.1021/la047336x

Feuston, B., and Garofalini, S. (1990). Oligomerization in silica sols. *J. Phys. Chem.* 94, 5351–5356. doi: 10.1016/j.jcis.2011.01.064

Hou, D., Li, D., Zhao, T., and Li, Z. (2016a). Confined water dissociation in disordered silicates nanometer-channels at elevated temperatures: mechanism, dynamics and impact on the substrates. *Langmuir* 32, 4153–4168. doi: 10.1021/acs.langmuir.6b00444

Hou, D., Li, Z., and Zhao, T. (2015a). Reactive force field simulation on polymerization and hydrolytic reactions in calcium aluminate silicate hydrate (C–A–S–H) gel: structure, dynamics and mechanical properties. *Rsc Adv.* 5, 448–461. doi: 10.1039/c4ra10645h

Hou, D., Lu, Z., Zhao, T., and Ding, Q. (2016b). Reactive molecular simulation on the ordered crystal and disordered glass of the calcium silicate hydrate gel. *Ceram. Int.* 42, 4333–4346. doi: 10.1016/j.ceramint.2015.11.112

Hou, D., Ma, H., Li, Z., and Jin, Z. (2014a). Molecular simulation of "hydrolytic weakening": a case study on silica. *Acta Mater.* 80, 264–277. doi: 10.1016/j.actamat.2014.07.059

Hou, D., Yu, J., and Wang, P. (2019a). Molecular dynamics modeling of the structure, dynamics, energetics and mechanical properties of cement-polymer nanocomposite. *Compos. Part B Eng.* 162, 433–444. doi: 10.1016/j.compositesb.2018.12.142

Hou, D., Zhang, J., Li, Z., and Zhu, Y. (2015b). Uniaxial tension study of calcium silicate hydrate (C–S–H): structure, dynamics and mechanical properties. *Mater. Struct.* 48, 3811–3824. doi: 10.1617/s11527-014-0441-1

Hou, D., Zhang, J., Pan, W., Zhang, Y., and Zhang, Z. (2019b). Nanoscale mechanism of ions immobilized by the geopolymer: a molecular dynamics study. *J. Nuclear Mater.* 528:151841. doi: 10.1016/j.jnucmat.2019.151841

Hou, D., Zhang, Q., Xu, X., Zhang, J., Li, W., and Wang, P. (2019c). Insights on ions migration in the nanometer channel of calcium silicate hydrate under external electric field. *Electrochim. Acta* 320, 134637. doi: 10.1016/j.electacta.2019.134637

Hou, D., Zhao, T., Ma, H., and Li, Z. (2015c). Reactive molecular simulation on water confined in the nanopores of the calcium silicate hydrate gel: structure, reactivity, and mechanical properties. *J. Phys. Chem. C* 119, 1346–1358. doi: 10.1021/jp509292q

Hou, D., Zhao, T., Wang, P., Li, Z., and Zhang, J. (2014b). Molecular dynamics study on the mode I fracture of calcium silicate hydrate under tensile loading. *Eng. Fract. Mech.* 131, 557–569. doi: 10.1016/j.engfracmech.2014.09.011

Irwin, A. D., Holmgren, J. S., and Jonas, J. (1988). 27 Al and 29 Si NMR study of sol-gel derived aluminosilicates and sodium aluminosilicates. *J. Mater. Sci.* 23, 2908–2912. doi: 10.1007/bf00547467

Kriven, W. M., Bell, J. L., and Gordon, M. (2003). Microstructure and microchemistry of fully-reacted geopolymers and geopolymer matrix composites. *Ceram. Trans.* 153, 227–250. doi: 10.1002/9781118406892.ch15

Leonelli, C., Lusvardi, G., Montorsi, M., Menziani, M. C., Menabue, L., Mustarelli, P., et al. (2001). Influence of small additions of Al2O3 on the properties of the Na2O⊙ 3SiO2 Glass. *J. Phys. Chem. B* 105, 919–927.

Li, Z. (2011). *Advanced Concrete Technology*. Hoboken, NJ: John Wiley & Sons.

Luukkonen, T., Abdollahnejad, Z. Yliniemi, J., Kinnunen, P., and Illikainen, M. (2018). One-part alkali-activated materials: a review. *Cem. Concr. Res.* 103, 21–34.

Mauri, F., Pasquarello, A., Pfrommer, B. G., Yoon, Y.-G., and Louie, S. G. (2000). Si-O-Si bond-angle distribution in vitreous silica from first-principles 29 Si NMR analysis. *Phys. Rev. B* 62:R4786.

McKeown, D., Galeener, F., and Brown, G. Jr. (1984). Raman studies of Al coordination in silica-rich sodium aluminosilicate glasses and some related minerals. *J. Non Crystall. Solids* 68, 361–378. doi: 10.1016/0022-3093(84)90017-6

Mozzi, R., and Warren, B. (1969). The structure of vitreous silica. *J. Appl. Crystallogr.* 2, 164–172.

Okuno, M., Zotov, N., Schmücker, M., and Schneider, H. (2005). Structure of SiO2–Al2O3 glasses: combined X-ray diffraction, IR and Raman studies. *J. Non Crystall. Solids* 351, 1032–1038. doi: 10.1016/j.jnoncrysol.2005.01.014

Palomo, A., and Glasser, F. (1992). Chemically-bonded cementitious materials based on metakaolin. *Br. Ceram. Trans. J.* 91, 107–112. doi: 10.3390/ma12030442

Palomo, A., Grutzeck, M., and Blanco, M. (1999). Alkali-activated fly ashes: a cement for the future. *Cem. Concr. Res.* 29, 1323–1329. doi: 10.1016/s0008-8846(98)00243-9

Parthasarathy, P., Hanif, A., Shao, H., and Li, Z. (2017). "Microstructural and morphological studies of ordinary portland cement paste and fly ash based geopolymer in the presence of chloride ions," in *Proceedings of the 71st RILEM Week and ICACMS 2017 – International Conference on Advances in Construction Materials and Systems*, Chennai, 623.

Rowles, M., and O'connor, B. (2003). Chemical optimisation of the compressive strength of aluminosilicate geopolymers synthesised by sodium silicate activation of metakaolinite. *J. Mater. Chem.* 13, 1161–1165. doi: 10.1039/b212629j

Sadat, M. R., Bringuier, S., Asaduzzaman, A., Muralidharan, K., and Zhang, L. (2016). A molecular dynamics study of the role of molecular water on the structure and mechanics of amorphous geopolymer binders. *J. Chem. Phys.* 145:134706. doi: 10.1063/1.4964301

Schmücker, M., and MacKenzie, K. J. (2005). Microstructure of sodium polysialate siloxo geopolymer. *Ceram. Int.* 31, 433–437. doi: 10.1016/j.ceramint.2004.06.006

Singh, P. S., Trigg, M., Burgar, I., and Bastow, T. (2005). Geopolymer formation processes at room temperature studied by 29Si and 27Al MAS-NMR. *Mater. Sci. Eng. A* 396, 392–402. doi: 10.1016/j.msea.2005.02.002

Uchino, T., Sakka, T., Ogata, Y., and Iwasaki, M. (1993). Local structure of sodium aluminosilicate glass: an ab initio molecular orbital study. *J. Phys. Chem.* 97, 9642–9649. doi: 10.1021/j100140a019

Van Jaarsveld, J., Van Deventer, J., and Lukey, G. (2002). The effect of composition and temperature on the properties of fly ash-and kaolinite-based geopolymers. *Chem. Eng. J.* 89, 63–73. doi: 10.1016/s1385-8947(02)00025-6

Walkley, B., Rees, G. J., San Nicolas, R., van Deventer, J. S., Hanna, J. V., and Provis, J. L. (2018). New structural model of hydrous sodium aluminosilicate gels and the role of charge-balancing extra-framework Al. *J. Phys. Chem. C* 122, 5673–5685. doi: 10.1021/acs.jpcc.8b00259

Wang, P., Zhang, Q., Wang, M., Yin, B., Hou, D., and Zhang, Y. (2019). Atomistic insights into cesium chloride solution transport through the ultra-confined calcium–silicate–hydrate channel. *Phys. Chem. Chem. Phys.* 21, 11892–11902. doi: 10.1039/c8cp07676f

White, C. E., Provis, J. L., Proffen, T., and van Deventer, J. S. (2012). Molecular mechanisms responsible for the structural changes occurring during geopolymerization: multiscale simulation. *AICHE J.* 58, 2241–2253. doi: 10.1002/aic.12743

Xiang, Y., Du, J., Smedskjaer, M. M., and Mauro, J. C. (2013). Structure and properties of sodium aluminosilicate glasses from molecular dynamics simulations. *J. Chem. Phys.* 139:044507. doi: 10.1063/1.4816378

Xu, H., and Van Deventer, J. (2000). The geopolymerisation of alumino-silicate minerals. *Int. J. Miner. Process.* 59, 247–266. doi: 10.1016/s0301-7516(99)00074-5

Zhang, M., Deskins, N. A., Zhang, G., Cygan, R. T., and Tao, M. (2018). Modeling the polymerization process for geopolymer synthesis through reactive molecular dynamics simulations. *J. Phys. Chem. C* 122, 6760–6773. doi: 10.1021/acs.jpcc.8b00697

Zhang, Y., Zhang, J., Jiang, J., Hou, D., and Zhang, J. (2018). The effect of water molecules on the structure, dynamics, and mechanical properties of sodium aluminosilicate hydrate (NASH) gel: a molecular dynamics study. *Constr. Build. Mater.* 193, 491–500. doi: 10.1016/j.conbuildmat.2018.10.221

Zhu, T., Li, J., Lin, X., and Yip, S. (2005). Stress-dependent molecular pathways of silica–water reaction. *J. Mech. Phys. Solids* 53, 1597–1623. doi: 10.1016/j.jmps.2005.02.002

Conflict of Interest: The authors declare that the research was conducted in the absence of any commercial or financial relationships that could be construed as a potential conflict of interest.

Copyright © 2020 Li, Zhang and Wang. This is an open-access article distributed under the terms of the Creative Commons Attribution License (CC BY). The use, distribution or reproduction in other forums is permitted, provided the original author(s) and the copyright owner(s) are credited and that the original publication in this journal is cited, in accordance with accepted academic practice. No use, distribution or reproduction is permitted which does not comply with these terms.

frontiers in Materials

ORIGINAL RESEARCH
published: 08 September 2020
doi: 10.3389/fmats.2020.00299

Screening Out Reactivity-Promoting Candidates for γ-Ca_2SiO_4 Carbonation by First-Principles Calculations

*Yong Tao, Yuandong Mu, Wenqin Zhang and Fazhou Wang**

State Key Laboratory of Silicate Materials for Architectures, Wuhan University of Technology, Wuhan, China

γ-Ca_2SiO_4 as a promising carbonation-activated cementitious material features an attractive capacity of carbon sequestration. Improving the carbonation reactivity of γ-Ca_2SiO_4 is of great significance for its practical application. In this paper, first-principles calculations are performed to single out the potential candidates for carbonation activation from a series of dopants. Electronic structure analyses reveal that the carbonation reactivity is related to the reactive site distribution and the binding strength of γ-Ca_2SiO_4 crystal. Ba, P, and F elements are found to decrease the overall binding strength of γ-Ca_2SiO_4 crystal, which benefits the dissolution of ions from the crystal to take part in the carbonation reactions. The theoretical conjectures are validated by designed and previous experiments, which confirms the first-principles-based method to effectively guide our experimental investigation.

Keywords: γ-dicalcium silicate, carbonation, reactivity, electronic structure, first-principles

OPEN ACCESS

Edited by:
Dongshuai Hou,
Qingdao University of Technology, China

Reviewed by:
Tim Kowalczyk,
Western Washington University, United States
Mehdi Shishehbor,
University of California, Irvine, United States

***Correspondence:**
Fazhou Wang
fzhwang@whut.edu.cn

Specialty section:
This article was submitted to Computational Materials Science, a section of the journal Frontiers in Materials

Received: *29 May 2020*
Accepted: *10 August 2020*
Published: *08 September 2020*

Citation:
Tao Y, Mu Y, Zhang W and Wang F (2020) Screening Out Reactivity-Promoting Candidates for γ -Ca_2SiO_4 Carbonation by First-Principles Calculations. Front. Mater. 7:299. doi: 10.3389/fmats.2020.00299

INTRODUCTION

Exploiting effective ways to suppress the carbon dioxide level of the atmosphere is one of the most important scientific issues, which mainly includes two aspects: reducing carbon dioxide emissions and capturing carbon dioxide. Regarding the former, taking the cement industry as an example, the production of cement contributes about 7% of anthropogenic carbon dioxide emissions (Liu et al., 2015), mainly derived from the calcination and decomposition of limestone (one of the main raw minerals). The two main components of ordinary Portland cement clinker are β-dicalcium silicate (β-Ca_2SiO_4, also belite) and tricalcium silicate (Ca_3SiO_5, also alite). Belite has a lower Ca/Si ratio than alite and requires a lower calcination temperature, which means manufacturing belite causes less energy consumption and carbon dioxide emissions. Thus, in recent years, experts in the cement field have been pushing the use of high belite content cement (compared to the composition of ordinary Portland cement clinker) (Ludwig and Zhang, 2015). However, belite has a much lower hydration reactivity than alite leading to slower development of the early strength of concrete (Scrivener et al., 2015), making it difficult to meet the needs of most practical projects.

On the other hand, regarding capturing carbon dioxide, the use of geological minerals to sequestrate carbon dioxide has long been an attractive topic in geological science (Olajire, 2013). Olivine minerals such as fayalite (Fe_2SiO_4), forsterite (Mg_2SiO_4), etc. are widely investigated as the candidates for carbon sequestration (Olsson et al., 2012; Todd Schaef et al., 2012). The Fe and Mg ions in olivine can be substituted by Ca ions without destroying the symmetry of the

crystal. The olivine Ca_2SiO_4 that belongs to the orthorhombic crystal system is also one of the polymorphs of belite (β-Ca_2SiO_4), known as γ-dicalcium silicate (γ-Ca_2SiO_4) (Naa et al., 2015). Previous studies have shown that among common olivine minerals, γ-Ca_2SiO_4 has a significantly dominant surface water absorption capacity (Kerisit et al., 2013), suggesting the potentially high carbonation reactivity. Besides, compared with the polymorph β-Ca_2SiO_4, γ-Ca_2SiO_4 also showed much higher carbonation reactivity (Chang et al., 2016). Mu et al. (2019) found that the γ-Ca_2SiO_4 samples exposed to a 100% carbon dioxide environment under high pressure achieved mechanical properties in hours equivalent to that of the hydration product of a cement clinker hydrated for days, which provides a perspective of using carbonation-activated cementitious materials to reduce the dependence on alite- and belite-based cementitious materials. Theoretically, the use of γ-Ca_2SiO_4 carbonation instead of cement clinker hydration not only reduces the carbon dioxide emissions from clinker production but also sequestrates the released carbon dioxide in a natural way, i.e., mineralization (Ashraf, 2016). However, the trace amount of carbon dioxide in the air does not allow γ-Ca_2SiO_4 to achieve a high degree of carbonation in a short time. Apart from the pre-carbonation process under carbon dioxide-rich conditions (Mu et al., 2018), the carbonation reactivity of γ-Ca_2SiO_4 needs to be improved. To this end, this article aims to select dopant ions that can theoretically increase the carbonation reactivity of γ-Ca_2SiO_4 through first-principles calculations.

Previous researches tried to reveal the carbonation mechanism of olivine minerals from the perspective of surface reactions. For example, Watson et al. (1997) studied the stability of seven low-index surfaces of forsterite and found that the (1 0 0) surface was the most stable one. De Leeuw et al. (2000) computed the associative and dissociative adsorption of water on the low-index surfaces of forsterite. They found that all surfaces, except the non-dipolar (1 0 0), were favorable for dissociative adsorption while the (1 0 0) surface was preferable for associative adsorption. Kerisit et al. (2013) revealed that calico-olivine (γ-Ca_2SiO_4) featured the largest adsorption energy (absolute value) among five olivine minerals, namely, forsterite, calico-olivine, tephroite, fayalite, and Co-olivine. These thermodynamic computations regarding the surface adsorption, dissolution, nucleation, and so on are conducive to understanding some steps of the carbonation process of olivine. However, they did not give a general indicator to predict the carbonation reactivity, and the performed thermodynamic calculations (like dissolution energy barrier) (Morrow et al., 2009) are too sophisticated to be used as indicators for singling out reactivity-promoting candidates from numerous dopant species. Herein, we are trying to find a simplified way to roughly give hints to our experiments for searching reactivity-promoting

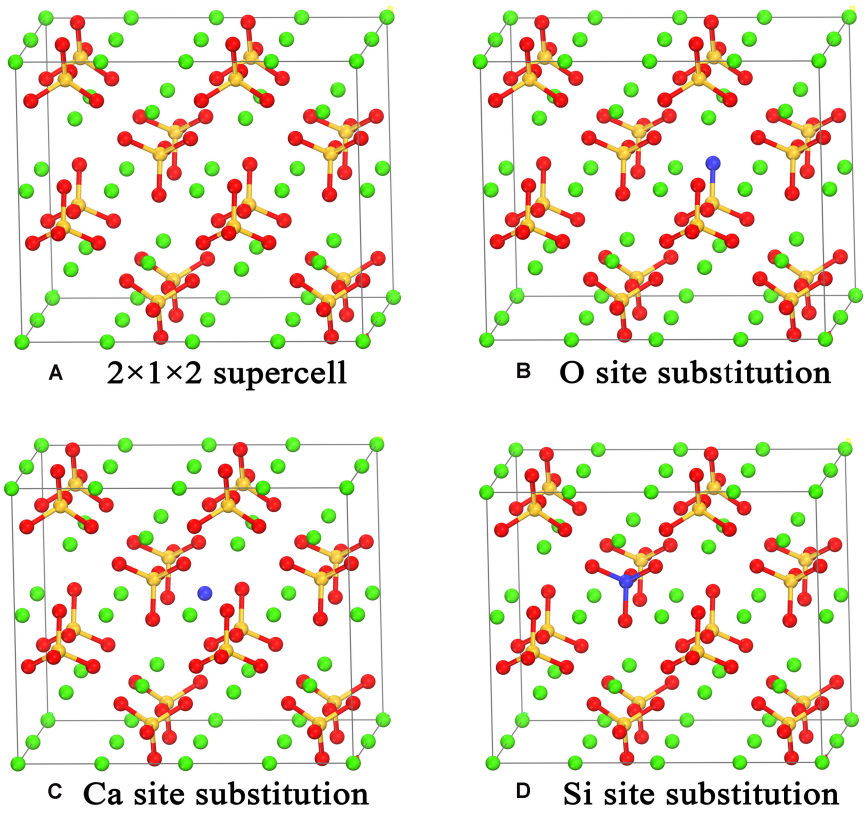

FIGURE 1 | Crystal models of the pristine **(A)**, O site substituted **(B)**, Ca site substituted **(C)**, and Si site substituted **(D)** γ-Ca_2SiO_4. The green, orange, and red spheres are Ca, Si, and O atoms, respectively. The blue spheres indicate the atom sites for different types of substitution.

candidates for γ-Ca_2SiO_4 carbonation, which is actually like the machine learning using simple indicators to screen out potential materials for desirable properties. We first analyzed the electronic structures of γ-Ca_2SiO_4 to reveal the latent relationship between electronic structures and carbonation reactivity, based on which the potential influence of 10 kinds of doping ions on γ-Ca_2SiO_4 was estimated. Promising doping candidates were singled out, and the theoretical conjectures were verified by experiments.

MATERIALS AND METHODS

The pristine γ-Ca_2SiO_4 crystal structure (Udagawa et al., 1980) was obtained from the inorganic crystal structure database (ICSD). The primary cell of γ-Ca_2SiO_4 contains 28 atoms (8 Ca, 4 Si, and 16 O atoms). To reduce the concentration of doped ions, a supercell of 2 × 1 × 2 was adopted as the matrix of doping models. We selected 10 common impurity ions of olivine as substituent ions: Mg, Sr, Ba, Al, Fe, Zn, P, F, Cl, and Br. As shown in **Figure 1**, according to the similarity of chemical properties, the anions F, Cl, and Br are supposed to replace the O ions in γ-Ca_2SiO_4, whereas the cations replace the Ca ions (Mg, Sr, Ba, Zn) or Si atoms (P). Since the Fe and Al ions can replace both the Ca ions and Si atoms as reported in previous researches (Manzano et al., 2011; Durgun et al., 2012), we calculated the two substitution methods for Fe and Al doping.

The Vienna *Ab initio* Simulation Package (VASP) (Kresse and Furthmüller, 1996; Kresse, 1999) was used to optimize the crystal structure through energy minimization with the conjugate gradient method. The constructed models were continuously optimized until the energy differences and the force differences were less than 10^{-5} eV/atom and 0.005 eV/Å, respectively. Then, the electronic structures were calculated and analyzed by the Cambridge Sequential Total Energy Package (CASTEP) (Clark et al., 2005). The exchange-correlation potential was estimated by the Perdew–Burke–Ernzerhof (PBE) method (Blöchl, 1994; Perdew et al., 1994) for both the VASP and CASTEP calculations. In addition, the projector augmented plane wave (PAW) method was implemented in the VASP calculation. A kinetic energy cutoff of 580 eV was adopted based on multiple tests as posted in the **Supplementary Material S1**. More computational details can be found in our previous studies (Tao et al., 2018a, 2019a).

To verify the doping effects on carbonation reactivity, corresponding experiments were implemented. γ-Ca_2SiO_4 was synthesized at 1400°C using the analytical reagent $Ca(OH)_2$

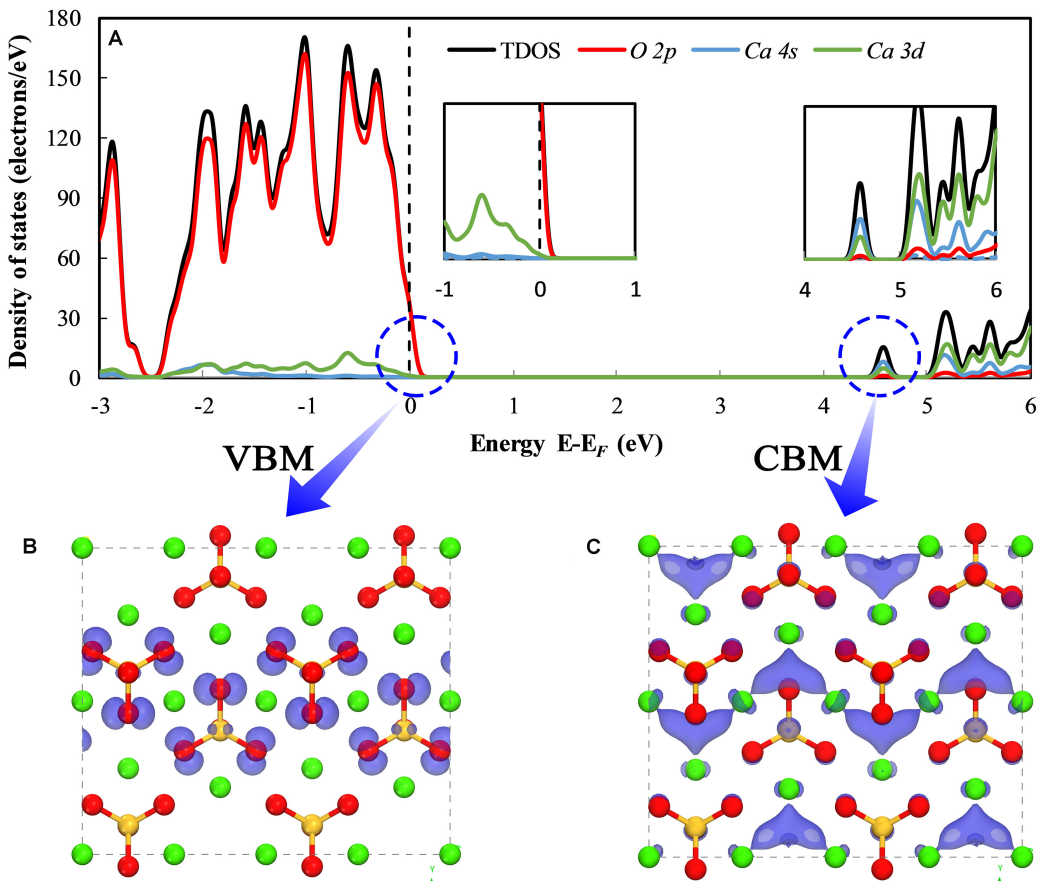

FIGURE 2 | The density of states **(A)** and local charge density distribution of the valence band maximum **(B)** and conduction band minimum **(C)** of pure γ-Ca_2SiO_4. The green, orange, and red spheres are Ca, Si, and O atoms, respectively. The blue translucent electron clouds represent the orbitals of energy band edges.

and SiO_2. Cationic dopants (Mg^{2+}, Al^{3+}, Ba^{2+}, P^{5+}) were introduced into the raw mix in the form of oxides while anionic dopant F^- was in the form of CaF_2. The dopant dosage was 2 mol% relative to the molar content of γ-Ca_2SiO_4 in the reference (undoped) group. The fabricated pure and doped specimens were ground into powders with a particle size smaller than 74 μm. For each group to be carbonated, 10 g of γ-Ca_2SiO_4 powder was mixed with 1.5 g water and compacted into cylindrical tablets, which were put into the carbon dioxide atmosphere (purity = 99.9%) for 3 days without extra pressure. We use the degree of carbonation (DOC) of γ-Ca_2SiO_4 to indicate the carbonation reactivity of different doping models. DOC was defined as

$$\mathrm{DOC} = \frac{m_{real}}{m_{theo}} \times 100\%$$

where m_{theo} and m_{real} are the theoretically maximal and real uptake of CO_2 respectively. m_{theo} can be estimated by the carbonation reaction equation as follows:

$$Ca_2SiO_4 + 2CO_2 \overset{H_2O}{\rightarrow} 2CaCO_3 + SiO_2(gel)$$

The details about the materials preparation and testing procedures can be attained by consulting our previous study (Mu et al., 2018, 2019).

RESULTS AND DISCUSSION

Electronic Structures of Pristine γ-Ca_2SiO_4

To understand the effects of doped ions on the carbonation reactivity of γ-Ca_2SiO_4, we first need to uncover the relationship between the electronic structures of the pure γ-Ca_2SiO_4 phase and its carbonation reactivity. Previous studies indicate that the carbonation reaction of γ-Ca_2SiO_4 requires water and involves the dissolution and migration of Ca ions from the crystal. Hence, mapping the reactive sites in the γ-Ca_2SiO_4 crystal and measuring the strength of the chemical bonds are essential for the analysis of carbonation reactivity. We calculated the energy band edge structures and bonding structures of γ-Ca_2SiO_4 as illustrated in **Figures 2**, **3**. **Figure 2A** is the partial density of states (PDOS) and the total density of states (TDOS) of γ-Ca_2SiO_4. The dashed line locates the highest occupied molecule orbital of the system (known as the valence band maximum or VBM), which is also set as the position of relative Fermi level. The closest TDOS peak above the Fermi level implies the lowest unoccupied molecule orbital of the system (known as the conduction band minimum or CBM) (Parr and Yang, 1984; Chattaraj, 2009). The VBM and CBM are separated by a large energy band gap (about 4.2 eV) because the pure γ-Ca_2SiO_4 crystal is a typical insulator. The VBM is the most vulnerable part of the system to lose electrons. Therefore, those species whose atomic energy level contributes to the VBM are the areas in the system that are most vulnerable to an electrophilic attack, i.e., electrophilic reactive sites. Correspondingly, the CBM is the most vulnerable part of the system to accept electrons, pointing to the nucleophilic reactive sites of the system (Manzano et al., 2009; Wang et al., 2015). **Figures 2B,C** visualize the local charge density (LCD) distributions of pure γ-Ca_2SiO_4 at the VBM and CBM, respectively. The blue translucent electron clouds indicate the electrophilic and nucleophilic reactive sites of the system, respectively. The electrophilic reactive sites are almost entirely on O atoms, which is consistent with the result of the PDOS (left inset of **Figure 2A**) as the VBM is predominantly contributed by the O 2*p* state. In contrast, the nucleophilic reactive sites are the regions surrounded by Ca ions, which is also understandable because the CBM is mainly contributed by the 4*s* and 3*d* states of Ca atoms (right inset of **Figure 2A**).

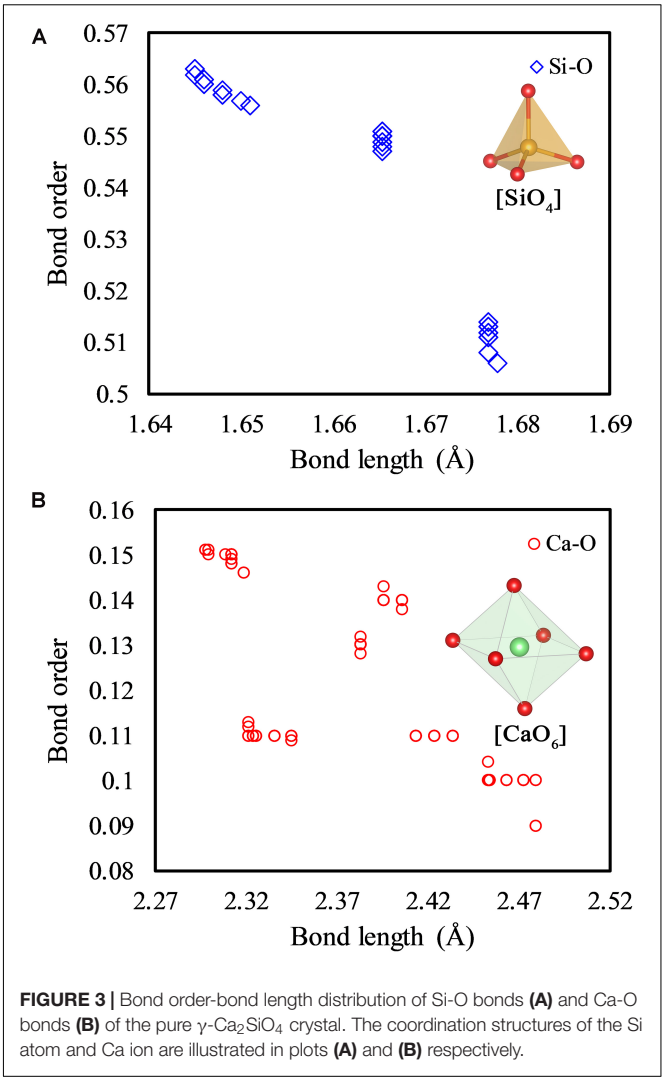

FIGURE 3 | Bond order-bond length distribution of Si-O bonds **(A)** and Ca-O bonds **(B)** of the pure γ-Ca_2SiO_4 crystal. The coordination structures of the Si atom and Ca ion are illustrated in plots **(A)** and **(B)** respectively.

The local charge density distribution of the energy band edges (VBM and CBM) qualitatively visualized the reactive sites of the pure γ-Ca_2SiO_4 crystal, while the binding strength of ions in the system can be quantitatively estimated by the bond length (BL)–bond order (BO) analysis (**Figure 3**). The BO is obtained by calculating the degree of overlap of the electron cloud between two bonding atoms, which directly reflects the strength of the bond: the larger the BO, the stronger the bond

(Dharmawardhana et al., 2013; Tao et al., 2018b). Therefore, the BO quantifies the difficulty of extracting ions from the crystal, which is related to the carbonation reactivity. It should be noted that there are a variety of methods of calculating the BO, and the Mulliken scheme (Mulliken, 1955) is adopted here. Although the absolute values of the BO calculated by different methods are different, it is reasonable to compare the relative magnitude of the BO calculated from the same system with the uniform method. The BL also indirectly maps the strength of chemical bonds, that is, the larger the bond length, the weaker the bond. Compared to the correlation of the BO and bond strength, the BL and bond strength are not strictly correlated. As shown in **Figure 3A**, the Si–O bonds in [SiO_4] tetrahedra are almost equal in length (around 1.66 Å), while their BO is clearly distinguished. The BL of Ca–O bonds varies widely from 2.31 to 2.48 Å, whereas their BO is around 0.12 (**Figure 3B**). Therefore, the BO is an effective indicator for measuring the binding strength of ions in a crystal, suggesting the difficulty of dissolving them from the crystal.

Reactivity Modification by Doping

Having revealed the correlation between the carbonation reactivity of pure γ-Ca_2SiO_4 and its electronic structures, we now can evaluate the doping effect on the carbonation reactivity by monitoring the changes in the electronic structures of the doped γ-Ca_2SiO_4. **Figures 4**, **5** depict the changes of LCD distribution of the VBM and CBM, indicating the electrophilic and nucleophilic reactive sites, respectively, as aforementioned. Compared with the undoped γ-Ca_2SiO_4 in **Figures 2B,C**, the anionic substitution (F, Cl, Br) significantly changes the electrophilic reactive site distribution (VBM). It is mainly because the substitution of F, Cl, or Br for O changes the effective charge of O ions, causing the shift of the original electrophilic reactive sites from O ions. For the Fe doping, both the electrophilic and nucleophilic reactive sites shifted from O ions and the Ca-blocked regions to the vicinity of Fe impurity. Previous studies have explained that this is due to the strong delocalization of the Fe 3*d* electron shell, almost spanning the Fermi level, which can lose or accept electrons easily (Tao et al., 2019b). Therefore, Fe ions become the new electrophilic and nucleophilic reactive center of the system. The substitution of Mg, Sr, and Ba for Ca causes less influence on the reactive sites as they come from the same family, namely the IIA group, sharing a similar valence electron structure. Compared with the diffuse distribution of reactive sites in the pure γ-Ca_2SiO_4, a slight local enhancement of some

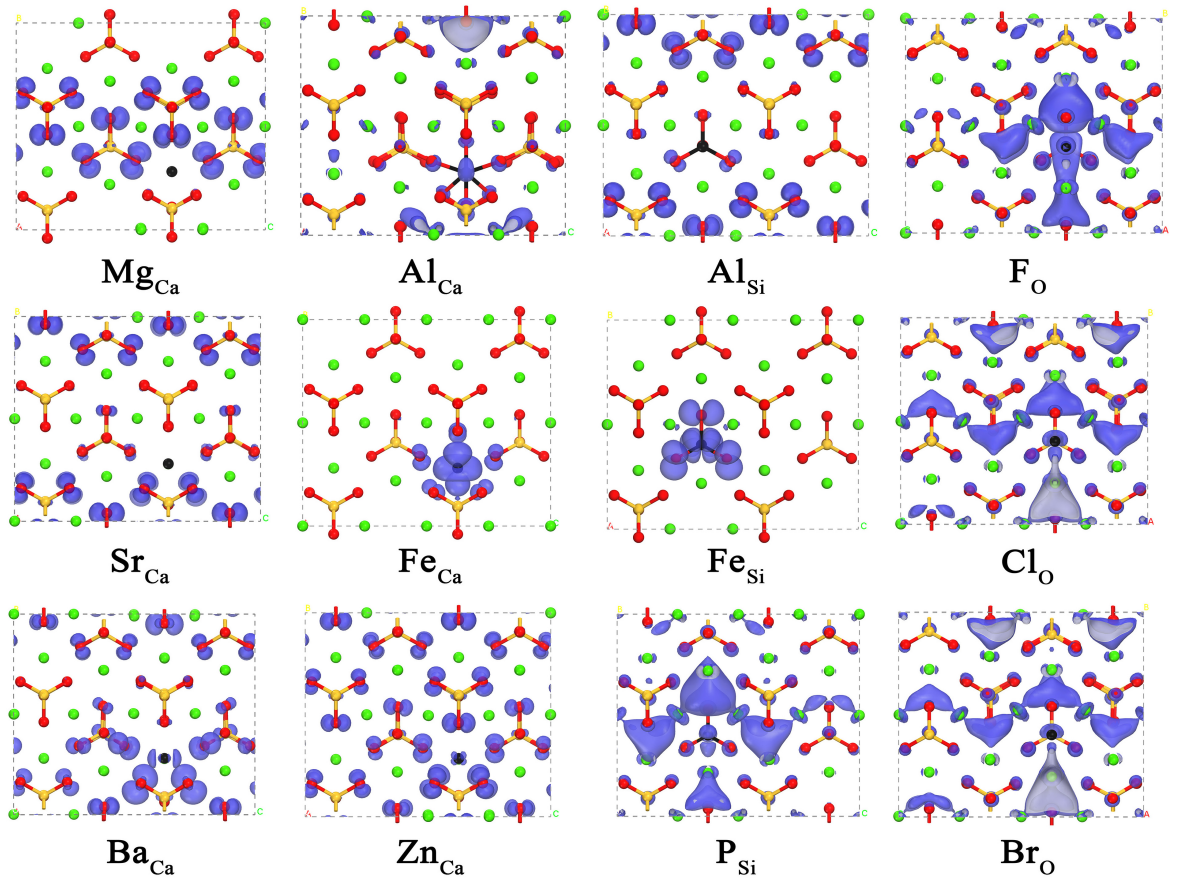

FIGURE 4 | The local charge density distribution of the valence band maximum of doped γ-Ca_2SiO_4 crystals. The green, orange, red, and black spheres are Ca, Si, O, and dopant atoms, respectively.

reactive sites (forming reactive center) is conducive to improving the overall reactivity. However, too strong localization of the reactive sites results in a significant decrease in the number of reactive sites, thereby reducing the overall reactivity. The difficulty lies in how to quantitatively measure the weight of these two aspects.

As discussed in the analysis of pure γ-Ca_2SiO_4, the BO can map the potential reactivity of ions from the perspective of their

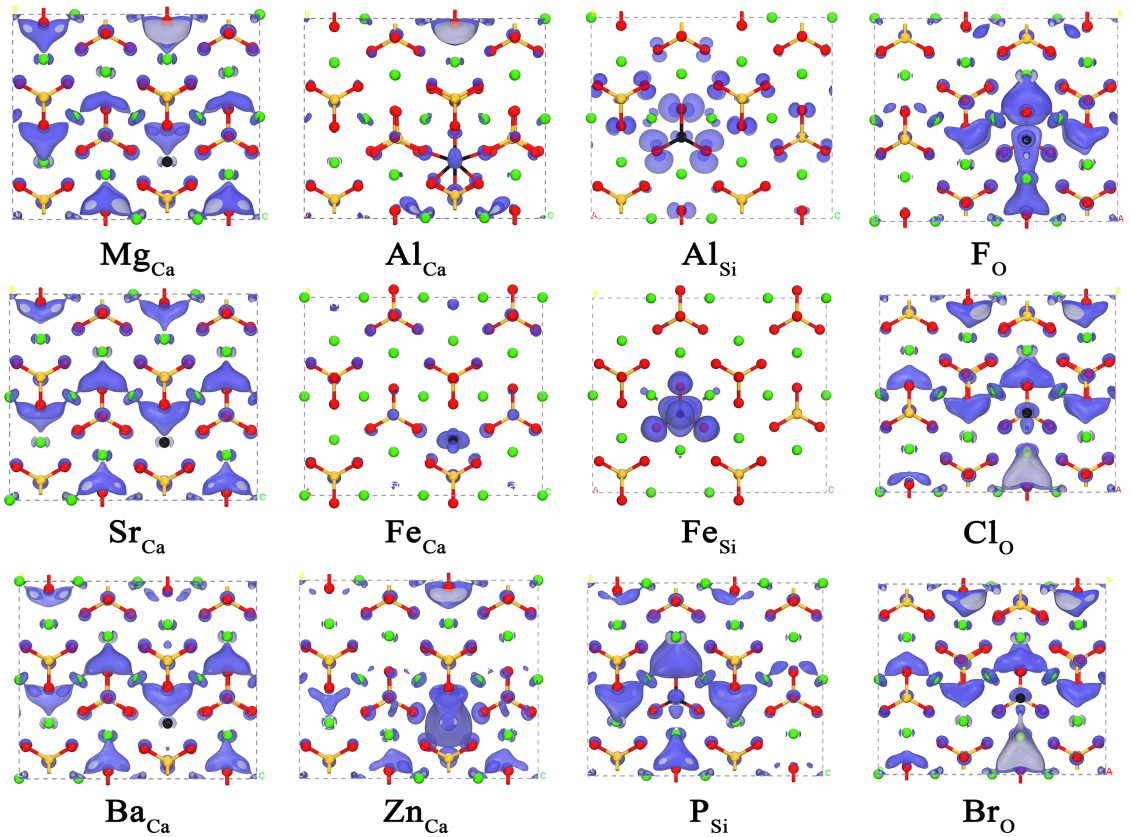

FIGURE 5 | The local charge density distribution of the conduction band minimum of doped γ-Ca_2SiO_4 crystals. The green, orange, red, and black spheres are Ca, Si, O, and dopant atoms, respectively.

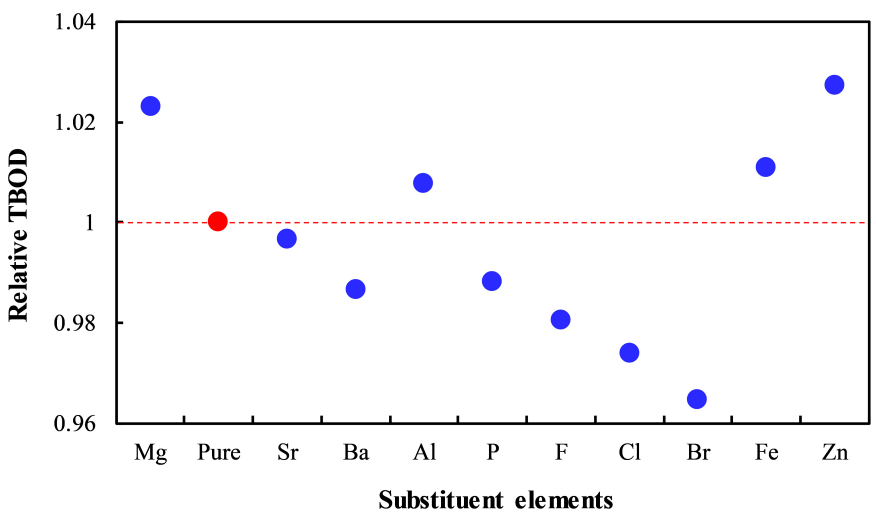

FIGURE 6 | Total bond order density of the doped γ-Ca_2SiO_4 crystals relative to the pure γ-Ca_2SiO_4.

binding strength in the system, which is an easy method to quantify. Therefore, we calculated the BO of Si–O and Ca–O bonds for different doping models and used the changes in the total bond order density (TBOD) to evaluate the doping effect (Dharmawardhana et al., 2016):

$$TBOD = \sum_{i}^{N} B(i)/V$$

where N is the number of bonds in the model and B(i) is the bond order of the i^{th} bond. V is the crystal volume. **Figure 6** shows the changes in the TBOD for different doped systems compared to the pure γ-Ca_2SiO_4. The TBOD of pure γ-Ca_2SiO_4 as a reference (set to unity) is marked in red in the figure. The tabulated data of the TBOD can be found in **Supplementary Material S2**. It should be noted that for the Al and Fe doping, the TBOD is an average of the two substitution schemes, that is, an arithmetic average of the TBOD of Ca site and Si site substitutions. The TBOD comprehensively considers the doping effect on Si–O and Ca–O bonds and the crystal volume. The smaller the TBOD, the weaker the overall binding strength of the system, and the more likely the crystal is to decompose by ion attacks, implying the potentially high carbonation reactivity. In this regard, it can be observed that some ion doping (Ba, P, F, Cl, Br) is conducive to improving the reactivity of γ-Ca_2SiO_4, whereas some ions (Mg, Al, Fe, Zn) induce the opposite effect, and the rest (Sr) causes negligible influence. The theoretical reasoning is tested by experiments discussed in the following section.

Experimental Verification

In order to verify the theoretical prediction of the doping effect based on the TBOD analysis, we experimentally tested the carbonation reactivity of different ion-doped systems. Due to the limitation of experimental conditions, here we only conducted tests for some representative ions: Mg, Al, Ba, P, and F. **Figure 7** compares the carbonation degree of γ-Ca_2SiO_4 with five different ion-doping schemes. Comparing **Figure 7** with **Figure 6**, our theoretical predictions are generally consistent with the experimental results. The theoretically predicted reactivity promoting ions Ba, P, and F indeed accelerated the γ-Ca_2SiO_4 carbonation, and the predicted reactivity inhibiting ions Mg and Al retarded the carbonation reaction. Moreover, Mu et al. (2018) studied in detail the Ba doping effect on the carbonation reactivity of γ-Ca_2SiO_4. They found that Ba doping significantly increased the carbonation degree of γ-Ca_2SiO_4. Although Mu and colleagues speculated from the macroscopic point of view that Ba doping modifies the surface structure, which improves carbon dioxide penetration, our calculations provide a different perspective from the electronic structure modification: Ba doping reduces the overall binding strength of γ-Ca_2SiO_4 crystal, making ions easier to dissolve and participate in the carbonation reaction. Therefore, based on our and previous experimental verifications, the theoretical method we proposed is effective to give qualitatively reliable results, which expedites exploring the activation methods of γ-Ca_2SiO_4 carbonation.

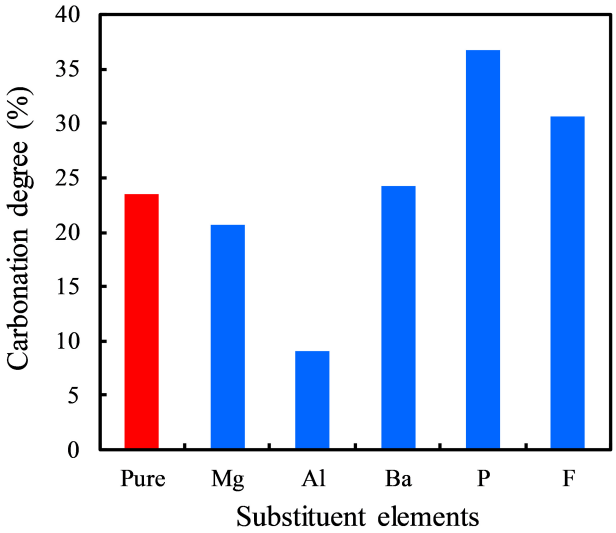

FIGURE 7 | Carbonation degree of γ-Ca_2SiO_4 specimens in 3 days under normal pressure with different doping schemes.

CONCLUSION

In this paper, the potential relationship between the carbonation reactivity of γ-Ca_2SiO_4 and its electronic structures is investigated by the first-principles calculations. By monitoring the changes in the electronic structures of γ-Ca_2SiO_4 by different doping schemes, the candidates for reactivity promotion are screened out and validated by experiments. If the carbonation reaction of γ-Ca_2SiO_4 is regarded as a typical ion attack reaction, the electrophilic reactive sites of γ-Ca_2SiO_4 are the O ions while the nucleophilic reactive sites are the Ca-blocked regions. Anionic doping strikingly changes the electrophilic reactive sites, whereas the ionic substitutions that happened within the same main group scarcely modify the reactive site distribution. Doping also changes the binding strength of ions in γ-Ca_2SiO_4 crystals, which affects the dissolution rate of ions in the carbonation reactions. For this reason, the total bond order density was proposed as an indicator to estimate the changes in binding strength to further predict the effect of different ion doping on the γ-Ca_2SiO_4 carbonation reactivity. This theoretical study provides novel perspectives of the carbonation reactivity of γ-Ca_2SiO_4 and accelerates the experimental modification of γ-Ca_2SiO_4.

DATA AVAILABILITY STATEMENT

All datasets generated for this study are included in the article/**Supplementary Material**.

AUTHOR CONTRIBUTIONS

YT designed and performed the research and wrote the manuscript. YM performed the experimental part of the research.

WZ and FW discussed and analyzed the data. All authors contributed to the article and approved the submitted version.

FUNDING

This research was supported by the National Key R&D Program of China (grant number 2016YFB0303501); National Natural Science Foundation of China (grant number 51872216); and China Scholarship Council (201906950033).

SUPPLEMENTARY MATERIAL

The Supplementary Material for this article can be found online at: https://www.frontiersin.org/articles/10.3389/fmats.2020.00299/full#supplementary-material

REFERENCES

Ashraf, W. (2016). Carbonation of cement-based materials: challenges and opportunities. *Constr. Build. Mater.* 120, 558–570. doi: 10.1016/j.conbuildmat.2016.05.080

Blöchl, P. E. (1994). Projector augmented-wave method. *Phys. Rev. B* 50, 17953–17979. doi: 10.1103/physrevb.50.17953

Chang, J., Fang, Y., and Shang, X. (2016). The role of β-C2S and γ-C2S in carbon capture and strength development. *Mater. Struct.* 49, 4417–4424. doi: 10.1617/s11527-016-0797-5

Chattaraj, P. K. (2009). *Chemical Reactivity Theory: A Density Functional View*, 1st Edn. Boca Raton: CRC Press.

Clark, S. J., Segall, M. D., Pickard, C. J., Hasnip, P. J., Probert, M. I. J., Refson, K., et al. (2005). First principles methods using CASTEP. *Z. Krist.* 220, 567–570.

De Leeuw, N., Parker, S., Catlow, C., and Price, G. (2000). Modelling the effect of water on the surface structure and stability of forsterite. *Phys. Chem. Miner.* 27, 332–341. doi: 10.1007/s002690050262

Dharmawardhana, C., Bakare, M., Misra, A., and Ching, W.-Y. (2016). Nature of interatomic bonding in controlling the mechanical properties of calcium silicate hydrates. *J. Am. Ceram Soc.* 99, 2120–2130. doi: 10.1111/jace.14214

Dharmawardhana, C. C., Misra, A., Aryal, S., Rulis, P., and Ching, W. Y. (2013). Role of interatomic bonding in the mechanical anisotropy and interlayer cohesion of CSH crystals. *Cem. Concr. Res.* 52, 123–130. doi: 10.1016/j.cemconres.2013.05.009

Durgun, E., Manzano, H., Pellenq, R. J. M., and Grossman, J. C. (2012). Understanding and controlling the reactivity of the calcium silicate phases from first principles. *Chem. Mater.* 24, 1262–1267. doi: 10.1021/cm203127m

Kerisit, S., Bylaska, E. J., and Felmy, A. R. (2013). Water and carbon dioxide adsorption at olivine surfaces. *Chem. Geol.* 59, 81–89. doi: 10.1016/j.chemgeo.2013.10.004

Kresse, G. (1999). From ultrasoft pseudopotentials to the projector augmented-wave method. *Phys. Rev. B* 59, 1758–1775. doi: 10.1103/physrevb.59.1758

Kresse, G., and Furthmüller, J. (1996). Efficiency of ab-initio total energy calculations for metals and semiconductors using a plane-wave basis set. *Comput. Mater. Sci.* 6, 15–50. doi: 10.1016/0927-0256(96)00008-0

Liu, Z., Guan, D., Wei, W., Davis, S. J., Ciais, P., Bai, J., et al. (2015). Reduced carbon emission estimates from fossil fuel combustion and cement production in China. *Nature* 524, 335–338. doi: 10.1038/nature14677

Ludwig, H.-M., and Zhang, W. (2015). Research review of cement clinker chemistry. *Cem. Concr. Res.* 8, 24–37. doi: 10.1016/j.cemconres.2015.05.018

Manzano, H., Dolado, J. S., and Ayuela, A. (2009). Structural, mechanical, and reactivity properties of tricalcium aluminate using first-principles calculations. *J. Am. Ceram Soc.* 92, 897–902. doi: 10.1111/j.1551-2916.2009.02963.x

Manzano, H., Durgun, E., Abdolhosseine Qomi, M. J., Ulm, F.-J., Pellenq, R. J. M., and Grossman, J. C. (2011). Impact of chemical impurities on the crystalline cement clinker phases determined by atomistic simulations. *Cryst. Growth Des.* 11, 2964–2972. doi: 10.1021/cg200212c

Morrow, C. P., Kubicki, J. D., Mueller, K. T., and Cole, D. R. (2009). Description of Mg2+ release from forsterite using Ab initio Methods†. *J. Phys. Chem. C* 114, 5417–5428. doi: 10.1021/jp9057719

Mu, Y., Liu, Z., and Wang, F. (2019). Comparative study on the carbonation-activated calcium silicates as sustainable binders: reactivity, mechanical performance, and microstructure. *ACS Sust. Chem. Eng.* 7, 7058–7070. doi: 10.1021/acssuschemeng.8b06841

Mu, Y., Liu, Z., Wang, F., and Huang, X. (2018). Effect of barium doping on carbonation behavior of γ-C2S. *J. CO2 Utiliz.* 27, 405–413. doi: 10.1016/j.jcou.2018.08.018

Mulliken, R. S. (1955). Electronic population analysis on LCAO–MO molecular wave functions. I. *J. Chem. Phys.* 23, 1833–1840. doi: 10.1063/1.1740588

Naa, S., Kangb, S., Leeb, S., and Songa, M. (2015). Gamma-C2S synthesis from Fly ash of fluidize-bed boiler for CO2 capture. *Acta Phys. Polon. A* 127, 1282–1285. doi: 10.12693/aphyspola.127.1282

Olajire, A. A. (2013). A review of mineral carbonation technology in sequestration of CO2. *J. Petrol. Sci. Eng.* 109, 364–392. doi: 10.1016/j.petrol.2013.03.013

Olsson, J., Bovet, N., Makovicky, E., Bechgaard, K., Balogh, Z., and Stipp, S. L. S. (2012). Olivine reactivity with CO2 and H2O on a microscale: Implications for carbon sequestration. *Geochim. Cosmochim. Acta* 77, 86–97. doi: 10.1016/j.gca.2011.11.001

Parr, R. G., and Yang, W. (1984). Density functional approach to the frontier-electron theory of chemical reactivity. *J. Am. Chem. Soc.* 106, 4049–4050. doi: 10.1021/ja00326a036

Perdew, J. P., Burke, K., and Ernzerhof, M. (1994). Generalized gradient approximation made simple. *Phys. Rev. Lett.* 77, 3865–3868. doi: 10.1103/physrevlett.77.3865

Scrivener, K. L., Juilland, P., and Monteiro, P. J. M. (2015). Advances in understanding hydration of portland cement. *Cem. Concr. Res.* 78, 38–56. doi: 10.1016/j.cemconres.2015.05.025

Tao, Y., Li, N., Zhang, W., Wang, F., and Hu, S. (2019a). Understanding the zinc incorporation into silicate clinker during waste co-disposal of cement kiln: a density functional theory study. *J. Cleaner Prod.* 232, 329–336. doi: 10.1016/j.jclepro.2019.05.078

Tao, Y., Zhang, W., Li, N., Wang, F., and Hu, S. (2019b). Predicting hydration reactivity of Cu-doped clinker crystals by capturing electronic structure modification. *ACS Sust. Chem. Eng.* 7, 6412–6421. doi: 10.1021/acssuschemeng.9b00327

Tao, Y., Zhang, W., Li, N., Shang, D., Xia, Z., and Wang, F. (2018a). Fundamental principles that govern the copper doping behavior in complex clinker system. *J. Am. Ceram Soc.* 101, 2527–2536. doi: 10.1111/jace.15393

Tao, Y., Zhang, W., Shang, D., Xia, Z., Li, N., Ching, W.-Y., et al. (2018b). Comprehending the occupying preference of manganese substitution in crystalline cement clinker phases: a theoretical study. *Cem. Concr. Res.* 109, 19–29. doi: 10.1016/j.cemconres.2018.04.003

Todd Schaef, H., McGrail, B. P., Loring, J. L., Bowden, M. E., Arey, B. W., and Rosso, K. M. (2012). Forsterite [Mg2SiO4)] carbonation in wet supercritical CO2: an in situ high-pressure X-ray diffraction study. *Environ. Sci. Technol.* 47, 174–181. doi: 10.1021/es301126f

Udagawa, S., Urabe, K., Natsume, M., and Yano, T. (1980). Refinement of the crystal structure of γ-Ca2SiO4. *Cem. Concr. Res.* 10, 139–144. doi: 10.1016/0008-8846(80)90070-8

Wang, Q., Manzano, H., Guo, Y., Lopez-Arbeloa, I., and Shen, X. (2015). Hydration mechanism of reactive and passive dicalcium silicate polymorphs from molecular simulations. *J. Phys. Chem. C* 119, 19869–19875. doi: 10.1021/acs.jpcc.5b05257

Watson, G., Oliver, P., and Parker, S. (1997). Computer simulation of the structure and stability of forsterite surfaces. *Phys. Chem. Miner.* 25, 70–78. doi: 10.1007/s002690050088

Conflict of Interest: The authors declare that the research was conducted in the absence of any commercial or financial relationships that could be construed as a potential conflict of interest.

Copyright © 2020 Tao, Mu, Zhang and Wang. This is an open-access article distributed under the terms of the Creative Commons Attribution License (CC BY). The use, distribution or reproduction in other forums is permitted, provided the original author(s) and the copyright owner(s) are credited and that the original publication in this journal is cited, in accordance with accepted academic practice. No use, distribution or reproduction is permitted which does not comply with these terms.

frontiers in Materials

ORIGINAL RESEARCH
published: 17 September 2020
doi: 10.3389/fmats.2020.536517

Coupled Transport of Sulfate and Chloride Ions With Adsorption Effect: A Numerical Analysis

Jun Xu[1,2], *Rui Mo*[3], *Penggang Wang*[3], *Jiguo Zhou*[4], *Xiaojin Dong*[5] *and Wei She*[1]*

[1] School of Materials Science and Engineering, Southeast University, Nanjing, China, [2] College of Civil Engineering and Architecture, Jiangsu University of Science and Technology, Zhenjiang, China, [3] School of Civil Engineering, Qingdao University of Technology, Qingdao, China, [4] School of Civil Engineering, Baicheng Normal University, Baicheng, China, [5] Taizhou Institute of Science and Technology, Nanjing University of Science and Technology, Taizhou, China

In the marine environment, reinforced concrete will suffer from chloride ion erosion and sulfate ion erosion at the same time. However, most scholars only study the interaction mechanism between chloride ion and sulfate ion, and the consideration of physical adsorption and chemical combination caused by hydration products is not perfect. Based on the law of conservation of mass, this study integrates the relationship between porosity and hydration time, the weakening of chemical binding of sulfate ions to chloride ions into the mathematical model, establishes the coupling transport model of sulfate and chloride, and verifies the rationality of the model by comparing with the measured data. And then, the physical adsorption and chemical binding of chloride ions under the action of sulfate ions were quantitatively analyzed. It is found that chemical binding is dominant and sulfate ion will reduce the chemical binding effect of chloride ion. With the decrease of the initial water/cement ratio, the diffusion depth of free chloride ion will also decrease.

Keywords: chemical binding, physical adsorption, coupled transport, free chloride ion, mathematical model

OPEN ACCESS

Edited by:
Hongyan Ma,
Missouri University of Science and Technology, United States

Reviewed by:
Guo Wen Sun,
Shijiazhuang Tiedao University, China
Zhiyong Liu,
Southeast University, China
Guoqing Geng,
National University of Singapore, Singapore

***Correspondence:**
Wei She
weishe@seu.edu.cn

Specialty section:
This article was submitted to Computational Materials Science, a section of the journal Frontiers in Materials

Received: *20 February 2020*
Accepted: *13 August 2020*
Published: *17 September 2020*

Citation:
Xu J, Mo R, Wang P, Zhou J, Dong X and She W (2020) Coupled Transport of Sulfate and Chloride Ions With Adsorption Effect: A Numerical Analysis. Front. Mater. 7:536517. doi: 10.3389/fmats.2020.536517

INTRODUCTION

The concrete structure is widely used admittedly in Ocean Engineering, for example, subsea tunnel engineering which tests the durability extremely. Concrete is buried under the seafloor for a long time to withstand the erosion of sea salt, which will not only cause damage to the concrete structure but also affect the normal service life of the building (Banthia et al., 2005; Choinska et al., 2007; Ghazy and Bassuoni, 2017; Montoya and Nagel, 2020; Wang et al., 2020a; Xu et al., 2020; Zhou et al., 2020). In the marine environment, the porous nature of concrete determines that it will inevitably be eroded by sea salt. This kind of erosion can be divided into two types, one is the diffusion of ions, the other is the combination of ions (Song et al., 2008; Medeiros et al., 2009). As we all know, there are many reasons for the damage of reinforced concrete structure, such as corrosion and expansion of reinforcement, resulting in concrete cracking and damage (Sofia and Alexandre, 2018; Wang et al., 2020b), loss of setting the strength of the concrete itself (Neville, 2004), mechanical wear of concrete structure surface (Fiorio, 2005), etc. In the marine environment, corrosion of reinforcement is mainly caused by the diffusion of chloride ions, while the loss of concrete strength is mainly caused by the chemical reaction of sulfate ions.

At present, many scholars have discussed the combination of chloride ions in concrete. Dhir et al. (1996) reported the results of the determination of the chloride binding capacity of Ground Granulated Blast-furnace Slag (GGBS) slurry. It was found that the higher the concentration of aluminate, the stronger the chloride binding capacity. Zhu et al. (2012) through exploring the influence of different types of chloride salts on the binding capacity of chloride ions in concrete, found that the binding capacity of chloride ions corresponding to calcium chloride is the strongest, while that of sodium chloride and potassium chloride is the weakest. Arya and Xu (1995) studied the influence of different types of cement on the chloride binding capacity. The chloride binding capacity was successively enhanced, and the order was GGBS, Pulverized Fuel Ash (PFA), and Ordinary Portland Cement (OPC). It is observed that although GGBS has the strongest chloride binding capacity, OPC concrete has the strongest corrosion resistance. Tang and Nilsson (1993) studied the sorption of chloride ions on OPC concrete under different water/cement ratio and aggregate content. The results showed that the sorption capacity of chlorine ion was closely related to the content of CSH gel, but had nothing to do with water/cement ratio and aggregate content. Geiker et al. (2007) studied the prediction and analysis of chloride binding capacity in OPC concrete by different salt types. The results showed that the ratio of chloride binding capacity to free chloride content in pore solution was the largest when AFm content was high. Jensen et al. (1999) tested the influence of different components of cement paste and mortar, as well as the different exposure conditions on the self-entry of chloride into the concrete. It was found that the combination of chloride ions changed the shape of the entrance profile of the model. Martin-Pérez et al. (2000) discussed the influence of three kinds of bind isothermal curves on the chloride ion permeability profile with a finite difference method and evaluated the service life of reinforced concrete in this way. Yoon et al. (2014) proposed the use of calcined layered double hydroxides to prevent chloride induction, which greatly improved the durability of reinforced concrete, not only adsorbed the memory effect in aqueous solution but also had a higher binding capacity than the original layered double hydroxides in cement-based materials. The effect of fly ash and slag on the binding capacity of chloride ion in the sulfate environment (Castellote et al., 1999; Xu et al., 2013; Geng et al., 2015). The results show that the addition of fly ash and slag increases the release of chloride ions.

Through the reading of the above literature, it is found that most of the researchers only study and discuss the diffusion law of combined chloride ion and free chloride ion under the action of a single factor. However, it is still shallow to discuss and study the combined chloride ion under the action of multi-factor and multi mechanism, which is divided into physically adsorbed chloride ion and chemically combined chloride ion. In this study, a multi-factor coupled chloride diffusion model is proposed. It will take into account the reduction of chloride binding to chloride ions, the adsorption, and chemical action of hydrated calcium silicate gel, and the quantitative analysis of free chlorine ions, physisorption chlorine ions, and chemically bound chloride ions through the PDE module of the finite element analysis software COMSOL. In this model, the diffusion coefficient of free chloride ion in a porous solution is established by considering the interaction between ions. Besides, it is assumed that there is no calcium corrosion under the coupling effect of sulfate and chloride, that is, the adsorbed free chloride ions do not have biological understanding adsorption. It is worth noting that even though the physically adsorbed chloride ions cannot be moved, they still carry electric charges.

MODELING

The time-depth relationship model of porous Fick law is adopted for chloride diffusion in concrete (Valdes-Parada et al., 2007):

$$\varepsilon_{tot}\frac{\partial C_{cl}}{\partial t} + div\boldsymbol{J}_{cl} = 0 \tag{1}$$

where ε_{tot} is the total porosity of concrete (m^3/m^3); C_{cl} is the total chloride ion concentration (%); t is the erosion time (s); $\boldsymbol{J}_{cl}$ is the material flux of the corresponding component (m/s).

Hirao et al. (2005) have studied that the cement hydration products in concrete have the binding ability to chloride ions, which are mainly calcium silicate hydrate (CSH) and calcium monosulfate hydrate (AFm). Among them, CSH is mainly physical adsorption, while AFm is mainly chemical binding (Florea and Brouwers, 2012). In this model, Equation (2-a) transformation is still carried out according to the law of conservation of mass. The difference is that only the chemical binding term of chloride ions is modeled as a sink term. The reason is that as long as there is calcium aluminate, the chemisorption of chloride ions in the combination will react with it. In the final analysis, it is only related to the concentration of reactants. Therefore, when considering the chloride ion transport of chemisorption, we use the form of sink term to model separately, see Equation (2-b). Add the part of chloride ions physically adsorbed to the first item of Equation (1). Component C_{cl} is divided into two parts, one is free chloride ion concentration, the other is physical adsorption chloride ion concentration.

$$\varepsilon_{tot}\frac{\partial(C_{pa}+C_f)}{\partial t} + div\boldsymbol{J}_{cl} + Q(C_{cb}) = 0 \tag{2-a}$$

$$Q(C_{cb}) = \frac{\partial C_{cb}}{\partial t} \tag{2-b}$$

$$C_{cb} = f(C_f) \tag{2-c}$$

$$C_{cb} = \beta C_f^{\alpha} \tag{2-d}$$

$$C_T = C_{pa} + C_{cb} + C_f \tag{2-e}$$

where C_{cb} is the concentration of chemically bound chloride ions (%); C_{pa} is the concentration of chloride ions adsorbed in the double layer region (Chatterji and Kawamura, 1992), that is, the concentration of physically adsorbed chloride ion (%); C_f is the concentration of free chloride ion in pore solution (%); $Q(C_{cb})$ is the sink term which is a function of chemically bound chloride ions (1/s); C_T is the concentration sum of free chloride ion, chemically bound chloride ion, and physically adsorbed chloride ion at the depth z from the erosion surface (%).

Hirao et al. (2005) through the study of the adsorption and combination of chloride ions by cement hydration products, found that ettringite, and calcium hydroxide does not have the ability of physical adsorption of chloride ions. However, through the comparison between the final model and the measured data, it is found that there may be a weak chemical combination. It can be seen from Carrara et al. (2016) that the concentration of chemically bound chloride ion is a function of the concentration of free chloride ion, using Carrara et al. (2016) research model ($\beta = 0.4366$, $\alpha = 0.58$), see Equation (2-d). According to Ishida and Maekawa (1999), the total porosity of chloride in concrete is divided into two categories, one is gel porosity and the other is capillary porosity, see Equation (3-a). Considering that the porosity of concrete is related to the degree of hydration of cement, Masi et al. (1997) established a functional relationship between the degree of hydration α and the time of hydration t by studying the hydration process from calcium aluminate to the hydration product. See Equation (3-b) for the specific expression.

$$\varepsilon_{tot} = \varepsilon_{gl} + \varepsilon_{cp} \tag{3-a}$$

$$\alpha = 1 - 0.5\left[(1 + 1.67\tau)^{-0.6} + (1 + 0.29\tau)^{-0.48}\right] \tag{3-b}$$

where ε_{gl} is the gel porosity (m^3/m^3); ε_{cp} is the capillary porosity (m^3/m^3); α is the degree of hydration of cementitious materials; τ is the time consumed in the hydration process(day).

Hansen (1986) has derived the formula for calculating the porosity and capillary porosity of the gel through the formula derived from the experimental data of (Powers and Brownyards, 1948).

$$\varepsilon_{gl} = \frac{(\frac{w_0}{c}) - 0.36\alpha}{(\frac{w_0}{c}) + 0.32} \tag{4-a}$$

$$\varepsilon_{cp} = \frac{0.19\alpha}{(\frac{w_0}{c}) + 0.32} \tag{4-b}$$

where $\frac{w_0}{c}$ is the initial water/cement ratio in the form of mass fraction (kg/kg).

The results show that the presence of Jin et al. (2019) sulfate ions will reduce the chemical binding capacity of chloride ions, and Equation (5-a) is used for calculation when the relationship between combined chloride and free chloride is non-linear. Because sulfate ion reacts mainly with calcium hydroxide and aluminate hydrate in concrete (Sun et al., 2013), it has little effect on the physical adsorption of chloride ion. In this study, the chemical binding weakening model of chloride ions under the influence of sulfate ions established by Jin et al. (2019) is used, see Equation (5-d). The specific derivation process is as follows.

$$R_0 = \frac{\partial C_b}{\partial C_f} \tag{5-a}$$

$$C_b = C_{cb} + C_{pa} \tag{5-b}$$

$$C_{pa} = \frac{\mathrm{K}C_f}{1 + \mathrm{N}C_f} \tag{5-c}$$

$$R = \frac{\partial C_b}{\partial C_f}(a + bC^c_{SO_4^{2-}}) \tag{5-d}$$

$$C_{cb,SO_4^{2-}} = RC_f - C_{pa} \tag{5-e}$$

$$Q\left(C_{cb,SO_4^{2-}}\right) = \frac{\partial C_{cb,SO_4^{2-}}}{\partial t} \tag{5-f}$$

where R_0 is the ability of chloride binding without the influence of sulfate ion; C_b is the total bound chloride concentration at depth z (%); and are fitting parameters (Carrara et al., 2016) ($K = 0.1228$, $N = 0.0747$); R is the chloride binding capacity under the influence of sulfate ion; $C_{cb,SO_4^{2-}}$ is the chemical binding content of chloride ion under the action of sulfate ion; $Q\left(C_{cb,SO_4^{2-}}\right)$ is the sink term produced by the action of sulfate ion (1/s); a, b, and c are fitting parameters (Jin et al., 2019), respectively ($a = 1$, $b = -0.011$, $c = 1.31$); $C_{SO_4^{2-}}$ is the free sulfate ion concentration (%).

In saturated concrete, ions are mainly transmitted to the medium in the form of diffusion. However, not all ions are presented in dynamic form. Static ions can be divided into two categories: one is physically adsorbed ions, the other is chemically combined ions. As mentioned above, although the physically adsorbed ions in static ions still carry charges, they cannot move. As we all know, only the free ions can conduct electricity. In this model, Einstein's law is used to establish the diffusion coefficient of free chloride ion in pore solution, see Equation (6).

$$D_f = R_g T \frac{\Lambda_{cl^-}}{z^2_{cl^-} F^2} \tag{6}$$

where D_f is the diffusion coefficient of chloride ion in the pore solution (m^2/s); R_g is the universal gas constant (J/K·mol); T is the ambient temperature (K); Λ_{cl^-} is the molar conductivity of free chloride ion in porous solution (Sm^2/mol); z_{cl^-} is the chloride ion valence ($= -1$); F is the Faraday constant (c/mol).

As we all know, the conductivity of mobile ion in solution is closely related to its concentration. In 1929 Onsager deduced the theoretical model of conductivity and concentration through the concept of the ion-atmosphere. However, this model is only applicable to dilute solution with ion concentration C $\leq$ 0.005 mol/l, not to the solution with higher concentration. Chandra and Bagchi (1989) modified the Onsager model and proposed an ion conductivity that can calculate the ion concentration up to 2,000 mmol/L, see Equation (7).

$$\Lambda_{cl^-} = \Lambda^{\infty}_{cl^-} - \left(Gz^2_{cl^-} + Hz^3_{cl^-} w_{cl^-} \Lambda^{\infty}_{cl^-}\right)\sqrt{C_f} \tag{7}$$

TABLE 1 | Parameter value in calculation formula of conductivity and free chloride ion diffusion coefficient.

R_g (J/K•mol)	T (K)	ε_0 (c^2/J • m)	ε_r	e (c)	F (c/mol)	η
8.31451	298	8.85×10^{-12}	78.54	1.602×10^{-19}	9.64853×10^{4}	0.000891

TABLE 2 | Parameter value of ions in pore solution (Chatterji and Kawamura, 1992).

Ionic species	Valence	Conductivity	Ionic radius
Cl^-	−1	7.635×10^{-3}	1.81×10^{-10}
SO_4^{2-}	−2	8.000×10^{-3}	2.58×10^{-10}
Ca^{2+}	+2	5.950×10^{-3}	0.99×10^{-10}
Na^+	+1	5.010×10^{-3}	0.95×10^{-10}
OH^-	−1	1.992×10^{-2}	1.33×10^{-10}

where $\Lambda_{cl^-}^{\infty}$ is the limit molar conductivity of free chloride ion in infinite dilution solution when the ambient temperature is 25°C, the corresponding $\Lambda_{cl^-}^{\infty}$ is $7.635 \times 10^{-3}[Sm^2/mol]$; G and H are parameters related to temperature, ion type, and medium; w_{cl^-} is the influence coefficient considering ion activity.

Here, G, H, and w_{cl^-} are calculated by Equations (8-a) to (8-c), respectively.

$$G = \frac{\sqrt{2\pi}eF^2}{3\pi\eta\sqrt{1000\varepsilon_0\varepsilon_r RT}} \tag{8-a}$$

$$H = \frac{\sqrt{2\pi}eF^2}{3\sqrt{1000}\,(\varepsilon_0\varepsilon_r RT)^{\frac{3}{2}}} \tag{8-b}$$

$$w_{cl^-} = 2\left[1 - \left(\frac{1}{2}\sum_{i=1}^{n}\frac{\Lambda_{cl^-}^{\infty}}{\Lambda_{cl^-}^{\infty} + \Lambda_i^{\infty}}\right)^{\frac{1}{2}}\right] \tag{8-c}$$

where e is the elementary charge (c); ε_0 is the vacuum dielectric constant (c^2/J·m); ε_r is the relative permittivity of water; Λ_i^{∞} is the limit molar conductivity of all ions in the pore solution (Sm^2/mol); n is the total number of ions; η is the viscosity coefficient of medium water (see **Table 1** for specific parameter values). The conductivity and ionic radius values are given in **Table 2**.

It is not only the interaction between ions but also the tortuosity of aggregate and pore structure that affects the diffusion of free chloride. Therefore, it is necessary to introduce tortuosity to correct the diffusion coefficient in the flux (see Equation 9).

$$\boldsymbol{J}_{cl} = -\frac{(\varepsilon_{cp} + \varepsilon_{gl})D_f}{\Omega}\nabla C_f \tag{9}$$

where Ω is the tortuosity of ion transport in porous media ($\Omega = 192$), the calculation of tortuosity is based on the method used by Ahmad et al. (2005). The tortuosity and porosity are both inherent properties of materials, but the former reflects the complexity of the transport path, which further affects the ion transport. Specifically, the larger the tortuosity is, the more difficult the transport is, and vice versa (see **Figure 1**).

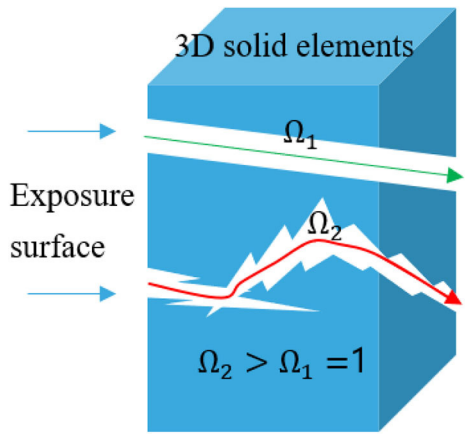

FIGURE 1 | Tortuosity of concrete solid phase.

By substituting Equations (2-a), (2-b), (3-a), and (9) into Equation (1), the following free chloride transport model can be obtained.

$$\left[(\varepsilon_{tot} - 1)\frac{dC_{pa}}{dC_f} + \varepsilon_{tot} + \frac{\partial C_b}{\partial C_f}(a + bC_{SO_4^{2-}}^{c})\right]\frac{\partial C_f}{\partial t} = \nabla\left(\varepsilon_{tot}\frac{D_f}{\Omega}\nabla C_f\right) \tag{10}$$

Equation (10) with the help of the COMSOL finite element analysis software, a one-dimensional solution of the two-dimensional geometric model is carried out for the model. The specific operation details are as follows. First, two-dimensional graphics (such as squares) are created in the geometry module. Here, it is emphasized that the creation of two-dimensional/three-dimensional graphics is only for a better presentation of the solution results. From the perspective of diffusion, Equation (10) is essentially one-dimensional. In this paper, the interface of partial differential equation in the form of a coefficient is selected for the transient solution. See **Figure 2**, 578 domain elements, and 60 boundary elements, that is, the number of triangles or quadrilaterals in 2D geometry. Among them, boundary elements are the number of triangles included in the boundary. For the mathematical model with complex boundary conditions, it needs to be rezoning. In this model, the boundary conditions are set as fixed values, so no modification is needed. It is worth noting that the fitting parameters involved

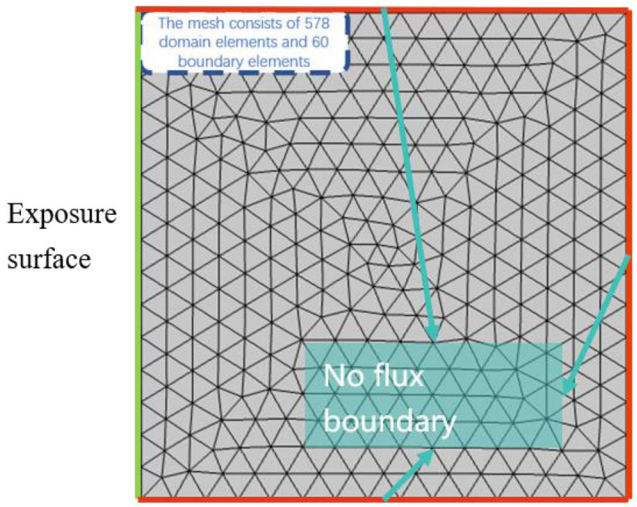

FIGURE 2 | Physical field control grid.

in this paper are all derived from the results of reference concrete (without any mineral admixture). If we want to simulate the concrete with mineral admixture, the retest is needed to determine the parameters.

NUMERICAL VERIFICATION

Based on the test data of Sandberg (1999) by Equation (10), the OPC concrete slab with a length of 100 cm, a width of 70 cm, and a thickness of 10 cm was immersed in seawater for 14 months in the literature. Here, the way of immersion is to use half of the immersion and half of the exposure in the thickness direction. Notice that this model only validates the submerged part of the test block. The specific mix proportion is 390 kg/m^3 dry weight cement, 0.5 water/cement ratio, 0–8 mm grain size sand, its density is 853 kg/m^3, 8–16 mm gravel aggregate, which is 787 kg/m^3. Through the comparison between the model and the measured data and error analysis, it is found that the calculation results are in good agreement with the experimental data. In the model, the surface concentration of free chloride ion is 1.05%, and the initial concentration value is 0. Because the concentration of chloride ion in the marine environment is about 7 times the concentration of sulfate ion, and assuming that the surface ion content of concrete to meet this relationship, the surface concentration of sulfate ion is 0.15%. As shown in **Figure 3**, the curve of free chloride ion concentration in concrete pore solution with 14 months, $\frac{w}{c} = 0.5$ in the immersion area with diffusion depth is depicted. **Figure 4** shows the free chloride concentration (C_f) Test values, calculated values, and relative error values at different depths. Here, the relative error is expressed as a percentage. Through comparison, it is found that the maximum error is not more than 10%. It can be found from **Figure 3** that the chloride concentration gradient decreases with the increase of depth.

Based on Equations (10) and (2-e), the test data of Tumidajski et al. (1995) are verified. In the literature, 50 type cement is

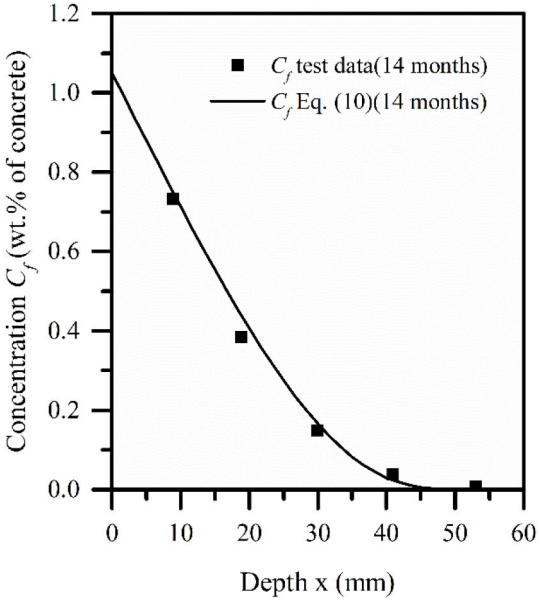

FIGURE 3 | Simulation and test comparison of free chloride ion of concrete slab exposed to marine environment for 14 months.

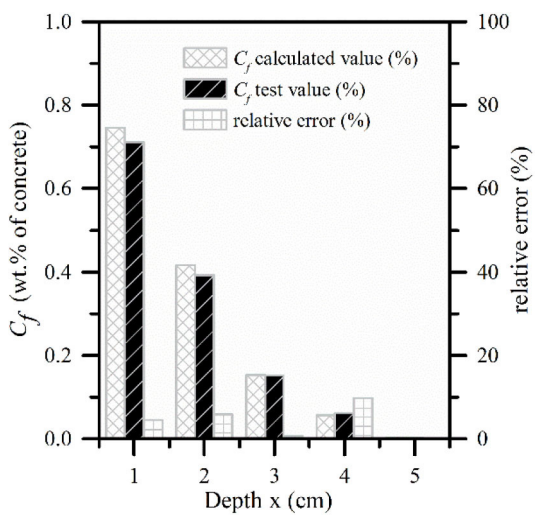

FIGURE 4 | Error analysis of calculation value and test value.

used for mix design, which is 370 kg/m^3, 1,107 kg/m^3 coarse aggregate, 148 kg/m^3 water, and 738 kg/m^3 fine aggregate. The size of a concrete specimen is 75 mm × 75 mm × 300 mm, and it is cured in a 100% humidity environment for 28 days. In this model, the surface concentration of free chloride ion is 1.05%, the initial concentration value is 0, the surface concentration of sulfate ion is 0.05%, the initial concentration value is 0, and see **Figure 6** for concentration distribution of free chloride ions under time and depth. **Figure 5** depicts the concentration distribution curve of concrete beams corroded by chloride ion

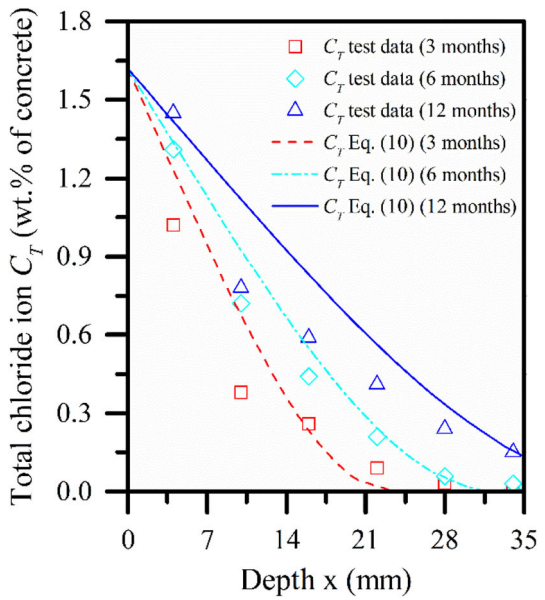

FIGURE 5 | Simulation and test comparison of total chloride ions in concrete beams exposed for 3, 6, and 12 months.

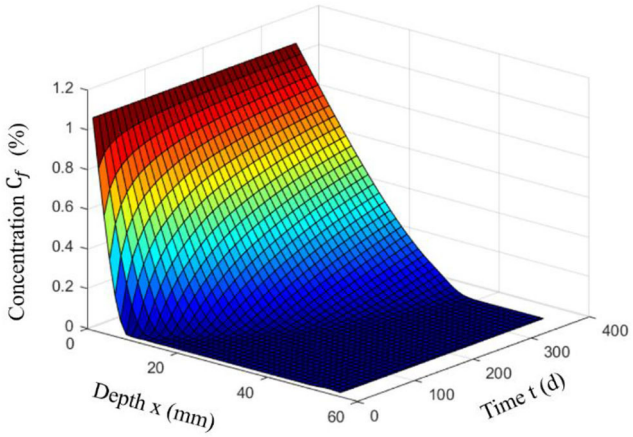

FIGURE 6 | Concentration distribution of free chloride ions under time and depth.

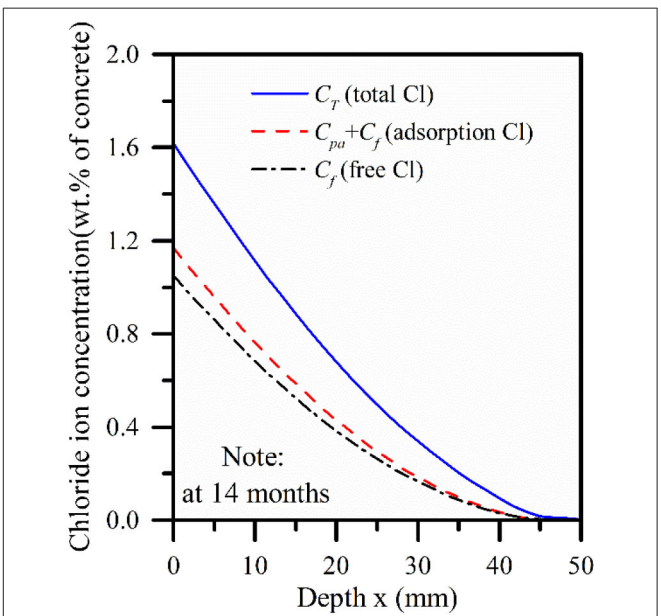

FIGURE 7 | The free chloride ion calculated by the model includes the physical adsorption and the total chloride concentration curve.

and sulfate ion in a multi-component solution for 3, 6, and 12 months in a saturated state. It can be seen from **Figures 5**, **6** that with the increase of time, the internal diffusion depth of concrete is also increasing and the increasing range is decreasing. Through the comparison between the numerical model Equation (2-e) and the measured data, it is found that the error value of the rest points decreases obviously with the increase of the diffusion depth, except for the points close to the erosion surface, which may be caused by the loss of ion concentration during the measurement. The reason why the point close to the erosion surface is more consistent with other points may be due to the measurement time, but on the whole, the calculated value of the model is in good agreement with the measured data. This model can well-reflect the trend of ion concentration.

RESULTS AND DISCUSSION

Effect of Physical Adsorption and Chemical Binding on Chloride Transport

This section discusses the analysis based on Sandberg's test data. Equations (2-d) and (5-c), respectively represent the chloride ion content of chemical binding and physical adsorption at different concentrations of free chloride ion. **Figure 7** shows the change curve of free chloride ion content with depth in 14 months pore solution of the concrete slab in immersion area, the distribution curve of chloride ion concentration in pore solution considering adsorption effect, and the curve of total chloride ion in chemical combination.

It can be found from **Figure 7** that the content of the chemical binding part is more than 5 times that of the physical adsorption part, and the effect is more obvious with the increase of diffusion depth. Therefore, it can be found that chemical binding plays a leading role while physical adsorption and chemical binding are simultaneously applied to the concrete interior. However, physical adsorption and chemical binding did not change the chloride concentration transport trend, and the three showed the same diffusion law. **Figure 8** describes the curve of chloride concentration with time under the action of physical adsorption and chemical combination. It can be found in **Figure 8** that compared with physical adsorption, chemical binding still dominates, and chemical binding takes place faster than physical adsorption.

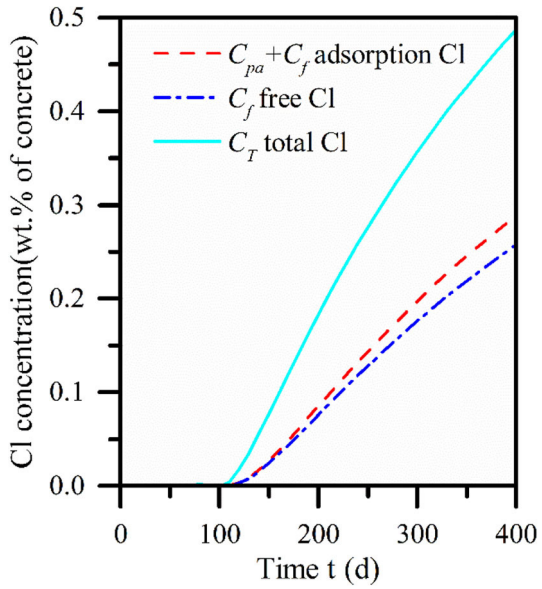

FIGURE 8 | Three forms of concrete interior calculated by model: the free chloride, the chloride of including the physical adsorption and the total chloride.

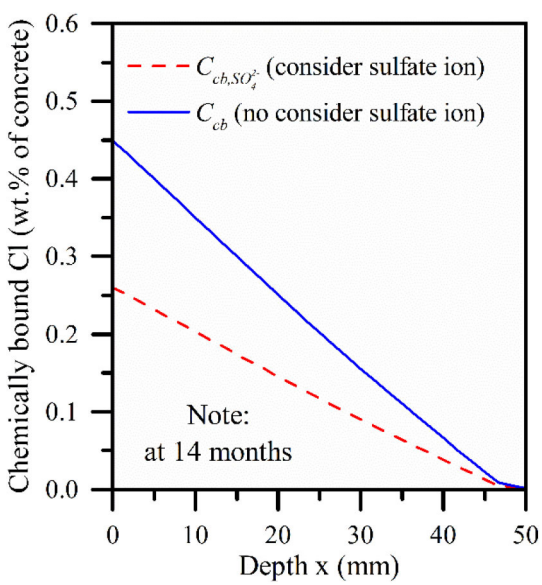

FIGURE 9 | Chemical binding curve of chloride ion: red solid line (sulfate ion is considered), blue solid line (sulfate ion is not considered).

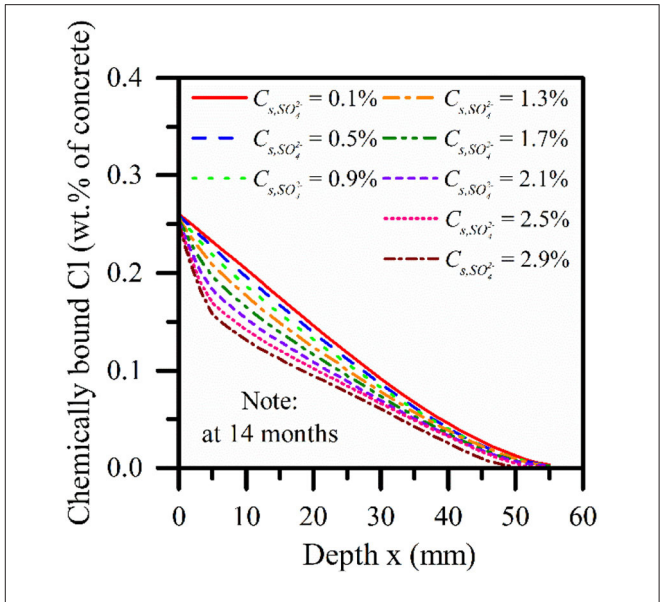

FIGURE 10 | Concentration of chemically bound chloride ions at different sulfate ion concentrations.

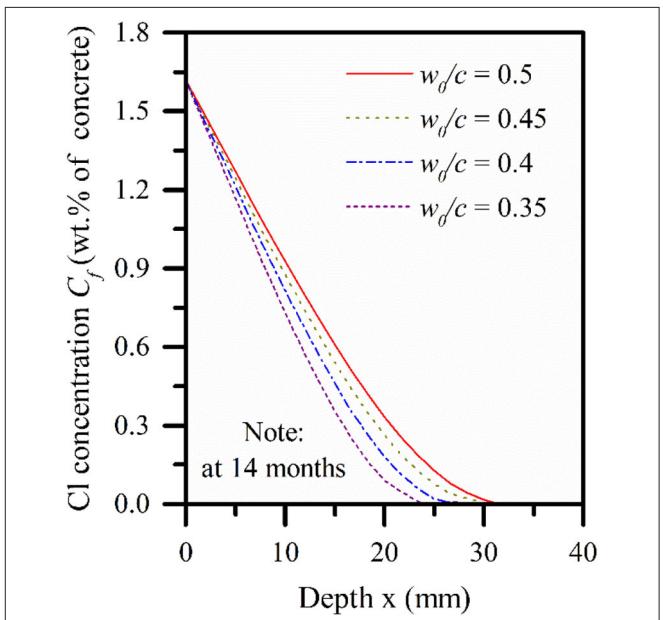

FIGURE 11 | Free chloride concentration under different initial water-cement ratio.

The Effect of Sulfate Ion on the Concentration of Chemically Bound Chloride Ion

Dehwah et al. (2002) studied the effect of cement alkalinity on chloride corrosion in OPC concrete and Sulfate Resistant Portland Cement Concrete (SRPC). It was found that the binding capacity of chloride decreased with the increase of sulfate ion concentration in pore solution. Shaheen and Pradhan (2015), respectively studied the determination of free chloride ion content in the mixed solution with the same chloride ion concentration by 3, 6, and 12% sulfate ion. The results showed that the free chloride ion concentration decreased with the increase of sulfate ion concentration. In this study, the chemical binding model established by Hirao et al. (2005), see Equation (2-d) and based on Paul's experimental data for quantitative analysis.

Figure 9 depicts the change curve of the concentration of chemically bound chloride ions with depth under the action of chemical binding. It can be seen from **Figure 9** that sulfate ions cause a decrease of chemically bound chloride ions, which verifies the correctness of the model. It can also be found that in the depth range of 0–45 mm, there is a linear relationship between the chemically bound chloride ions and the diffusion depth, which decreases with the increase of the erosion depth. **Figure 10** depicts the relationship between the concentration of chemically bound chloride ions and the depth of diffusion under different concentrations of sulfate ions. It can be seen from **Figure 10** that with the increase of sulfate ion concentration, the concentration of chemically bound chloride ion at the same depth decreases continuously, and the decreased amplitude increases with the increase of sulfate ion concentration at the same step length. When the concentration of sulfate ion reaches more than 1.7%, the curve is segmented, and the decrease of the content of chemically bound chloride ion in the range of 0–5 mm is much higher than that in the range of 5–50 mm. This is consistent with the conclusion of Dehwah et al. (2002).

Effect of Initial Water/Cement Ratio on Free Chloride Diffusion

Based on Equation (10), the law of chloride diffusion under different initial water/cement ratio was studied. As above, Paul test data is still used as a reference. **Figure 11** depicts the diffusion curve of free chloride ion in concrete under different water/cement ratios, among which the blue solid line represents the diffusion curve of free chloride ion eroded for 6 months in Paul's literature. It can be seen from **Figure 11** that the diffusion depth of free chloride ion decreases with the decrease of water/cement ratio, which is 31, 30, 27.5, and 23.3 mm in turn. It can be seen that the decreased amplitude has an increasing trend.

Figure 11 shows that the decrease of the water/cement ratio does not change the diffusion rule of free chloride ion. It only reduces the penetration of free chloride ions.

CONCLUSIONS

Through the verification of the mathematical model, it is shown that the model can be used to predict the diffusion process of chloride ions into the concrete. After discussing the coupled transport model of sulfate and chloride, the following conclusions can be obtained:

- The diffusion of chloride in concrete can be reflected more truly by separately modeling of chloride binding and integrating the relationship between porosity and hydration time into the mathematical model.
- It is found that the chemical binding at different depths is more than 5 times the content of physical adsorption chloride ions. However, chemical binding and physical adsorption do not change the diffusion trend of chloride ions.
- The results show that sulfate ion can reduce the chemical binding capacity of chloride ion. With the increase of sulfate ion concentration, the trend is increasingly obvious. When the concentration of sulfate ion is more than 1.7%, the curve of the change of the chemical bound chloride ion with the depth is segmented.
- With the decrease of the initial water/cement ratio, the diffusion depth of free chloride ion decreased. When the initial water/cement ratio increases in the same step ($H = 0.05$), it can be found that the increasing speed of diffusion depth slows down.

DATA AVAILABILITY STATEMENT

All datasets generated for this study are included in the article/supplementary material.

AUTHOR CONTRIBUTIONS

JX: conceptualization, methodology, and writing—review and editing. RM: data curation and writing—original draft. JZ and XD: data curation, visualization, and investigation. PW and WS: suggestions and supervision. All authors contributed to the article and approved the submitted version.

FUNDING

This project was supported by the Natural Science Foundation of the Jiangsu Higher Education Institutions of China (No. 19KJB560004), China Postdoctoral Science Foundation (No. 2019M661693), National Natural Science Foundation of China (Nos. 51578497, U1706222, 51608286, and 51708483), National Key R&D Program of China (No. 2017YFB0309904), Natural Science Foundation of Shandong province (No. 2019GSF110006), and the Source Innovation Program of Qingdao City (No. 17-1-1-13-jch).

REFERENCES

Ahmad, S., Azad, A. K., and Loughlin, K. F. (2005). "A study of permeability and tortuosity of concrete," in *Conference on Our World in Concrete and Structures*, Vol. 45 (Singapore), 23–30.

Arya, C., and Xu, Y. (1995). Effect of cement type on chloride binding and corrosion of steel in concrete. *Cement Concrete Res.* 25, 893–902. doi: 10.1016/0008-8846(95)00080-V

Banthia, N., Biparva, A., and Mindess, S. (2005). Permeability of concrete under stress. *Cement Concrete Res.* 35, 1651–1655. doi: 10.1016/j.cemconres.2004.10.044

Carrara, P., Lorenzis, L. D., and Bentz, D. P. (2016). Chloride diffusivity in hardened cement paste from microscale analyses and accounting for binding effects. *Model. Simul. Mater. Sci. Eng.* 24, 1–26. doi: 10.1088/0965-0393/24/6/065009

Castellote, M., Andrade, C., and Alonso, C. (1999). Chloride-binding isotherms in concrete submitted to non-steady-state migration experiments. *Cement Concrete Res.* 29, 1799–1806. doi: 10.1016/S0008-8846(99)00173-8

Chandra, A., and Bagchi, B. (1989). Breakdown of onsager's conjecture on distance dependent polarization relaxation in solvation dynamics. *J. Chem. Phys.* 91, 2594–2598. doi: 10.1063/1.457020

Chatterji, S., and Kawamura, M. (1992). Electrical double layer, ion transport and reactions in hardened cement paste. *Cement Concrete Res*. 22, 774–782. doi: 10.1016/0008-8846(92)90101-Z

Choinska, M., Khelidj, A., Chatzigeorgiou, G., and Pijaudier-Cabot, G. (2007). Effects and interactions of temperature and stress-level related damage on permeability of concrete. *Cement Concrete Res*. 37, 79–88. doi: 10.1016/j.cemconres.2006.09.015

Dehwah, H., Austin, S., and Maslehuddin, M. (2002). Effect of cement alkalinity on pore solution chemistry and chloride-induced reinforcement corrosion. *ACI Mater. J*. 99, 227–233. doi: 10.14359/11967

Dhir, R. K., El-Mohr, M. A. K., and Dyer, T. D. (1996). Chloride binding in GGBS concrete. *Cement Concrete Res*. 26, 1767–1773. doi: 10.1016/S0008-8846(96)00180-9

Fiorio, B. (2005). Wear characterisation and degradation mechanisms of a concrete surface under ice friction. *Construct. Build. Mater*. 19, 366–375. doi: 10.1016/j.conbuildmat.2004.07.020

Florea, M., and Brouwers, H. (2012). Chloride binding related to hydration products part?: ordinary portland cement. *Cement Concrete Res*. 42, 282–290. doi: 10.1016/j.cemconres.2011.09.016

Geiker, M., Nielsen, E. P., and Herfort, D. (2007). Prediction of chloride ingress and binding in cement paste. *Mater. Struct*. 40, 405–417. doi: 10.1617/s11527-006-9148-2

Geng, J., Easterbrook, D., Li, L. Y., and Mo, L. (2015). The stability of bound chlorides in cement paste with sulfate attack. *Cement Concrete Res*. 68, 211–222. doi: 10.1016/j.cemconres.2014.11.010

Ghazy, A., and Bassuoni, M. T. (2017). Resistance of concrete to different exposures with chloride-based salts. *Cem. Concr. Res*. 101, 144–158. doi: 10.1016/j.cemconres.2017.09.001

Hansen, T. C. (1986). Physical structure of hardened cement paste: a classical approach. *Mater. Struct*. 19, 423–436. doi: 10.1007/BF02472146

Hirao, H., Yamada, K., Takahashi, H., and Zibara, H. (2005). Chloride binding of cement estimated by binding isotherms of hydrates. *J. Adv. Concrete Technol*. 3, 77–84. doi: 10.3151/jact.3.77

Ishida, T., and Maekawa, K. (1999). An integrated computational system for mass/energy generation, transport, and mechanics of materials and structures. *Doboku Gakkai Ronbunshu*. 627, 13–25. doi: 10.2208/jscej.1999.627_13

Jensen, O. M., Hansen, P. F., Coats, A. M., and Glasser, F. P. (1999). Chloride ingress in cement paste and mortar. *Cement Concrete Res*. 29, 1497–1504. doi: 10.1016/S0008-8846(99)00131-3

Jin, Z., Sun, W., Zhao, T., and Li, Q. (2019). Chloride binding in concrete exposed to corrosive solutions. *J. Chin. Ceramic Soc*. 37, 1068–1072. doi: 10.1109/CLEOE-EQEC.2009.5194697

Martin-Pérez, B., Zibara, H., Hooton, R. D., and Thomas, M. D. A. (2000). A study of the effect of chloride binding on service life predictions. *Cement Concrete Res*. 30, 1215–1223. doi: 10.1016/S0008-8846(00)00339-2

Masi, M., Colella, D., Radaelli, G., and Bertolini, L. (1997). Simulation of chloride penetration in cement-based materials. *Cement Concrete Res*. 27, 1591–1601. doi: 10.1016/S0008-8846(97)00200-7

Medeiros, M. H. F., Filho, J. H., and Helene, P. (2009). Influence of the slice position on chloride migration tests for concrete in marine conditions. *Mar. Struct*. 22, 128–141. doi: 10.1016/j.marstruc.2008.09.003

Montoya, R., and Nagel, V. (2020). Capillary water absorption and chloride transport into mortar samples: a finite element analysis. *Front. Mater*. 7:28. doi: 10.3389/fmats.2020.00028

Neville, A. (2004). The confused world of sulfate attack on concrete. *Cement Concrete Composit*. 34, 1275–1296. doi: 10.1016/j.cemconres.2004.04.004

Powers, T. C., and Brownyards, T. L. (1948). Studies of the physical properties of hardened cement paste. *Portland Chem. Assoc*. 22, 53–66.

Sandberg, P. (1999). Studies of chloride binding in concrete exposed in a marine environment. *Cement Concrete Res*. 29, 473–477. doi: 10.1016/S0008-8846(98)00191-4

Shaheen, F., and Pradhan, B. (2015). Effect of chloride and conjoint chloride–sulfate ions on corrosion of reinforcing steel in electrolytic concrete powder solution (ECPS). *Construct. Build. Mater*. 101, 99–112. doi: 10.1016/j.conbuildmat.2015.10.028

Sofia, R., and Alexandre, B. J. (2018). Chloride ingress into structural lightweight aggregate concrete in real marine environment. *Mar. Struct*. 61, 170–187. doi: 10.1016/j.marstruc.2018.05.008

Song, H. W., Lee, C. H., and Ann, K. Y. (2008). Factors influencing chloride transport in concrete structures exposed to marine environments. *Cement Concrete Composit*. 30, 113–121. doi: 10.1016/j.cemconcomp.2007.09.005

Sun, C., Chen, J., Zhu, J., Zhang, M., and Ye,. J. (2013). A new diffusion model of sulfate ions in concrete. *Constr. Build. Mater*. 39, 39–45. doi: 10.1016/j.conbuildmat.2012.05.022

Tang, L., and Nilsson, L. O. (1993). Chloride binding capacity and binding isotherms of OPC pastes and mortars. *Cement Concrete Res*. 23, 247–253. doi: 10.1016/0008-8846(93)90089-R

Tumidajski, P. J., Chan, G. W., Feldman, R. F., and Strathdee, G. (1995). A boltzmann-matano analysis of chloride diffusion. *Cement Concrete Res*. 25, 1556–1566. doi: 10.1016/0008-8846(95)00149-7

Valdes-Parada, F. J., Ochoa-Tapia, J. A., and Alvarez-Ramirez, J. (2007). Effective medium equations for fractional Fick's law in porous media. *Phys. Stat. Mech. Appl*. 373, 339–353. doi: 10.1016/j.physa.2006.06.007

Wang, P., Jiao, M., Hu, C., Tian, L., Zhao, T., Lei, D., et al. (2020b). Research on bonding and shrinkage properties of SHCC-repaired concrete beams. *Materials* 13, 1557–1574. doi: 10.3390/ma13071757

Wang, P., Wang, Y., Zhao, T., Xiong, C., Xu, P., Zhou, J., et al. (2020a). Effectiveness protection performance of an internal blending organic corrosion inhibitor for carbon steel in chloride contaminated simulated concrete pore solution. *J. Adv. Concrete Technol*. 18, 116–128. doi: 10.3151/jact.18.116

Xu, J., Peng, C., Wan, L., Wu, Q., and She, W. (2020). Effect of crack self-healing on concrete diffusivity: mesoscale dynamics simulation study. *ASCE J. Mater. Civil Eng*. 32:04020149. doi: 10.1061/(ASCE)MT.1943-5533.0003214

Xu, J., Zhang, C., Jiang, L., Tang, L., Gao, G., and Xu, Y. (2013). Releases of bound chlorides from chloride-admixed plain and blended cement pastes subjected to sulfate attacks. *Const. Build. Mater*. 45, 53–59. doi: 10.1016/j.conbuildmat.2013.03.068

Yoon, S., Moon, J., Bae, S., Duan, X., Giannelis, E., and Monteiro, P. (2014). Chloride adsorption by calcined layered double hydroxides in hardened Portland cement paste. *Mater. Chem. Phys*. 145, 376–386. doi: 10.1016/j.matchemphys.2014.02.026

Zhou, Y., Cai, J., Chen, R. X., Hou, D., Xu, J., Lv, K., et al. (2020). The design and evaluation of a smart polymer-based fluids transport inhibitor. *J. Clean. Prod*. 257, 1–12. doi: 10.1016/j.jclepro.2020.120528

Zhu, Q., Jiang, L., Chen, Y., Xu, J. X., and Mo, L. (2012). Effect of chloride salt type on chloride binding behavior of concrete. *Construct. Build. Mater*. 37, 512–517. doi: 10.1016/j.conbuildmat.2012.07.079

Conflict of Interest: The authors declare that the research was conducted in the absence of any commercial or financial relationships that could be construed as a potential conflict of interest.

Copyright © 2020 Xu, Mo, Wang, Zhou, Dong and She. This is an open-access article distributed under the terms of the Creative Commons Attribution License (CC BY). The use, distribution or reproduction in other forums is permitted, provided the original author(s) and the copyright owner(s) are credited and that the original publication in this journal is cited, in accordance with accepted academic practice. No use, distribution or reproduction is permitted which does not comply with these terms.

GLOSSARY

C_{cl}	Total chloride ion concentration (%)
ε_{tot}	Total porosity of concrete (m^3/m^3)
t	Erosion time (s)
$\boldsymbol{J}_{cl}$	Material flux of the corresponding component (m/s per unit area perpendicular to the direction of diffusion)
C_{cb}	Concentration of chemically bound chloride ions (%)
C_{pa}	Concentration of chloride ions adsorbed in the double layer region (%)
C_f	Concentration of free chloride ion in pore solution (%)
$Q(C_{cb})$	Sink term which is a function of chemically bound chloride ions (1/s)
C_T	Total chloride ion concentration (%)
ε_{gl}	Gel porosity (m^3/m^3)
ε_{cp}	Capillary porosity (m^3/m^3)
α	Degree of hydration of cementitious materials
τ	Time consumed in the hydration process (day)
$\frac{w_0}{c}$	Initial water-cement ratio in the form of mass fraction (kg/kg)
R_0	Ability of chloride binding without the influence of sulfate ion
C_b	Total bound chloride concentration at depth z (%)
R	Chloride binding capacity under the influence of sulfate ion
$C_{cb,SO_4^{2-}}$	Chemical binding content of chloride ion under the action of sulfate ion (%)
$Q\left(C_{cb,SO_4^{2-}}\right)$	Sink term produced by the action of sulfate ion (1/s)
$C_{SO_4^{2-}}$	Free sulfate ion concentration
D_f	Diffusion coefficient of chloride ion in the pore solution (m^2/s)
R_g	Universal gas constant (J/K·mol)
T	Ambient temperature (K)
Λ_{cl^-}	Molar conductivity of free chloride ion in porous solution (Sm^2/mol)
z_{cl^-}	Chloride ion valence ($=-1$)
F	Faraday constant (c/mol)
$\Lambda_{cl^-}^{\infty}$	Limit molar conductivity of free chloride ion in infinite dilution solution (Sm^2/mol at 25°C)
w_{cl^-}	Influence coefficient considering ion activity
e	Elementary charge (c)
ε_0	Vacuum dielectric constant ($c^2/J{\cdot}m$)
ε_r	Relative permittivity of water
Λ_i^{∞}	Limit molar conductivity of ions in the pore Solution (Sm^2/mol at 25°C)
n	Total number of ions
η	Viscosity coefficient of medium water
Ω	Tortuosity of ion transport in porous media

frontiers in Materials

ORIGINAL RESEARCH
published: 21 September 2020
doi: 10.3389/fmats.2020.560621

Numerical Simulation of Water Transport in Unsaturated Recycled Aggregate Concrete

Zhaolin Liu[1,2], *Peng Zhang*[1]*, *Jiuwen Bao*[1] and *Yu Hu*[2]

[1] Center for Durability & Sustainability Studies of Shandong Province, Qingdao University of Technology, Qingdao, China, [2] State Key Laboratory of Hydroscience and Engineering, Tsinghua University, Beijing, China

The old mortar attached to recycled aggregate (RA) is the main reason for the difference in water movement between RA concrete (RAC) and natural aggregate concrete. In this study, considering the old and new interfacial transition zones, a five-phase composite model for describing the water transport and distribution in RAC is established at the mesoscale. The key parameters describing water unsaturated transport in two types of mortar, saturated hydraulic conductivity (K_s) and van Genuchten model parameters (α, n), are obtained through the constant-head permeability test and isothermal adsorption test. By using the finite element method, the numerical simulations of unsaturated moisture movement in the homogeneous mortar, natural aggregate concrete, and five-phase RAC are systematically carried out. The proposed water transport model in the matrix is validated by comparison with the available experimental findings from the literature. The results show that the model can well predict unsaturated water transport in cement-based materials, including RAC. A parameter sensitivity analysis is undertaken to ascertain the main influencing factors of water transport in RAC. It is concluded that the RA replacement rate (R_{ra}), the thickness of the old mortar (d_m), and the aggregate volume fraction (F_a) are the primary parameters affecting moisture movement in RAC.

Keywords: mesoscale model, recycled aggregate concrete, Richards' equation, interfacial transition zone, water unsaturated transport

OPEN ACCESS

Edited by:
Hongyan Ma,
Missouri University of Science and Technology, United States

Reviewed by:
Haitao Zhao,
Hohai University, China
Jinbo Yang,
Shandong Agricultural University, China
Qiang Zeng,
Zhejiang University, China

***Correspondence:**
Peng Zhang
zhp0221@163.com

Specialty section:
This article was submitted to Computational Materials Science, a section of the journal Frontiers in Materials

Received: *09 May 2020*
Accepted: *24 August 2020*
Published: *21 September 2020*

Citation:
Liu Z, Zhang P, Bao J and Hu Y (2020) Numerical Simulation of Water Transport in Unsaturated Recycled Aggregate Concrete. Front. Mater. 7:560621. doi: 10.3389/fmats.2020.560621

INTRODUCTION

With the rapid progress of infrastructure construction, two contradictions have gradually emerged. One is the imbalance between excessive and unsustainable exploitation of natural resources and the ever-growing requirements of building materials. Another is that the increasing wastes from construction and demolition conflicts with inadequate waste disposal methods. This phenomenon poses a severe threat to the economic development and ecological equilibrium in many countries and regions all over the world (Oikonomou, 2005; Xiao et al., 2012; Fraj and Idir, 2017; Tam et al., 2018; Lam et al., 2019; Song et al., 2020). Thus, processing the construction waste into recycled aggregates (RAs) instead of the natural aggregates (NAs) is known as an effective way to resolve these two contradictions. However, compared with NA concrete (NAC), RA concrete (RAC) whose applications are limited to low-level civil construction works are rarely used in modern infrastructure construction due to the inferior performance of RA caused by its complicated composition.

As is known to all, there are at least two interface transition zones (ITZs) in RAC (Tam et al., 2005; Xiao et al., 2013): 1) the old ITZ between NA and its adhered old cement mortar, which already exist in RA; and 2) the new ITZ between the RA and new cement mortar. Compared to traditional concrete, this caused more defects in mechanical properties and more significant hidden dangers of durability problems (Bao et al., 2020a; Wang et al., 2020). Thus far, investigations mainly focused on the mechanical properties of RAC (Folino and Xargay, 2014; Kim and Yun, 2014; Velay-Lizancos et al., 2018; Wang and Xiao, 2018; Munir et al., 2020), yet still limited in durability problems.

Most of the durability degradation mechanisms of cement-based materials can almost be attributed to the distribution and migration of moisture which either causes physical damage to the concrete structure such as freeze-thaw cycles (Zhang et al., 2017b; Wang et al., 2019; Bao et al., 2020b) (Zhang et al., 2017b; Bao et al., 2020b) or carries deleterious agents, such as chloride and sulfate, into the interior of cement-based materials (Phillipson et al., 2007; Tian et al., 2020; Zhang et al., 2020). Thus far, there are few experimental methods to study water transport directly. Neutron radiography is an excellent non-destructive testing method (Zhang et al., 2017a). However, inhomogeneous moisture distribution in the thickness direction caused by the complex structure of RAs will result in the moisture distribution overlap during the imaging process and eventually lead to abnormal images. As for other advanced non-destructive testing techniques such as X-ray computed tomography and nuclear magnetic resonance, there are also certain limitations. X-ray computed tomography (Smyl et al., 2016; Xue et al., 2020) has higher resolution than neutron imaging and can realize spatial detection of structures relatively faster, yet limited by the distinction between matrix and moisture. Nuclear magnetic resonance (Rucker-Gramm and Beddoe, 2010; Wyrzykowski et al., 2017; McDonald et al., 2020) is sensitive to hydrogen nucleus, however, it is limited by its parameters setting (such as the determination of surface relaxation rate) and imaging resolution. Thus, numerical methods may be an effective method for moisture distribution research.

In recent years, some contributions have been made to improve the mass transfer theory of cement-based materials by using numerical simulation methods. For example, considering the coupling effect of moisture and heat, Burkan Isgor and Razaqpur (2004) developed a macroscopic spatial and temporal simulation of the carbonation front advancement in cracked concrete. Based on Voronoi tessellation, Wang et al. (2016) presented a 2D numerical lattice model of mass transport in concrete on the mesoscale level to study the migration of moisture and chloride ions in cracked concrete under the action of dry and wet cycles. According to the theory of computational mechanics, Caggiano et al. (2018) conducted mesoscopic numerical simulation research on water transport of concrete under capillary action by combining zero-thickness interface and pipe elements. On the basis of the unsaturated flow theory, Li et al. (2017, 2018) carried out a numerical simulation study on the moisture distribution characteristic of ITZ and the crack network. Zhao K. et al. (2020) carried out study on chloride transport in cement mortar during drying process which evaluates the influence of diffusion and convection on chloride transport by experiments and numerical simulation. Zhao H. et al. (2020) proposed a coupled hygro-thermo-chemical model, and accurately predicted the three stage of coupled humidity and temperature filed via numerical and experimental method. However, there are still few studies on numerical simulation of the mass transfer process in RAC, especially lacking the water unsaturated transport research.

For the purpose of revealing the water migration in a heterogeneous RAC of multiple phases, this work is aimed to find the water transport characteristic in RAC and calculate the distribution of water content at any elapsed time instead of developing a complicated model for water transport in real RAC. The model in this paper focused on the mesoscale, whereby RAC was idealized as a five-phase composite porous media made up of two kinds of ITZs, two types of mortars, and NCs. Nonlinear diffusion equations based on unsaturated flow theory, were used to describe the water movement, and solved by the finite element method (FEM). And the model parameters were determined by the experimental method in this paper.

UNSATURATED FLOW THEORY

In principle, the moisture migration in cement-based materials is dominated by two mechanisms: permeability and absorption. If the cement-based materials are thoroughly saturated with water, Darcy's law can be used to describe the process of moisture movement, i.e., permeability. Nevertheless, saturated flow is the exception, and most building constructions can not serve in a saturated state so that capillary absorption should be considered as the primary mechanism of water transport. According to the work of Swartzendruber (1969) in the field of soil, the extended Darcy's law can be used as the governing equation for describing water unsaturated transport,

$$\mathrm{u} = -K(\Theta)\nabla\Psi \tag{1}$$

where u is the flow velocity (LT^{-1}); $K(\Theta)$ is the unsaturated hydraulic conductivity which is also known as unsaturated permeability (LT^{-1}); Ψ is the capillary potential (L); ∇ is the Gradient tensor operator (L^{-1}). Θ denotes the normalized water content (–), and it can be written as

$$\Theta = \frac{\theta - \theta_r}{\theta_s - \theta_r} \, 0 \le \Theta \le 1 \tag{2}$$

where θ, denoted the ratio of water volume to sample bulk volume, is the volumetric water content (–); θ_r is the residual water content (i.e., the water content at dry condition, generally 0) (–) (Lockington et al., 1999), and θ_s is the saturated water content (i.e., the water content in the saturated condition) (–).

In fluid mechanics, the law of conservation of mass is expressed as a Continuity Equation, which is as follows:

$$\frac{\partial\theta}{\partial t} + \nabla u = 0 \tag{3}$$

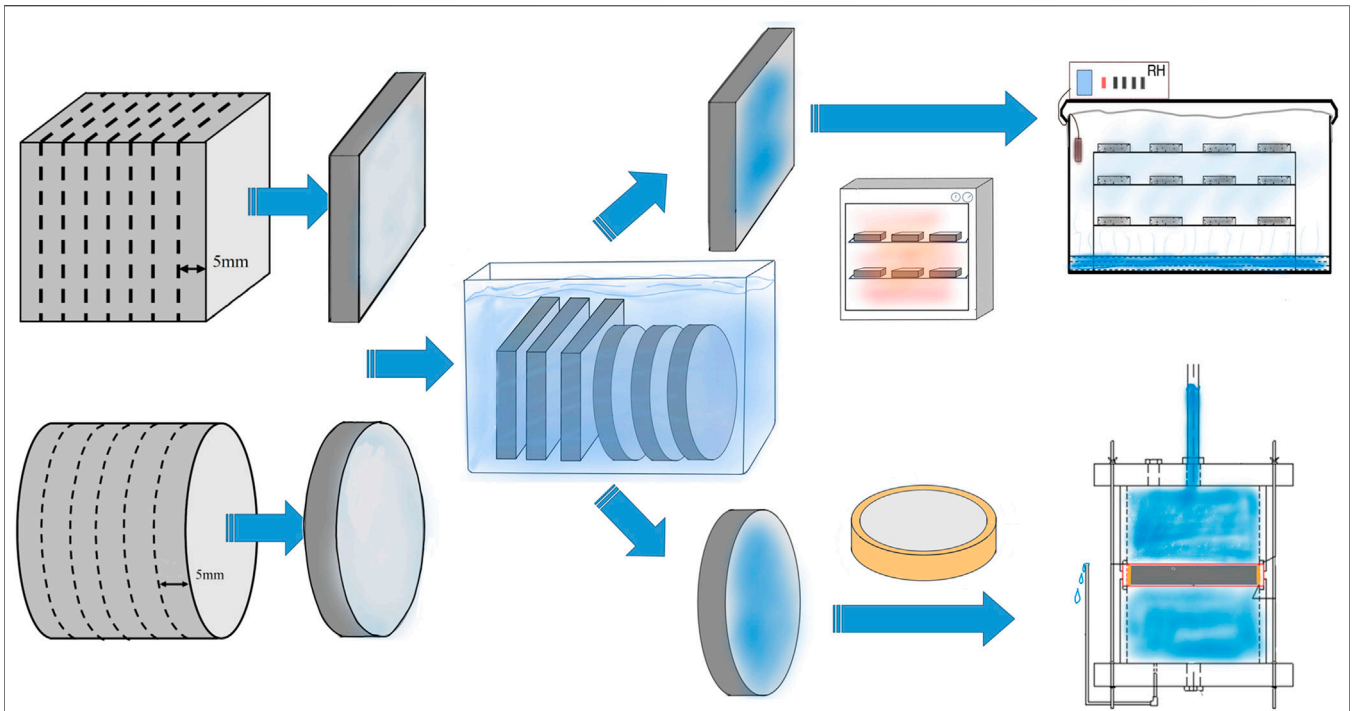

FIGURE 1 | Process of specimens' preparation.

Combining **Eq. 1** with **Eq. 3** leads to the fundamental equation of unsaturated flow, namely the Richards' equation

$$\frac{\partial \theta}{\partial t} = \nabla K(\Theta)\nabla\Psi \tag{4}$$

Usually, Richards' equation can also be expressed in another two equivalent forms:

$$(1) \quad \Theta \text{ based form}: \frac{\partial \Theta}{\partial t} - \nabla D(\Theta)\nabla\Theta = 0$$

$$(2) \quad \Psi \text{ based form}: C(\Psi)\frac{\partial \Psi}{\partial t} - \nabla \cdot K(\Psi)\nabla\Psi = 0$$

where $C(\Psi) = \frac{d\Theta}{d\dot{\Psi}}$

A serious limitation of the Θ-based Richards Equation is that the materials of interest must be homogeneous. However, RAC is a kind of multiple-phase composite material which can not be considered as a homogeneous material. In this way, across the interfaces between different phases, the distribution of water content becomes discontinuous. In other words, the Ψ-based form, which can balance the saturation and the capillary potential well, is more suitable for this study.

In **Eq. 1**, the unsaturated hydraulic conductivity $K(\Theta)$ can hardly be obtained experimentally for cementitious materials. According to soil mechanics theory, it can be well estimated by the most widely used model, Mualem equation (Mualem, 1976),

$$K(\Theta) = K_s\Theta^l\left[1 - \left(1 - \Theta^{\frac{1}{m}}\right)^m\right]^2 \tag{5}$$

where m is the van Genuchten parameter (–), usually simplified to $m = 1/(1-n)$; l is a constant equal to −0.5 for cementitious materials (–); K_s is the saturated hydraulic conductivity, also known as permeability (LT^{-1}). The relationship between saturation Θ and capillary potential Ψ can be easily established by van Genuchten model (van Genuchten, 1980),

$$\Theta(\Psi) = \begin{cases} \left[\frac{1}{1+(\alpha\Psi)^n}\right]^m & \Psi < 0 \\ 1 & \Psi \geq 0 \end{cases} \tag{6}$$

with α (L^{-1}) and n as fitting constants and properties of the material. These parameters can adequately describe the water retention curve of cement-based materials, so as to express the unsaturated water transport characteristics of different phase under capillary suction.

DETERMINATION AND VALIDATION OF PARAMETERS

In order to solve the governing equation, the first issue is to determine the parameters (i.e., K_s, α, and n) of different phases. Since the data for cementitious materials are sparse, to ensure the accuracy and effectiveness of the simulation results, adsorption tests, and static pressure penetration tests were conducted in this work. The process is as shown in **Figure 1**.

Materials and Specimen Preparation

Ordinary Portland cement 52.5 type and river sand with a maximum grain size of 5 mm were used to prepare the mortar specimen. Cube specimens with the side length of 70.7 mm and

TABLE 1 | Mix proportion of cement mortar, kg/m^3 (The permission has been obtained from the copyright holders).

Mix	*W/C*	Cement	Sand	Water
M1	0.6	500	1,350	300
M2	0.4	562	1,350	225

cylinder specimens with the size of Φ100 mm × 50 mm were prepared separately. All these specimens were demolded after 24 h and then cured in water at an ambient temperature of 20 ± 2°C. After 7 days, specimens were cut into slices of 5 mm thin and then soaked in water for 90 days to minimize the negative impact of hydration on subsequent tests. The mix proportion was determined, according to the research of Zhang et al. (2017a), as shown in **Table 1**.

Isothermal Adsorption Test

The adsorption isotherm is the basis for studying the properties related to water transport of materials. In order to obtain the van Genuchten parameters α and n, it is necessary to achieve the time-dependent adsorption curves. The following experiments were therefore carried out.

In the beginning, different humidity environments need to be established. Five inorganic salts were selected to prepare supersaturated salt solutions namely $MgCl_2$, NaBr, NaCl, KCl, and K_2SO_4, by whose theoretical humidity that they can regulate is 33, 58, 76, 86, and 98%, respectively. Correspondingly, five humidity chambers with different salt solutions were prepared in a constant temperature and humidity room [T = 20 ± 2°C and relative humidity (RH) = 50 ± 2%]. The RH (–) of each chamber was measured repeatedly by using humidity sensors until it reached a steady state (the fluctuation in 24 h did not exceed ±1.5%). The actual RH were shown in **Table 2**.

Secondly, the cured square sheet specimens of M1 and M2 were dried to a constant weight at 105 C (mass variation in 7 days is less than 0.01 g), and the dried mass was recorded as m_d. Six pieces of M1 and M2 specimens had been placed and numbered in each humidity chambers, followed by a long-term test. After 3 months, the specimens were weighed every 7 days until the constant weight was reached. Each specimen's mass m at this time was the mass with the adsorption reached equilibrium. Then these specimens were soaked into the water again until saturated, and the water-saturated mass m_s was recorded. By transforming **Eq. 2** as follows,

$$\Theta = \frac{\theta - \theta_r}{\theta_s - \theta_r} = \frac{m - m_d}{m_s - m_d} \tag{7}$$

the relationship between Θ and RH can then be successfully established. According to this relationship, the isothermal adsorption curves were plotted, as shown in **Figure 2A**.

The relationship between hydrostatic pressure and RH can be described by the Kelvin-Laplace equation,

$$P_w = \frac{\rho_w RT}{M_w} \ln(RH) \tag{8}$$

where P_w denotes the hydrostatic pressure (L^{-1} MT^{-2}), $P_w = \rho_w g \Psi$; ρ_w is the water density, $\rho_w = 1\ g/cm^3$; R denotes the ideal gas constant, which is 8.3144 J/(mol K); T is the Kelvin temperature, which is 293.15 K in this paper; M_w denotes the relative molecular weight of water. Combining **Eq. 6** with **Eq. 8** leads to the following equation,

$$\Theta = \begin{cases} \left\{ \dfrac{1}{1 + [\alpha \frac{RT}{M_w g} \ln(RH)]^n} \right\}^{\frac{1}{1-n}} & \Psi < 0 \\ 1 & \Psi \geq 0 \end{cases} \tag{9}$$

The value of α and n were obtained by fitting **Eq. 9**, as shown in **Figure 2A**.

The isotherm adsorption curves fitted in **Figure 2A** can be transformed into water retention curves in **Figure 2B** by **Eq. 6**. The saturation can be easily converted into capillary potential according to these curves, and the initial condition value and boundary condition value of the matrix can be determined quantitatively. It can be manifested from the profiles that when the capillary potential reaches $\Psi = -2.16 \times 10^{-6}$ mm, the saturation of M1 and M2 is almost equal to zero (that is, the dry state).

The Static Pressure Penetration Test

In Richards' equation, the value of saturated hydraulic conductivity K_s is also an important parameter to define the properties of the matrix material, which can be obtained by the static pressure penetration test. The pressure penetration apparatus shown in **Figure 3A** is manufactured according to the research of Ludirdja and Young (1989).

Firstly, each mortar specimen was wrapped with the rubber ring and sealed at the junction by epoxy resin to prevent water leakage. And then, the upper chamber, the rubber ring, and the lower chamber were connected in sequence. The lower chamber was filled with water until the liquid level in the stainless-steel pipe reached the top. In the same way, the upper chamber and the pipette were filled with water carefully to 305 mm. The top of the stainless-steel pipe was kept horizontal with the upper surface of the specimen so that the water at the top will penetrate through the specimen into the lower chamber under the single action of water pressure and flow out from the stainless-steel pipe. The volume change of the water in the pipette was recorded every 24 h as q_i (L^3), and then water was filled again to 305 mm height. Due to the little change of water level within 24 h, the specimens can be considered to be under the load of a constant head at all times.

TABLE 2 | Relative humidity of supersaturated salt solution.

	$MgCl_2$ (%)	NaBr (%)	NaCl (%)	KCl (%)	K_2SO_4 (%)
Theoretical humidity	33	58	76	86	98
Actual humidity after stabilization	35.1	57.9	71.4	80.4	92.7

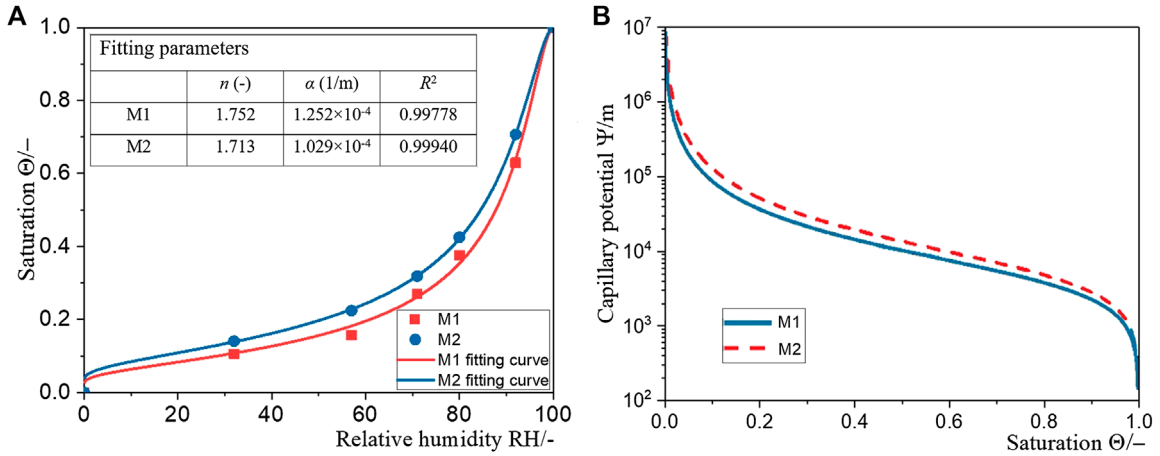

FIGURE 2 | (A) Isothermal adsorption curves and **(B)** water retention curves of M1 and M2.

The above procedure was repeated until q_i reached a constant value. The relationship between Q (that is, the accumulated amount of q_i) and observation time t was plotted in **Figure 3B**. K_s can be obtained by fitting the following **Eq. 10**,

$$K_s = \frac{QL}{hAt} \tag{10}$$

where L denotes the thickness of the specimen (L); A denotes the permeability area (L^2), which is the cut surface area of each specimen; h denotes the water head (L), which is the distance from the liquid surface at the top of the pipette to each specimen.

Validation of the Models

It is difficult to measure the distribution of moisture in non-transparent cement-based materials by experimental methods, and the process of non-destructive testing is also limited. Therefore, in order to verify the accuracy of the theoretical model and parameters, the results of the neutron radiography test carried out by Zhang et al. (2017a) were chosen to compare with the simulation results in this paper. The specimens used in the analysis are mortar specimens with a water-cement ratio of 0.6, whose mix proportion is the same as that of M1 in **Table 1**. The prepared mortar specimen was cut into thin slices of 100 mm × 100 mm × 25 mm and sealed with aluminum foil tape around to prevent moisture intrusion from other boundaries instead of the bottom surface (**Figure 4A**). The sealed specimen was placed in a flume for the capillary water absorption experiment, and the neutron radiography test was administered in the meantime.

According to the capillary absorption test, the cement mortar absorption model can be established, as shown in **Figure 4B**. The matrix is initially in a dry state and can only contact the water through the bottom boundary. The remaining boundaries do not exchange water with the outside environment. Therefore, the initial condition and boundary condition can be expressed by

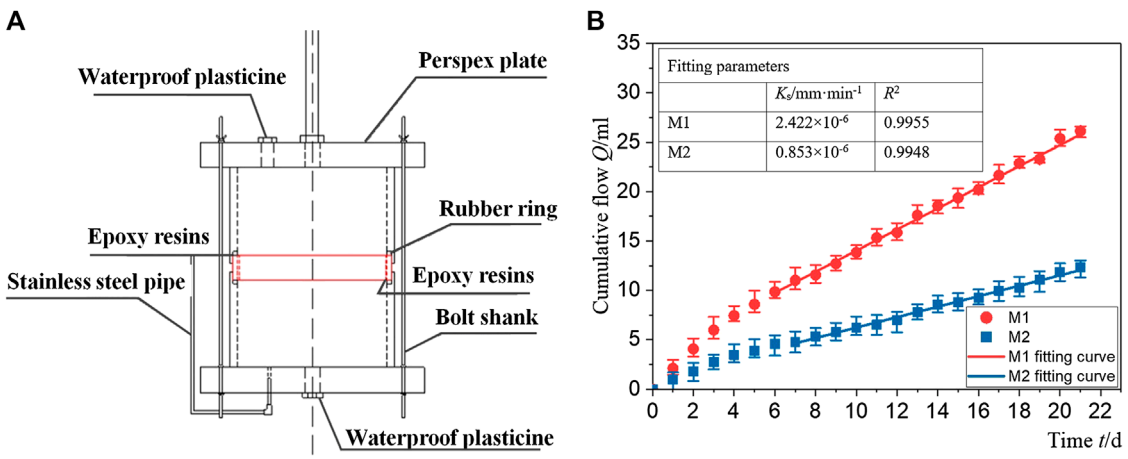

FIGURE 3 | Static pressure test: **(A)** penetration apparatus, and **(B)** curves of cumulative volume of water permeated vs. time for M1 and M2.

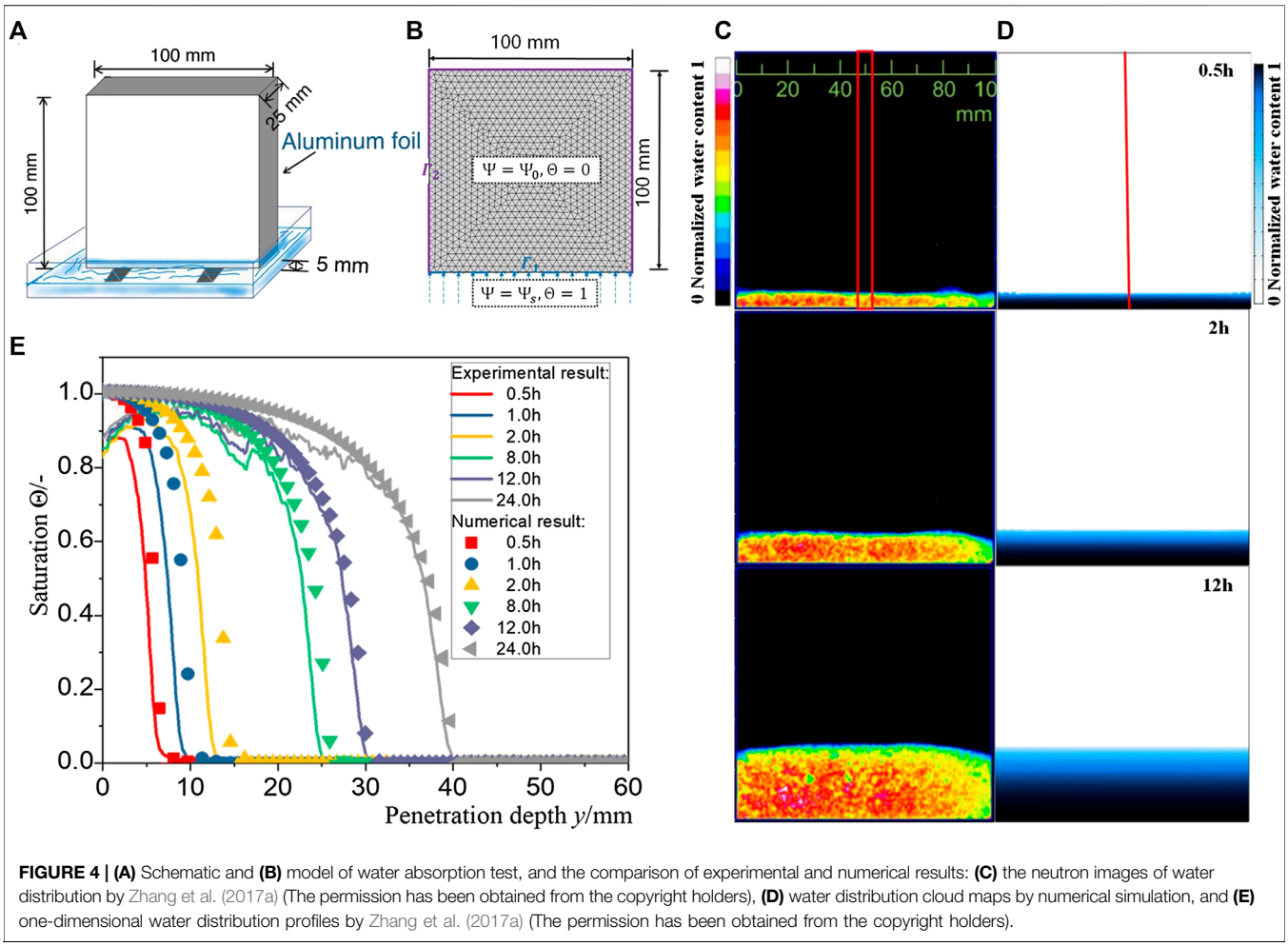

FIGURE 4 | (A) Schematic and **(B)** model of water absorption test, and the comparison of experimental and numerical results: **(C)** the neutron images of water distribution by Zhang et al. (2017a) (The permission has been obtained from the copyright holders), **(D)** water distribution cloud maps by numerical simulation, and **(E)** one-dimensional water distribution profiles by Zhang et al. (2017a) (The permission has been obtained from the copyright holders).

$$\begin{cases} \Psi|_{t=0} = \Psi_{0,m} & \Psi \in \Omega \\ \Psi_{\Gamma_1} = \Psi_{p,m} & \Psi \in \Gamma_1 \\ \left.\dfrac{\partial \Psi}{\partial \{n\}}\right|_{\Gamma_2} = f = 0 & \Psi \in \Gamma_2 \end{cases} \tag{11}$$

where Ω is the mortar matrix; Γ_1 and Γ_2 are the water absorption boundaries of the mortar specimen and the remaining boundaries, respectively, $\Gamma_1 \cup \Gamma_2 = \Gamma$; f denotes the flow velocity through boundary Γ_2 (LT^{-1}); $\Psi_{0,m}$ is the capillary potential at matrix saturation of 0 (L); $\Psi_{p,m}$ is the capillary potential at matrix saturation of 1 (L). The parameters for numerical computation are listed in **Table 3**.

TABLE 3 | Summary of parameters for M1.

Parameters	Values
Residual water content θ_r, –	0
Saturated water content θ_s, –	0.127
Saturated hydraulic conductivity K_s, mm min^{-1}	2.422×10^{-6}
van Genuchten parameter α, 1/m	1.252×10^{-4}
van Genuchten parameter n, –	1.752
Capillary potential at dry condition $\Psi_{0,m}$, m	2.16×10^{-6}
Capillary potential at boundary $\Psi_{p,m}$, m	0.05

The cloud maps of water distribution at different times can be obtained by employing numerical simulation, and the results are compared with the experimental results of neutron imaging. By comparing **Figures 4C,D**, it can be observed intuitively that the moisture in the specimen is absorbed upward from the lower surface of the specimen under the action of the capillary adsorption force. Due to the inhomogeneity of the mortar composite, the water front is not completely parallel to the water absorption surface, and the water distribution at different coordinates is also slightly different. However, these differences did not substantially affect the results. The distribution of water front illustrates that the water transport is almost one-dimensional parallel to the bottom of the boundary, and the movement of the water front slows down gradually with time elapsing. The simulated position of the water front at different times shows good agreement with the experimental results.

The marked central area shown in **Figures 4C,D** is selected for quantitative analysis to obtain numerical and experimental water distribution shown in **Figure 4E**. It can be seen quantitatively that the water distribution along the y-axis in the simulation results is roughly the same as that in the test results. The difference between the simulation results and the test results mainly comes from the

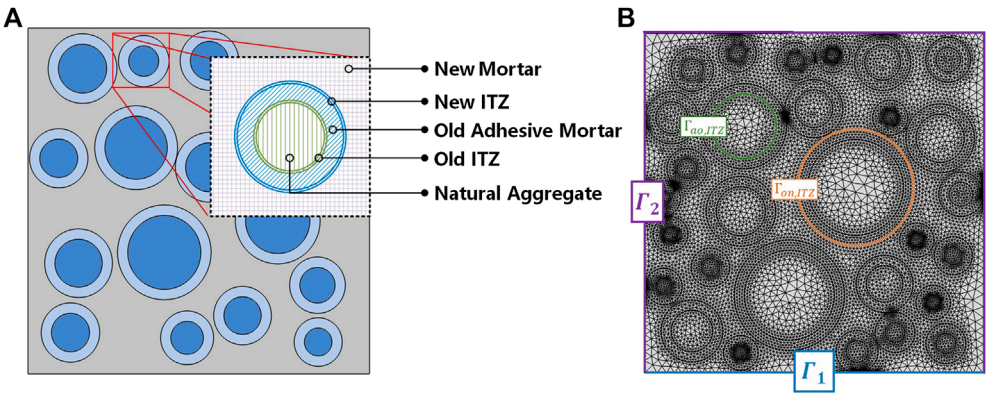

FIGURE 5 | Mesoscale structure of recycled aggregate concrete: **(A)** schematic diagrams and **(B)** finite element meshes diagrams.

following points: a) The mortar model is simplified to a homogeneous model structure whereby water is uniformly distributed in the horizontal direction. However, in the capillary absorption test, due to various factors such as uneven distribution of sand particles and insufficient hydration, the results will inevitably be different from the idealized model's. Sand and insufficient hydration will cause the lag of unsaturated water transport. b) In the capillary water absorption test, the sample needs to be dried by oven. High temperature will damage the material, enhance the connectivity of the pores, and accelerate the process of water transport in the matrix. c) The inhomogeneity of the mortar specimens causes the saturation water content at each position to be different, so it is inevitable to underestimate or overestimate the saturation of certain areas after normalization by the formula. However, the influence of these errors is very weak and within an acceptable range, thus overall results show well agreement. This agreement suggests that the numerical model and substitute parameters correctly describe the capillary absorption process in the cement mortar matrix, which provides a guarantee for the accuracy of subsequent studies on water unsaturated transport in RAC.

TRANSPORT ANALYSIS FOR RECYCLED AGGREGATE CONCRETE

Mesoscale Recycled Aggregate Concrete Model

Considering that the polygonal aggregate has a huge amount of calculation for the simulation and the limited influence on water transport (Li et al., 2016; Liu et al., 2018), the round aggregates are used in our study to simplify the calculation. As mentioned before, the essential difference between RAC and NAC is the coarse aggregate. Compared to NA, RAC can not be considered as traditional aggregate-matrix two-phase material structure nor aggregate-ITZ-matrix three-phase material structure because of the old mortar attached to old NA. The old ITZ initially existed between the old aggregate and the old mortar, and new ITZ gradually forms between the old mortar and the new mortar after setting. As a consequence, in order to describe the migration of water in RAC more accurately, the five-phase RAC model consisting of old aggregate, old mortar paste, old ITZ, new mortar paste, and new ITZ were established by simplifying the actual RA into a concentric circle model (**Figure 5A**).

By means of the Monte Carlo method, in other words, cyclically putting concentric circles of different sizes into a square area until it reaches the expected area fraction (i.e., coarse aggregate volume fraction), the two-dimensional RAC random aggregate model can be established. This process was achieved by randomly generating NC aggregate center coordinates, radius, and adhesive mortar thickness and running a set of MATLAB codes. The meshed RAC model is shown in **Figure 5B**.

Definition of Interface Transition Zones Phase

According to the description of the smooth plate crack flow method (Chen et al., 2013; Li et al., 2017), a variant of extended Darcy's law was adopted to describe the water flow in ITZ. In this way, ITZs in the model will have no geometric width, and water transport in it might be simplified to flow along interior boundaries between the two different phases. The governing equation of water transport in the crack is as follows,

$$\begin{cases} d_{\mathrm{ITZ}} C_{\mathrm{ITZ}}(\Psi)\dfrac{\partial \Psi}{\partial t} + \nabla_T \times [d_{\mathrm{ITZ}}(-K_{\mathrm{ITZ}}(\Psi)\nabla_{\mathrm{T}}\Psi)] = f_{\mathrm{a}} + f_{\mathrm{o}} \\ d_{\mathrm{ITZ}} C_{\mathrm{ITZ}}(\Psi)\dfrac{\partial \Psi}{\partial t} + \nabla_T \times [d_{\mathrm{ITZ}}(-K_{\mathrm{ITZ}}(\Psi)\nabla_{\mathrm{T}}\Psi)] = f_{\mathrm{o}} + f_{\mathrm{n}} \end{cases} \tag{12}$$

where d_{ITZ} is the ITZ width, and ∇_{T} denotes the tangential derivatives of ITZ. f_i is the exchange item (i.e., the flow rate) between ITZ and matrix, the subscript i represents the three matrix NA(a), old adhesive mortar (o), and new mortar (n). Since the width of ITZ is far smaller than that of the matrix, the capillary potential at the two sides of it is identical to Ψ. Therefore f_i can be expressed as follows

$$\begin{cases} -K_n \dfrac{\partial \Psi}{\partial\{n\}}\Big|_{\Gamma_{\text{on, ITZ}}} = f_{\text{n}} & \Psi \in \Gamma_{\text{on,ITZ}} \\ -K_o \dfrac{\partial \Psi}{\partial\{n\}}\Big|_{\Gamma_{\text{on, ITZ}}} = f_{\text{o}} & \Psi \in \Gamma_{\text{on,ITZ}} \\ -K_a \dfrac{\partial \Psi}{\partial\{n\}}\Big|_{\Gamma_{\text{an, ITZ}}} = f_{\text{a}} & \Psi \in \Gamma_{\text{ao,ITZ}} \\ -K_o \dfrac{\partial \Psi}{\partial\{n\}}\Big|_{\Gamma_{\text{ao, ITZ}}} = f_{\text{o}} & \Psi \in \Gamma_{\text{ao,ITZ}} \end{cases} \tag{13}$$

where $\Gamma_{j,\text{ITZ}}$ is different interfaces. K_i is the hydraulic conductivity of different matrix.$K_{\text{ITZ}}(\Psi)$ in **Eq. 12** denotes the unsaturated hydraulic conductivity of ITZ,

$$K_{\text{ITZ}}(\Psi) = K_{\text{s,ITZ}}\Theta^l\left[1-\left(1-\Theta^{\frac{1}{m}}\right)^m\right]^2 \tag{14}$$

where l is a constant equal to −0.5 for cementitious materials (–); m is the van Genuchten parameter (–), $m = 1 - 1/n$. It is reported that the value of n is generally between 1 and 2, fluctuating little in similar materials. In this work, n is assumed as 2 for ITZs. $K_{s,\text{ITZ}}(\Psi)$ is the saturated hydraulic conductivity of ITZ. According to the cubic law (Witherspoon et al., 1980; Wang et al., 2016), the relationship between $K_{s,\text{ITZ}}$ and width can be expressed as **Eq. 15**

$$K_{\text{s, ITZ}} = \frac{d_{\text{ITZ}}^3}{12 l_{\text{ITZ}}}\frac{\rho g}{\mu} \tag{15}$$

where μ is the viscous coefficient of water. With these formulations above, the ITZ domain can be idealized as a porous and zero-model-thickness interface with higher hydraulic conductivity in RAC.

Definition of Natural Aggregate and Mortar Phases

The pore structure determines the mass transfer performance of cementitious material. Since the pore structure of RC is different from NC, the water transfer law in RAC is naturally different from NAC. The migration velocity of water in the matrix can be regarded as a function of the characteristics of the RAC's different phases. In other words, correctly distinguishing and defining the properties of each phase to represent its pore structure characteristic in numerical simulation is an essential factor in ascertaining the water distribution in RAC. In this model, both the cement mortar phase and the aggregate phase are considered as the porous material so that the water transport in them follows the Richards' Equation (i.e., **Eq. 3**). Consequently, combining the previously mentioned theory of water transport in the matrix, the governing equation of water transport in recycled concrete can be obtained, which is expressed as follows,

$$\begin{cases} C_n(\Psi)\dfrac{\partial \Psi}{\partial t} - \nabla K_n(\Psi)\nabla\Psi = 0 & \Psi \in \Omega_n \\ C_o(\Psi)\dfrac{\partial \Psi}{\partial t} - \nabla K_o(\Psi)\nabla\Psi = 0 & \Psi \in \Omega_o \\ C_a(\Psi)\dfrac{\partial \Psi}{\partial t} - \nabla K_a(\Psi)\nabla\Psi = 0 & \Psi \in \Omega_a \\ d_{ao,\text{ITZ}}C(\Psi)\dfrac{\partial \Psi}{\partial t} + \nabla\left(d_{ao,\text{ITZ}}K_{ao,\text{ITZ}}(\Psi)\nabla\Psi\right) = 0 & \Psi \in \Gamma_{ao,\text{ITZ}} \\ d_{on,\text{ITZ}}C(\Psi)\dfrac{\partial \Psi}{\partial t} + \nabla\left(d_{on,\text{ITZ}}K_{om,\text{ITZ}}(\Psi)\nabla\Psi\right) = 0 & \Psi \in \Gamma_{on,\text{ITZ}} \end{cases} \tag{16}$$

And the initial and boundary condition can be expressed as

$$\begin{cases} \Psi|_{t=0} = \Psi_0 & \Psi \in \Omega \\ \Psi_{\Gamma_1} = \Psi_p & \Psi \in \Gamma_1 \\ \dfrac{\partial \Psi}{\partial\{n\}}\Big|_{\Gamma_2} = f = 0 & \Psi \in \Gamma_2 \end{cases} \tag{17}$$

In the **Eq. 16**, if the governing equation in domain Ω_o is replaced with that in domain Ω_n, the unsaturated transport simulation of NAC can be implemented.

Compared with the new cement mortar matrix, due to various factors such as crushing and grinding, the micro-cracks of the old adhesive mortar and the old ITZ increase, and their saturated water content and permeability also increase accordingly. This means that the saturated water content θ_s and hydraulic conductivity K_s of new mortar are higher than these of old adhesive mortar. For this purpose, the parameters of M1 and M2 are used to describe the old adhesive mortar and new mortar in the model, respectively. Considering the extremely low water absorption rate, NA can be regarded as an impermeable porous media. It is found through trial calculation that, when $K_s(\text{NA})/K_s(\text{mortar matrix}) \leq 1\times10^{-6}$, $\theta_s(\text{NA})/\theta_s(\text{Matrix}) \leq 1\times10^{-3}$, there is hardly water movement in NA. To simplify the calculation, the K_s and θ_s are assumed as 1×10^{-20} m/sec and 0.0001 in this work. The parameter settings of RAC are summarized in **Table 4**.

TABLE 4 | Summary of material parameters for recycled aggregate concrete.

	Parameters	Values
Old mortar	Saturated water content $\theta_{s,n}$, –	0.127
	Saturated hydraulic conductivity $K_{s,n}$, mm·min^{-1}	2.422×10^{-6}
	van Genuchten parameter α, 1/m	1.252×10^{-4}
	van Genuchten parameter n, –	1.752
New mortar	Saturated water content $\theta_{s,o}$, –	0.107
	Saturated hydraulic conductivity $K_{s,o}$, mm·min^{-1}	0.853×10^{-6}
	van Genuchten parameter α, 1/m	1.029×10^{-4}
	van Genuchten parameter n, –	1.713
NA	Saturated hydraulic conductivity $K_{s,a}$, mm·min^{-1}	0.853×10^{-6}
	Saturated water content $\theta_{s,a}$, –	1×10^{-4}
Other parameters	Capillary potential at dry condition Ψ_0, m	2.16×10^{-6}
	Capillary potential at boundary Ψ_p, m	0.05
	New ITZ width $d_{ao,\text{ITZ}}$, μm	20
	Old ITZ width $d_{on,\text{ITZ}}$, μm	40
	van Genuchten parameter of ITZ n,–	2

ITZ, interface transition zone.

Validation of the Recycled Aggregate Concrete Models

To verify the accuracy of the model, we compared the simulation results with the capillary water absorption test results of Bao et al. (2020a) which is shown in **Figures 6A,B**. It is illustrated that,

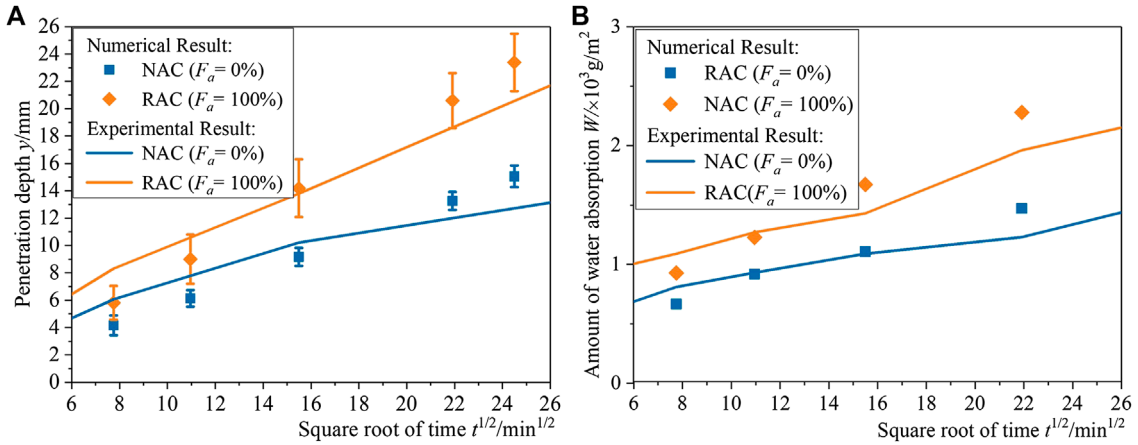

FIGURE 6 | Comparison of numerical results and the experimental results of Bao et al. (2020a) on **(A)** water penetration depth and **(B)** amount of water absorption (The permission has been obtained from the copyright holders).

both the macroscopic water absorption and the microscopic water penetration depth, the simulation results agree well with experimental results. The differences are mainly due to the following factors: a) There is a slight difference in water cement ratio between experiment (W/C = 0.39) and simulation (W/C = 0.40) which might cause differences in results; b) There are some uncertainties in practice, such as the insufficient hydration and the heterogeneity of mortar matrix, which is difficult to achieve by numerical model; c) Although a complex RA model has been established, it is still a simplified form of practical RA. These factors may cause small changes in the results but will not have a substantial impact on the conclusions. Hence one can conclude that the RAC model used in this study is accurate and reliable.

Modeling Results of Water Uptake in Recycled Aggregate Concrete and Natural Aggregate Concrete

Equation 16 was implemented in the commercial finite element software, COMSOL Multiphysics, the multi-field coupled FEM simulation program, and the cloud map of water distribution of NAC and RAC at different times were obtained to describe the 2D water distribution in RAC and NAC at different times (**Figures 7A,B**).

It can be seen that, as t = 30 min, the water front in RAC has wholly surpassed the marked aggregate, and the water front behind the aggregate penetrates deeper than it in the mortar matrix. While the moisture penetrating speed in NAC slows down, and the water front in the mortar penetrates is deeper. When t = 60 min, the difference in the penetration depth is more prominent. The peak of the water front has reached a depth of about 13 mm in RAC, while barely about 7 mm in NAC.

Despite considering the influence of ITZ of NAC, the hindrance effect of NA on water transport is much higher than the promoting effect of ITZ. By comparing the flow flux arrow diagram shown in **Figures 7C,D**, one can see in NAC that although the flow velocity of ITZ is higher than that of the ordinary mortar matrix, it is still lower than the moisture transmission in the narrow and long domain between NAs. However, in RAC, the flow velocity between RAs is relatively low, and the main flow velocity is concentrated in the old adhesive mortar and ITZ area. This phenomenon can be explained that water only moves in the matrix and single ITZ on condition that NA is assumed as impermeable, whereby the real water transport area is equivalent to narrowing. Thus, due to the limitation of water transport capacity, the vast majority of water still crowds in the mortar matrix, so that the convex surface of the water front is formed between the aggregates (**Figure 7E**). However, the old mortar and the double ITZs are all weak areas for RAC. Both of the porosity and hydraulic conductivity are relatively large. On the one hand, similar to NAC, the water absorption of RAC is accelerated due to the existence of ITZ. On the other hand, as moving in ITZ, water also transfers rapidly into the old mortar whose capillary pressure is higher than that of the new mortar, which further accelerates the penetration of water. Because of the higher penetration velocity in RA, the convex surface of the moisture front is formed behind RA (**Figure 7F**).

The relationship between the water penetration depth and the square root of the time were plotted in **Figure 8**, which is approximated to a positive linear correlation. The slope of the curve corresponds to the velocity of water uptake, which indicated that the water absorption velocity in RAC is much larger than the other two materials. As t = 600 min, the penetration depth of water in RAC even reaches 1.6 times that in NAC. By comparing NAC and cement mortar, it can be illustrated that the penetration depth in RAC always slightly lags behind in cement mortar, which confirms that the hindrance effect of NA on moisture is stronger than the promoting effect of single ITZ as mentioned before. However, the error bars of moisture penetration in NAC shows lower variability, which indicates that NA and single ITZ have limited effects on water

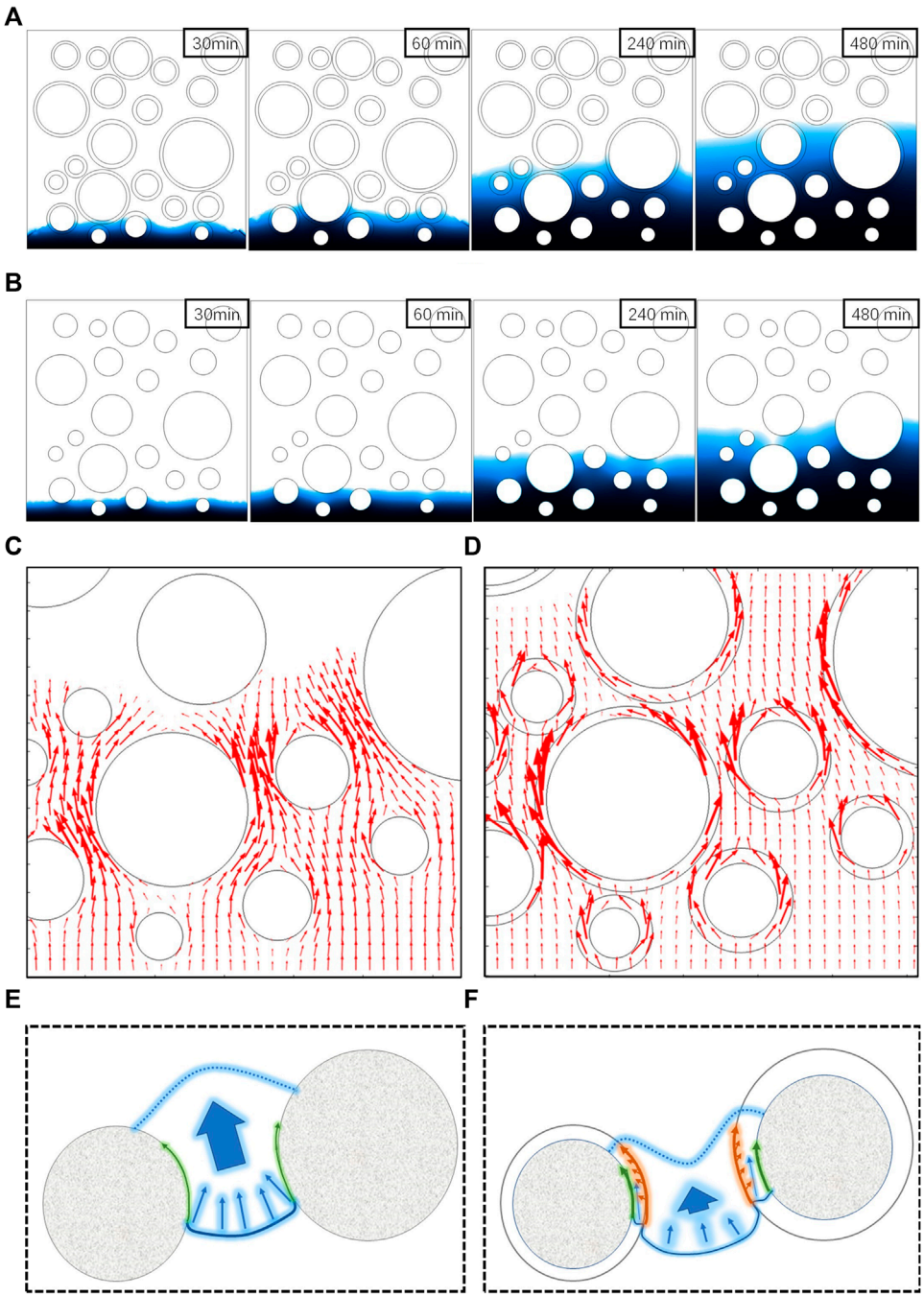

FIGURE 7 | Comparison of numerical simulation results between recycled aggregate concrete (RAC) and natural aggregate concrete (NAC): cloud maps of water distribution in **(A)** RAC and **(B)** NAC, the arrow diagram of flow flux in **(C)** RAC and **(D)** NAC, and the schematic of water movement characteristic between aggregates in **(E)** RAC and **(F)** NAC.

uptake. Instead, this situation is quite different in RAC. "Convenient access" of RA occupies a dominant position in water transport, which leads to the increased influence of matrix heterogeneity, and then causes larger variability of penetration depth showed in profile. This feature can also be found intuitively in the cloud map in **Figures 7A,B**, as t = 480 min.

PARAMETER SENSITIVITY

The previous content illustrates the critical role RA plays in unsaturated absorption of RAC. Therefore, it is necessary to conduct a more detailed study on the impact of aggregate. For this purpose, parameter sensitivity analyses on RA replacement

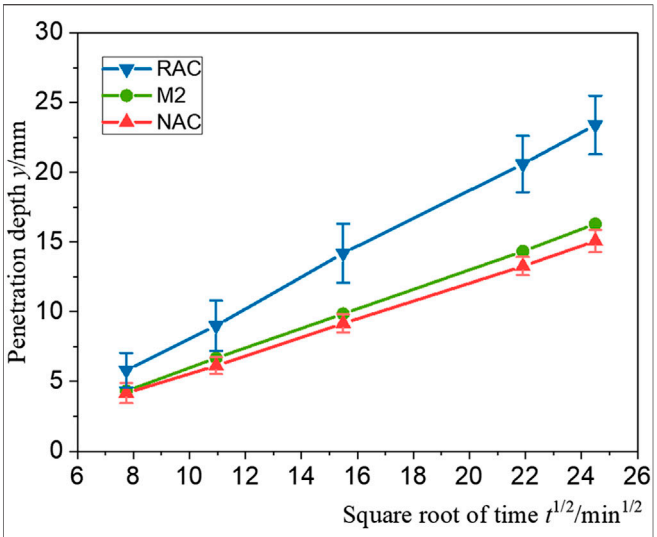

FIGURE 8 | The profiles of water penetration depth in recycled aggregate concrete (RAC), natural aggregate concrete (NAC), and cement mortar at different time.

rate (R_{ra}), the thickness of old mortar (d_m) and the RA volume fraction (F_a) were implemented.

Effect of Recycled Aggregate Replacement Rate on Water Absorption

R_{ra} refers to the volume ratio of RA to all aggregates, which is assumed to be the area ratio in 2D condition. To investigate its influence on the water absorption of RAC, five R_{ra} of 0, 25, 50, 75, and 100% were used, and then a random aggregate model was generated.

As shown in **Figure 9A**, it can be learned that with the R_{ra} increases, the penetration depth of the water front advances slightly. By observing the marked red area, the difference in water distribution can be distinguished. **Figure 9B** shows the water penetration depth against the different square root of *t*, with the given values of R_{ra}. One can see that with the increase of *R*, water uptake is gradually accelerated, and the depth of water penetration also obviously increases. The reason for this phenomenon is mainly that the appearance of old adhesion mortar and double ITZs increase the overall capillary potential macroscopically, thereby enhance the water absorption performance of concrete. It can be found that water penetration depth in concrete with R_{ra} of 50% advances nearly 5 mm more than it with R_{ra} of 0%, which is almost equivalent to 1.35 times depth of the latter. It can also be seen that the volatility of the water front gradually rises with the R_{ra} becoming greater. It can be attributed that the increase of RA causes greater heterogeneity of concrete matrix by randomly increasing weak areas. This phenomenon evidences that it is necessary to reduce water absorption performance of RA if higher R_{ra} are pursued.

Effect of Thickness of Old Mortar on Water Absorption

To investigate the influence of old adhesive mortar on water movement in RAC, without changing the size of the NC, the RAC model is generated. **Figure 10A** indicates that with the increase of d_m, wet front reaches much deeper. The quantitative depth of water penetration over time can be learned in **Figure 10B**. In the beginning, it indicates no significant difference. However, the influence of d_m becomes noticeable over time. The reason might be that the increase of d_m directly leads to the increase of volumetric ratio of old mortar to NA, which increases the overall porosity of RA and accelerates water movement. It is

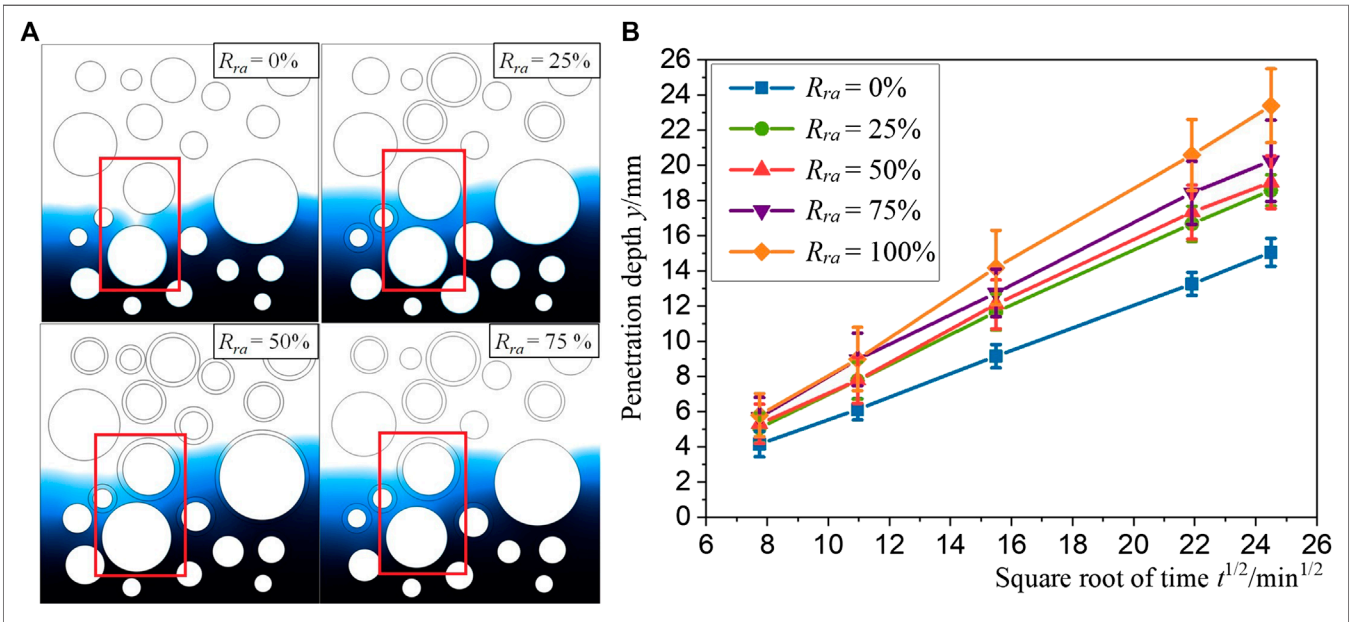

FIGURE 9 | (A) 2D cloud diagram and **(B)** profiles of moisture distribution with different R_{ra} (F_a = 50%).

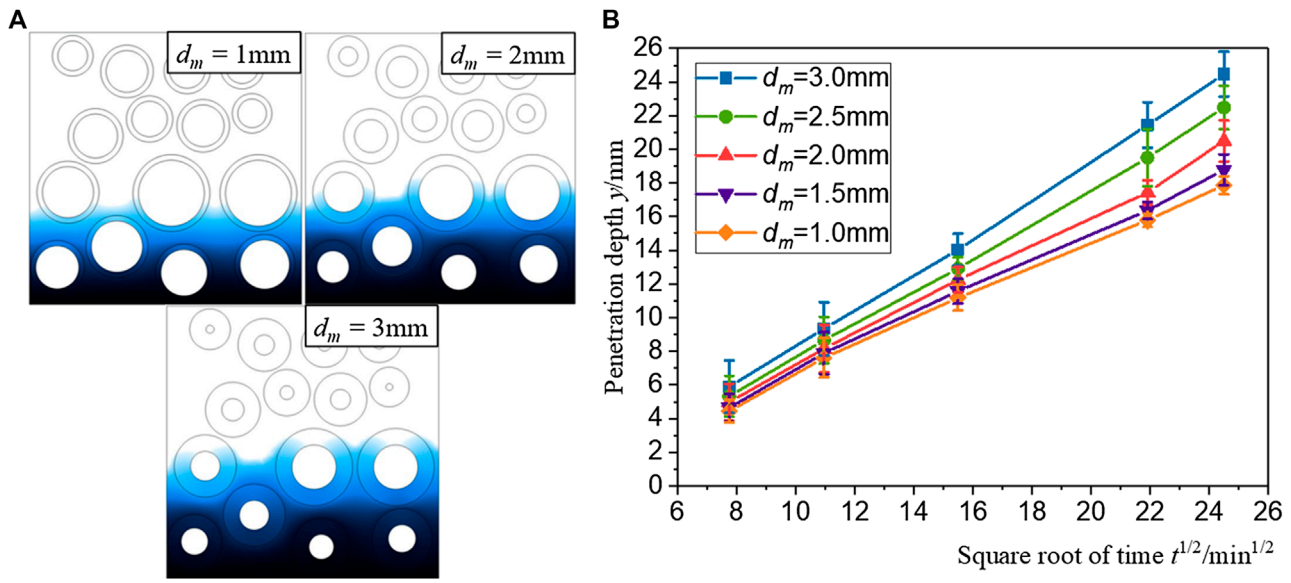

FIGURE 10 | (A) 2D cloud diagram and **(B)** profiles of moisture distribution with different d_m (F_a = 50%).

worth to mention that radius of NA is reduced to keep F_a unchanged. This means that when d_m increases, it not only promotes moisture absorption, but also reduces the blocking effect of the aggregate on the moisture. Therefore, in order to improve the durability of RAC, it is necessary to minimize d_m as much as possible.

Effect of Recycled Aggregate Volume Fraction on Water Absorption

F_a refers to the volume ratio of RA to the concrete matrix, which is assumed to area ratio in the 2D model. The presence of adhesive mortar and ITZ plays a certain role in promoting water transport, and that of NA plays a certain role in inhibiting water transport. When the F_a changes, the volume fraction of adhesive mortar and old aggregate has also changed accordingly. To investigate the influence of F_a, a RA model with d_m of 1.5 mm and particle size of 5–20 mm is generated.

The cloud map in **Figure 11A** shows that the change in F_a causes the difference in moisture distribution. However, this change seems to be reflected only in the difference of water front tortuosity instead of the depth. The water penetration depth of different F_a plotted against the square root of time is shown in

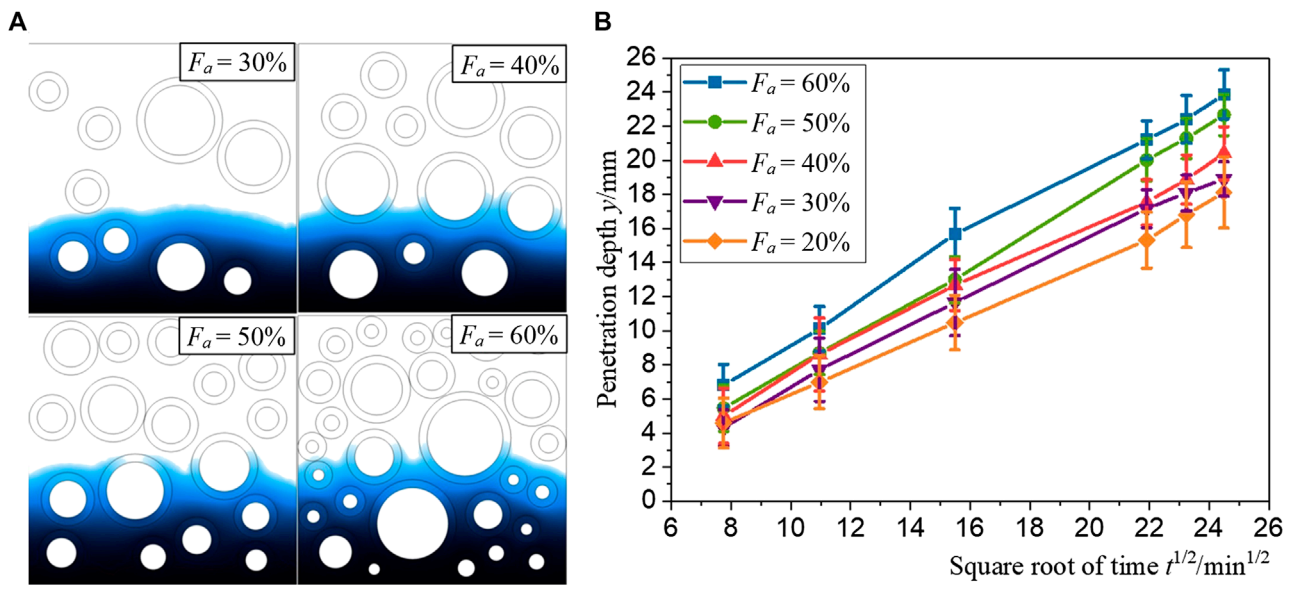

FIGURE 11 | (A) 2D cloud diagram and **(B)** profiles of moisture distribution with different F_a.

Figure 11B The profiles show that the slope slightly increases with the growth of volume fraction, which signifies that the velocity of water absorption increases. In *Validation of the RAC Models*, it has been reported that the hindrance effect of NA in NAC is the reason for the lower water absorption velocity than in cement mortar. In this section, one can see when F_a is relatively low, there is no RA in lower area of the concrete model, which makes the early moisture absorption only proceed in the mortar matrix and caused a lower velocity of moisture absorption during the first 60 min. This result indicates that the promoting effect of the old mortar exceeds the hindrance effect of NAs.

CONCLUSIONS

In this paper, the influence of aggregates and ITZs on the water transport performance of concrete are studied by combining the FEM and unsaturated theory. The numerical simulation approach is reported to evaluate the unsaturated transport process in RAC. The following conclusion can be drawn:

- On the basis of the non-homogeneous characteristic of concrete, the five-phase RAC model consisting of old aggregate, old adhesive mortar, old ITZ, new mortar, and new ITZ is established on the mesoscopic level. The capillary absorption equation in unsaturated RAC is reasonably derived, and the model parameters required in the equation are determined by the experimental method. The accuracy of the model and parameters are validated by comparing experimental data.
- The double ITZs and old mortar in RAC provide a more convenient channel for moisture movement, which results in moisture preferentially transporting along the aggregate instead of the new mortar matrix and causing the forefront of the wet front always forming behind the RA. This transmission mode greatly accelerates the capillary absorption rate of water in the concrete, thereby seriously threatening the durability of this concrete.
- The parameter sensitivity analysis of recycled concrete is conducted. It is found that as the thickness of the old adhesive mortar and the replacement rate of RA increase, the water absorption velocity in RAC is significantly accelerated. The moisture uptake velocity increases with the growth of aggregate volume fraction, but the amplitude is relatively small, which shows that the hindrance effect of NA on moisture is offset by the promotion effect of adhesive mortar with dual ITZs.

DATA AVAILABILITY STATEMENT

All datasets presented in this study are included in the article.

AUTHOR CONTRIBUTIONS

The corresponding author is responsible for ensuring that the descriptions are accurate. ZL: writing original draft, implementation of the numerical simulation and data curation. PZ: Formulation of overarching research goals and aims. JB: development of methodology. YH: investigation, modifying and editing.

FUNDING

Financial support for on-going projects by the Natural Science Foundation of China (51922052, U1706222, 51778309), Natural Science Foundation of Shandong Province (ZR2018JL018, ZR2019PEE001) and Open Research Fund Program of State Key Laboratory of Hydroscience and Engineering (SKLHSE-2019-C-04) is gratefully acknowledged.

REFERENCES

Bao, J., Li, S., Zhang, P., Ding, X., Xue, S., Cui, Y., et al. (2020a). Influence of the incorporation of recycled coarse aggregate on water absorption and chloride penetration into concrete. *Constr. Build. Mater.* 239, 117845. doi:10.1016/j.conbuildmat.2019.117845

Bao, J., Xue, S., Zhang, P., Dai, Z., and Cui, Y. (2020b). Coupled effects of sustained compressive loading and freeze-thaw cycles on water penetration into concrete. *Struct. Concr.* 2020, 1–11. doi:10.1002/suco.201900200

Burkan Isgor, O., and Razaqpur, A. G. (2004). Finite element modeling of coupled heat transfer, moisture transport and carbonation processes in concrete structures. *Cem. Concr. Compos.* 26 (1), 57–73. doi:10.1016/s0958-9465(02)00125-7

Caggiano, A., Said Schicchi, D., Mankel, C., Ukrainczyk, N., and Koenders, E. A. B. (2018). A mesoscale approach for modeling capillary water absorption and transport phenomena in cementitious materials. *Comput. Struct.* 200, 1–10. doi:10.1016/j.compstruc.2018.01.013

Chen, B., Song, E., and Cheng, X. (2013). "Plane-symmetrical simulation of flow and heat transport in fractured geological media: a discrete fracture model with comsol," in *Multiphysical testing of soils and shales* (Berlin, Germany: Springer), 149–154.

Folino, P., and Xargay, H. (2014). Recycled aggregate concrete – mechanical behavior under uniaxial and triaxial compression. *Constr. Build. Mater.* 56, 21–31. doi:10.1016/j.conbuildmat.2014.01.073

Fraj, A. B., and Idir, R. (2017). Concrete based on recycled aggregates – recycling and environmental analysis: a case study of Paris' region. *Constr. Build. Mater.* 157, 952–964. doi:10.1016/j.conbuildmat.2017.09.059

Kim, S.-W., and Yun, H.-D. (2014). Evaluation of the bond behavior of steel reinforcing bars in recycled fine aggregate concrete. *Cem. Concr. Compos.* 46, 8–18. doi:10.1016/j.cemconcomp.2013.10.013

Lam, P. T. I., Yu, A. T. W., Wu, Z., and Poon, C. S. (2019). Methodology for upstream estimation of construction waste for new building projects. *J. Clean. Prod.* 230, 1003–1012. doi:10.1016/j.jclepro.2019.04.183

Li, X., Chen, S., Xu, Q., and Xu, Y. (2017). Modeling the three-dimensional unsaturated water transport in concrete at the mesoscale. *Comput. Struct.* 190, 61–74. doi:10.1016/j.compstruc.2017.05.005

Li, X., Chen, S., Xu, Q., and Xu, Y. (2018). Modeling capillary water absorption in concrete with discrete crack network. *J. Mater. Civ. Eng.* 30 (1), 04017263. doi:10.1061/(asce)mt.1943-5533.0002122

Li, X., Xu, Y., and Chen, S. (2016). Computational homogenization of effective permeability in three-phase mesoscale concrete. *Constr. Build. Mater.* 121, 100–111. doi:10.1016/j.conbuildmat.2016.05.141

Liu, Q.-f., Feng, G.-l., Xia, J., Yang, J., and Li, L.-y. (2018). Ionic transport features in concrete composites containing various shaped aggregates: a numerical study. *Compos. Struct.* 183, 371–380. doi:10.1016/j.compstruct.2017.03.088

Lockington, D., Parlange, J.-Y., and Dux, P. (1999). Sorptivity and the estimation of water penetration into unsaturated concrete. *Mater. Struct.* 32 (5), 342. doi:10.1007/BF02479625

Ludirdja, D., Berger, R. L., and Young, J. F. (1989). Simple method for measuring water permeability of concrete. *ACI Mater. J.* 86 (5), 433–439. doi:10.14359/2000

McDonald, P. J., Istok, O., Janota, M., Gajewicz-Jaromin, A. M., and Faux, D. A. (2020). Sorption, anomalous water transport and dynamic porosity in cement paste: a spatially localised 1H NMR relaxation study and a proposed mechanism. *Cem. Concr. Res.* 133, 106045. doi:10.1016/j.cemconres.2020.106045

Mualem, Y. (1976). A new model for predicting the hydraulic conductivity of unsaturated porous media. *Water Resour. Res.* 12 (3), 513–522. doi:10.1029/WR012i003p00513

Munir, M. J., Kazmi, S. M. S., Wu, Y.-F., Patnaikuni, I., Zhou, Y., and Xing, F. (2020). Stress strain performance of steel spiral confined recycled aggregate concrete. *Cem. Concr. Compos.* 108, 103535. doi:10.1016/j.cemconcomp.2020.103535

Oikonomou, N. D. (2005). Recycled concrete aggregates. *Cem. Concr. Compos.* 27 (2), 315–318. doi:10.1016/j.cemconcomp.2004.02.020

Phillipson, M. C., Baker, P. H., Davies, M., Ye, Z., McNaughtan, A., Galbraith, G. H., et al. (2007). Moisture measurement in building materials: an overview of current methods and new approaches. *Build. Serv. Eng. Res. Technol.* 28 (4), 303–316. doi:10.1177/0143624407084184

Rucker-Gramm, P., and Beddoe, R. E. (2010). Effect of moisture content of concrete on water uptake. *Cem. Concr. Res.* 40 (1), 102–108. doi:10.1016/j.cemconres.2009.09.001

Smyl, D., Hallaji, M., Seppänen, A., and Pour-Ghaz, M. (2016). Quantitative electrical imaging of three-dimensional moisture flow in cement-based materials. *Int. J. Heat Mass Tran.* 103, 1348–1358. doi:10.1016/j.ijheatmasstransfer.2016.08.039

Song, Q., Zhao, H., Jia, J., Yang, L., Lv, W., Bao, J., et al. (2020). Pyrolysis of municipal solid waste with iron-based additives: a study on the kinetic, product distribution and catalytic mechanisms. *J. Clean. Prod.* 258, 120682. doi:10.1016/j.jclepro.2020.120682

Swartzendruber, D. (1969). "The flow of water in unsaturated soils," in *Flow through porous media*. Editor R. J. M. De Weist (New York, NY: Academic Press), 215–292.

Tam, V. W. Y., Gao, X. F., and Tam, C. M. (2005). Microstructural analysis of recycled aggregate concrete produced from two-stage mixing approach. *Cem. Concr. Res.* 35 (6), 1195–1203. doi:10.1016/j.cemconres.2004.10.025

Tam, V. W. Y., Soomro, M., and Evangelista, A. C. J. (2018). A review of recycled aggregate in concrete applications (2000–2017). *Constr. Build. Mater.* 172, 272–292. doi:10.1016/j.conbuildmat.2018.03.240

Tian, Y., Zhang, P., Zhao, K., Du, Z., and Zhao, T. (2020). Application of Ag/AgCl sensor for chloride monitoring of mortar under dry-wet cycles. *Sensors* 20 (5), 1394. doi:10.3390/s20051394

van Genuchten, M. T. (1980). A closed-form equation for predicting the hydraulic conductivity of unsaturated soils. *Soil Sci. Soc. Am. J.* 44 (5), 892–898. doi:10.2136/sssaj1980.03615995004400050002x

Velay-Lizancos, M., Vazquez-Burgo, P., Restrepo, D., and Martinez-Lage, I. (2018). Effect of fine and coarse recycled concrete aggregate on the mechanical behavior of precast reinforced beams: comparison of FE simulations, theoretical, and experimental results on real scale beams. *Constr. Build. Mater.* 191, 1109–1119. doi:10.1016/j.conbuildmat.2018.10.075

Wang, C., and Xiao, J. (2018). Evaluation of the stress-strain behavior of confined recycled aggregate concrete under monotonic dynamic loadings. *Cem. Concr. Compos.* 87, 149–163. doi:10.1016/j.cemconcomp.2017.12.012

Wang, L., Bao, J., and Ueda, T. (2016). Prediction of mass transport in cracked-unsaturated concrete by mesoscale lattice model. *Ocean Eng.* 127, 144–157. doi:10.1016/j.oceaneng.2016.09.044

Wang, R., Yu, N., and Li, Y. (2020). Methods for improving the microstructure of recycled concrete aggregate: a review. *Constr. Build. Mater.* 242, 118164. doi:10.1016/j.conbuildmat.2020.118164

Wang, Y., Cao, Y., Zhang, P., Ma, Y., Zhao, T., Wang, H., et al. (2019). Water absorption and chloride diffusivity of concrete under the coupling effect of uniaxial compressive load and freeze-thaw cycles. *Constr. Build. Mater.* 209, 566–576. doi:10.1016/j.conbuildmat.2019.03.091

Witherspoon, P. A., Wang, J. S. Y., Iwai, K., and Gale, J. E. (1980). Validity of Cubic Law for fluid flow in a deformable rock fracture. *Water Resour. Res.* 16 (6), 1016–1024. doi:10.1029/WR016i006p01016

Wyrzykowski, M., McDonald, P. J., Scrivener, K. L., and Lura, P. (2017). Water redistribution within the microstructure of cementitious materials due to temperature changes studied with ^{1}H NMR. *J. Phys. Chem. C* 121 (50), 27950–27962. doi:10.1021/acs.jpcc.7b08141

Xiao, J., Li, W., Corr, D. J., and Shah, S. P. (2013). Effects of interfacial transition zones on the stress–strain behavior of modeled recycled aggregate concrete. *Cem. Concr. Res.* 52, 82–99. doi:10.1016/j.cemconres.2013.05.004

Xiao, J., Li, W., Fan, Y., and Huang, X. (2012). An overview of study on recycled aggregate concrete in China (1996–2011). *Constr. Build. Mater.* 31, 364–383. doi:10.1016/j.conbuildmat.2011.12.074

Xue, S., Zhang, P., Bao, J., He, L., Hu, Y., and Yang, S. (2020). Comparison of Mercury Intrusion Porosimetry and multi-scale X-ray CT on characterizing the microstructure of heat-treated cement mortar. *Mater. Charact.* 160, 110085. doi:10.1016/j.matchar.2019.110085

Zhang, P., Dai, Y., Wang, W., Yang, J., Mo, L., Guo, W., et al. (2020). Effects of magnesia expansive agents on the self-healing performance of microcracks in strain-hardening cement-based composites (SHCC). *Mater. Today Commun.* 25, 101421. doi:10.1016/j.mtcomm.2020.101421

Zhang, P., Hou, D., Liu, Q., Liu, Z., and Yu, J. (2017a). Water and chloride ions migration in porous cementitious materials: an experimental and molecular dynamics investigation. *Cem. Concr. Res.* 102, 161–174. doi:10.1016/j.cemconres.2017.09.010

Zhang, P., Wittmann, F. H., Vogel, M., Müller, H. S., and Zhao, T. (2017b). Influence of freeze-thaw cycles on capillary absorption and chloride penetration into concrete. *Cem. Concr. Res.* 100, 60–67. doi:10.1016/j.cemconres.2017.05.018

Zhao, H., Jiang, K., Yang, R., Tang, Y., and Liu, J. (2020). Experimental and theoretical analysis on coupled effect of hydration, temperature and humidity in early-age cement-based materials. *Int. J. Heat Mass Transf.* 146, 118784. doi:10.1016/j.ijheatmasstransfer.2019.118784

Zhao, K., Qiao, Y., Zhang, P., Bao, J., and Tian, Y. (2020). Experimental and numerical study on chloride transport in cement mortar during drying process. *Constr. Build. Mater.* 258, 119655. doi:10.1016/j.conbuildmat.2020.119655

Conflict of Interest: The authors declare that the research was conducted in the absence of any commercial or financial relationships that could be construed as a potential conflict of interest.

Copyright © 2020 Liu, Zhang, Bao and Hu. This is an open-access article distributed under the terms of the Creative Commons Attribution License (CC BY). The use, distribution or reproduction in other forums is permitted, provided the original author(s) and the copyright owner(s) are credited and that the original publication in this journal is cited, in accordance with accepted academic practice. No use, distribution or reproduction is permitted which does not comply with these terms.

frontiers in Materials

ORIGINAL RESEARCH
published: 05 October 2020
doi: 10.3389/fmats.2020.590661

Optimum Design of High-Strength Concrete Mix Proportion for Crack Resistance Using Artificial Neural Networks and Genetic Algorithm

Li Yue[1], *Li Hongwen*[1], *Li Yinuo*[2] *and Jin Caiyun*[3]*

[1]Key Laboratory of Urban Security and Disaster Engineering of Ministry of Education, Beijing Key Laboratory of Earthquake Engineering and Structural Retrofit, Beijing University of Technology, Beijing, China, [2]Materials Engineering CO-OP, McGill University, Montreal, Canada, [3]College of Applied Sciences, Beijing University of Technology, Beijing, China

The fact that high-strength concrete is easily to crack has a significant negative impact on its durability and strength. This paper gives an optimum design method of high-strength concrete for improving crack resistance based on orthogonal test artificial neural networks (ANN) and genetic algorithm. First, orthogonal test is operated to determine the influence of the concrete mix proportion to the slump, compressive strength, tensile strength, and elastic modulus, followed by calculating and predicting the concrete performance using ANN. Based on results from orthogonal test and ANN, a functional relationship among slump, compressive strength, tensile strength, elastic modulus, and mix proportion has been built. On this basis, using the widely used shrinkage and creep models, the functional relationship between the concrete cracking risk coefficient and the mix proportion is derived, and finally genetic algorithm is used to optimize the concrete mix proportion to improve its crack resistance. The research results showed that, compared with the control concrete, the cracking risk coefficient of the optimized concrete was reduced by 25%, and its crack resistance was significantly improved.

Keywords: optimum design, concrete mix proportion, crack resistance, artificial neural networks, genetic algorithm

OPEN ACCESS

Edited by:
Dongshuai Hou,
Qingdao University of Technology, China

Reviewed by:
Bing Chen,
Shanghai Jiao Tong University, China
Jiaqi Li,
University of California, Berkeley, United States

***Correspondence:**
Jin Caiyun
jincaiyun@bjut.edu.cn

Specialty section:
This article was submitted to Computational Materials Science, a section of the journal Frontiers in Materials

Received: *02 August 2020*
Accepted: *03 September 2020*
Published: *05 October 2020*

Citation:
Yue L, Hongwen L, Yinuo L and Caiyun J (2020) Optimum Design of High-Strength Concrete Mix Proportion for Crack Resistance Using Artificial Neural Networks and Genetic Algorithm. Front. Mater. 7:590661. doi: 10.3389/fmats.2020.590661

INTRODUCTION

The characteristics of high-strength concrete are the low water-binder ratio and the extensive use of mineral admixtures. Therefore, compared with ordinary concrete, high-strength concrete has the properties of rapid early hydration, rapid internal temperature rise, rapid reduction of internal humidity, and large shrinkage, which leads to very prominent early cracking phenomenon (Yun-sheng et al., 2002). The early cracking of concrete seriously reduces its durability and safety, so it is of great significance to prevent early cracking of concrete (Bentz et al., 1999; Wittmann, 2002; Liu et al., 2012).

There are many factors that may affect the cracking of concrete, such as its compressive and tensile strength, elastic modulus, shrinkage, and creep (Zhang et al., 2012; Huang et al., 2020; Li et al., 2020; Xin et al., 2020). Bruce Menu studied the effect of shrinkage of concrete on cracking. He found that when the water-to-binder ratio decreases, the shrinkage of concrete increases as well as the risk of cracking (Menu et al., 2020). Inamullah Khan found that the creep coefficient has a significant impact on the cracking risk of concrete. The higher the creep coefficient, the lower the cracking risk of concrete (Khan et al., 2019). Bendimerad et al. (2020) have observed the same phenomenon. The concrete mix proportion determines its performance (Li et al., 2019). In order to reduce the cracking risk of concrete, it is an effective method to

directly optimize the mix proportion. However, the current methods to improve the crack resistance of concrete are mainly use of internal curing and incorporation of fibers (Schroefl et al., 2012; Feng et al., 2019). The research on the optimization of concrete mix proportion is urgently needed.

Artificial neural networks (ANN) have already been applied in the field of concrete research, mainly to predict various properties of concrete (Yeh, 2007; Far et al., 2009; Mangalathu et al., 2018; Abellan Garcia et al., 2020). For example, Chithra applied regression analysis and ANN, respectively, to predict the compressive strength of concrete mixed with copper slag. The results show that results predicted by ANN were more accurate (Chithra et al., 2016). Xu et al. (2019) used ANN to predict the performance of recycled aggregate concrete under triaxial loads. Zhou et al. (2020) used ANN to predict the interface bond strength between fiber and concrete. It has been found that the prediction results of the ANN had high accuracy and good application effects. Many studies have shown that it is feasible to predict the performance of concrete through ANN.

Genetic algorithm (GA) is a parallel random search optimization that combines the principles of biological evolution and genetic mechanism. As a kind of biological modeling algorithm, GA has the advantages of global search, which consideration of whether the function is continuous, differentiable and derivable is unnecessary. Therefore, GA has been put into extensive use in various fields (Shahnewaz et al., 2016; Chowdhury and Garai, 2017). In the field of concrete, GA is often used to optimize the mix proportion of concrete. Considering the cost, strength, workability and carbonation durability of concrete, Wang (2019) used GA to optimize the content of fly ash and mineral powder, and obtained satisfactory results. Lee et al. (2009) applied GA to optimize the mix proportion of concrete, which reduced the price of unilateral concrete. Rita et al. (2018) also optimized the concrete mix proportion by GA to reduce the project cost. However, there are only few reports on the use of GA to optimize the mix proportion of concrete in order to improve crack resistance.

This paper optimizes the mix proportion of concrete based on orthogonal test, ANN and GA to improve its cracking resistance. First, orthogonal tests are used to determine the effects of concrete components on slump, compressive strength, tensile strength, and elastic modulus. Then ANN is used to predict the above properties. Based on the results of orthogonal test and ANN prediction, the functional relationship between concrete slump, compressive strength, tensile strength, and elastic modulus and the mix proportion was fitted. On this basis, shrinkage and creep models are used to derive the functional relationship between the concrete cracking risk coefficient and the mix proportion. In the end, GA is used to optimize the concrete mix ratio to proportion its crack resistance.

MATERIALS AND METHODS

Material

The cement used is PO42.5 Portland cement and its compressive strength of 28 days is 47.3 MPa. The type of fly ash is Class F Class I, while the water demand ratio is 88%. The slag grade is S95 and its 7 days activity index is 78%. The pozzolanic activity index of silica fume is 120%. The chemical composition of cement, fly ash, slag, and silica fume is shown in **Table 1**. The fine aggregate is made of finely graded river sand with a fineness modulus of 2.65. The coarse aggregate is made of continuously graded calcareous gravel with a particle size of 5–20 mm. The type of water reducing agent is polycarboxylate superplasticizers with a water reduction rate of 33%.

TABLE 1 | The chemical components of cementitious materials (wt%).

	CaO	SiO_2	Al_2O_3	Fe_2O_3	SO_3	MgO	Loi
Cement	59.1	24.2	7.6	2.9	2.1	1.9	2.2
Fly ash	3.2	57.2	25.5	7.7	0.5	2.2	3.7
Slag	42.5	38.7	7.5	0.4	0.9	6.9	3.1
Silica fume	0.4	93.4	0.4	0.8	0.5	0.3	4.0

Concrete Mix Proportion

The goal is to prepare concrete with its compressive strength above 60 MPa. In order to establish a mathematical model between the performance of concrete and its mix proportion, six factors affecting the mix proportion have been determined, expressed as x_1–x_6: water to binder ratio (x_1), sand ratio (x_2), the amount of cement per cubic meter of concrete (x_3), the ratio of fly ash mass to cementitious materials mass (x_4), the ratio of slag mass to cementitious materials mass (x_5), and the ratio of silica fume mass to cementitious materials mass (x_6). In order to effectively analyze the influence of various factors on the performance of concrete, orthogonal experiments are used. Since each factor is selected at five levels, a total of 25 sets of experiments are designed. The concrete mix proportion is shown in **Table 2**. The mass of polycarboxylate superplasticizers in all proportions is 2.4% of the mass of cementitious materials.

TABLE 2 | Concrete mix proportion.

No	x_1 (%)	x_2 (%)	x_3 (kg/m^3)	x_4 (%)	x_5 (%)	x_6 (%)
E1	27	43	240	15	11	4
E2	27	46	270	20	14	5.5
E3	27	49	300	25	17	7
E4	27	52	330	30	20	8.5
E5	27	55	360	35	23	10
E6	29	43	270	25	20	10
E7	29	46	300	30	23	4
E8	29	49	330	35	11	5.5
E9	29	52	360	15	14	7
E10	29	55	240	20	17	8.5
E11	31	43	300	35	14	8.5
E12	31	46	330	15	17	10
E13	31	49	360	20	20	4
E14	31	52	240	25	23	5.5
E15	31	55	270	30	11	7
E16	33	43	330	20	23	7
E17	33	46	360	25	11	8.5
E18	33	49	240	30	14	10
E19	33	52	270	35	17	4
E20	33	55	300	15	20	7
E21	35	43	360	30	17	5.5
E22	35	46	240	35	20	7
E23	35	49	270	15	23	8.5
E24	35	52	300	20	11	10
E25	35	55	330	25	14	4

Method

Slump, Strength, and Elastic Modulus

The slump is measured in accordance with the test method in "Standard for test method of performance on ordinary fresh concrete" (GB/T 50080-2016). Compressive strength, tensile strength, and modulus of elasticity are determined in accordance with the test methods in "Standard for test methods for mechanical properties on ordinary concrete" (GB/T 50081-2016). The size of the sample used in the compressive strength test is 100 × 100 × 100 mm. The size of the sample used in the tensile strength and elastic modulus test is 100 × 100 × 300 mm. The loading rate of compressive strength test and tensile strength test is 0.8 MPa/s.

Shrinkage and Creep

The test method of shrinkage and creep refers to the "Standard for test methods of long-term performance and durability of ordinary concrete" (GB/T 50082-2009). The size of the sample for shrinkage test is 100 × 100 × 515 mm. The size of specimen for creep test is 100 × 100 × 400 mm, while the loading stress is 40% of its compressive strength. The curing temperature for shrinkage and creep is 20 ± 2°C, and the relative humidity is 65%. The drying shrinkage test and creep test were carried out when the concrete age was 1 day. The creep performance of concrete is usually expressed in terms of the creep coefficient and its calculation method is shown in **Eq. 1**:

$$\varphi_t = \left(\frac{\Delta L_t - \Delta L_0}{L_b}\right) \Big/ \varepsilon_0 \tag{1}$$

where φ_t is the creep coefficient after loading for t days; ΔL_t is the total deformation after loading for t days; ΔL_0 is the initial deformation during loading; L_b is the measured gauge length. ε_t is the same age shrinkage and ε_0 is the initial strain during loading.

Early Cracking Test

A slab cracking frame is used to detect the cracking of concrete, as shown in **Figure 1**. The size of the slab cracking frame is 800 × 600 × 100 mm. The side plates, bolts and are applied to fix the steel formwork of the cracking frame, as well as the crack inducer to induce the early concrete cracking caused by shrinkage.

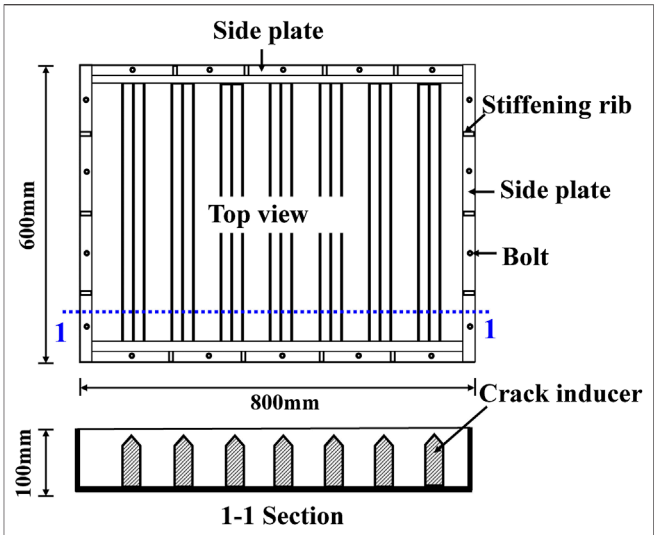

FIGURE 1 | Schematic diagram of slab cracking frame test.

PREDICTION OF CONCRETE PROPERTIES BY ARTIFICIAL NEURAL NETWORKS

Artificial Neural Networks Calculation Process

The process of ANN is shown in **Figure 2A**. First, the system assigns weights to each group of input data. Then trains according to the set parameters to calculate the predicted value. After that, calculate the error between the predicted value and the test value. If the error meets the requirements, the predicted value is output. If the error is too large, the system resets weights and re-predict until the error meets the requirements. The simplest forward artificial neural network could be divided into three layers: input layer, hidden layer, and output layer, as shown in **Figure 2B**. The role of the input layer is to input data. Hidden layer is for data analysis and calculation. Output layer is to output predicted values. Calculation method of the ANN is explained in detail by following.

Processing of Input Data

When the magnitude of each group of input data differs greatly, the accuracy of the system's prediction is reduced. Therefore, in order to avoid this situation, it is necessary to normalize the input data on each neuron. The data is converted to [0,1], as shown in **Eq. 2** (Yan and Lin, 2016).

$$\overline{x}_i = \frac{x_i - x_{\min}}{x_{\max} - x_{\min}} \tag{2}$$

where x_i is the ith data before normalization. $x_{\min}$ and $x_{\max}$ are the minimum and maximum of all data before normalization respectively. $\overline{x}_i$ is the ith data after normalization.

Weights and Activation Function

Based on the characteristics of neurons, it is needed to assign weights to input data and set activation functions (also known as transfer function).

The sum of data is expressed by weight and input data, as shown in **Eq. 3**.

$$net_j = \sum_{i=1}^{n} \overline{x}_i \omega_{ij} \tag{3}$$

where ω_{ij} is the weight from the ith neuron in the previous layer to the jth neuron in the current layer. net_j represents the sum of the weighted inputs of the jth neuron.

After the neuron receives the information, data needs to be processed and transmitted. At this time, an activation function needs to be set to output data. The general form of the activation function is shown in **Eq. 4**.

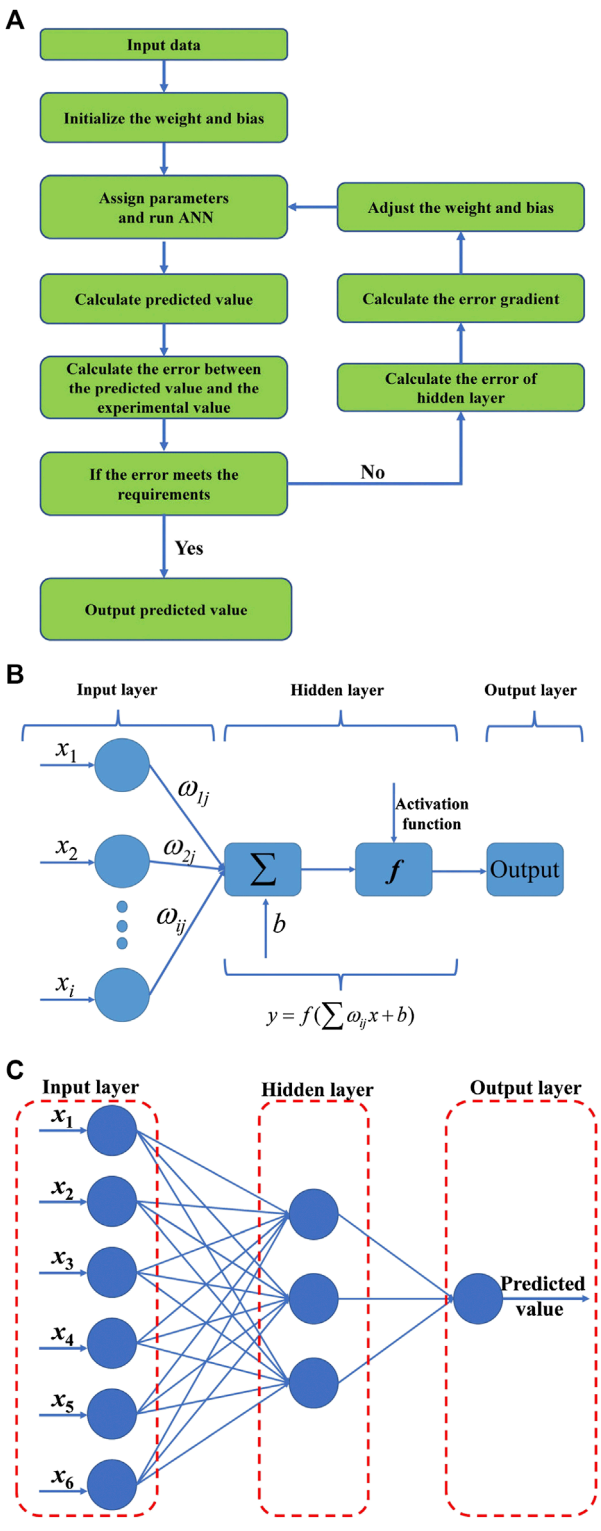

FIGURE 2 | The process and models of ANN. **(A)** the process of ANN, **(B)** a typical neuron Model, **(C)** the ANN model used in the test.

$$y = f\left(net_j + b_j\right) \tag{4}$$

where b_j is the bias.

Commonly used activation functions are Purelin function (**Eq. 5**), Sigmoid function (**Eq. 6**), Tansigmoid (**Eq. 7**) function, and Relu function (**Eq. 8**).

$$Purelin\,(x) = x \tag{5}$$

$$Sigmoid\,(x) = \frac{1}{1+e^{-x}} \tag{6}$$

$$Tansigmoid\,(x) = \frac{e^{x}-e^{-x}}{e^{x}+e^{-x}} \tag{7}$$

$$Relu\,(x) = max\,(0,x) \tag{8}$$

Training: When the predicted value calculated by the system is not equal to the expected value, an error E_{error} occurs. The weight between the input layer and the hidden layer is ω_{ij}, the weight between the hidden layer and the output layer is ω_{jk}, d represents the expected output, then:

$$E_{error} = \frac{1}{2}\sum_{k=1}^{l}\left\{d - f\left[\sum_{j=0}^{m}\omega_{jk} f\left(\sum_{i=0}^{n}\omega_{ij}x_i\right)\right]\right\}^2 \tag{9}$$

According to **Eq. 9**, the error is determined by the weight of each layer. Therefore, training is a process which continuously adjusts the weight of each layer to make the error meet the requirements. The principle of weight adjustment is to reduce the error. Therefore, the adjustment of the weight is proportional to the gradient of the error, see **Eqs 10** and **11**.

$$\Delta\omega_{ij} = -\chi\frac{\partial E_{error}}{\partial\omega_{ij}} \tag{10}$$

$$\Delta\omega_{jk} = -\chi\frac{\partial E_{error}}{\partial\omega_{jk}} \tag{11}$$

where χ is the learning efficiency, and the value is between (0,1).

Artificial Neural Networks Model Establishment

It can be seen from Artificial Neural Networks Calculation Process that the model first requires the ANN structure, which is the number of nodes in each layer (the number of neurons) and the number of hidden layers. For the prediction of concrete performance, a simple ANN structure of three layers can meet the requirements (Ji et al., 2006). The experiment set six variables, so the number of nodes in the input layer is 6. Although it is necessary to predict multiple properties of concrete, only one type is predicted at a time. Therefore, the number of nodes in the output layer is 1. The number of nodes in the hidden layer can be determined by **Eq. 12** (Peng and Gao, 2018). In this case, the number of nodes in the hidden layer is 3. The ANN model used in the test is shown in **Figure 2C**, where x_1–x_6 represent the water to binder ratio, sand ratio, the amount of cement per cubic meter of concrete, the ratio of fly ash mass to cementitious materials mass,

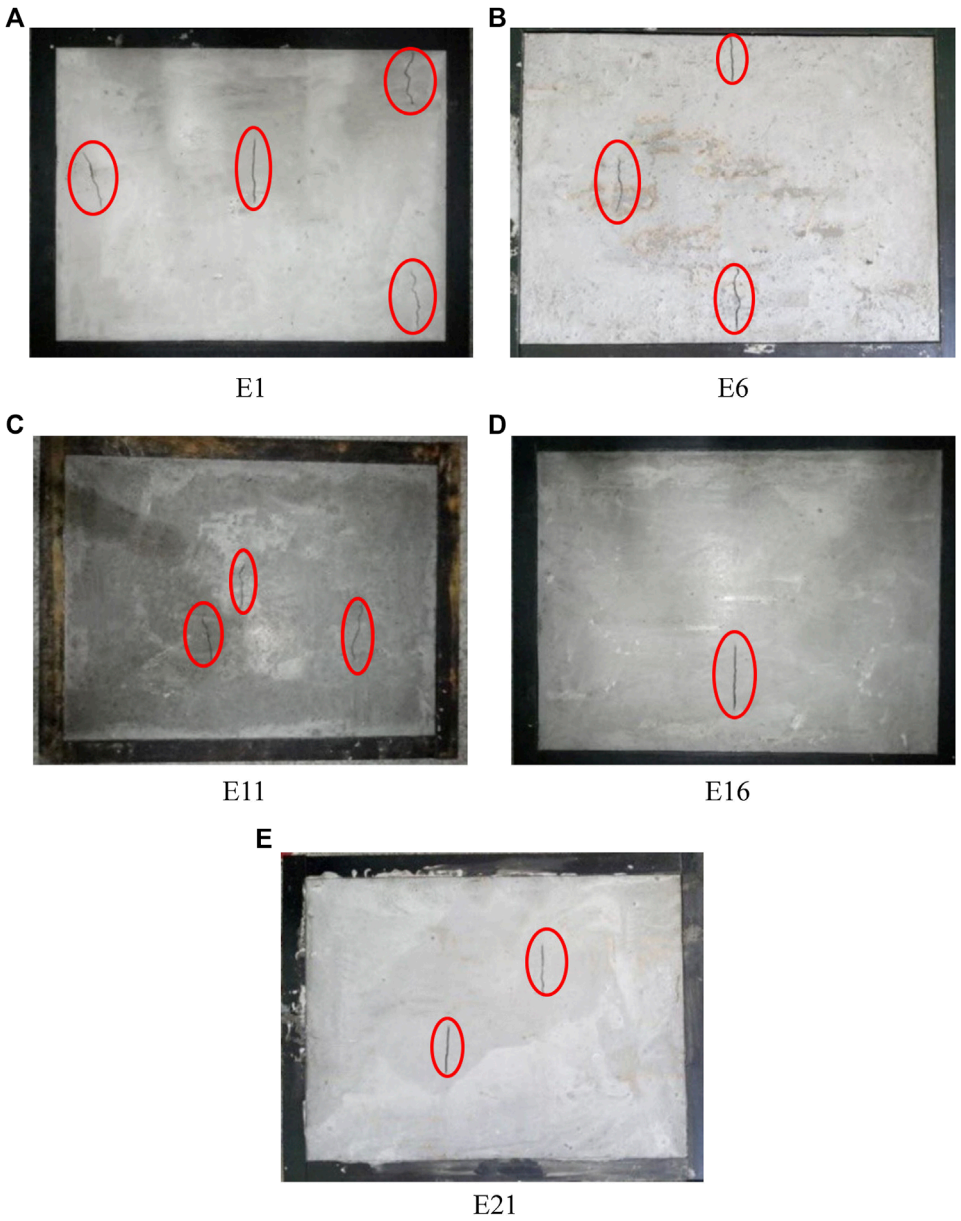

FIGURE 3 | Cracking state of concrete at the age of 3 days. **(A)** E1, **(B)** E6, **(C)** E11, **(D)** E16, **(E)** E21.

the ratio of slag mass to cementitious materials mass and the ratio of silica fume mass to cementitious materials mass, respectively.

$$m = \log_2 n \tag{12}$$

Where m is the number of hidden layer nodes, and n is the number of input layer nodes.

The weight is set to a value between [−1,1]. For the prediction of concrete performance, many studies have shown that the Tansigmoid function has good applicability (Yan et al., 2017). Therefore, this paper chooses the Tansigmoid function as the activation function. The learning efficiency is an empirical value, which is 0.1 in this paper (Yan and Lin, 2016).

Performance Assessment Indices

The performances of ANN prediction are usually evaluated by Mean Absolute Error (MAE), Mean Square Error (MSE), Root Mean Square Error (RMSE), and Correlation Coefficient (R^2), which is shown in **Eqs 13–16**. MAE demonstrates the residual error between the target values and predicted values for each data set. MSE demonstrates the mean of the sum of squares of the errors of the target values and predicted values. RMSE demonstrates the square root of average residual error between the target values and predicted values for each data set. The smaller the MAE, MSE, and RMSE, the larger R^2, the better the prediction performance of ANN.

TABLE 3 | Concrete performance test results and ANN prediction results.

No	Slump (mm)		Compressive strength (MPa)		Tensile strength (MPa)		Elastic Modulus (MPa)	
	Exp	Pre	Exp	Pre	Exp	Pre	Exp	Pre
E1	248	251	76.1	76.4	6.74	6.59	37.37	37.08
E2	255	252	77.3	76.7	6.92	6.81	37.43	36.75
E3	252	254	77.4	76.9	6.97	7.02	37.46	37.15
E4	261	257	78.4	77.1	7.16	7.09	37.51	37.93
E5	258	260	78.6	77.3	7.25	7.10	37.54	37.01
E6	260	258	72.8	71.1	6.79	6.80	37.10	37.93
E7	262	261	70.3	71.6	6.61	6.54	37.01	36.14
E8	265	266	72.4	73.0	6.56	6.57	37.07	36.76
E9	256	257	74.8	76.2	6.83	6.81	37.25	38.02
E10	261	261	71.9	72.2	6.53	6.68	37.05	36.23
E11	267	270	66.9	66.1	6.04	6.07	36.33	37.16
E12	259	260	69.9	69.6	6.31	6.39	36.97	35.78
E13	262	261	68.4	70.1	6.07	6.14	36.43	36.63
E14	266	268	66.5	66.0	5.87	5.90	36.06	36.02
E15	271	271	66.4	66.9	5.93	5.95	36.01	36.35
E16	263	263	66.2	64.7	5.84	5.72	35.97	36.08
E17	265	267	67.9	65.3	5.89	5.70	36.41	36.71
E18	272	273	65.7	63.8	5.64	5.66	35.95	36.74
E19	278	276	63.9	63.9	5.48	5.29	35.54	35.01
E20	263	265	66.1	65.2	5.74	5.64	35.96	36.86
E21	272	273	63.1	63.5	5.18	5.37	35.25	34.62
E22	277	279	62.2	63.3	5.06	5.33	35.07	35.88
E23	268	268	62.6	63.5	5.27	5.45	35.13	35.72
E24	276	274	63.2	63.6	5.36	5.47	35.27	34.96
E25	280	277	61.8	63.7	5.05	5.08	34.99	35.27

Note: Exp is the experimental value and Pre is the predicted value.

$$MAE = \frac{1}{N}\sum_{i=1}^{N}|E_i - P_i| \tag{13}$$

$$MSE = \frac{1}{N}\sum_{i=1}^{N}(E_i - P_i)^2 \tag{14}$$

$$RMSE = \sqrt{\frac{1}{N}\sum_{i=1}^{N}(E_i - P_i)^2} \tag{15}$$

$$R^2 = \frac{\left[\sum_{i=1}^{N}(E_i - \overline{E})(P_i - \overline{P})\right]^2}{\sum_{i=1}^{N}(E_i - \overline{E})^2 \sum_{i=1}^{N}(P_i - \overline{P})^2} \tag{16}$$

where E_i is the ith experimental value, $\overline{E}$ is the average of the experimental values, P_i is the ith predicted value, $\overline{P}$ is the average of the predicted values.

Artificial Neural Networks Prediction Results

Table 3 shows the test results and ANN prediction results of all the 25 groups of concrete properties in Concrete Mix Proportion. In the table, Exp represents the test results and Pre represents the ANN prediction results. **Table 4** shows the MAE, MSE, RMSE, and R^2 values of slump, compressive strength, tensile strength, elastic modulus, and shrinkage. For each performance, the error between the predicted value and the test value was very small and R^2 was above 0.94, which shows that ANN has very high accuracy in predicting concrete performance.

OPTIMIZATION CONCRETE FOR CRACK RESISTANCE BY GENETIC ALGORITHM

Mathematical Model Between Concrete Performance and Mix Proportion

The objection of this paper was to improve crack resistance of concrete, thus we should find a criterion to evaluate it firstly. According to the concrete cracking criterion (Bendimerad et al., 2016), the cracking risk coefficient η is used to evaluate the early anti-cracking performance of concrete, as shown in **Eq. 17**:

$$\eta = \frac{E(t) \cdot \varepsilon_{sh-e}(t)}{f_t(t)} \tag{17}$$

where $f_t(t)$ is the tensile strength of concrete at age of t, $E(t)$ is the elastic modulus of concrete at the age of t, $\varepsilon_{sh-e}(t)$ is the effective shrinkage strain at the age of t.

When $\eta < 0.7$, the concrete does not crack; when $0.7 \le \eta \le 1.0$, the concrete may crack; when $\eta > 1.0$, the concrete cracks.

Studies have shown (Andrade et al., 1999; Gao et al., 2013) that the effective shrinkage strain is the result of the combined effect of

TABLE 4 | Assessment indices for prediction.

Properties	MAE	MSE	RMSE	R^2
Slump	1.650	3.897	1.974	0.941
Compressive strength	0.987	1.369	1.170	0.952
Tensile strength	0.097	0.014	0.120	0.970
Elastic modulus	0.125	0.021	0.145	0.972

concrete shrinkage strain and creep strain (the strain produced by concrete creep), as shown in **Eq. 18**:

$$\varepsilon_{sh-e}(t) = \varepsilon_{sh}(t) - \varepsilon_{creep}(t, t_0) \tag{18}$$

where t and t_0 are the age of concrete and the age of concrete when loaded respectively, $\varepsilon_{sh}(t)$ is the shrinkage strain at the age t, $\varepsilon_{creep}(t, t_0)$ is the shrinkage strain caused by creep during the concrete age $(t\text{-}t_0)$.

Bentz (2008) believes that the relationship between creep strain and effective shrinkage strain can be expressed by the creep coefficient, as shown in **Eq. 19**:

$$\varphi(t, t_0) = \frac{\varepsilon_{creep}(t, t_0)}{\varepsilon_{sh-e}(t, t_0)} \tag{19}$$

where $\varphi(t, t_0)$ is the creep coefficient during the early age of concrete $(t\text{-}t_0)$.

Therefore, the relationship between the effective shrinkage strain $\varepsilon_{sh-e}(t, t_0)$ in the age $(t\text{-}t_0)$ and the shrinkage strain $\varepsilon_{sh}(t)$ with creep coefficient $\varphi(t, t_0)$ can be expressed as **Eq. 20**.

$$\varepsilon_{sh-e}(t, t_0) = \frac{\varepsilon_{sh}(t)}{1 + \varphi(t, t_0)} \tag{20}$$

Substituting **Eq. 20** into **Eq. 17**, the concrete early cracking risk prediction model shown in **Eq. 21** is obtained.

$$\eta = \frac{E(t) \cdot \varepsilon_{sh}(t)}{f_t(t) \cdot [1 + \varphi(t, t_0)]} \tag{21}$$

Therefore, η is affected by elastic modulus, tensile strength shrinkage and creep coefficient s.

To apply GA to optimize concrete mix, a mathematical model between concrete performance and mix proportion is required. The result of GA optimization is highly dependent on the accuracy of the mathematical model. Therefore, a large amount of data is required for fitting to ensure the accuracy of the model. Many studies use literature data for fitting. However, since the composition of concrete and the performance of materials varies greatly, using other research's data may result in large errors. In Prediction of Concrete Properties by ANN, we showed that ANN has a very high accuracy in predicting concrete performance. Therefore, 81 sets of experiments based on the principle of orthogonal experiment were designed. ANN is applied to predict the slump and compressive strength, tensile strength and elastic modulus. The concrete mix proportion and ANN prediction results are shown in **Supplementary Material**.

Based on the test and ANN prediction results, the mathematical model between slump, compressive strength, tensile strength, elastic modulus and mix ratio parameters is obtained by multiple linear fitting method. Many factors affect shrinkage and creep. There are many factors affecting shrinkage and creep, and the fitting is difficult. Therefore, the functional relationship between shrinkage and creep and concrete mix proportion is derived based on the existing formula. Thus, the functional relationship between cracking risk coefficient and concrete mix proportion is obtained according to **Eq. 21**.

Mathematical Models of Slump, Compressive Strength, Tensile Strength and Elastic Modulus

Studies have shown that the slump, compressive strength, tensile strength and elastic modulus of concrete have a linear relationship with the mix proportion, as it is shown in **Eq. 22**. a_0–a_n are the coefficients to be fitted, and x represents the concrete mix proportion (Lim et al., 2004).

$$y = a_0 + a_1x_1 + a_2x_2 + a_3x_3 + \ldots + a_nx_n \tag{22}$$

Therefore, based on the results from experiments and ANN predictions, a multiple linear fit is performed on **Eq. 17**. The fit results and R^2 are shown in **Table 5**. The R^2 of all fitting results is greater than 0.950, indicating that the fitted formula has very high accuracy.

Mathematical Model of Shrinkage

Shrinkage is affected by many factors. It is nearly impossible to use multiple linear fitting to obtain the relationship between shrinkage and mix proportion. At present, there are many widely used shrinkage models, such as EN 1992-2-2:2005 model, CEB-FIP (MC 2010) model, Bazant-Panula model and Dilger model. Among them, Dilger model is suitable for high performance concrete with water to cement ratio ranging from 0.15 to 0.40 and using superplasticizer and silica fume, which is consistent with the type of concrete studied in this paper. Therefore, Dilger model is used in this paper (Gilliland and Andrew, 2000).

The Dilger model divides the total shrinkage into two parts: basic shrinkage and drying shrinkage, as shown in **Eqs 23–25**.

$$\varepsilon_{cs}(t, t_s) = \varepsilon_{bs}(t) + \varepsilon_{ds}(t, t_s) \tag{23}$$

$$\varepsilon_{bs}(t) = \varepsilon_{bs0}\beta_{bs}(t) \tag{24}$$

$$\varepsilon_{ds}(t) = \varepsilon_{ds0}\beta_{RH}\beta_{ds}(t, t_s) \tag{25}$$

where

$$\varepsilon_{bs0} = 700 \times \exp(-3.5w/c) + 120$$

$$\beta_{bs}(t) = \frac{t^{0.7}}{16.7 \times \left(-0.04 + \frac{1}{3}w/c\right) + \left(1.04 - \frac{1}{3}w/c\right)t^{0.7}}$$

$$\varepsilon_{ds0} = (100w/c)^2\left(0.8 \times f_{cu}^{1.05}\right)^{-0.23} + 200$$

$$\beta_{RH} = 1.22 - 1.75 \times \left(\frac{RH}{100}\right)^3$$

TABLE 5 | Multiple linear fitting results between concrete properties and mix proportion.

Properties	Multiple linear fitting results	R^2
Slump	$y = 2.165x_1 + 0.277x_2 - 0.028x_3 + 0.51x_4 - 0.153x_5 + 0.005x_6 + 182.437$	0.953
Compressive strength	$y = -1.896x_1 + 0.049x_2 + 0.021x_3 + 0.069x_4 + 0.153x_5 + 0.014x_6 + 119.611$	0.961
Tensile strength	$y = -0.23x_1 - 0.003x_2 + 0.002x_3 - 0.004x_4 + 0.006x_5 + 0.047x_6 + 12.419$	0.987
Elastic modulus	$y = -0.288x_1 + 0.013x_2 + 0.003x_3 - 0.008x_4 - 0.002x_5 + 0.053x_6 + 43.571$	0.955

$$\beta_{ds}(t,t_s)=\frac{(t-t_s)^{0.6}}{0.0016(v/s)^2[6.42+1.5\ln(t_s)]+(t-t_s)^{0.6}}$$

t and t_s, respectively, indicate the age of concrete and the age of the beginning of drying shrinkage; w/c is the water to binder ratio (x_1); f_{cu} is the cube compressive strength;

$$f_{cu}=-1.896x_1+0.049x_2+0.021x_3+0.069x_4+0.153x_5+0.014x_6+119.611$$

RH is the relative humidity, which 60% has been applied, therefore $\beta_{RH}=0.739$; v/s is the body-to-surface ratio, which is 22.8 in this paper.

Based on the above equations, the relationship between concrete shrinkage and mix proportion can be derived (**Eq. 26**)

$$\begin{aligned}\varepsilon_{cs}(t,t_s)=&\left[700\times\exp(-3.5x_1)+120\right]\\&\times\frac{t^{0.7}}{16.7\times\left(-0.04-\frac{1}{3}x_1\right)+\left(1.04-\frac{1}{3}x_1\right)t^{0.7}}+0.842\\&\times\left\{(100x_1)^2\left[0.8\times(-1.896x_1+0.049x_2+0.021x_3\right.\right.\\&\left.+0.069x_4+0.153x_5+0.014x_6+119.611)^{1.05}\right]^{-0.23}\\&\left.+200\right\}\times\frac{(t-t_s)^{0.6}}{0.832\times\left[6.42+1.5\ln(t_s)\right]+(t-t_s)^{0.6}}\end{aligned}\tag{26}$$

Mathematical Model of Creep

Creep is also affected by many factors (Geng et al., 2018). There are many creep models such as CEB-FIP (1990) model, EN 1992-1-1:2004, ACI-209R model, etc. The CEB-FIP (1990) model contains many parameters with a wide range of applications. Therefore, it is applied in this paper (Betonbau, 2013) as shown in **Eq. 27**.

$$\varphi(t,t_0)=\varphi(\infty,t_0)\beta_c(t-t_0)\tag{27}$$

where

$$\varphi(\infty,t_0)=\beta(f_c)\cdot\beta(t_0)\phi_{RH}$$

$$\beta(f_c)=\frac{16.76}{f_c^{0.5}}$$

$$\beta(t_0)=\frac{1}{0.1+t_0^{0.2}}$$

$$\phi_{RH}=\left[1+\frac{1-RH/100}{0.1(2A/u)^{1/3}}\cdot\alpha_1\right]\cdot\alpha_2$$

$$\beta_c(t-t_0)=\left[\frac{t-t_0}{\beta_H+(t-t_0)}\right]^{0.3}$$

$$\beta_H=1.5\times\left[1+\left(1.2\times\frac{RH}{100}\right)^{18}\right]\times\frac{2A}{u}+250\times\alpha_3$$

$$\alpha_1=\left(\frac{35}{f_c}\right)^{0.7}$$

$$\alpha_2=\left(\frac{35}{f_c}\right)^{0.2}$$

$$\alpha_3=\left(\frac{35}{f_c}\right)^{0.5}$$

t and t_0, respectively; indicate the age of concrete and the age since loading starts; f_c is the cube compressive strength of the cube, described as:

$$f_c=-1.896x_1+0.049x_2+0.021x_3+0.069x_4+0.153x_5+0.014x_6+119.611$$

RH is relative humidity, which in this article is 65%; A is the cross-sectional area of the member; u is the perimeter of the member exposed to the air; Based on the equations above, the relationship between concrete creep coefficient and mix proportion can be derived (**Eq. 28**):

$$\begin{aligned}\varphi(t,t_0)=&\frac{16.76}{(-1.896x_1+0.049x_2+0.021x_3+0.069x_4+0.153x_5+0.014x_6+119.611)^{0.5}}\\&\times\left[1+\frac{1-RH/100}{0.1(2A/u)^{1/3}}\cdot\left(\frac{35}{-1.896x_1+0.049x_2+0.021x_3+0.069x_4+0.153x_5+0.014x_6+119.611}\right)^{0.7}\right]\\&\times\left(\frac{35}{-1.896x_1+0.049x_2+0.021x_3+0.069x_4+0.153x_5+0.014x_6+119.611}\right)^{0.2}\times\frac{1}{0.1+t_0^{0.2}}\\&\times\left\{\frac{t-t_0}{\left\{1.5\times\left[1+\left(1.2\times\frac{RH}{100}\right)^{18}\right]\times\frac{2A}{u}\right.\right.\\&\left.\left.+250\cdot\left(\frac{35}{-1.896x_1+0.049x_2+0.021x_3+0.069x_4+0.153x_5+0.014x_6+119.611}\right)^{0.5}\right\}+(t-t_0)}\right\}^{0.3}\end{aligned}\tag{28}$$

TABLE 6 | Experimental value and predicted value of concrete properties at the age of 3 and 7 days.

No	Tensile strength (MPa)			Elastic modulus (MPa)			Shrinkage			Creep coefficient			Cracking risk coefficient		
	Exp	Pre	Err	Exp	Pre	Err	Exp	Pre	Err	Exp	Pre	Err	Exp	Pre	Err
E1	4.58	4.47	2.4	28.7	27.6	3.8	346	337	1.6	0.641	0.658	2.7	1.32	1.26	4.9
	5.73	5.52	3.7	34.5	33.3	3.5	498	490	2.6	0.715	0.742	3.8	1.75	1.70	2.9
E6	4.41	4.50	2.0	26.7	27.3	2.2	323	319	1.2	0.652	0.673	3.2	1.18	1.16	2.3
	5.47	5.56	1.6	33.2	32.9	1.0	487	482	1.0	0.733	0.759	3.5	1.71	1.62	4.9
E11	4.21	4.01	4.7	26.1	26.7	2.3	317	303	4.4	0.728	0.695	4.5	1.14	1.19	4.7
	5.13	4.94	3.7	32.7	32.1	1.8	471	478	1.5	0.802	0.784	2.2	1.67	1.74	4.5
E16	3.98	3.87	2.8	26.3	25.9	2.8	284	289	1.8	0.761	0.733	3.7	1.11	1.19	3.6
	4.86	4.78	1.6	32.5	31.6	1.5	452	467	3.3	0.845	0.827	2.1	1.64	1.69	3.1
E21	3.31	3.44	3.9	24.7	25.4	2.8	271	278	2.6	0.782	0.759	2.9	1.13	1.17	2.8
	4.11	4.24	3.2	29.5	30.8	4.4	449	459	2.2	0.881	0.857	2.7	1.71	1.80	4.8

Note: Exp is the experimental value, Pre is the predicted value and Err (Unit: %) is the error between Exp and Pre. The upper and lower data indicate that the concrete age is 3 and 7 days respectively.

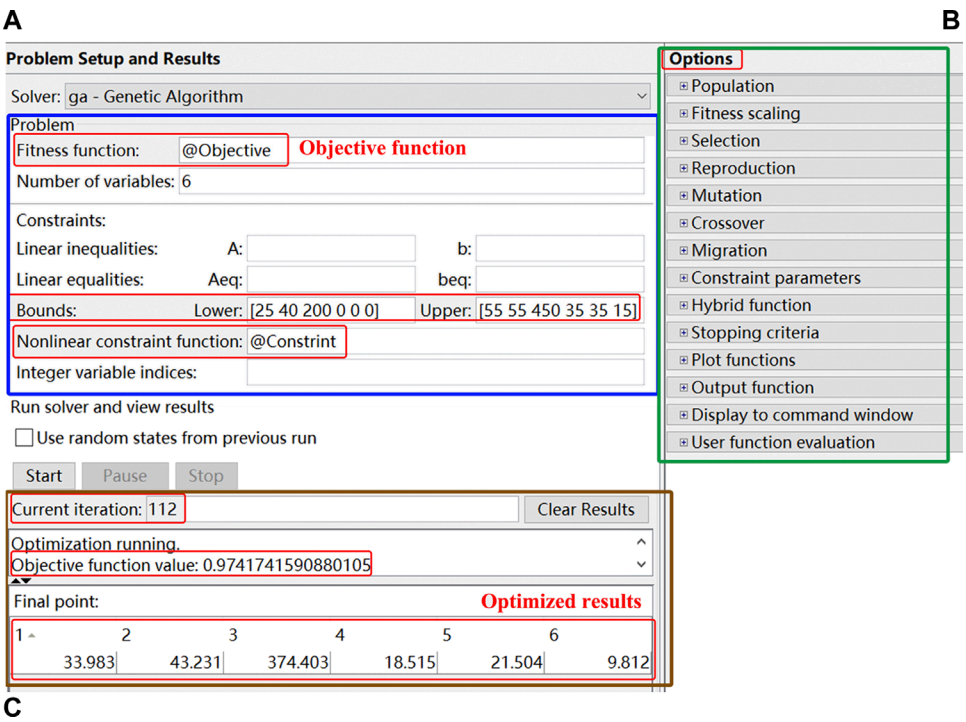

FIGURE 4 | Application of genetic algorithm toolbox.

Mathematical Model of Cracking Risk Coefficient

The calculation of cracking risk coefficient is shown in **Eq. 21**. $\varepsilon_{sh}(t)$ and $\varphi(t, t_0)$can be calculated by **Eqs 26** and **28**. $E(t)$ $[f_t(t)]$ can be expressed as a function of 28 days elastic modulus (tensile strength) and age t, as shown in **Eqs 29** and **30**.

$$E(t) = 3,500 + 4,300 \times \sqrt{\{\exp[0.2 \times (1 - \sqrt{28/t})]\}^2 \times (E_{28}/19.4)^3 \times 10} \quad (29)$$

$$f(t) = f_{t,28} \times \exp[0.2 \times (1 - \sqrt{28/t})] \quad (30)$$

where

$$E_{28} = -0.288x_1 + 0.013x_2 + 0.003x_3 - 0.008x_4 - 0.002x_5 + 0.053x_6 + 43.571$$

$$f_{t,28} = -0.23x_1 - 0.003x_2 + 0.002x_3 - 0.004x_4 + 0.006x_5 + 0.047x_6 + 12.419$$

TABLE 7 | Range of independent variables.

Independent variables	Value range
x_1 (water to binder ratio)	25–55 (%)
x_2 (sand ratio)	40–55 (%)
x_3 (the amount of cement)	200–450 (kg/m^3)
x_4 (the proportion of fly ash)	0–30 (%)
x_5 (the proportion of slag)	0–30 (%)
x_6 (the proportion of silica fume)	0–15 (%)

Therefore, the cracking risk coefficient can be expressed as a function of concrete mix proportion and age:

$$\eta = f(x_1, x_2, x_3, x_4, x_5, x_6, t, t_0, t_s) \quad (31)$$

Model Validation

The relationship between tensile strength, elastic modulus, shrinkage, creep coefficient, cracking risk coefficient and

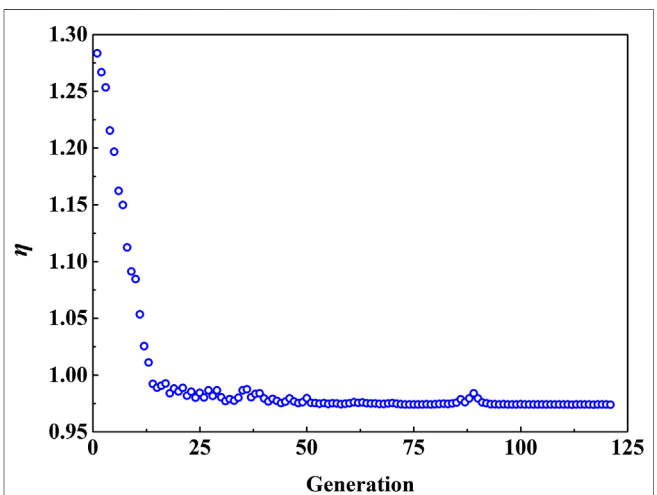

FIGURE 5 | Changes of cracking risk coefficient with evolution times.

TABLE 8 | Mix proportion of Control and Optimal.

No	x_1 (%)	x_2 (%)	x_3 (kg/m^3)	x_4 (%)	x_5 (%)	x_6 (%)
Control	30	47	320	25	16.7	5.8
Optimal	34	43	374	18.5	21.5	9.8

concrete mix ratio and age are all derived from existing models. In order to verify the accuracy of the model, select E1, E6, E11, E16, E21 five groups of mix proportion from **Table 2** to test. The performance of each group of 3 and 7 days are measured and compared with the predicted value of the model. Results were shown in **Table 6**. When the concrete age is 3 days, the maximum errors between the experimental and predicted values of the tensile strength, elastic modulus, shrinkage, creep coefficient, and cracking risk coefficient of the five groups are 4.7, 3.8,4.4, 4.5, and 4.9%, respectively. When the concrete age is 7 days, the maximum errors between the experimental and predicted values of the tensile strength, elastic modulus, shrinkage, creep coefficient and cracking risk coefficient of the five groups are respectively 3.7, 4.4, 3.3, 3.8, and 3.8%. The errors between the experimental values and predicted values of various properties at different ages are all less than 5%, which indicates that the model established in this paper is accurate.

The cracking risk factor was calculated by **Eq. 28** from the tensile strength, elastic modulus, shrinkage rate, and creep coefficient, and the Results was shown in **Figure 4**. It is obvious that the cracking risk coefficient of the five groups of concrete with 3-day age is already greater than 1, Which means that the concrete cracks. Therefore, in order to verify the accuracy of the calculation results, the five groups were tested with a slab-plate cracking frame to observe the cracking situation when the concrete reached an age of 3 days, and the results were shown in **Table 6**. There were cracks circled with red ellipse in the five groups of concrete, indicating that the calculation results of the cracking risk coefficient were accurate.

Model Establishment of Genetic Algorithm

After building the mathematical model between concrete performance and mix proportion, the objective function and constraint function are further determined, after which GA can be used to optimize concrete mix proportion. The process of GA is shown as following. First create a population, then calculate the fitness of each individual. Continue to evolve through selection, crossover and mutation, which finally leads to the optimal solution.

The purpose of this paper is to improve the anti-cracking performance of high-strength concrete. In this case, the cracking risk coefficient is taken as the objective function. It can be seen from Mathematical Model Between Concrete Performance and Mix Proportion that the concrete has cracked at the age of 3 days, thus the crack resistance performance of the concrete with the age of 3 days is optimized. It is necessary to meet the requirements of slump and strength while improving the crack resistance. Therefore, the slump and strength are taken as the constraint function. The design slump is greater than 260 mm and the strength is greater than 60 MPa. The independent variable is x_1-x_6, and their range of values is shown in **Table 7**.

GA toolbox is used to optimize concrete mix proportion, as shown in **Figure 4**. The objective function, constraint function, number of variables, and variable value range are set in the A area. The selection method, crossover probability, and mutation probability are set in the B area, and in the calculation process, keep the default settings for the parameters in Options. The selection function is uniform, and the method of crossover and mutation is constraint dependent. The number of iterations and optimization results are displayed in the C area.

Genetic Algorithm Optimization Results

When applying genetic algorithm to optimize the mix proportion, the variation of the cracking risk coefficient with the number of evolutions is shown in **Figure 5**. The cracking risk coefficient dropped sharply in the first few generations, while basically stabilized after 50 generations of evolution, and stopped when the final number of evolutions was 121. The minimum value of the cracking risk coefficient was 0.974.

In order to compare the change of concrete performance after optimization, a group of concrete proportion commonly used in engineering is used as the control. **Table 8** shows the mix proportion of engineering concrete (named Control) and optimized concrete (named Optimal). Through experiments, the mechanical properties such as the compressive strength and elastic modulus of the two groups of concrete were determined, the cracking risk coefficient was calculated and their results are shown in **Table 9**. The test result showed that the slump and strength of the optimized concrete are 262 mm and 71 MPa respectively, which meet the constraint conditions. The cracking risk coefficient of Control is 1.276, while that of Optimal is 0.951. The cracking risk coefficient of Optimal was reduced by 25% to less than 1 compared with that of Control, indicating that the concrete with an age of 3 days switched from the inevitable cracking state to the state that may not crack. The optimization effect is obvious. **Figure 6** shows the slab-plate cracking frame test of Control and Optimal. There were many cracks in the Control, while Optimal had not cracked, indicating that the crack

TABLE 9 | Performance comparison between control and optimal.

No	Slump (mm)	Compressive strength (MPa)	Tensile strength (MPa)	Elastic modulus (GPa)	Shrinkage (×10^{-6})	Creep cofficiens	η
Control	257	75	4.09	27.2	321	0.673	1.276
Optimal	262	71	3.95	25.7	258	0.764	0.951

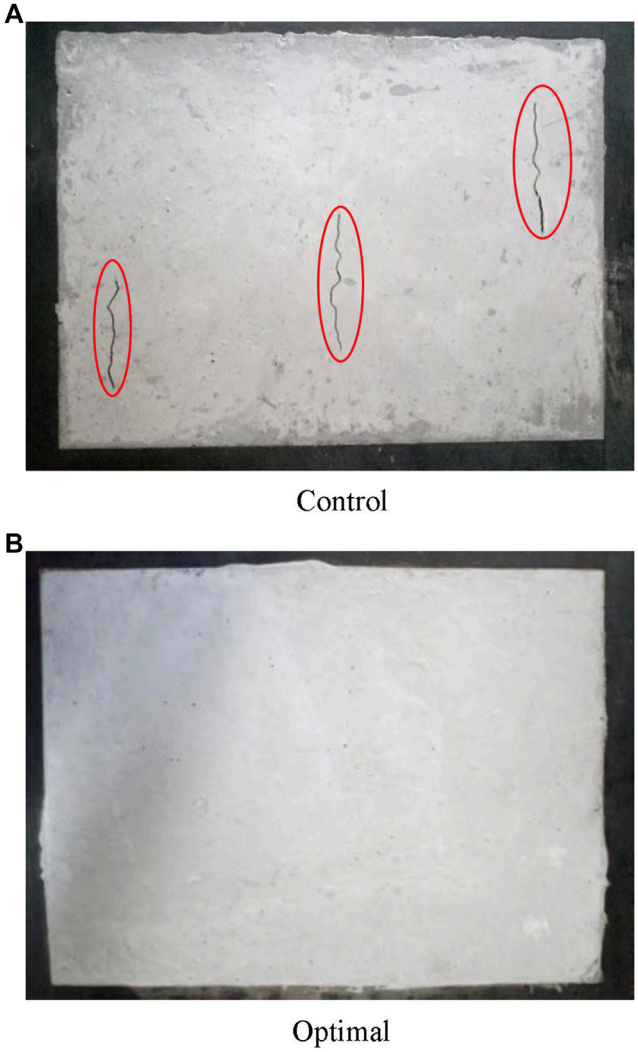

FIGURE 6 | Cracking states of control and optimal at the age of 3 days. **(A)** Control; **(B)** Optimal.

resistance of the optimized concrete was significantly improved and the optimization goal were achieved.

CONCLUSION

(1) ANN is applied to predict concrete slump, compressive strength, tensile strength and elastic modulus. Errors between the predicted value and the test value were very small and R^2 was above 0.94, indicating that ANN is very accurate in concrete performance prediction.

(2) Based on the test results and ANN prediction results, the functional relationship between slump, compressive strength, tensile strength and elastic modulus and concrete mix proportion was established. Based on the existing shrinkage and creep models, the functional relationship between the shrinkage, creep coefficient and cracking risk coefficient and the concrete mix proportion was derived. The error between the test value and the model prediction value is within 5%, indicating the accuracy of the model.

(3) GA is used to optimize the concrete mix proportion to improve its crack resistance. The research results show that the cracking risk coefficient of the optimized concrete is significantly reduced compared with the that of commonly used engineering concrete. The established GA optimized concrete mix design method has a good applicability.

DATA AVAILABILITY STATEMENT

The raw data supporting the conclusions of this article will be made available by the authors, without undue reservation, to any qualified researcher.

AUTHOR CONTRIBUTIONS

YL contributed conception and research method of the study. HL was responsible for testing and organizing the database. NL performed the statistical analysis. CJ wrote the first draft of the manuscript. All authors contributed to manuscript revision, read and approved the submitted version.

FUNDING

We declare all sources of funding received for the research being submitted. National Natural Science Foundation of China (51808015); National Key R&D Program of China–Key Materials and Preparation Technology of high crack resistant ready-mixed concrete (2017YFB0310100).

SUPPLEMENTARY MATERIAL

The Supplementary Material for this article can be found online at: https://www.frontiersin.org/articles/10.3389/fmats.2020.590661/full#supplementary-material

REFERENCES

Abellán García, J., Fernández Gómez, J., and Torres Castellanos, N. (2020). Properties prediction of environmentally friendly ultra-high-performance concrete using artificial neural networks. *Eur. J. Environ. Civ. En.* 26, 1–25. doi:10.1080/19648189.2020.1762749

Andrade, C., Sarría, J., and Alonso, C. (1999). Relative humidity in the interior of concrete exposed to natural and artificial weathering. *Cement Concr. Res.* 29 (8), 1249–1259. doi:10.1016/s0008-8846(99)00123-4

Bendimerad, A. Z., Delsaute, B., Rozière, E., Staquet, S., and Loukili, A. (2020). Advanced techniques for the study of shrinkage-induced cracking of concrete with recycled aggregates at early age. *Construct. Build. Mater.* 233, 117340–117415. doi:10.1016/j.conbuildmat.2019.117340

Bendimerad, A. Z., Rozière, E., and Loukili, A. (2016). Plastic shrinkage and cracking risk of recycled aggregates concrete. *Construct. Build. Mater.* 121, 733–745. doi:10.1016/j.conbuildmat.2016.06.056

Bentz, D. P. (2008). A review of early-age properties of cement-based materials. *Cement Concr. Res.* 38 (2), 196–204. doi:10.1016/j.cemconres.2007.09.005

Bentz, D. P., Garboczi, E. J., Haecker, C. J., and Jensen, O. M. (1999). Effects of cement particle size distribution on performance properties of Portland cement-based materials. *Cement Concr. Res.* 29 (10), 1663–1671. doi:10.1016/S0008-8846(99)00163-5

Betonbau (2013). *Fib model code for concrete structures Lausanne*: Shanghai, China: International Federation for Structural Concrete.

Chithra, S., Kumar, S. R. R. S., Chinnaraju, K., and Alfin Ashmita, F. (2016). A comparative study on the compressive strength prediction models for High Performance Concrete containing nano silica and copper slag using regression analysis and Artificial Neural Networks. *Construct. Build. Mater.* 114, 528–535. doi:10.1016/j.conbuildmat.2016.03.214

Chowdhury, B., and Garai, G. (2017). A review on multiple sequence alignment from the perspective of genetic algorithm. *Genomics* 109 (5–6), 419–431. doi:10.1016/j.ygeno.2017.06.007

Far, M. S. S., Underwood, B. S., Ranjithan, S. R., Kim, Y. R., and Jackson, N. (2009). Application of artificial neural networks for estimating dynamic modulus of asphalt concrete. *Transport. Res. Rec.* 2127, 173–186. doi:10.3141/2127-20

Feng, J., Su, Y., and Qian, C. (2019). Coupled effect of PP fiber, PVA fiber and bacteria on self-healing efficiency of early-age cracks in concrete. *Construct. Build. Mater.* 228, 116810–116819. doi:10.1016/j.conbuildmat.2019.116810

Gao, Y., Zhang, J., and Han, P. (2013). Determination of stress relaxation parameters of concrete in tension at early-age by ring test. *Construct. Build. Mater.* 41, 152–164. doi:10.1016/j.conbuildmat.2012.12.004

Geng, G., Vasin, R. N., Li, J., Qomi, M. J. A., Yan, J., Wenk, H.-R., et al. (2018). Preferred orientation of calcium aluminosilicate hydrate induced by confined compression. *Cement Concr. Res.* 113, 186–196. doi:10.1016/j.cemconres.2018.09.002

Gillilandand Andrew, J. (2000). *Thermal and shrinkage effects in high performance concrete structures during construction*. Dissertation/Master's thesis. Calgary (AB): University of Calgary.

Huang, L., Chen, Z., and Ye, H. (2020). A mechanistic model for the time-dependent autogenous shrinkage of high performance concrete. *Construct. Build. Mater.* 255, 119335–119410. doi:10.1016/j.conbuildmat.2020.119335

Ji, T., Lin, T., and Lin, X. (2006). A concrete mix proportion design algorithm based on artificial neural networks. *Cement Concr. Res.* 36 (7), 1399–1408. doi:10.1016/j.cemconres.2006.01.009

Khan, I., Xu, T., Castel, A., Gilbert, R. I., and Babaee, M. (2019). Risk of early age cracking in geopolymer concrete due to restrained shrinkage. *Construct. Build. Mater.* 229, 116840. doi:10.1016/j.conbuildmat.2019.116840

Lee, B. Y., Kim, J. H., and Kim, J.-K. (2009). Optimum concrete mixture proportion based on a database considering regional characteristics. *J. Comput. Civ. Eng.* 23 (5), 258–265. doi:10.1061/(asce)0887-3801(2009)23:5(258)

Li, J., Zhang, W., Li, C., and Monteiro, P. J. M. (2019). Green concrete containing diatomaceous earth and limestone: workability, mechanical properties, and life-cycle assessment. *J. Clean. Prod.* 223, 662–679. doi:10.1016/j.jclepro.2019.03.077

Li, J., Zhang, W., Li, C., and Monteiro, P. J. M. (2020). Eco-friendly mortar with high-volume diatomite and fly ash: performance and life-cycle assessment with regional variability. *J. Clean. Prod.* 261, 121224. doi:10.1016/j.jclepro.2020.121224

Lim, C.-H., Yoon, Y.-S., and Kim, J.-H. (2004). Genetic algorithm in mix proportioning of high-performance concrete. *Cement Concr. Res.* 34 (3), 409–420. doi:10.1016/j.cemconres.2003.08.018

Liu, J.-p., Tian, Q., and Miao, C.-w. (2012). Investigation on the plastic shrinkage of cementitious materials under drying conditions: mechanism and theoretical model. *Mag. Concr. Res.* 64 (6), 551–561. doi:10.1680/macr.11.00037

Mangalathu, S., Heo, G., and Jeon, J.-S. (2018). Artificial neural network based multi-dimensional fragility development of skewed concrete bridge classes. *Eng. Struct.* 162, 166–176. doi:10.1016/j.engstruct.2018.01.053

Menu, B., Jolin, M., and Bissonnette, B. (2020). Assessing the shrinkage cracking potential of concrete using ring specimens with different boundary conditions. *Adv. Mater. Sci. Eng.* 2020, 1–13. doi:10.1155/2020/4842369

Peng, Z., and Gao, Y. (2018). Application of BP neural network in elevation fitting of underwater terrain. *J. Chongqing Jianzhu Univ.* 37 (11), 64–68. doi:10.3969/j.issn.1674-0696.2018.11.11

Rita, M., Fairbairn, E., Ribeiro, F., Andrade, H., and Barbosa, H. (2018). Optimization of mass concrete construction using a twofold parallel genetic algorithm. *Appl. Sci.* 8 (3), 399–418. doi:10.3390/app8030399

Schroefl, C., Mechtcherine, V., and Gorges, M. (2012). Relation between the molecular structure and the efficiency of superabsorbent polymers (SAP) as concrete admixture to mitigate autogenous shrinkage. *Cement Concr. Res.* 42 (6), 865–873. doi:10.1016/j.cemconres.2012.03.011

Shahnewaz, M., Machial, R., Alam, M. S., and Rteil, A. (2016). Optimized shear design equation for slender concrete beams reinforced with FRP bars and stirrups using Genetic Algorithm and reliability analysis. *Eng. Struct.* 107, 151–165. doi:10.1016/j.engstruct.2015.10.049

Wang, X.-Y. (2019). Optimal design of the cement, fly ash, and slag mixture in ternary blended concrete based on gene expression programming and the genetic algorithm. *Materials* 12 (15), 2448. doi:10.3390/ma12152448

Wittmann, F. H. (2002). Crack formation and fracture energy of normal and high strength concrete. *Sadhana* 27 (4), 413–423. doi:10.1007/BF02706991

Xin, J., Zhang, G., Liu, Y., Wang, Z., and Wu, Z. (2020). Evaluation of behavior and cracking potential of early-age cementitious systems using uniaxial restraint tests: a review. *Construct. Build. Mater.* 231, 117146. doi:10.1016/j.conbuildmat.2019.117146

Xu, J., Chen, Y., Xie, T., Zhao, X., Xiong, B., and Chen, Z. (2019). Prediction of triaxial behavior of recycled aggregate concrete using multivariable regression and artificial neural network techniques. *Construct. Build. Mater.* 226, 534–554. doi:10.1016/j.conbuildmat.2019.07.155

Yan, F., and Lin, Z. (2016). New strategy for anchorage reliability assessment of GFRP bars to concrete using hybrid artificial neural network with genetic algorithm. *Compos. B Eng.* 92, 420–433. doi:10.1016/j.compositesb.2016.02.008

Yan, F., Lin, Z., Wang, X., Azarmi, F., and Sobolev, K. (2017). Evaluation and prediction of bond strength of GFRP-bar reinforced concrete using artificial neural network optimized with genetic algorithm. *Compos. Struct.* 161, 441–452. doi:10.1016/j.compstruct.2016.11.068

Yeh, I.-C. (2007). Modeling slump flow of concrete using second-order regressions and artificial neural networks. *Cem. Concr. Compos.* 29 (6), 474–480. doi:10.1016/j.cemconcomp.2007.02.001

Yun-sheng, Z., Wei, S., Shu-guang, H., and Qing-jun, D. (2002). Performances of the high strength low heat pump concrete (HLPC). *J. Wuhan Univ. Technol.-Mater. Sci. Ed.* 17 (3), 56–59. doi:10.1007/BF02838541

Zhang, Y., Zhang, W., She, W., Ma, L., and Zhu, W. (2012). Ultrasound monitoring of setting and hardening process of ultra-high performance cementitious materials. *NDT E Int.* 47, 177–184. doi:10.1016/j.ndteint.2009.10.006

Zhou, Y., Zheng, S., Huang, Z., Sui, L., and Chen, Y. (2020). Explicit neural network model for predicting FRP-concrete interfacial bond strength based on a large database. *Compos. Struct.* 240, 111998–112015. doi:10.1016/j.compstruct.2020.111998

Conflict of Interest: The authors declare that the research was conducted in the absence of any commercial or financial relationships that could be construed as a potential conflict of interest.

Copyright © 2020 Yue, Hongwen, Yinuo and Caiyun. This is an open-access article distributed under the terms of the Creative Commons Attribution License (CC BY). The use, distribution or reproduction in other forums is permitted, provided the original author(s) and the copyright owner(s) are credited and that the original publication in this journal is cited, in accordance with accepted academic practice. No use, distribution or reproduction is permitted which does not comply with these terms.

frontiers in Materials

ORIGINAL RESEARCH
published: 20 January 2021
doi: 10.3389/fmats.2020.563234

Mechanism Analysis of the Influence of Delay Period on Mechanical Properties of Reactive Powder Concrete

Xiaohui Wang[1,2], *Qingxin Zhao*[1]*, *Xiaojun He*[3] and *Shuang Zhang*[1]

[1]Key Laboratory of Green Construction and Intelligent Maintenance for Civil Engineering of Hebei Province, Yanshan University, Qinhuangdao, China, [2]College of Civil Engineering and Architecture, Hebei University, Baoding, China, [3]Shijiazhuang Institution of Railway Technology, Shijiazhuang, China

OPEN ACCESS

Edited by:
Dongshuai Hou, Qingdao University of Technology, China

Reviewed by:
Anatolijus Eisinas, Kaunas University of Technology, Lithuania
Neven Ukrainczyk, Darmstadt University of Technology, Germany

***Correspondence:**
Qingxin Zhao
zhaoqx2002@163.com

Specialty section:
This article was submitted to Structural Materials, a section of the journal Frontiers in Materials

Received: *18 May 2020*
Accepted: *15 December 2020*
Published: *20 January 2021*

Citation:
Wang X, Zhao Q, He X and Zhang S (2021) Mechanism Analysis of the Influence of Delay Period on Mechanical Properties of Reactive Powder Concrete. Front. Mater. 7:563234. doi: 10.3389/fmats.2020.563234

In order to analyze the influence mechanism of delay period on the mechanical properties of reactive powder concrete (RPC), the compressive strength of RPC with delay periods of 18, 24, and 30 h was tested at the age of 7, 28, and 90 days, respectively. The results show that compared with the RPC with delay period of 18 h, the compressive strength of the RPC with delay periods of 24 and 30 h increases by 3.2 and 4.2%, respectively, and the long-term strength reduction ratio decreases by 22.8 and 71.9%, respectively. The constitutive model curves of RPC under different delay period show that the initial elastic modulus *E* increases with the delay period and the strength and rigidity of RPC increase with the extension of delay period. According to the non-evaporation water quantity test, it could be speculated that the quantities of hydration products of the RPC with delay periods of 24 and 30 h slightly increase compared with the RPC with delay period of 18 h. X-ray diffraction (XRD) analysis show that the delay periods of 24 and 30 h consume more $3CaO{\cdot}SiO_2$ (C_3S) and $2CaO{\cdot}SiO_2$ (C_2S) compared with delay period of 18 h. Seen from the scanning electron microscope (SEM) image, the structures of the three groups of samples are relatively dense and have no significant difference. Through energy dispersive X-ray spectroscopy (EDS) analysis, the calcium-silicon ratios of hydration products of the RPC with delay periods of 18, 24, and 30 h are 1.81, 1.56, and 1.54, respectively. The existence of C-S-H gel and $Ca(OH)_2$ in hydration products is confirmed by thermogravimetric-differential scanning calorimetry (DSC-TG) analysis. An appropriate delay period (30 h in this paper) generates more hydration products, then improves the compactness of the internal structure and reduces the calcium-silicon ratio of hydration products, and it is conducive to the growth of RPC compressive strength and the stability of long-term compressive strength.

Keywords: reactive powder concrete, delay period, compressive strength, long-term strength reduction ratio, mechanism analysis

INTRODUCTION

Reactive powder concrete (RPC) is a new type of concrete prepared by steam curing, which has removed the coarse aggregate to improve uniformity of the matrix (Abid et al., 2017). The fineness and reactivity of the components of RPC are increased by steam curing (Cheyrezy et al., 1995). According to the most compact principle, the initial defects such as voids and micro-cracks in the structure are greatly reduced (Chan and Chu, 2004).

Compared to common cement-based materials, RPC has excellent mechanical properties and durability (Huynh et al., 2015; Mostofinejad et al., 2016; Song and Liu, 2016). By now, it has not been widely used for two reasons. First, the cost is high (Yazici et al., 2008), and the maintenance conditions are complex. Steam curing is only suitable for preparing smaller prefabricated components, and it is difficult to prepare RPC in construction site. Secondly, the strength of RPC will decrease in the long term, which is not negligible for structures that need to bear long-term load. The long-term strength reduction of concrete refers to the condition that the strength in the later age (90 days) is lower than that in the earlier age (7, 28 days) under the normal mix proportion and curing conditions (Soroka, et al., 1978). Some scholars have found that the long-term strength of RPC decreases gradually (Zhang et al., 2007; Yazici et al., 2010; Wang et al., 2014). Zhang et al. (2007) showed that the strength of RPC would be decreased in the middle and later age due to steam curing. It was speculated that the early hydration was too fast and too many hydration products hindered the later strength improvement. Wang et al. (2014) tested the uniaxial compressive strength of RPC at the age of 7 days, 3 months, and 3 years after hot water curing. It was found that the strength of RPC did not decrease after 3 months, but it did after 3 years.

High and stable compressive strength could better ensure the quality of concrete structure design, thereby improving the safety and stability of the structure (Nadiger et al., 2018). Zhao (2010) showed that changing the delay period may reduce the strength reduction ratio of steam cured cement paste. Delay period refers to the stage of standard maintenance from specimens molding to steam curing (Erdem et al., 2003). There are many studies on the effect of delay period on ordinary concrete (Soroka et al., 1978; Talakokula et al., 2015). Many researchers have indicated that a suitable delay period is beneficial to concrete properties, such as strength and durability (Shideler and Chamberlin, 1949; Hanson, 1963). Shideler and Chamberlin (1949) showed that the concrete with delay periods of 2–6 h had 15–40% higher strengths than the concrete with steam curing immediately after casting. Hanson (1963) proved that compressive strengths of concrete increased at all ages, as the delay period increased from 1 to 5 h. Erdem et al. (2003) tested the compressive strength of ordinary concrete at different ages under the steam curing of 80 °C with the delay periods of 1, 2, and 3 h. It was found that when the paste was hardened before steam curing, concrete tended to obtain higher strength. Taylor et al. (2001) showed that if delay periods are not chosen properly, thermal stresses can cause micro-cracks, and affect the strength of concrete. However, there are few studies related to the effect of delay period on RPC. Liu et al. (2020) investigated the effects of steam curing parameters on the capillary water absorption of concrete, and it was found that long delay period is beneficial to the development of concrete structure. Zdeb (2017) explored the strength of RPC under the delay periods of 0, 3, 6, 12, and 24 h at the steam curing of 90 °C. The results showed that the strength of RPC was the highest when the delay period was 6 h, and the length of the delay period obviously affected the mechanical properties of RPC.

The function of the delay period is to make the harden paste form a certain plastic structure strength to prevent the heat damage during the steam curing (Yang et al., 2003). Previous studies had proved that the delay period has an effect on the mechanical properties and internal microstructure of concrete, but the mechanism of the effect of delay period on the long-term mechanical properties of RPC had not been discussed. Wu et al. (2019) studied the effect of delay period under steam curing on high strength mortar. It was found that the different delay period will result in the difference of the composition of the paste, and insufficient delay period (6 h) will cause the strength of the specimen under steam curing to be lower than the standard curing.

Previous studies had proved that the delay period has an effect on the mechanical properties and internal microstructure of concrete, but the mechanism of the effect of delay period on the long-term mechanical properties of RPC had not been discussed. Based on this, in order to analyze the influence of delay period on the mechanical properties of RPC, the compressive strength of RPC at the age of 7, 28, and 90 days were tested under the delay periods of 18, 24, and 30 h, and the long-term compressive strength reduction ratio was calculated. Meanwhile, in order to study the mechanism of the effect of delay period on the long-term mechanical properties of RPC from microstructure, the composition and microstructure was explored by non-evaporative water volume, X-ray diffraction (XRD), the scanning electron microscope (SEM), energy dispersive X-ray spectroscopy (EDS) and thermogravimetric-differential scanning calorimetry (DSC-TG).

TABLE 1 | Chemical composition and specific surface area of cement, SF and GS.

Material	Mass fraction w/%								Specific surface area/ ($m^2 \cdot kg^{-1}$)
	CaO	SiO_2	Al_2O_3	Fe_2O_3	MgO	K_2O	TiO_2	SO_3	
P·II52.5	64.2	21.3	4.89	3.25	1.25	1.04	0.21	3.59	369
SF	0.77	95.3	0.38	—	2.29	0.35	—	0.79	22,000
GS	37.70	30.60	17.40	0.41	8.94	0.51	1.01	2.44	588

EXPERIMENTAL

Raw Materials

P. II 52.5 Portland cement, encrypted silica fume (SF) and S115 ground slag (GS) were used as cementitious materials, with the main chemical composition and specific surface area were shown in **Table 1**. The method used to obtain the specific surface area

TABLE 2 | Performance index of polycarboxylate superplasticizer.

Color	Density/g/ml	Solid content/%	Chloride content/%	PH
light yellow	1.05	20	≤0.01	6.7–6.8

TABLE 3 | Mix proportions of RPC/Kg·m-3.

Cement	SF	GS	Water	River sand	Superplasticizer	Steel fiber
584	90	224	162	1,347	27	157

was Blaine method. The aggregate was natural river sand with particle size ranging from 0.16 to 2.36 mm, and steel fibers were copper-plated round straight steel fibers with a length of 12–13 mm and a diameter of 0.15–0.20 mm. Polycarboxylic acid (standard high performance water reducer) was used as superplasticizer. The performance index of polycarboxylate superplasticizer was shown in **Table 2**.

METHODS

Preparation of RPC specimens

The cement mortar was stirred evenly and the RPC specimens of 40 × 40 × 160 mm were prepared according to the mix proportion in **Table 3**. The prepared process of RPC was shown as **Figure 1**.

Non-evaporated Water Volume Test of Cement-Silica Fume-Slag System

The test results of non-evaporated water under different delay periods were compared, and the amount of hydration products under different delay period were measured by measuring the amount of non-evaporated water in the paste from hydration to the specified age. Testing methods for non-evaporated water were shown as **Figure 2**.

X-Ray Diffraction, SEM Image, EDS and DSC-TG Analysis of the Paste

At the age of 90 days, the internal non-carbonated zone of the hardened paste was taken under different delay periods, and the appropriate amount of fine powder filtered and dried by *Non-evaporated Water Volume Test of Cement-Silica Fume-Slag System* method was used for X-ray diffraction (XRD) analysis. The 2θ values ranged from 10° to 80° and the scanning rate applied was 1°min for all specimens.

The microstructure of the hardened paste prepared by *Non-evaporated Water Volume Test of Cement-Silica Fume-Slag System* method was observed by scanning electron microscope (SEM) image after the vacuum and gold spray treatment. And the energy dispersive X-ray spectroscopy (EDS) analysis of the hydration products was carried out.

DSC-TG analysis of the paste prepared by *Non-evaporated Water Volume Test of Cement-Silica Fume-Slag System* method was carried out by the STA 449F5 integrated thermal analyzer (Zhao et al., 2016). The temperature rising rate was 10 °C/min, and the Ar was used as the protective gas to prevent the carbonization of the specimens during the heating process.

RESULTS AND DISCUSSION

Effect of Delay Period on Compressive Strength and Long-Term Strength Reduction Ratio of RPC

The compressive strength of RPC specimens under different age were shown in **Table 4**. Results in **Table 4** were expressed as mean value ± 1x standard deviation. The difference of compressive strength under different delay period was analyzed by one-way analysis of variance. The test value of F was 5.272, $p = 0.007 < 0.05$. It was shown that the compressive strength of RPC had statistically significant difference with the prolongation of delay

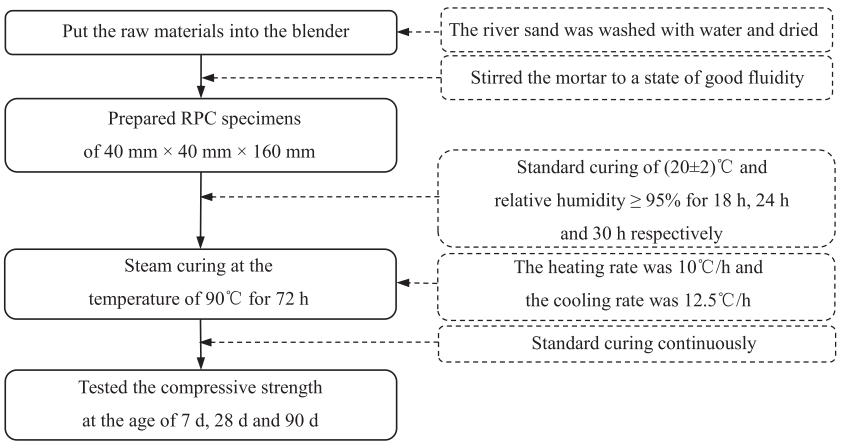

Figure 1 | Schematic diagram of RPC preparation.

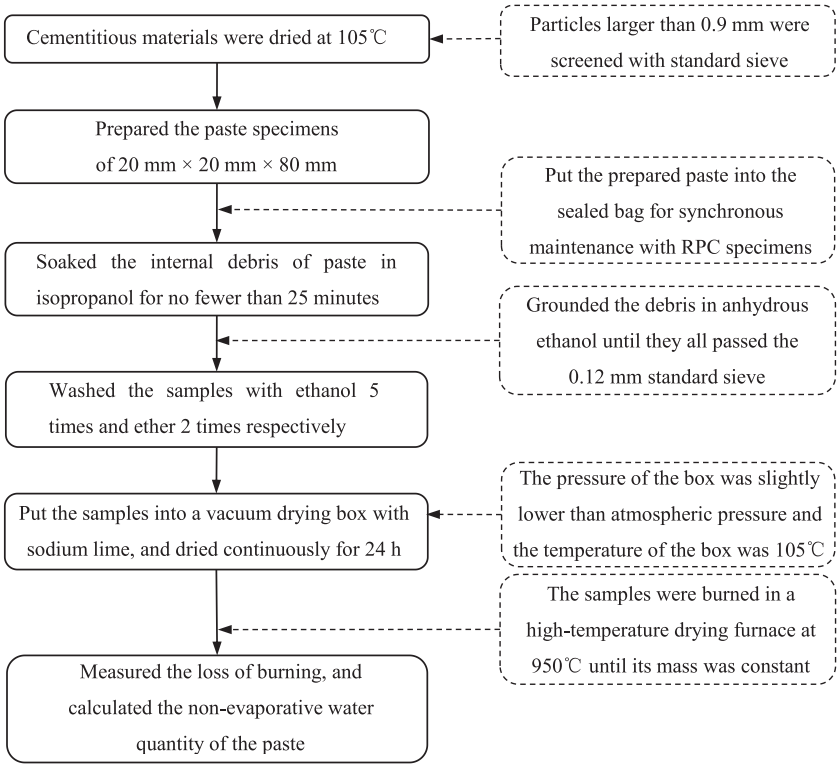

Figure 2 | Schematic diagram of non-evaporated water volume test.

TABLE 4 | Compressive strength of RPC.

Delay period/h	7 days/MPa	28 days/MPa	90 days/MPa
18	184.46 ± 7.38	182.18 ± 6.21	179.28 ± 7.57
24	189.05 ± 7.06	186.95 ± 6.39	184.95 ± 5.80
30	186.06 ± 6.75	188.20 ± 9.66	186.71 ± 7.26

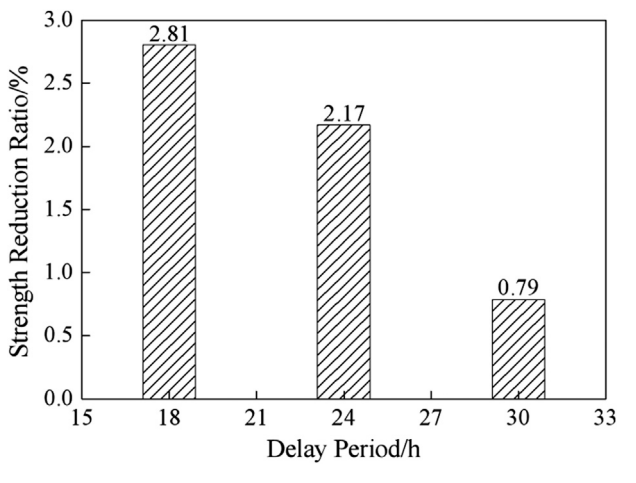

Figure 3 | Strength reduction ratio of RPC under different delay period.

period. Compared with the maximum values of 7 and 28 days compressive strength, the reduction ratio of RPC long-term compressive strength at the age of 90 days was calculated. The results were shown in **Figure 3**.

According to the compressive strength from **Table 4**, it could be seen that the compressive strength of RPC at the age of 90 days was 179.28, 184.95, and 186.71 MPa under the delay periods of 18, 24, and 30 h respectively. Compared with delay period of 18 h, the compressive strength of RPC with delay periods of 24 and 30 h increased by 3.2 and 4.2%, respectively. It could be seen that the compressive strength of RPC increased with delay periods.

Table 4 showed that the maximum compressive strength of RPC under the delay periods of 18, 24, and 30 h was 184.46, 189.05, and 188.20 MPa, respectively. The maximum compressive strength of 7 and 28 days was taken as the reference value, and the compressive strength of 90 days was compared with it to calculate the long-term reduction rate. **Figure 3** showed that the long-term strength reduction ratio of 24 and 30 h was 22.8 and 71.9% lower than that of 18 h. It could be seen that the long-term strength reduction ratio of RPC decreases gradually with the increase of delay periods.

Effect of Delay Period on Initial Elastic Modulus of RPC

At the age of 90 days, the stress-strain curves of RPC specimens were obtained by uniaxial compression test. The stress-strain

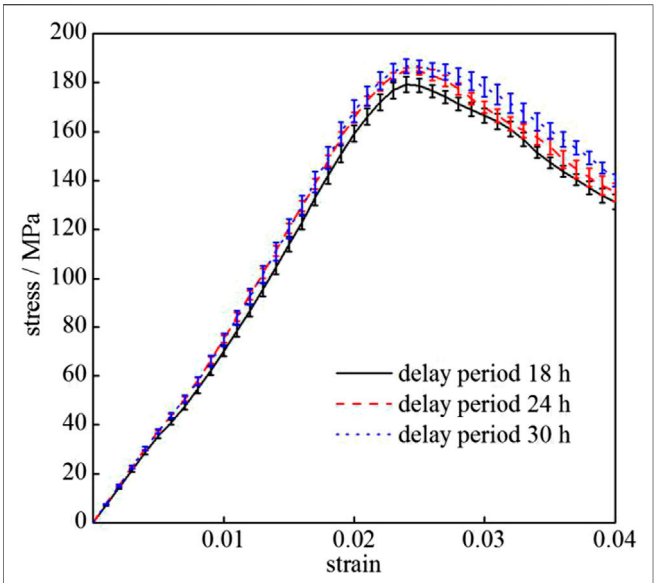

Figure 4 | Stress-strain curves of RPC under different delay period.

curves and error bars were shown in **Figure 4**. The difference of compressive strength under different delay period at the age of 90 days was analyzed by one-way analysis of variance. The test value of F was 3.852, $p = 0.03 < 0.05$. It was shown that the compressive strength of RPC at the age of 90 days had statistically significant difference with the prolongation of delay period.

Based on Weibull distribution phenomenological method and equivalent strain hypothesis theory (Lemaitre, 1983), Wang et al. (2006) established the constitutive model of damage of steel fiber concrete as **Eq. 1**.

$$\sigma = E\varepsilon\left\{exp\left[-\frac{1}{m}\left(\frac{\varepsilon}{\varepsilon_{pk}}\right)^{m}\right]\right\}. \quad (1)$$

In the formula, σ is stress; ε is strain; E is initial elastic modulus; ε_{pk} is the strain corresponding to peak load; m is shape parameter. According to **Eq. 1**, parameters E and m could be deduced by least square method based on the experimental data. The calculation was implemented by software of Origin. The calculation procedure was shown as **Figure 5**, fitting residual sum of squares and constitutive model expressions were shown in **Table 5**.

It could be seen from **Table 5** that the values of m under the delay periods of 18, 24, and 30 h was 2.5748, 2.5585, and 2.4798, respectively. The difference between them were small. In order to analyze the influence of delay period on initial elastic modulus E, the average value 2.5377 of m was taken and parameter E was deduced by least square method again based on the experimental data. The results and constitutive model expressions were shown in **Table 6**. The constitutive model curves of RPC under different delay period were shown in **Figure 6**.

It could be seen from **Table 6** that the values of E under the delay periods of 18, 24, and 30 h was 9,933, 10,306, and 10,548 MPa, respectively. The initial elastic modulus E in the constitutive model increased with the delay period. As could be seen from **Figure 6**, the strength and rigidity of RPC increased with the extension of delay period. It was conformed that the delay period was helpful to improve the mechanical properties of RPC, generated more hydration products, then improved the compactness of the internal structure. And it was conducive to the growth of RPC compressive strength and rigidity.

Effect of Delay Period on Non-evaporated Water Volume of the Paste

The amount of non-evaporative water in the paste at the age of 7, 28, and 90 days were measured. The results were shown in **Figure 7**. It could be seen from **Figure 7** that at the age of 7 days, the non-evaporative water of 18, 24, and 30 h was 7.8, 7.8, and 7.9%, respectively. The non-evaporated water volume at the

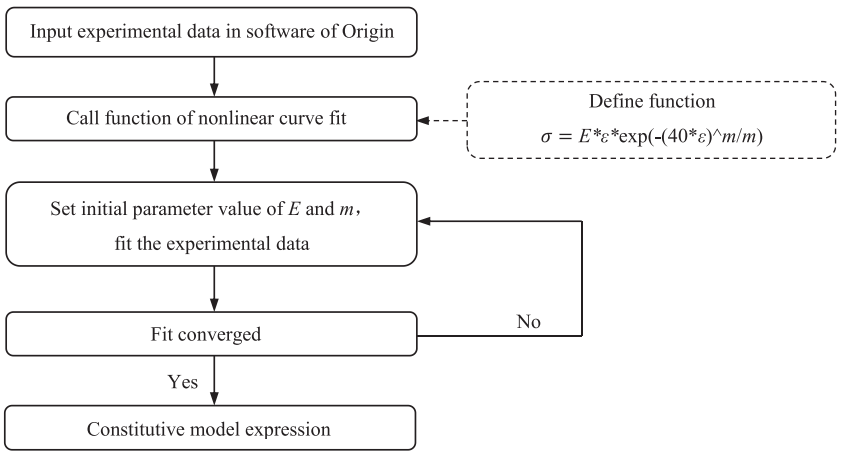

Figure 5 | Schematic diagram of the calculation procedure of the constitutive model.

TABLE 5 | Parameters of constitutive model of RPC under uniaxial compression.

Delay period	ε_{pk}	*E* (MPa)	*m*	Constitutive model expression	Residual sum of squares
18 h	0.025	9,898.2	2.5748	$\sigma = 9898.2\varepsilon\{exp[-0.3884(40\varepsilon)^{2.5748}]\}$	8,907.8
24 h	0.025	10,286	2.5585	$\sigma = 10286\varepsilon\{exp[-0.3909(40\varepsilon)^{2.5585}]\}$	8,096.5
30 h	0.025	10,616	2.4798	$\sigma = 10616\varepsilon\{exp[-0.4033(40\varepsilon)^{2.4798}]\}$	10,710

TABLE 6 | Parameters of constitutive model of RPC with m equal to 2.5377.

Delay period (h)	ε_{pk}	*E* (MPa)	*m*	Constitutive model expression	Residual sum of squares
18	0.025	9,933	2.5377	$\sigma = 9933\varepsilon\{\exp[-0.3941(40\varepsilon)^{2.5377}]\}$	8912.4
24	0.025	10,306	2.5377	$\sigma = 10306\varepsilon\{\exp[-0.3941(40\varepsilon)^{2.5377}]\}$	8097.8
30	0.025	10,548	2.5377	$\sigma = 10548\varepsilon\{\exp[-0.3941(40\varepsilon)^{2.5377}]\}$	10,727

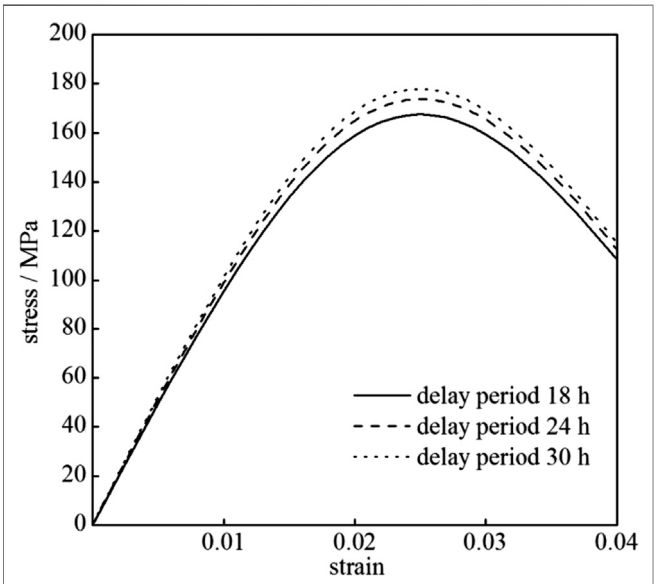

Figure 6 | Constitutive model curves of RPC under different delay period.

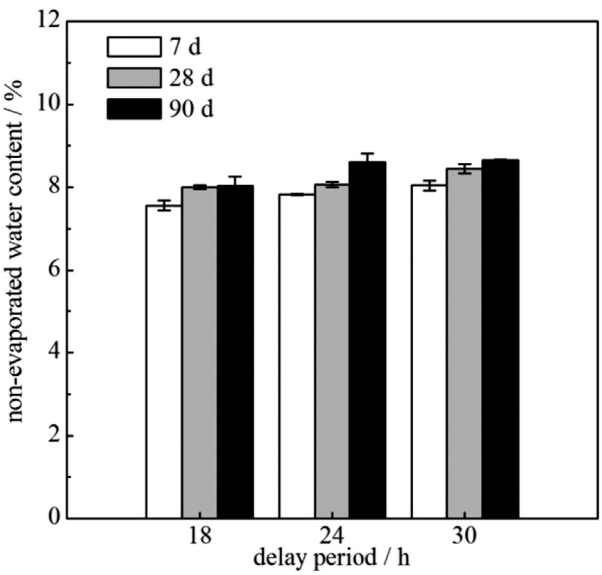

Figure 7 | The amount of non-evaporated water in the paste at different delay period.

age of 28 days increased by 0.3, 0.4, and 0.4%, respectively compared with that of 7 days. The non-evaporated water of 90 days increased by 0.2, 0.3, and 0.3%, respectively compared with 28 days. The difference of non-evaporative water under different delay period was analyzed by one-way analysis of variance. The test value of F was 5.190, $p = 0.013 < 0.05$. It was shown that the content of non-evaporative water had statistically significant difference with the prolongation of delay period. It could be seen that the amount of non-evaporated water increases slightly with the prolongation of delay period. The difference of non-evaporative water at different age was analyzed by one-way analysis of variance. The test value of F was 9.497, $p = 0.001 < 0.05$. It was shown that the content of non-evaporative water had statistically significant difference with the age of RPC.

As the age progresses, hydration products were continuously separated out, which made the space for new hydration products to be contained in the paste become smaller and smaller. When there was no room to accommodate, the new hydration products produce compressive stress on the surrounding raw hydration products, resulting in micro-cracks in the structure, and consequently strength retrogression. At the same time, compared with the early hydration stage, the increase of hydration products decreased gradually during the 90-day period. The reason was that the hydration rate of cement was very fast during the steam curing period, and the hydration products gradually formed a layer of film on the surface of un-hydrated particles. As the age progressed, the hydration product films accumulated and they gradually wrapped up the surface, which hindered the internal water

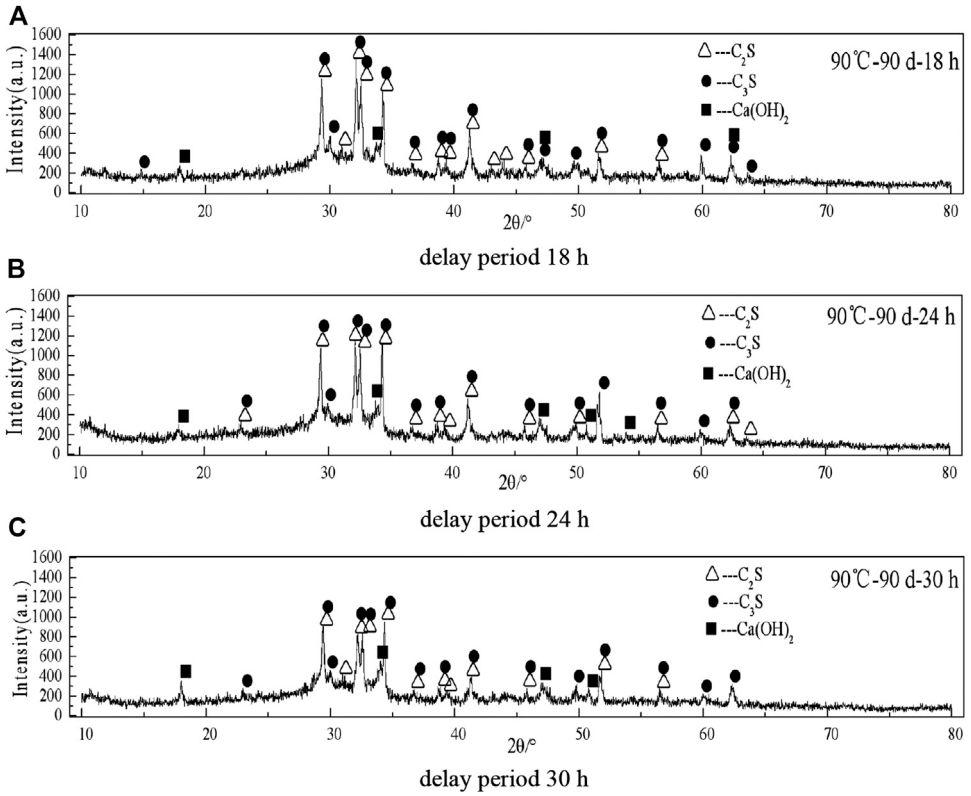

Figure 8 | XRD pattern of the paste sample under different delay period. **(A)** delay period 18 h. **(B)** delay period 24 h. **(C)** delay period 30 h.

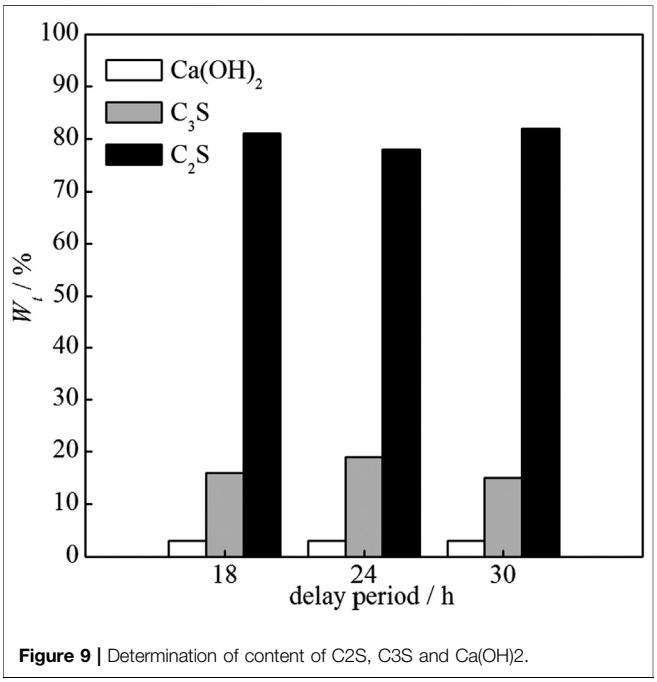

Figure 9 | Determination of content of C2S, C3S and Ca(OH)2.

entry and the outward precipitation of hydration products, thus affecting the further hydration in the later age (Zhao et al., 2010).

XRD Analysis of Hydration Products

A suitable delay period could not only make cement hydration more fully and produce more hydration products, but also improve the compactness of RPC structure. The amount of hydration products also changed with the delay period. In order to analyze the mechanism of the effect of delay period on the compressive strength and long-term strength reduction of RPC from the micro-structure level, XRD analysis was used to verify the relationship between hydration degree of the paste and the delay period at the age of 90 days. The results were shown in **Figure 8**, and the pdf number of C_2S, C_3S, and $Ca(OH)_2$ was 83-0460, 73-0599, and 72-0156, respectively. Determination of content of C_2S, C_3S, and $Ca(OH)_2$ by internal standard method, the result was shown in **Figure 9**.

Figure 8 indicated that the main phase composition of RPC hydration products were basically the same under different delay periods. They were mainly composed of hydrated calcium silicate, $Ca(OH)_2$ crystals, un-hydrated cement particles $3CaO{\cdot}SiO_2$ (C_3S) and $2CaO{\cdot}SiO_2$ (C_2S). Calcium silicate hydrate was amorphous and cannot be recognized by XRD. The diffraction peaks of C_3S and C_2S were more obvious in **Figure 8**, mainly because the water-cement ratio of RPC was very low, the hydration speed was very fast at 90 °C, the internal structure was compact, and the cement cannot be completely hydrated due to a lack of water and space. Compared with the intensity of the diffraction peaks of C_3S and C_2S under different delay periods at 90 days, the relationship was: 18 h > 24 h > 30 h. The results showed that at the age of

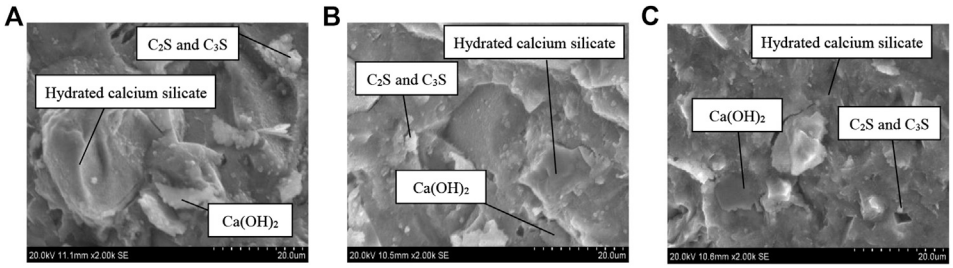

Figure 10 | SEM image of hydration products at 90 days age under different delay period. **(A)** delay period 18 h. **(B)** delay period 24 h. **(C)** delay period 30 h.

90 days, the consumption of un-hydrated particles was greater, the degree of hydration was higher and the hydration products were more when the paste was delayed by 30 h. The conclusion was consistent with that of *Effect of Delay Period on Non-evaporated Water Volume of the Paste* about the quantity of non-evaporative water. At the same time, the diffraction peaks of $Ca(OH)_2$ crystals at $2\theta = 18^{\circ}$ and $2\theta = 34^{\circ}$ were observed for three groups of paste specimens.

It could be seen from **Figures 8**, **9** that the corresponding peak of $Ca(OH)_2$ crystals at 90 days was relatively weak under the three delay periods. Because the reaction rate between the admixture and $Ca(OH)_2$ was greatly accelerated by steam at 90 °C, and the consumption of $Ca(OH)_2$ was very large.

SEM Image Analysis of Hydration Products

A certain delay period was conducive to the formation of finer hydration product particles in the cement, so that RPC can obtain higher strength in the steam curing stage. In order to elucidate the mechanism of the effect of delay period on hydration products, the micro-morphology characteristics of hydration products of the paste at the age of 90 days were observed by SEM.

Figure 10 showed that the hydration products were closely connected to each other and formed a dense continuous phase. The internal structure of RPC remained complete and compact. The hydrated calcium silicate cured by steam at 90°C were amorphous and continuous. Flake crystals were $Ca(OH)_2$ crystals and spherical particles were un-hydrated particles (Cheyrezy et al., 1995; Liu and Song, 2010). It could be seen from **Figure 10** that there was no significant difference in the morphology of hydration products among the three groups of samples, and no complete crystalline $Ca(OH)_2$ crystal was found. Because the reaction activity of silica fume was fully stimulated and a large amount of $Ca(OH)_2$ crystals were consumed under steam curing at 90°C. The cementation between hydration products was relatively dense.

Energy Dispersive Spectrum Analysis of Hydration Products

Figure 10 indicated that there was no obvious difference in the morphological characteristics of hydration products under different delay periods, but the development of long-term compressive strength of RPC specimens were obviously different. Based on this difference, the chemical composition and elemental composition of hydration products were determined through the analysis of the back-scattered-electron (BSE) images and energy dispersive spectrum analysis (EDS). The results were shown in **Figure 11** and **Table 7**. The ratio of calcium to silicon of hydration products was calculated, and the hydrated calcium silicate was analyzed qualitatively to prove the influence mechanism of delay period on the long-term mechanical properties of RPC.

It could be seen from **Figure 11** and **Table 7** that the Ca/Si ratio of hydration products under the delay period of 18 h was 1.81, which belonged to needle hydrated calcium silicate (C_2SH crystal) with relatively high Ca/Si ratio. The Ca/Si ratio of hydration products under the delay period of 24 h was 1.56, which belonged to columnar hydrated calcium silicate (C_3S_2H crystal). The Ca/Si ratio of hydration products under the delay period of 30 h was 1.54, which belonged to C_3S_2H crystal as well. Documents have shown that the compressive strength of hydration products was higher when the calcium-silicon ratio of hydration products was lower under certain conditions (Wang et al., 2007), and the lower the calcium-silicon ratio was, the denser the morphology of hydration products was, which was consistent with the strength law of *Effect of Delay Period on Compressive Strength and Long-Term Strength Reduction Ratio of RPC*.

DSC-TG Analysis of Hydration Products

The DSC-TG patterns of the paste at the age of 90 days under different delay period were shown in **Figures 12**, **13**. It could be seen from **Figure 12** that the TG curves of the paste under the delay period of 18, 24, and 30 h were relatively close, the hydration products increased slightly with the prolongation of delay period, which was consistent with the results of non-evaporated water. The endothermic peak at 110 °C was the result of dehydration reactions because of the loss of water from C-S-H (Sha et al., 1999; Yang and Yue, 2000). By the analyzation of DSC-TG, the existence of C-S-H gel in hydration products was evidenced, which was consistent with the results of SEM and EDS analysis. The second major peak which occurred between 400 and 500 °C corresponds to the dehydroxylation of $Ca(OH)_2$ (Mohammed et al., 2020). The existence of $Ca(OH)_2$ in the paste specimens was showed in the XRD patterns. The enthalpy (ΔH) of second major peak under the delay period of 18, 24, and 30 h was 4.156 J/g, 6.627 J/g

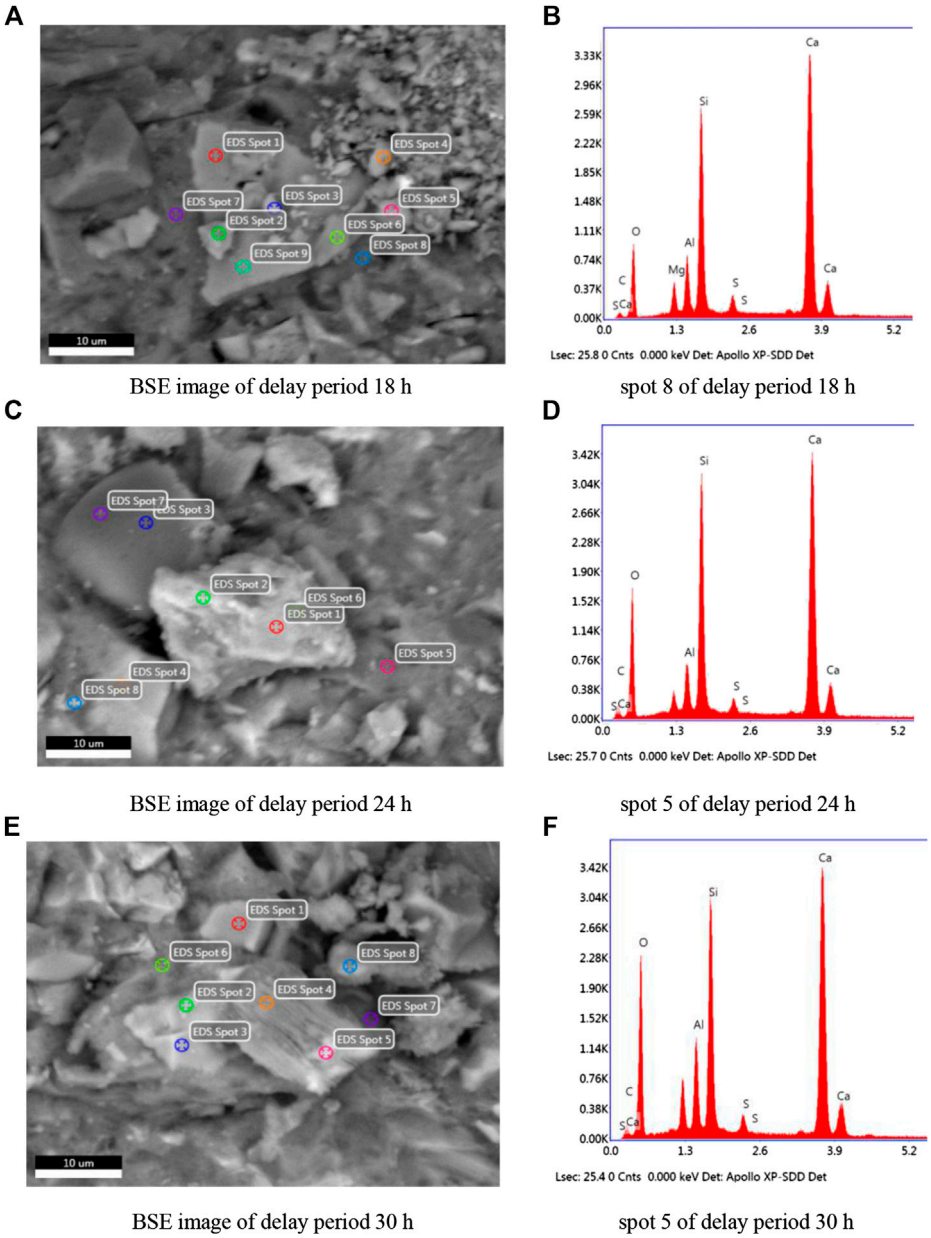

Figure 11 | Elemental energy spectrum of hydration products under different delay period. **(A)** BSE image of delay period 18 h. **(B)** spot eight of delay period 18 h. **(C)** BSE image of delay period 24 h. **(D)** spot five of delay period 24 h. **(E)** BSE image of delay period 30 h. **(F)** spot five of delay period 30 h.

TABLE 7 | Elemental composition and mass fraction of hydration products/%.

Item	Spot 8 of delay period 18 h		Spot 5 of delay period 24 h		Spot 5 of delay period 30 h	
	Weight	Error	Weight	Error	Weight	Error
O	37.50	11.07	45.91	10.51	51.17	10.03
C	2.30	21.46	5.80	14.05	3.66	15.57
Al	4.06	6.9	3.24	6.81	4.99	6.24
Si	14.60	4.85	13.61	4.45	12.21	4.63
S	1.45	9.37	1.10	12.02	1.07	9.44
Ca	37.71	2.11	30.33	2.02	26.90	2.02

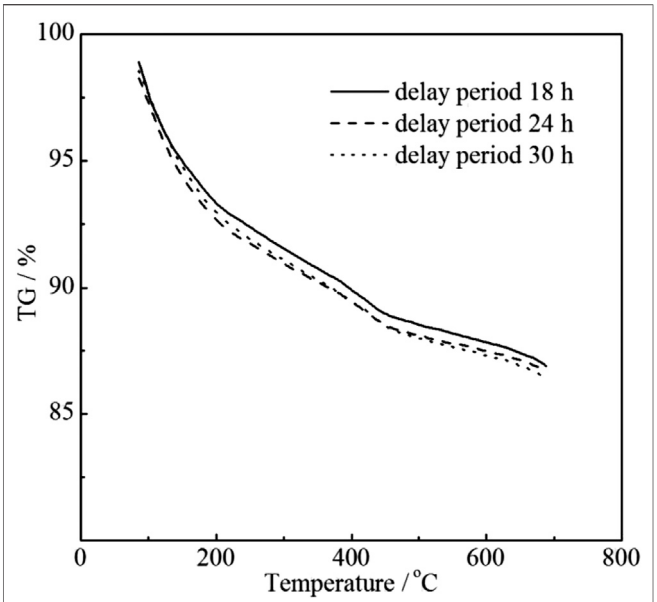

Figure 12 | TG curves of the paste under different delay period.

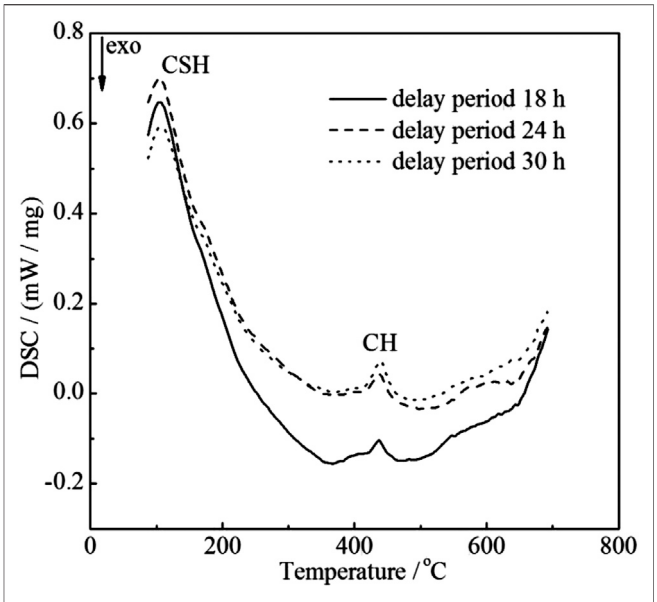

Figure 13 | DSC curves of the paste under different delay period.

and 9.089 J/g respectively. It can be seen that the degree of hydration was higher with the prolongation of delay period, and the hydration products were more when the paste was delayed by 30 h. That was consistent with the results of XRD analysis.

Mechanism Analyses

Relevant literature (Erdem et al., 2003) had shown that during the delay period, the hydration of cement was uniform and the crystalline particles of hydration products were finer, which was conducive to more adequate hydration reaction during steam curing and the rehydration of the paste in later age. Within the suitable range, the hydration reaction was more sufficient and the long-term strength of the paste was more stable with the prolongation of delay period.

The delay period had two effects on the mechanical properties of RPC. Compared with the delay period of 18 h, the delay period of 24 and 30 h could not only improve the compressive strength of RPC, but also reduce the damage of high temperature steam to the internal structure of RPC in the initial stage of hydration. It could be seen that the appropriate delay period made the early hydration degree of RPC higher, the initial strength higher, and the calcium-silicon ratio of hydration products relatively lower. The dual effects of structure compactness and protection of hydration products on RPC enhanced the compressive strength and long-term strength stability of RPC.

CONCLUSION

From the test and the analytical results, the following conclusions could be drawn.

1) Compared with the delay period of 18 h, the compressive strength of RPC specimens delayed by 24 and 30 h increased 3.2 and 4.2% respectively. The difference of compressive strength under different delay period was analyzed by one-way analysis of variance. It was shown that the compressive strength of RPC had statistically significant difference with the prolongation of delay period. The long-term strength reduction ratio of RPC specimens under the delay periods of 24 and 30 h decreased 22.8% and 71.9% respectively compared with the delay period of 18 h. Therefore, the appropriate delay period was conducive to increasing the compressive strength of RPC and reducing the reduction ratio of long-term compressive strength.
2) Based on the delay period, there was more adequate hydration reaction during steam curing and the rehydration of the paste in later age. The strength and rigidity of RPC increased with the extension of delay period. The initial elastic modulus E in the constitutive model increased with the delay period.
3) The hydration products of the paste under the delay periods of 24 and 30 h increased compared with the delay period of 18 h. The calcium-silicon ratio of hydration products under the delay periods of 24 and 30 h decreased significantly compared with the delay period of 18 h. And the structure compactness increased gradually with the prolongation of delay periods. Therefore, the suitable delay period could make RPC produce more hydration products with low Ca/Si ratio, improve the compactness of internal structure, and enhance the compressive strength and long-term strength stability of RPC.

DATA AVAILABILITY STATEMENT

The original contributions presented in the study are included in the article/Supplementary Material, further inquiries can be directed to the corresponding author.

AUTHOR CONTRIBUTIONS

XW: Experimental design, investigation, methodology and writing. QZ: Funding acquisition, investigation, methodology, project administration and writing. XH: Conceptualization, data analysis, supervision, validation, writing and revising. SZ: Data analysis, methodology and writing.

FUNDING

Financial support from the National Natural Science Foundation of China under the grants of 51578477, the Key Research and Development Project of Hebei Province under the grant of 19211505D.

REFERENCES

Abid, M., Hou, X. M., Zheng, W. Z., and Waqar, G. Q. (2017). Mechanical properties of steel fiber-reinforced reactive powder concrete at high temperature and after cooling. *Procedia Eng.* 210, 597–604. doi:10.1016/j.proeng.2017.11.119

Chan, Y. W., and Chu, S. H. (2004). Effect of silica fume on steel fiber bond characteristics in reactive powder concrete. *Cem. Concr. Res.* 34 (7), 1167–1172. doi:10.1016/j.cemconres.2003.12.023

Cheyrezy, M., Maret, V., and Frouin, L. (1995). Microstructural analysis of RPC (reactive powder concrete). *Cem. Concr. Res.* 25 (7), 1491–1500. doi:10.1016/0008-8846(95)00143-Z

Erdem, T. K., Turanli, L., and Erdogan, T. Y. (2003). Setting time: an important criterion to determine the length of the delay period before steam curing of concrete. *Cem. Concr. Res.* 33 (5), 741–745. doi:10.1016/s0008-8846(02)01058-x

Hanson, J. A. (1963). Optimum steam curing procedure in precasting plants. *J. ACI Journal Proceedings*. 60 (1), 75–100. doi:10.14359/7843

Huynh, L., Foster, S., Valipour, H., and Randall, R. (2015). High strength and reactive powder concrete columns subjected to impact: experimental investigation. *Constr Build Mater.* 78, 153–171. doi:10.1016/j.conbuildmat.2015.01.026

Lemaitre, J. (1983). How to use damage mechanics. *Nucl. Eng. Des.* 80 (2), 233–245. doi:10.1016/0029-5493(84)90169-9

Liu, B. J., Shi, J. Y., Zhou, F., Shen, S., Ding, Y. B., and Qin, J. L. (2020). Effects of steam curing regimes on the capillary water absorption of concrete: prediction using multivariable regression models. *Constr. Build. Mater.* 256, 119426. doi:10.1016/j.conbuildmat.2020.119426

Liu, J. H., and Song, S. M. (2010). Effects of curing systems on properties of high volume fine mineral powder RPC and appearance of hydrates. *J. Wuhan Univ. Technol.-Mater. Sci. Ed.* 25 (4), 619–623. doi:10.1007/s11595-010-0056-5

Mohammed, A., Rafiq, S., Mahmood, W., Noaman, R., AL-Darkazali, H., Ghafor, K., et al. (2020). Microstructure characterizations, thermal properties, yield stress, plastic viscosity and compression strength of cement paste modified with nanosilica. *J. Mater. Res.* 9 (5), 10941–10956. doi:10.1016/j.jmrt.2020.07.083

Mostofinejad, D., Nikoo, M. R., and Hosseini, S. A. (2016). Determination of optimized mix design and curing conditions of reactive powder concrete (RPC). *Constr. Build. Mater.* 123, 754–767. doi:10.1016/j.conbuildmat.2016.07.082

Nadiger, A., Harinath Reddy, C., Vasudevan, S., and Mini, K. M. (2018). "Fuzzy logic modeling for strength prediction of reactive powder concrete." in 3rd International Conference on Intelligent Computing and Applications, ICICAAkurdi, Pune, India, Singapore: Springer, 632, 375–386. doi:10.1007/978-981-10-5520-1_35

Sha, W., O'Neill, E. A., and Guo, Z. (1999). Differential scanning calorimetry study of ordinary Portland cement. *Cem Concr Res.* 29 (9), 1487–1489. doi:10.1016/S0008-8846(99)00128-3

Shideler, J. J., and Chamberlin, W. H. (1949). Early strength of concrete as affected by steam curing temperatures. *J. ACI Journal Proceedings*. 46 (12), 273–283. doi:10.14359/12057

Song, J. W., and Liu, S. H. (2016). Properties of reactive powder concrete and its application in highway bridge. *Adv. Mater Sci. Eng.*, 2016, 1–7. doi:10.1155/2016/5460241

Soroka, I., Jaegermann, C. H., and Bentur, A. (1978). Short-term steam-curing and concrete later-age strength. *Mater Struct.* 11 (62), 93–96. doi:10.1007/BF02478955

Talakokula, V., Singh, R., and Vysakh, K. (2015). "Effect of delay time and duration of steam curing on compressive strength and microstructure of geopolymer concrete." *Advances in Structural Engineering.*, New Delhi, India: Springer, 1635–1641. doi:10.1007/978-81-322-2187-6_124

Taylor, H. F. W., Famy, C., and Scrivener, K. L. (2001). Delayed ettringite formation. *Cem. Concr. Res.* 31 (5), 683–693. doi:10.1016/S0008-8846(01)00466-5

Wang, C. L., Xu, B. G., Li, S. L., and Tang, H. Y. (2006). Study on a constitutive model of damage of SFRC under uniaxial compression. *Rock and Soil Mech.* 27 (1), 151–154. doi:10.16285/j.rsm.2006.01.030

Wang, X. F., Wang, Y. P., and Wu, L. C. (2014). Degradation phenomenon of basic mechanical properties of plain reactive powder concrete with time. *J. Adv. Mater. Res.* 1065–1069, 1871–1874. doi:10.4028/www.scientific.net/AMR.1065-1069.1871

Wang, Z., Yang, Y. Z., and Li, J. H. (2007). Preparation of C-S-H-Phase nuclei and its effects on compressive strength of cement. *J. Mater. Sci. Technol.* 15 (6), 789–796. doi:10.3969/j.issn.1005-0299.2007.06.013

Wu, Y. J., Ren, S. R., Zhang, H., Shao, Z., and Wang, J. F. (2019). Effect of pre-curing time under steam curing on high strength mortar. J. *Bulletin of The Chinese Ceramic Society*. 38 (8), 2397–2402. doi:10.16552/j.cnki.issn1001-1625.2019.08.009

Yang, N. R., and Yue, W. H. (2000). *The handbook of inorganic matalloid materials atlas*. Wuhan, China: Wuhan University of Technology Press, 245–267.

Yang, Q. B., Yang, Q. R., and Zhu, P. R. (2003). Scaling and corrosion resistance of steam-cured concrete. *Cem. Concr. Res.* 33 (7), 1057–1061. doi:10.1016/S0008-8846(03)00010-3

Yazici, H., Yardimci, M. Y., Yigiter, H., Aydin, S., and Turkel, S. (2010). Mechanical properties of reactive powder concrete containing high volumes of ground granulated blast furnace slag. *Cem. Concr. Compos.* 32 (8), 639–648. doi:10.1016/j.cemconcomp.2010.07.005

Yazici, H., Yigiter, H., Karabulut, A. S., and Baradan, B. (2008). Utilization of fly ash and ground granulated blast furnace slag as an alternative silica source in reactive powder concrete. *J. Fuel.* 87 (12), 2401–2407. doi:10.1016/j.fuel.2008.03.005

Zdeb, T. (2017). An analysis of the steam curing and autoclaving process parameters for reactive powder concretes. *Constr. Build. Mater.* 131, 758–766. doi:10.1016/j.conbuildmat.2016.11.026

Zhang, S., Zhou, X. L., Xie, Y. J., and Wang, G. J. (2007). Study on the effect of curing system on the strength and microstructure of reactive powder concrete. *J. Concrete.* 28, (6), 16–18. doi:10.3969/j.issn.1002-3550.2007.06.006

Zhao, Q. X., He, X. J., Zhang, J. R., and Jiang, J. Y. (2016). Long-age wet curing effect on performance of carbonation resistance of fly ash concrete. *J. Constr Build Mater.* 127, 577–587. doi:10.1016/j.conbuildmat.2016.10.065

Zhao, X. Y., Liu, B. J., and Jiang, N. N. (2010). Effect of the steam curing paramaters on the hydration characteristics of hardened cement paste. MS dissertation. Changsha (China): Central South University of China.

Zhao, X. Y. (2010). *The study of influence factors of cement pastes under steam curing*. Changsha, China: Central South University.

Conflict of Interest: The author declares that the research was conducted in the absence of any commercial or financial relationships that could be construed as a potential conflict of interest.

Copyright © 2021 Wang, Zhao, He and Zhang. This is an open-access article distributed under the terms of the Creative Commons Attribution License (CC BY). The use, distribution or reproduction in other forums is permitted, provided the original author(s) and the copyright owner(s) are credited and that the original publication in this journal is cited, in accordance with accepted academic practice. No use, distribution or reproduction is permitted which does not comply with these terms.

frontiers in Materials

ORIGINAL RESEARCH
published: 08 February 2021
doi: 10.3389/fmats.2020.603154

Simulation of the Flowability of Fresh Concrete by Discrete Element Method

Yue Li[1], *Ji Hao*[1,2], *Caiyun Jin*[3], *Zigeng Wang*[1]* *and Jianglin Liu*[1]

[1]*The Key Laboratory of Urban Security and Disaster Engineering, MOE, Beijing University of Technology, Beijing, China,* [2]*Department of Material Science and Engineering, Beijing University of Technology, Beijing, China,* [3]*College of Applied Sciences, Beijing University of Technology, Beijing, China*

The discrete element method (DEM) was used to establish the slump model and J-Ring model of concrete to describe the flow behavior in the slump test and J-Ring test. Then, the contact parameters of particle-particle and particle-geometry for the concrete DEM model, including restitution coefficient, rolling friction coefficient, static friction coefficient, and surface energy, were measured. In order to avoid the influence of the shape and size of the aggregate, this paper used high-precision glass spheres as the aggregate of the concrete for meso-calibration test, slump test, and J-Ring test. Comparing the simulation results of DEM model with slump test result, a very high agreement between the initial stage, the rapid flow stage, and the slow flow stage of the slump flow–time curve can be found as well as the final slump and slump flow. Moreover, similar to the slump DEM model, the DEM models of J-Ring test, V-funnel test, and U-channel test were established to study the passing ability and filling ability of concrete with outstanding accuracy. Therefore, the concrete DEM model with contact parameters and JKR model can be adopted to study the flow behavior of the fresh concrete.

Keywords: discrete element method, meso-calibration test, contact parameter, Hertz–Mindlin with JKR, concrete flowability, passing ability

OPEN ACCESS

Edited by:
Dongshuai Hou,
Qingdao University of Technology, China

Reviewed by:
Zhengwu Jiang,
Tongji University, China
Qiang Yuan,
Central South University, China

***Correspondence:**
Zigeng Wang
zigengw@bjut.edu.cn

Specialty section:
This article was submitted to Computational Materials Science, a section of the journal Frontiers in Materials

Received: *05 September 2020*
Accepted: *28 December 2020*
Published: *08 February 2021*

Citation:
Li Y, Hao J, Jin C, Wang Z and Liu J (2021) Simulation of the Flowability of Fresh Concrete by Discrete Element Method. Front. Mater. 7:603154. doi: 10.3389/fmats.2020.603154

INTRODUCTION

Fresh concrete is a kind of complex composite material with highly uneven composition and structure. The trajectory of aggregate particles in fresh concrete greatly affects the flow behavior of concrete. Under the influence of aggregate particles, fresh concrete shows a flow behavior similar to particle flow (Hou et al., 2017). Considering the non-uniformity of fresh concrete on the meso level, the discrete element method (DEM) can truly simulate the flow behavior of the fresh concrete (Mechtcherine et al., 2013).

In recent years, the DEM has been widely used in the numerical simulation of fresh concrete. A variety of DEM contact models of fresh concrete have been proposed. Shyshko and Mechtcherine (2008) and Shyshko and Mechtcherine (2013) obtained the force-displacement relationship between the particles according to the experiments, establishing the interaction model of adjacent particles in the vertical direction, then directly introducing the model to establish a DEM model of fresh concrete with different workability. Finally, extensive simulations were conducted to study the effects of various model parameters on the numerical simulation results of the slump test. Guo et al. (2010) used the DEM and rheological model to simulate the workability test of fresh concrete by proposing the determination of the DEM parameters of the concrete (spring coefficient, friction coefficient, contact thickness, and damping coefficient). Remond and Pizette (2014) implemented a hard-core soft-shell DEM model to simulate concrete flowability. The fresh concrete was described as an

assembly of composite particles made of spherical hard grains representing coarse aggregates surrounded by concentric spherical layers representing mortar. This mechanical model can make the rheological properties of mortar directly relate to the rheological properties of simulated concrete. Hoornahad and Koenders (2014) used the two-phase paste-bridge system as the particle-paste-particle interaction in the DEM model of fresh concrete to establish the rheological model of self-compacting concrete (SCC). According to the interaction between cement slurry and aggregate in fresh pervious concrete, Pieralisi et al. (2016) proposed a DEM constitutive relation suitable for pervious concrete. Zhao et al. (2018) established a new dynamic coupling discrete element contact model to study fresh concrete with different grades and workability and proved the correctness of the DEM model according to the rheological test results of the fresh concrete. Krenzera et al. (2019) came up with a DEM model to simulate the mixing process of fresh concrete. The model provided the liquid transport process from wet solid particles to dry solid particles, including volume adaptation and mass conservation. Mechtcherine and Shyshko (2015) derived the DEM model parameters related to yield stress based on the Bingham model and established a reliable numerical model of fresh concrete due to the flow shape of concrete in the numerical simulation. Because of the mechanism of thixotropy and static and shear time dependence of fresh concrete, Li et al. (2018) proposed a DEM for predicting flow characteristics of static and mixing time dependence.

The DEM has been deeply applied to the simulation of the flowability of fresh concrete. Cui et al. (2016) and Cui et al. (2018) offered a fast and effective method to establish irregular polyhedral particles to simulate real shape coarse aggregate. Then, the slump test and L-box of fresh SCC were carried out to verify the feasibility of the method. Zhan et al. (2019) used the DEM to numerically investigate the flowability of pumped concrete in the pipe by modeling the coarse aggregates as rigid agglomerates and defining the contact model appropriately. Cao et al. (2015) exploited the DEM model to study the effect of the volume fraction of coarse aggregate on the yield stress of concrete, and the contact parameters were verified by concrete rheology test. Then, the pumping process of fresh concrete was simulated, and the effect of the volume fraction of coarse aggregate on the pumping pressure and wall wear was studied. Zhang et al. (2020) used the DEM to simulate the filling performance of rock-filled concrete. Based upon the excess paste theory and slump test results, the thickness of the mortar layer and the meso parameters of the particle unit were calibrated. The pouring process of the calibrated SCC in the rockfill was simplified as L-box flow. Through the comparison between the DEM simulation results and the test results, the influence of the rockfill voidage on the passability of SCC was analyzed. Tan et al. (2015) considered the thixotropy of fresh concrete by introducing the time-varying contact parameters into the DEM model. Then, based on the thixotropy DEM model, the lateral pressure of fresh concrete on the rheometer barrel wall was numerically studied, the change characteristics of pressure with time were verified, and the influence of thixotropy on yield stress was solved.

At present, the main challenge of DEM simulation of fresh concrete was to find a quantitative correlation between model parameters and the properties and proportions of concrete components (Coetzee, 2017). There were two approaches in the literature to calibrate DEM input parameters. The first approach was to use the test to measure the bulk property of the material, and then to establish a numerical model of the test. The DEM parameter values were changed iteratively until the predicted bulk response matched the measured results (Coetzee, 2016; Rackl and Hanley, 2017). The bulk response of the numerical test can be influenced by more than one parameter, and more than one combination of the parameter values resulted in the same bulk behavior. Therefore, the potential problem with this approach was that there is no unique solution. As a result, the combination of parameter values used in DEM model was not completely the correct combination. The second approach was to directly measure the contact parameters of the DEM model using the meso-calibration test method, and then comparing the DEM simulation results with the macro test results to verify the reliability of the calibration parameters. The advantage of this approach was that the meso-calibration test results were close to the actual results of the DEM model input parameters. However, due to the short development time of DEM and the large difference in the shape and size of the particles used for simulation, it was still in the stage of perfecting the input parameter test method.

In this paper, the quantitative correlation between contact parameters of DEM model and the properties and proportions of concrete components was established through meso-calibration tests. Fresh concrete was considered to be composed of particles wrapped by mortar. Hertz–Mindlin with JKR (Johnson–Kendall–Roberts) cohesion contact model (Kendall, 1971) was utilized to represent the contact force between particles. Through a series of meso-calibration tests, the contact parameters of particle-particle and particle-geometry in the concrete DEM model were measured, including the restitution coefficient, static friction coefficient, rolling friction coefficient, and surface energy. In order to avoid the influence of the shape and size of aggregate on the meso input parameters of particles, high-precision spherical glass was used to replace the aggregates in concrete. According to the particle size distribution of glass aggregate, the DEM models of slump test, J-Ring test, V-funnel test, and U-channel test of the fresh concrete were established, and then the meso contact parameters were input into DEM model for numerical simulation. The simulation results of DEM were compared with the test results to verify the feasibility of the method used in this paper.

MATERIALS AND TESTS

Materials

Cementitious Materials

P·II 42.5 Portland cement, F-type fly ash, S95 ultra-fine slag powder, and ultra-fine micro silica fume were used as the cementitious materials.

TABLE 1 | Mixture proportions of concrete (kg/m^3).

	w/c	Water	Cement	Fly ash	Slag	Silica fume	Fine aggregate	Coarse aggregate	Admixture
A1	0.40	180.0	250	120	60	20	950	910	2.1
A2	0.42	189.0	250	120	60	20	950	910	2.1
A3	0.44	198.0	250	120	60	20	950	910	2.1
B1	0.30	181.5	320	150	100	35	780	890	3.5
B2	0.32	193.6	320	150	100	35	780	890	3.5
B3	0.34	205.7	320	150	100	35	780	890	3.5
C1	0.24	151.2	350	130	100	50	647.5	971.3	5.2
C2	0.26	163.8	350	130	100	50	647.5	971.3	5.2
C3	0.28	176.4	350	130	100	50	647.5	971.3	5.2

Aggregate

In order to avoid the influence of the shape and size of aggregate on the meso contact parameters of particles, this paper used high-precision glass spheres as the coarse aggregate for slump test, J-Ring test, and meso-calibration test. The glass sphere has smooth surface, good wear resistance, and high compressive strength. The density is 2,530 kg/m^3, the shear modulus is 1.97 GPa, Poisson's ratio is 0.25, and the particle size error is less than 0.02 mm. The particle sizes of coarse aggregate used in this paper are 3, 4, 5, 6, 7, 8, 9, and 10 mm, respectively, and the corresponding volume fractions are 1.24, 3.76, 5.32, 7.61, 20.01, 22.34, 24.71, and 15.01%.

In this paper, spherical glass beads were used as fine aggregate. The density of the glass beads is 2,487 kg/m^3, the shear modulus is 1.96 GPa, and Poisson's ratio is 0.25. The sieve residues of 1.25, 0.63, 0.315, 0.160, and 0.074 mm were 3.75, 27.98, 43.54, 17.44, and 7.29%, respectively.

Mixture Proportion

In this paper, glass aggregates of different particle sizes were used to replace sand and gravel with equal volume. According to the amount of cementitious material and aggregate, the mix proportion of this paper can be divided into three groups: A, B, and C; each group has three different water-binder ratios. The nine types of concrete mixture proportion used for fluidity test and DEM parameter calibration test are shown in **Table 1**. The admixture is polycarboxylate superplasticizer with water reduction rate of 27% and solid content of 15.6%.

Fluidity Tests

Slump Test

The slump test of spherical aggregate concrete was carried out according to the standard GB/T 50,080-2016, and the lifting speed of the slump cone was 0.06 m/s. A camera was arranged right above the slump cone to record the change of concrete slump flow with time, and the recording time interval was 0.05s. The slump test was repeated three times for each mix proportion, and the average value was taken as the test value of the slump and slump flow of spherical aggregate concrete. The slump and slump flow of A1 were 210 and 464 mm; the slump and slump flow of A2 were 227 and 506 mm; the slump and slump flow of A3 were 231 and 552 mm; the slump and slump flow of B1 were 201 and 449 mm; the slump and slump flow of B2 were 211 and 486 mm; the slump and slump flow of B3 were 226 and 517 mm; the slump and slump flow of C1 were 197 and 437 mm; the slump and slump flow of C2 were 209 and 469 mm; the slump and slump flow of C3 were 201 and 501 mm.

J-Ring Test

In this paper, the spherical aggregate concrete J-Ring test was conducted to investigate the passing ability of the concrete according to the standard GB/T 50,080-2016, and the lifting speed of the slump cone was 0.06 m/s. The J-Ring test was repeated three times for each mix proportion, and the average value was taken as the J-Ring slump-flow test value of spherical aggregate concrete. The J-Ring slump flow of A1, A2, A3, B1, B2, B3, C1, C2, and C3 was 448, 489, 534, 432, 471, 501, 422, 451, and 485 mm, respectively.

V-Funnel Test

The V-funnel tests were conducted according to the standard GB/T 50,080-2016. The outflow time (T_V) of concrete in V-funnel was recorded. The value of T_V can reflect the viscosity and segregation resistance of concrete. The smaller the T_V value, the smaller the plastic viscosity of concrete and the better the segregation resistance of concrete. The T_V of A1, A2, A3, B1, B2, B3, C1, C2, and C3 was 5.5, 5.3, 5.1, 6.5, 6.3, 6.0, 7.3, 7.1, and 6.9 s, respectively.

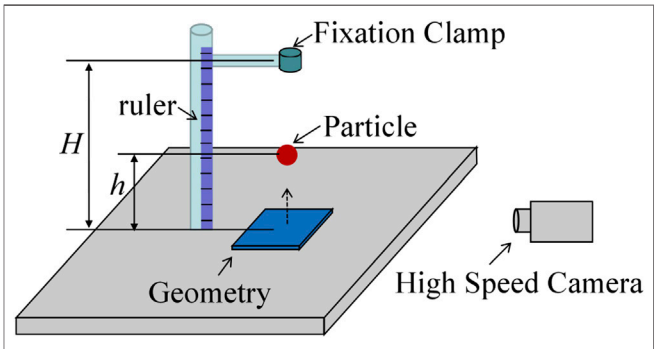

FIGURE 1 | Test device for restitution coefficient.

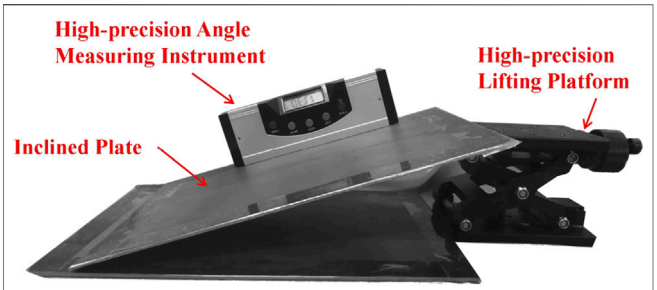

FIGURE 2 | Inclined test device.

U-Channel Test

The U-channel test was used to measure the filling height (*Bh*) of concrete. *Bh* can reflect the filling ability of concrete; that is, the smaller the *Bh*, the better the filling ability of concrete. The test was carried out according to the standard GB/T 50,080-2016. In the U-channel test, the lifting speed of the gate was 0.08 m/s. The test value of *Bh* of A1, A2, A3, B1, B2, B3, C1, C2, and C3 was 263, 264, 266, 250, 253, 255, 237, 239, and 241 mm, respectively.

Calibration Test

Coefficient of Restitution

The coefficient of restitution (e) reflected the degree of conservation of kinetic energy after collision between particle and geometry or between particle and particle in DEM. The value depended on the material, shape, collision direction, or collision speed that made up the collision element. The value of the coefficient of restitution was calculated from the relationship between the kinetic energy of the particle after the collision and the kinetic energy of the particle before the collision. According to González-Montellano et al. (2012), when the particles in the collision were not affected by rotation, the coefficient of restitution (for any type of collision) can be calculated using **Eq. 1**. The collision test to measure the coefficient of restitution is shown in **Figure 1**.

$$e = \frac{v_1 - v_2}{u_1 - u_2}, \tag{1}$$

where u_1 is the characteristic velocity before collision of free-falling particle; v_1 is the characteristic velocity after collision of particle; u_2 is the characteristic velocity before collision of the geometry; v_2 is the characteristic velocity after collision of the geometry.

In this paper, the meso-calibration test of particle-geometry restitution coefficient (e_g) was similar to that of Gabriel KP Barrios (Barrios et al., 2013). The device allowed controllable collision between free-falling particles and the geometry plate, as shown in **Figure 1**. The particle was released from a fixed height H, falling freely and colliding with the geometry plate, and then bouncing to the height of h (lower than H). The free-fall height H and the bounce height h were determined using images taken by an i-SPEED 716 high-speed camera (Ix-camera, United Kingdom) at a rate of 100 frames per second.

The velocity v_2 and u_2 (**Eq. 1**) corresponding to the stationary geometry plate were taken as zero, and it was assumed that the energy was conserved before and after the collision. Therefore, the value of particle-geometry restitution coefficient can be expressed as a function of particle initial height H and bounce height h in **Eq. 2**:

$$e_g = -\frac{v_1}{u_1} = \sqrt{\frac{h}{H}}, \tag{2}$$

In this paper, the concrete was regarded as composed of particles of aggregate wrapped by paste. In the particle-geometry restitution coefficient test, the free-falling particle was a glass sphere wrapped by paste (the composition of the paste was the same as that in the concrete), and the geometry plate was a stainless steel plate with the same material as the slump plate.

If the particle collision particle was directly used to measure the particle-particle restitution coefficient (e_p), there were strict requirements on the collision angle between particles. Grima (2011) accurately measured particle-particle restitution coefficient by using a plate of the same material as the particle instead of the collided particle. In this paper, the glass plate with the same material and process as the glass particle was used instead of the collided particle. The geometry plate in **Figure 1** was replaced with the glass plate for the particle-particle restitution coefficient test. The particle-particle restitution coefficient test procedure and device were the same as the particle-geometry restitution coefficient test.

The spherical glass aggregate (wrapped with mortar) taken directly from the fresh concrete was used as free-falling particle for the restitution coefficient test. The particles fell freely from four different fixed heights of 100, 90, 80, and 70 mm and collided with the geometry plate or glass plate. The test was repeated 10 times for each fixed height to obtain the average bounce height h.

Coefficient of Rolling Friction

The coefficient of rolling friction (μ_r) was an index to measure the resistance of a rolling object. This value represented the relationship between the tangential force of the rolling bodies and the normal force that kept the rolling body in contact. Ai et al. (2011) conducted the inclined test to measure the rolling friction coefficient of particle.

The inclined test device used in this paper was made up of an inclined plate, a high-precision angle measuring instrument (accuracy of 0.01°), and a high-precision lifting platform (lifting speed of 0.008 m/s), as shown in **Figure 2**. When the particle-geometry rolling friction coefficient (μ_{rg}) was measured, the stainless steel geometry plate was used as the inclined plate for testing.

When testing the particle-geometry rolling friction coefficient, the particles were placed on the horizontal stainless steel inclined plate, and the handwheel of the lifting table was rotated to slowly raise the lifting table in order to increase the tilt angle of the stainless steel plate. When the particles rolled, a high-speed camera was recording the tilt angle of the inclined plate. The force condition of the particle on the stainless steel plate is shown in **Figure 3**.

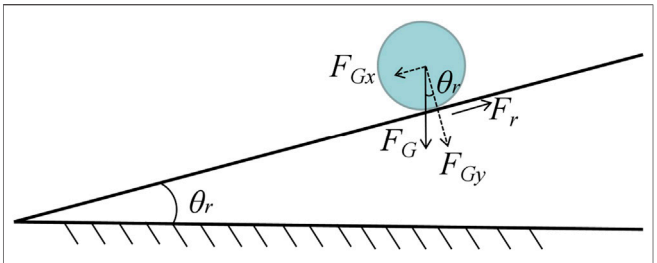

FIGURE 3 | Balance of force in rolling friction test.

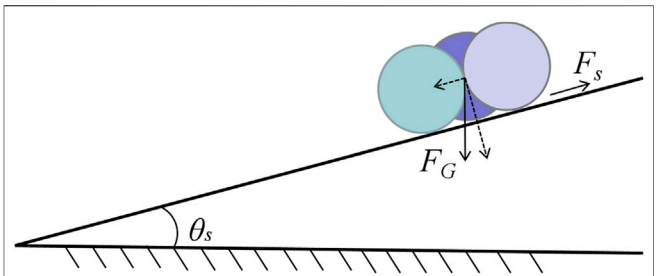

FIGURE 4 | Balance of force in static friction test.

Equation 3 is the balance equation of the force of the particle on the inclined plate.

$$F_{rg} = \mu_{rg} \cdot F_{Gy} = \mu_{rg} \cdot F_G \cdot \cos\theta_{rg}, \tag{3}$$

where F_{rg} is the rolling friction force between the particle and the geometry inclined plate, in N; μ_{rg} is the rolling friction coefficient between the particle and the geometry inclined plate; F_G is the gravity of the particle, in N; F_{Gy} is the normal component of gravity on the geometry inclined plate, and the unit is N; θ_{rg} is the angle between the geometry inclined plate and the horizontal plane, and the unit is °.

In the critical state where the particle was about to roll,

$$F_{rg} = F_{Gx} = F_G \cdot \sin\theta_{rgc}, \tag{4}$$

where F_{Gx} is the tangential component of gravity on the geometry inclined plate, and the unit is N; θ_{rgc} is the critical rolling angle of particle on the geometry inclined plate, and the unit is °.

Equation 4 was substituted into **Eq. 3** to obtain

$$\mu_{rg} = \tan\theta_{rgc} \tag{5}$$

From **Eq. 5**, the value of particle-geometry rolling friction coefficient (μ_{rg}) was equal to the tangent value of the inclination angle when the particle was in the critical rolling state.

In the particle-particle rolling friction coefficient (μ_{rp}) test, the glass plate with the same material and production technology as the particle was used as the inclined plate to measure the particle-particle rolling friction coefficient (Grima, 2011). The test procedure and method were the same as the particle-geometry rolling friction coefficient.

The spherical glass aggregate (wrapped with mortar) taken directly from the fresh concrete was used as rolling particle for the rolling friction coefficient test. The test was conducted using glass spheres with particle sizes of 10, 9, 8, and 7 mm. The particle-geometry rolling friction coefficient test and particle-particle rolling friction coefficient test of each particle size were repeated 10 times to obtain the average critical rolling angle.

Coefficient of Static Friction

The coefficient of static friction (μ_s) was the ratio of the maximum static friction force to the normal force between the contact surfaces, calculated by measuring the critical slide angle when the concrete particles began to slide through the inclined test. The operation and procedure of the static friction coefficient inclined test were the same as the rolling friction coefficient inclined test.

Before testing the particle-geometry static friction coefficient (μ_{sg}), in order to avoid the particles rolling on the inclined plate, three particles with the same particle size were bonded together (Grima, 2011). This can effectively prevent the particles from rolling, before sliding occurred, and did not affect the calculation of the static friction coefficient of the particles, as shown in **Figure 4**.

The balance equation of the force of the particles on the inclined plate was

$$F_{sg} = \mu_{sg} \cdot F_{Gy} = \mu_{sg} \cdot F_G \cdot \cos\theta_{sg}, \tag{6}$$

where F_{sg} is the static friction force between the particle and the geometry inclined plate, in N; μ_{sg} is the static friction coefficient between the particle and the geometry inclined plate; θ_{sg} is the angle between the geometry inclined plate and the horizontal plane, in °. When the particles were in a sliding critical state,

$$F_{sg} = F_{Gx} = F_G \cdot \sin\theta_{sgc}, \tag{7}$$

where θ_{sgc} is the critical sliding angle of particles on the geometry inclined plate, in °. **Equation 7** was substituted into **Eq. 6** to calculate the particle-geometry static friction coefficient (μ_{sg}):

$$\mu_{sg} = \tan\theta_{sgc}, \tag{8}$$

It can be seen from **Eq. 8** that the value of particle-geometry static friction coefficient (μ_{sg}) was equal to the tangent value of critical sliding angle (θ_{sgc}).

The spherical glass aggregate (wrapped with mortar) taken directly from the fresh concrete was used as slipping particle for the static friction coefficient test. In the particle-particle

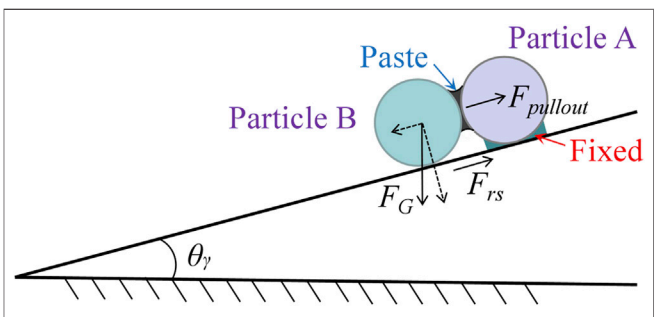

FIGURE 5 | Balance of force in $F_{pullout}$ test.

static friction coefficient (μ_{sp}) test, the glass plate with the same material and production technology as the particle was used as the inclined plate to measure the particle-particle static friction coefficient (Grima, 2011). The test procedure and method were the same as the particle-geometry static friction coefficient.

The Surface Energy

The surface energy (γ) affected the adhesion of fresh concrete particles (Zafar et al., 2014). The surface energy value of fresh concrete particles was determined by the surface tension and wetting angle of the paste. In this paper, the pullout force between fresh concrete particles was measured by inclined test, and then the value of surface energy was calculated according to **Eq. 9**. In the incline test to measure the surface energy of JKR, the surface of the glass sphere was smooth, and the paste was only daubed on the contact position between the two particles, as shown in **Figure 5**. Particle A was fixed on the inclined plate. The tilting angle of the inclined plate increased evenly by adjusting the lifting table. When the inclined plate reached a certain angle, particle B began to get rid of the adhesion of the paste under the influence of gravity and rolled down. A high-speed camera was used to record the tilt angle of the inclined plate when the two particles separated.

$$F_{\text{pullout}} = -\frac{3}{2}\pi\gamma R^*, \tag{9}$$

where F_{pullout} is the pullout force exerted on particle B by the paste between the particles, in N; γ is the surface energy of the slurry, in J/m^2; R^* is the equivalent radius of particle A and particle B, in J/m^2.

The force of particle B on the inclined plate is shown in **Figure 5**. The equilibrium equation of force for particle B was as follows:

$$F_{pullout} + F_{rs} = F_{Gx} = F_G \cdot \sin\theta_\gamma, \tag{10}$$

where F_{rs} is the rolling friction force between particle B and the inclined plate, in N; θ_γ is the angle between the inclined plate and the horizontal plane, in °.

The critical rolling angle ($\theta_{\gamma c}$) of particle B was larger than that of smooth particle when there was adhesion force between particles. When the inclination angle of particle B was larger than θ_{rsc} of smooth particle, the rolling friction force of particle B was

$$F_{rs} = \mu_{rs} \cdot F_{Gy} = \mu_{rs} \cdot F_G \cdot \cos\theta_\gamma, \tag{11}$$

where μ_{rs} is the rolling friction coefficient of smooth glass particles and inclined plate. When particle B was in rolling critical state, **Eq. 11** was substituted into **Eq. 10**, and F_{pullout} was calculated as follows:

$$F_{\text{pullout}} = F_G \cdot \sin\theta_{\gamma c} - \mu_{rs} \cdot F_G \cdot \cos\theta_{\gamma c}, \tag{12}$$

Therefore, before calculating F_{pullout}, the rolling friction coefficient between the smooth glass particles and the inclined plate needed to be tested. This paper used the method of measuring the rolling friction coefficient of fresh concrete particles in "Coefficient of Rolling Friction" section to measure the critical rolling angle (θ_{rsc}) of the smooth glass particles and the inclined plate, and then μ_{rs} was calculated using **Eq. 5**.

This paper used 10, 9, 8, and 7 mm glass spheres for surface energy test. The surface energy test for each particle size was repeated 10 times to obtain the average separation angle between particles.

Before measuring F_{pullout} of the paste, the rolling friction coefficient of the smooth particles and the inclined plate was tested. After determining the rolling friction coefficient of the smooth glass particles and the inclined plate, the inclined test in **Figure 5** was conducted to measure the critical rolling angle ($\theta_{\gamma c}$) of particles B when there was paste between the particles. Then, **Eq. 12** was utilized to calculate F_{pullout} of the paste between the particles, and **Eq. 9** was adopted to calculate the surface energy γ between the particles.

SIMULATION OF CONCRETE FLOWABILITY

DEM Contact Model

The Hertz–Mindlin with JKR (Johnson–Kendall–Roberts) cohesion (Kendall, 1971) was a cohesive force contact model, which considered the influence of cohesion in the particle contact area and mainly was used for discrete element simulation of particles with Van der Waals forces or wet particles. At present, the theoretical research of JKR model has been mature, and the physical meaning of contact parameters has been clear. In addition, the contact parameters of JKR model can be directly measured by test. In this paper, Hertz–Mindlin with JKR cohesion was used as the contact model of the concrete particles. Hertz–Mindlin with JKR model was an improvement of normal force based on Hertz–Mindlin (no slip) contact mode. In JKR model, the normal elastic contact force was realized based on JKR theory (Kendall, 1971). The tangential force of Hertz–Mindlin with JKR model was the same as that of Hertz–Mindlin (no slip) contact model.

The normal force component of the Hertz–Mindlin (no slip) model was calculated based on the Hertz contact theory (Hertz, 1880). The tangential force model was calculated based on the research results of Mindlin and Deresiewicz (Mindlin, 1949; Deresiewicz, 1953). The tangential friction followed the Coulomb friction law and was limited by $\mu_s F_n$. Both the normal force and the tangential force had damping components, and the damping coefficient was related to the restitution coefficient (Tsuji et al., 1992).

The normal force F_n was a function of the normal overlap δ_n between particles, calculated by **Eq. 13**:

$$F_n = \frac{4}{3}E^*\sqrt{R^*}\delta_n^{\frac{3}{2}}, \tag{13}$$

where the equivalent Young's modulus E^* and equivalent radius R^* were defined as

$$\frac{1}{E^*} = \frac{\left(1-\nu_i^2\right)}{E_i} + \frac{\left(1-\nu_j^2\right)}{E_j}, \tag{14}$$

TABLE 2 | The restitution coefficient test results of B1 concrete.

	H (mm)	*h*		$e = \sqrt{\frac{h}{H}}$
		Mean (mm)	Standard deviation	
Particle-geometry (e_g)	100	6.01	0.308	0.245
	90	5.62	0.334	0.250
	80	4.84	0.220	0.246
	70	4.36	0.262	0.250
Particle-particle (e_p)	100	5.39	0.335	0.243
	90	5.73	0.293	0.252
	80	4.87	0.283	0.247
	70	4.47	0.279	0.253

TABLE 3 | The rolling friction coefficient test results of B1 concrete.

	Particle size	θ_{rc}		$\mu_r = \tan\theta_{rc}$
		Mean	Standard deviation	
Particle-geometry (μ_{rg})	10	6.19°	0.227	0.108
	9	5.98°	0.203	0.104
	8	6.50°	0.229	0.114
	7	5.73°	0.255	0.100
Particle-particle (μ_{rp})	10	5.38°	0.308	0.094
	9	4.81°	0.329	0.084
	8	5.20°	0.278	0.091
	7	5.07°	0.297	0.088

$$\frac{1}{R^*} = \frac{1}{R_i} + \frac{1}{R_j}, \tag{15}$$

where E_i, ν_i, R_i and E_j, ν_j, R_j are Young's moduli, Poisson's ratios, and radiuses of particle i and particle j.

Normal damping force $F_n{}^d$ is calculated as follows:

$$F_n^d = -2\sqrt{\frac{5}{6}}\beta\sqrt{S_n m^*}v_n^{rel}, \tag{16}$$

where $m^* = \left(\frac{1}{m_i} + \frac{1}{m_j}\right)^{-1}$ is the equivalent mass, v_n^{rel} is the normal component of the relative velocity, and β (damping ratio) and S_n (normal stiffness) are given by

$$\beta = \frac{\ln e}{\sqrt{\ln^2 e + \pi^2}}, \tag{17}$$

$$S_n = 2E^*\sqrt{R^*\delta_n}, \tag{18}$$

where e is the coefficient of restitution.

The tangential force F_t depended on the tangential overlap δ_t and the tangential stiffness S_t, as follows:

$$F_t = -S_t\delta_t, \tag{19}$$

$$S_t = 8G^*\sqrt{R^*\delta_n}, \tag{20}$$

where $G^\star$ is the equivalent shear modulus.

Tangential damping force F_t^d is calculated as follows:

$$F_t^d = -2\sqrt{\frac{5}{6}}\beta\sqrt{S_t m^*}v_n^{rel}, \tag{21}$$

where v_t^{rel} is the relative tangential velocity.

The rolling friction torque was proportional to the normal contact force, and its direction was opposite to the relative rotation direction (Zhou et al., 1999). The rolling friction of the particles was performed by applying torque to the contact surface.

$$\tau_i = -\mu_r F_n R_i \omega_i, \tag{22}$$

where μ_r is the rolling friction coefficient, R_i is the distance from the contact point to the center of mass, and ω_i is the unit angular velocity vector of the object at the contact point.

The normal force of Hertz–Mindlin with JKR cohesion model increased a kind of cohesion on the basis of Hertz–Mindlin (no slip) normal force. The normal force F_{JKR} of JKR model depended on the amount of overlap δ between particles and surface energy γ.

$$F_{JKR} = -4\sqrt{\pi\gamma E^*}a^{\frac{3}{2}} + \frac{4E^*}{3R^*}a^3, \tag{23}$$

$$\delta = \frac{a^2}{R^*} - \sqrt{4\pi\gamma a/E^*}, \tag{24}$$

where a is the radius of the circular contact area formed between particles.

When $\gamma = 0$, the normal force of the JKR model was equal to the normal force of Hertz–Mindlin (no slip).

$$F_{Hertz} = \frac{4}{3}E^*\sqrt{R^*}\delta_n^{\frac{3}{2}} \tag{25}$$

The JKR model can still provide the cohesive force when the particles were not in direct contact. The maximum gap δ_c and critical contact radius α_c of non-zero cohesive force between particles were calculated by the following **Eqs. 26, 27**:

$$\delta_c = \frac{\alpha_c^2}{R^*} - \sqrt{4\pi\alpha_c/E^*}, \tag{26}$$

$$\alpha_c = \left[\frac{9\pi\gamma R^*}{2E^*}\left(\frac{3}{4} - \frac{1}{\sqrt{2}}\right)\right]^{\frac{1}{3}}, \tag{27}$$

The maximum cohesion force occurred when the particles were not in contact and the separation gap was less than δ_c. This maximum cohesion force was called F_{pullout}, calculated by **Eq. 9**.

Results of Calibration Test

The Test Results of Restitution Coefficient

The restitution coefficient test results of B1 concrete are shown in **Table 2**. After the particles fell freely from different heights and collided with the geometry, the rebound height h decreased as the initial height H decreased. The restitution coefficients of different fixed heights were basically the same, and the average value of particle-geometry restitution coefficient (e_g) was 0.248. The particle-particle collision test results were similar to the particle-geometry test results, and the average particle-particle restitution coefficient (e_p) was 0.249.

According to the test results of restitution coefficient of concrete particles with different mix proportions, the average

TABLE 4 | The static friction coefficient test results of B1 concrete.

	Particle size	θ_{sc}		$\mu_s = \tan\theta_{sc}$
		Mean	Standard deviation	
Particle-geometry (μ_{sg})	10	12.42°	0.439	0.220
	9	13.12°	0.501	0.233
	8	12.70°	0.406	0.225
	7	13.21°	0.491	0.235
Particle-particle (μ_{sp})	10	11.26°	0.453	0.199
	9	10.44°	0.454	0.184
	8	10.49°	0.478	0.185
	7	11.29°	0.372	0.200

TABLE 5 | The test results of rolling friction coefficient of smooth glass particles.

	Particle size (mm)	θ_{rs}		$\mu_{rs} = \tan\theta_{rs}$
		Mean	Standard deviation	
Particle-plate (μ_{rs})	10	1.04°	0.026	0.018
	9	1.05°	0.019	0.018
	8	1.02°	0.024	0.018
	7	1.03°	0.020	0.018

restitution coefficients of nine concrete particles were calculated. The e_g of nine concrete particles was 0.249, 0.254, 0.255, 0.248, 0.252, 0.254, 0.244, 0.250, and 0.253, respectively. The e_p of nine concrete particles was 0.251, 0.255, 0.257, 0.249, 0.253, 0.256, 0.246, 0.251, and 0.255, respectively. The restitution coefficient of the three groups of concrete particles A, B, and C decreased with the increasing of the water-binder ratio.

The Test Results of Rolling Friction Coefficient

The rolling friction coefficient test results of B1 concrete are shown in **Table 3**. The critical rolling angles (θ_{rc}) of particle-geometry of different particle sizes were similar, and the average value of particle-geometry rolling friction coefficient (μ_{rg}) was 0.107. The critical rolling angles (θ_{rc}) of particle-particle of different particle sizes were basically the same, and the average value of particle-particle rolling friction coefficient (μ_{rp}) was 0.090.

The average rolling friction coefficients (μ_{rg}) of the concrete particles of the nine mix ratios were 0.104, 0.094, 0.090, 0.106, 0.102, 0.095, 0.113, 0.101, and 0.097, respectively. The average rolling friction coefficients (μ_{rp}) of the concrete particles of the nine mix ratios were 0.083, 0.073, 0.071, 0.086, 0.083, 0.080, 0.104, 0.081, and 0.079, respectively. The particle-geometry rolling friction coefficient and particle-particle rolling friction coefficient values of the three groups of concrete of A, B, and C decreased with the increase of the water-binder ratio.

The Test Results of Static Friction Coefficient

The static friction coefficient test results of B1 concrete are shown in **Table 4**. The critical slide angles (θ_{sc}) of particle-geometry of different particle sizes were close, and the average value of particle-geometry static friction coefficient (μ_{sg}) was 0.228. The critical slide angles (θ_{sc}) of particle-particle of different particle sizes were about the same, and the average value of particle-particle static friction coefficient (μ_{sp}) was 0.192.

The average particle-geometry static friction coefficients (μ_{sg}) of nine concrete particles were 0.221, 0.201, 0.188, 0.228, 0.206, 0.196, 0.233, 0.225, and 0.204, respectively. The average particle-particle static friction coefficients (μ_{sp}) of nine concrete particles were 0.190, 0.184, 0.182, 0.192, 0.185, 0.174, 0.223, 0.191, and 0.186, respectively. The values of static friction coefficient of concrete in groups A, B, and C decreased with the increase of water-binder ratio.

TABLE 6 | The surface energy test results of B1 concrete.

Particle size (mm)	θ_{ys}		$F_{pullout}$ (N)	γ (J/m^2)
	Mean	Standard deviation		
10	20.91°	0.579	0.00424	0.369
9	25.70°	0.631	0.00400	0.378
8	32.54°	0.541	0.00347	0.369
7	44.71°	0.674	0.00301	0.365

The Test Results of Surface Energy

The test results of rolling friction coefficient of glass sphere are shown in **Table 5**. The critical rolling angle (θ_{rs}) between the four smooth particles and the inclined plate was basically close, and the average rolling friction coefficient was 0.018.

After determining the rolling friction coefficient between the smooth particles and the inclined plate, the critical rolling angle ($\theta_{\gamma c}$) of particle B was measured using the tilt test of **Figure 5**, and then F_{pullout} and surface energy (γ) of the paste between the particles were calculated. The test results of surface energy of B1 concrete are shown in **Table 6**. The surface energy of the paste between particles of different sizes was basically the same, and the average surface energy γ was 0.370 J/m^2. As the particle size decreased, the critical separation angle ($\theta_{\gamma c}$) of particle B increased. The reason was that when the gravity of particle B decreased, a larger separation angle was needed to increase the tangential force of particle B on the inclined plate to get rid of F_{pullout} of the paste.

According to the surface energy test results of concrete particles with different mix proportions, the average surface energy of paste in the nine types of concrete mix proportions were calculated. The surface energy (γ) of the nine concrete particles was 0.368, 0.364, 0.363, 0.370, 0.366, 0.361, 0.373, 0.368, and 0.364 J/m^2, respectively. The surface energy of the three groups of concrete particles decreased with the increase of the water-binder ratio.

The amount of cementitious material and water-binder ratio are the main factors affecting the contact parameters of concrete particles. With the change of the composition and amount of cementitious materials, the viscosity of the paste on the surface of concrete particles also changed. When the viscosity of paste increased, the restitution coefficient of concrete particles decreased, and the static friction coefficient, rolling friction coefficient, and surface energy increased.

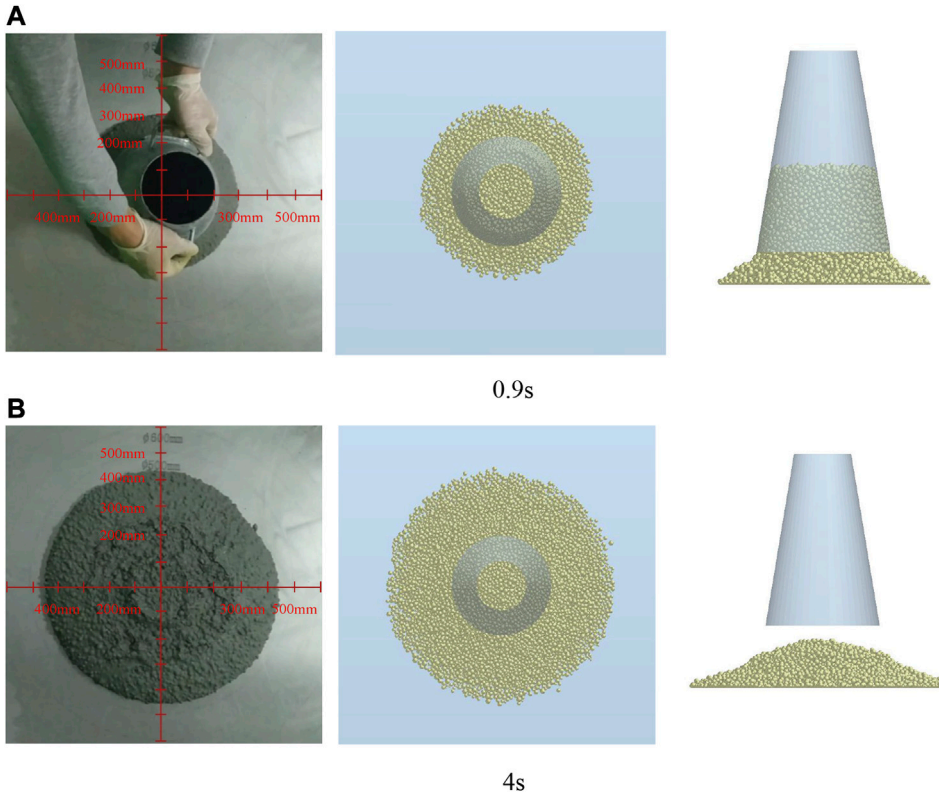

FIGURE 6 | Comparison between slump test process and DEM simulation of B1 concrete: **(A)** 0.9 s and **(B)** 4 s.

Establishing the DEM Model of Concrete

DEM Model of Slump Test

The slump test model was established according to the actual size of the slump cone and slump plate, and then the intrinsic parameters (density, shear modulus, and Poisson's ratio) of the geometry (slump cone and slump plate) were defined. The material of the test equipment used in the slump test and calibration test was stainless steel, the density was 7,750 kg/m^3, the shear modulus was 72.797 GPa, and Poisson's ratio was 0.305.

This paper used EDEM software to establish a single-phase element concrete DEM model (Hoornahad and Koenders, 2014). The concrete was considered to be composed of mortar-wrapped glass aggregate particles. The intrinsic parameters of the particles were defined according to the aggregate density, shear modulus, and Poisson's ratio in "Aggregate" section. Then, the test results of restitution coefficient, rolling friction coefficient, static friction coefficient, and surface energy were used as the contact parameters of particle-geometry and particle-particle in the concrete DEM model to simulate. Finally, the concrete particles were generated in the slump cone. Before generating the concrete particles, a funnel was added above the slump cone to increase the rate of particle generation. After the particles filled the slump cone, the funnel and excess particles above the slump cone were removed. The establishment of the DEM model of concrete slump test was finished.

DEM Model of J-Ring Test

The J-Ring model was added to the DEM model of the slump test to investigate the passing ability of concrete. The J-Ring test DEM model was established based on the J-Ring size recommended by the standard GB/T 50,080-2016. The material of J-Ring was the same as that of the slump test.

DEM Model of V-Funnel and U-Channel

The V-funnel model and U-channel model were established based on the size recommended by the standard GB/T 50,080-2016. The materials of V-funnel and U-channel were the same as that of the slump test.

DEM SIMULATION RESULTS OF CONCRETE FLOWABILITY

Comparison of DEM Simulation Results with Slump Test Results

The slump cone in the DEM model was lifted off at a speed of 0.06 m/s to simulate the concrete slump test. The results of the slump test and the DEM model of B1 concrete at 0.9 and 4 s are shown in **Figures 6A,B**. At 0.9 s, the test value of the slump flow was 302 mm, and the slump flow and slump of the DEM model were 303 and 178 mm, respectively. At 4 s, the test values of the slump flow and slump were 449 and 201 mm, the slump flow and slump of the DEM model were

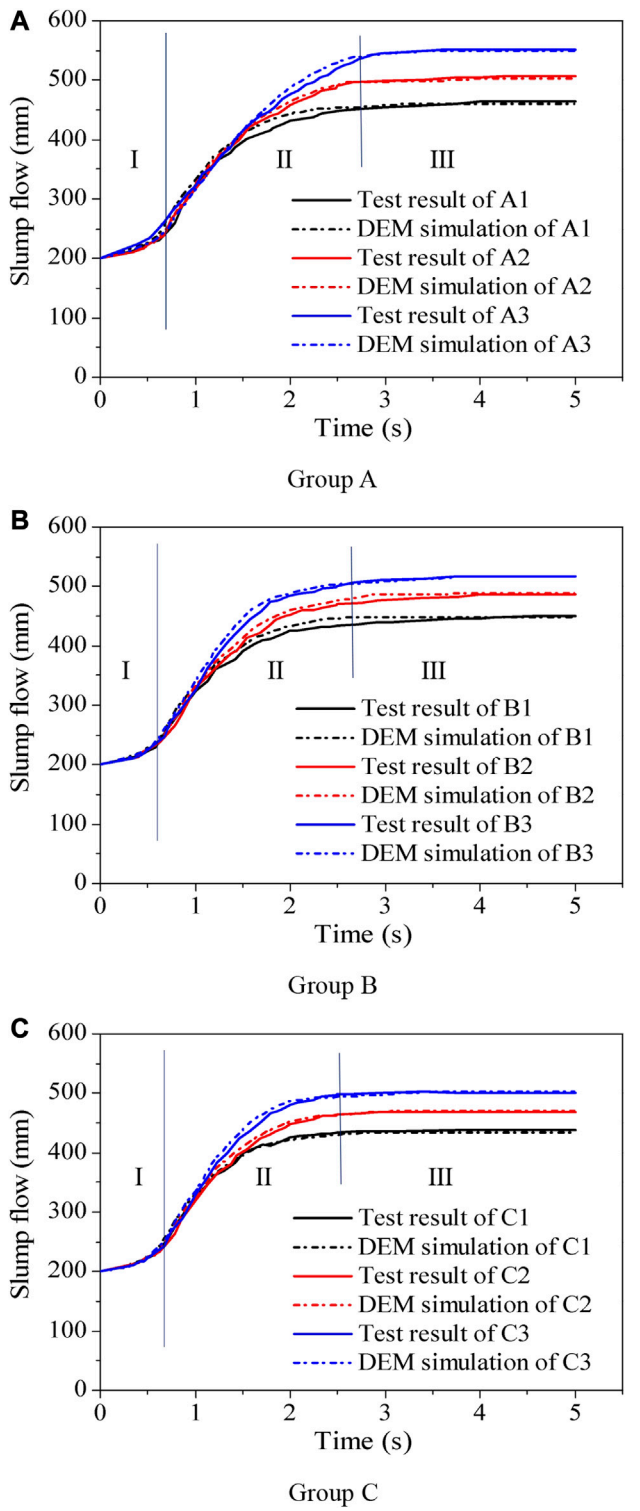

FIGURE 7 | Comparison of test and simulation by slump flow–time curves: **(A)** Group A, **(B)** Group B, and **(C)** Group C.

407 and 203 mm, and the relative deviations were 0.445 and 0.995%, respectively. The simulation results of B1 concrete DEM model at 0.9 and 4 s were in good agreement with the test results.

The changes in the slump flow of the DEM model and the test over time were recorded, and the slump flow–time curve is shown in **Figure 7**. The slump flow–time curves of test and DEM model can be divided into three stages. Stage I was the initial stage. When the slump cone began to lift off, the lift-off distance between the bottom of slump cone and the slump plate was small, and the large-size aggregates in concrete were hindered by the bottom of slump cone, which limited the flow of concrete. Stage II was the rapid flow stage. The gravity potential energy of concrete in slump cone was rapidly converted into kinetic energy, and the concrete flowed rapidly under the action of gravity. Stage III was the slow flow stage. After the gravity potential energy of concrete decreased, the kinetic energy of concrete was gradually consumed by the friction force of slump plate, and the flow velocity of concrete decreased and finally tended to be static. In these three stages, the slump flow–time curve simulated by DEM was in good agreement with the test results.

The relative deviation of slump simulation of nine types of concrete was 0.952, 0.881, 1.299, 0.995, 0.474, 0.442, 1.015, 0.478, and 0.459%, respectively. The relative deviation of slump-flow simulation of the nine concrete types was 0.647, 0.791, 0.362, 0.445, 0.412, 0.193, 0.686, 0.213, and 0.399%, respectively. The relative deviations between the slump and slump-flow simulation results of the concrete DEM model and the test results were very small. The average relative deviation between the slump simulation value and the test value of nine types of concrete was 0.777%, and the average relative deviation between the slump-flow simulation value and the test value was 0.461%. The DEM contact model and calibrated contact parameters used in this paper can accurately simulate the process and results of concrete slump test.

Comparison of DEM Simulation Results with J-Ring Test Results

The slump cone was lifted up at a speed of 0.06 m/s. The J-Ring DEM simulation of B1 concrete is shown in **Figure 8**. The J-Ring slump flow of the concrete DEM model was 297 mm at 0.9 s and 431 mm at 4 s. The simulation results of DEM model were close to the test results of concrete J-Ring slump flow. The difference between the slump flow of concrete and the J-Ring slump flow was used as the performance index of the passing ability. The DEM simulation results of J-Ring slump flow were 446, 487, 532, 431, 472, 499, 418, 453, and 486 mm, and the relative deviation was 0.446, 0.409, 0.375, 0.231, 0.212, 0.399, 0.948, 0.444, and 0.206%, respectively. The passing ability of nine types of concrete was 15, 15, 18, 16, 16, 17, 16, 17, and 17 mm, and the relative deviation was 6.25, 11.76, 0.00, 5.88, 6.67, 6.25, 6.67, 5.56, and 6.25%, respectively. The simulation results of J-Ring slump flow and passing ability of concrete DEM model were similar to the test results. The average relative deviation between the J-Ring slump-flow simulation value and the test value of nine types of concrete was 0.408%, and the average relative deviation between the passing ability simulation value and the test value was 6.14%. The concrete DEM model established in this paper can simulate the passing ability of concrete well.

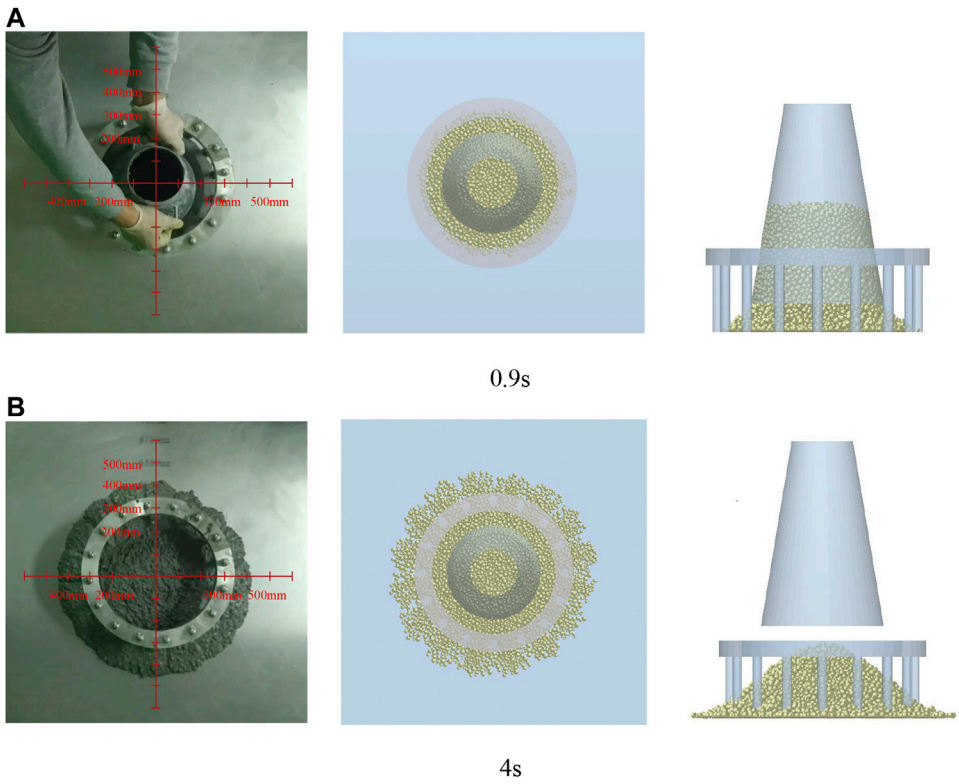

FIGURE 8 | Comparison between J-Ring test process and DEM simulation of B1 concrete: **(A)** 0.9 s and **(B)** 4 s.

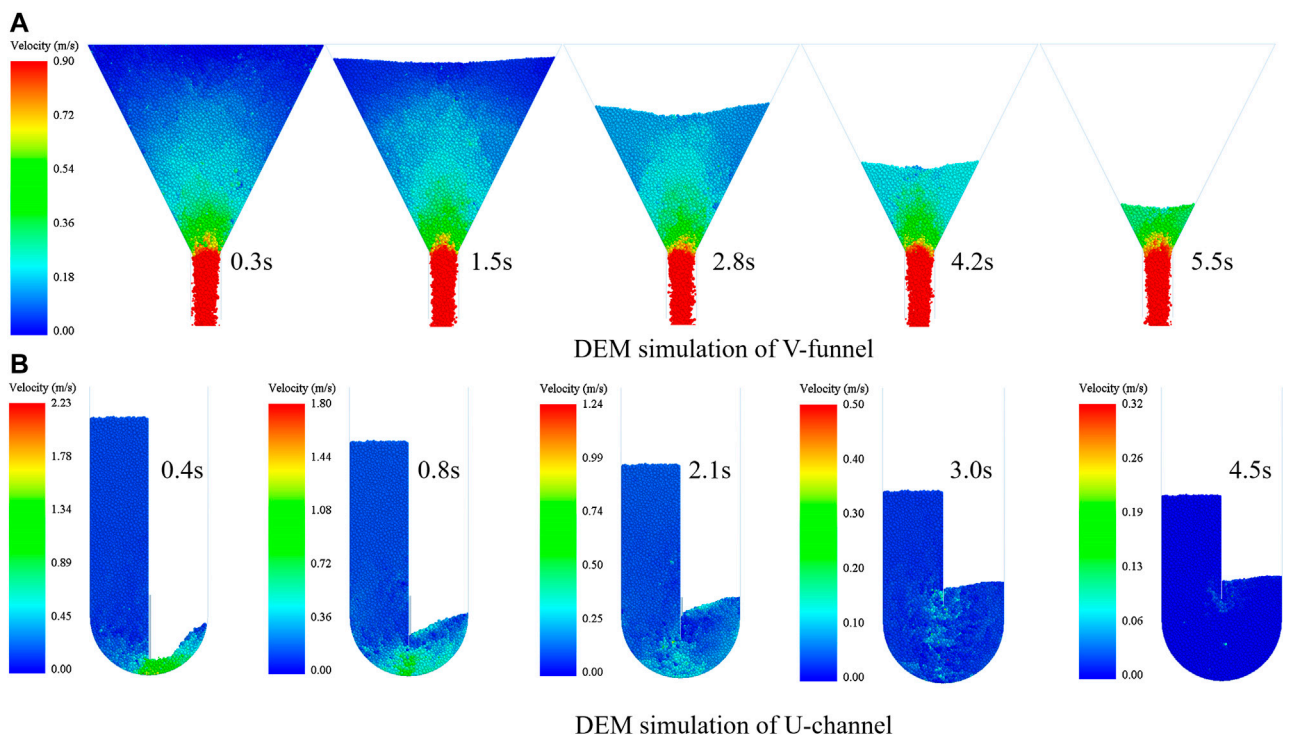

FIGURE 9 | Simulation of V-funnel and U-channel: **(A)** DEM simulation of V-funnel and **(B)** DEM simulation of U-channel.

Simulation Results of V-Funnel and U-Channel

The velocity distribution of B1 concrete in V-funnel is shown in **Figure 9A**. At the beginning of flow, the flow velocity at the outlet was maximum, the flow velocity of concrete particles above the outlet decreased gradually, and the flow velocity of concrete particles above the funnel was close to zero. Above the outlet of V-funnel, the velocity distribution of concrete particles at different outflow time was basically similar, and the velocity distribution near the outlet was almost not affected by the flow time. The simulation values of T_V of A1, A2, A3, B1, B2, B3, C1, C2, and C3 were 5.4, 5.3, 5.2, 6.4, 6.2, 6.1, 7.1, 6.8, and 6.6 s, respectively. The relative deviation of V-funnel simulation of the nine types of concrete was 1.82, 0.00, 1.96, 1.54, 1.59, 1.67, 2.74, 4.2, and 4.35%, respectively, and the average relative deviation was 2.21%. With the increase of water-cement ratio, the viscosity of concrete decreased, which led to the decrease of T_V.

The velocity distribution of B1 concrete in U-channel is shown in **Figure 9B**. The gate was lifted at a speed of 0.08 m/s, and the concrete flowed quickly to the right side. The concrete particles in the left side of U-channel flowed down uniformly and slowly. With the increase of flow time, the maximum flow velocity of concrete gradually decreased, and the velocity distribution of concrete changed greatly. The maximum flow velocity occurred below the gate, and the position of the maximum flow velocity moved up with the lifting of the gate. After 4.5 s, the concrete gradually tended to static state. The simulation values of *Bh* of A1, A2, A3, B1, B2, B3, C1, C2, and C3 were 261, 262, 264, 248, 251, 252, 235, 236, and 238 mm, respectively. The average relative deviation of the simulation result was 0.931%. The simulation results were in good agreement with the test results.

In the simulation of concrete fluidity, the static friction coefficient had the greatest influence on the simulation results, followed by the rolling friction coefficient, and the restitution coefficient had the least influence on the simulation results. Therefore, it is necessary to accurately measure the contact parameters of concrete particles, and the contact parameters of concrete particles measured by tests are closer to the real results than the trial-error method.

CONCLUSIONS

In this paper, high-precision glass spheres were used as aggregates for the slump test and meso-calibration test of fresh concrete. Through a series of meso-calibration tests, the contact parameters of the discrete element model of fresh concrete were accurately measured, and the reliability of the DEM model was verified by the slump test. Through meso-calibration tests and DEM model verification, the following conclusions are obtained:

(1) The contact parameters of JKR contact model, such as coefficient of restitution, coefficient of rolling friction, coefficient of static friction, and surface energy, can be measured accurately by collision test and inclined test.
(2) It is feasible to use glass sphere instead of concrete aggregate for parameter measure of DEM model.
(3) The DEM model established by the JKR model and contact parameter calibration method can accurately simulate the flowability of concrete.

Limitations and Future Scope

In this paper, spherical aggregate was used instead of gravel in concrete fluidity test and calibration test, which verified the reliability of meso-calibration test. In the following work, the author will use the actual aggregate to carry out systematic calibration tests to measure the contact parameters of the real aggregate.

DATA AVAILABILITY STATEMENT

The original contributions presented in the study are included in the article/Supplementary Material. Further inquiries can be directed to the corresponding author.

AUTHOR CONTRIBUTIONS

YL contributed to the conception and research method of the study. JH was responsible for testing and organizing the database. ZW performed the statistical analysis. JL and CJ wrote the first draft of the manuscript. All authors contributed to manuscript revision and read and approved the submitted version.

FUNDING

The authors would like to acknowledge the financial support by the National Key R&D Program of China-Key materials and preparation technology of high crack resistant ready-mixed concrete (2017YFB0310100), National Natural Science Foundation of China (51808015) and General project of science and technology plan of Beijing Municipal Commission of Education (KM202110005018).

REFERENCES

Ai, J., Chen, J.-F., Rotter, J. M., and Ooi, J. Y. (2011). Assessment of rolling resistance models in discrete element simulations. *Powder Technol.* 206 (3), 269–282. doi:10.1016/j.powtec.2010.09.030

Barrios, G. K. P., de Carvalho, R. M., Kwade, A., and Tavares, L. M. (2013). Contact parameter estimation for DEM simulation of iron ore pellet handling. *Powder Technol.* 248, 84–93. doi:10.1016/j.powtec.2013.01.063

Cao, G., Zhang, H., Tan, Y., Wang, J., Deng, R., Xiao, X., et al. (2015). Study on the effect of coarse aggregate volume fraction on the flow behavior of fresh concrete via DEM. *Procedia Eng.* 102, 1820–1826. doi:10.1016/j.proeng.2015.01.319

Coetzee, C. J. (2016). Calibration of the discrete element method and the effect of particle shape. *Powder Technol.* 297, 50–70. doi:10.1016/j.powtec.2016.04.003

Coetzee, C. J. (2017). Review: calibration of the discrete element method. *Powder Technol.* 310, 104–142. doi:10.1016/j.powtec.2017.01.015

Chinese Standard (2002). *Chinese Standard GB/T 50081-2002, Standard for test method of mechanical properties on ordinary concrete.* China: Ministry of Construction of the People's Republic of China. [in Chinese].

Cui, W., Ji, T., Li, M., and Wu, X. (2016). Simulating the workability of fresh self-compacting concrete with random polyhedron aggregate based on DEM. *Mater. Struct.* 50 (1), 1–12. doi:10.1617/s11527-016-0963-9

Cui, W., Yan, W.-s., Song, H.-f., and Wu, X.-l. (2018). Blocking analysis of fresh self-compacting concrete based on the DEM. *Construct. Build. Mater.* 168, 412–421. doi:10.1016/j.conbuildmat.2018.02.078

Deresiewicz, H. (1953). Elastic spheres in contact under varying oblique forces. *J. Appl. Mech.* 20 (3), 327–344. doi:10.1007/978-1-4613-8865-4_35

González-Montellano, C., Fuentes, J. M., Ayuga-Téllez, E., and Ayuga, F. (2012). Determination of the mechanical properties of maize grains and olives required for use in DEM simulations. *J. Food Eng.* 111 (4), 553–562. doi:10.1016/j.jfoodeng.2012.03.017

Grima, A. P. (2011). *Quantifying and modelling mechanisms of flow in cohesionless and cohesive granular materials*. Wollongong, NSW: University of Wollongong.

Guo, Z.-Q., Yuan, Q., Stroeven, P., Fraaij, A. L. A., Lu, J. W. Z., Leung, A. Y. T., et al. (2010). Discrete element method simulating workability of fresh concrete. *AIP Conf. Proc.* 14, 430–435. doi:10.1063/1.3452210

Hertz, H. (1880). On the contact of elastic solids. *J. für die Reine Angewandte Math. (Crelle's J.).* 92, 156–171.

Hoornahad, H., and Koenders, E. A. B. (2014). Simulating macroscopic behavior of self-compacting mixtures with DEM. *Cement Concr. Compos.* 54, 80–88. doi:10.1016/j.cemconcomp.2014.04.006

Hou, D., Lu, Z., Li, X., Ma, H., and Li, Z. (2017). Reactive molecular dynamics and experimental study of graphene cement composites: structure, dynamics and reinforcement mechanisms. *Carbon* 115, 188–208.

Krenzer, K., Mechtcherine, V., and Palzer, U. (2019). Simulating mixing processes of fresh concrete using the discrete element method (DEM) under consideration of water addition and changes in moisture distribution. *Cement Concr. Res.* 115, 274–282. doi:10.1016/j.cemconres.2018.05.012

Kendall, K. (1971). Surface energy and the contact of elastic solids. *Proc. Math. Phys. Eng. Sci.* 324 (1558), 301–313. doi:10.1098/rspa.1971.0141

Li, Z., Cao, G., and Guo, K. (2018). Numerical method for thixotropic behavior of fresh concrete. *Construct. Build. Mater.* 187, 931–941. doi:10.1016/j.conbuildmat.2018.07.201

Mechtcherine, V., Gram, A., Krenzer, K., Schwabe, J.-H., Shyshko, S., and Roussel, N. (2013). Simulation of fresh concrete flow using Discrete Element Method (DEM): theory and applications. *Mater. Struct.* 47 (4), 615–630. doi:10.1617/s11527-013-0084-7

Mechtcherine, V., and Shyshko, S. (2015). Simulating the behaviour of fresh concrete with the Distinct Element Method—deriving model parameters related to the yield stress. *Cement Concr. Compos.* 55, 81–90. doi:10.1016/j.cemconcomp.2014.08.004

Mindlin, R. D. (1989). Compliance of elastic bodies in contact. *J. Appl. Mech.* 16, 197–268. doi:10.1007/978-1-4613-8865-4_24

Pieralisi, R., Cavalaro, S. H. P., and Aguado, A. (2016). Discrete element modelling of the fresh state behavior of pervious concrete. *Cement Concr. Res.* 90, 6–18. doi:10.1016/j.cemconres.2016.09.010

Rackl, M., and Hanley, K. J. (2017). A methodical calibration procedure for discrete element models. *Powder Technol.* 307, 73–83. doi:10.1016/j.powtec.2016.11.048

Remond, S., and Pizette, P. (2014). A DEM hard-core soft-shell model for the simulation of concrete flow. *Cement Concr. Res.* 58, 169–178. doi:10.1016/j.cemconres.2014.01.022

Shyshko, S., and Mechtcherine, V. (2013). Developing a Discrete Element Model for simulating fresh concrete: experimental investigation and modelling of interactions between discrete aggregate particles with fine mortar between them. *Construct. Build. Mater.* 47, 601–615. doi:10.1016/j.conbuildmat.2013.05.071

Shyshko, S., and Mechtcherine, V. (2008). "Simulating the workability of fresh concrete," in International RILEM Symposium on Concrete Modelling, 173–181.

Tan, Y., Cao, G., Zhang, H., Wang, J., Deng, R., Xiao, X., et al. (2015). Study on the thixotropy of the fresh concrete using DEM. *Procedia Eng.* 102, 1944–1950. doi:10.1016/j.proeng.2015.06.138

Tsuji, Y., Tanaka, T., and Ishida, T. (1992). Lagrangian numerical simulation of plug flow of cohesionless particles in a horizontal pipe. *Powder Technol.* 71 (3), 239–250. doi:10.1016/0032-5910(92)88030-L

Zafar, U., Hare, C., Hassanpour, A., and Ghadiri, M. (2014). Drop test: a new method to measure the particle adhesion force. *Powder Technol.* 264, 236–241. doi:10.1016/j.powtec.2014.04.022

Zhan, Y., Gong, J., Huang, Y., Shi, C., Zuo, Z., and Chen, Y. (2019). Numerical study on concrete pumping behavior via local flow simulation with discrete element method. *Materials* 12 (9), 1415–1435. doi:10.3390/ma12091415

Zhang, X., Zhang, Z., Li, Z., Li, Y., and Sun, T. (2020). Filling capacity analysis of self-compacting concrete in rock-filled concrete based on DEM. *Construct. Build. Mater.* 233, 117321. doi:10.1016/j.conbuildmat.2019.117321

Zhao, Y., Han, Z., Ma, Y., and Zhang, Q. (2018). Establishment and verification of a contact model of flowing fresh concrete. *Eng. Comput.* 35 (7), 2589–2611. doi:10.1108/ec-11-2017-0447

Zhou, Y. C., Wright, B. D., Yang, R. Y., Xu, B. H., and Yu, A. B. (1999). Rolling friction in the dynamic simulation of sandpile formation. *Phys. Stat. Mech. Appl.* 269, 536–553. doi:10.1016/S0378-4371(99)00183-1

Conflict of Interest: The authors declare that the research was conducted in the absence of any commercial or financial relationships that could be construed as a potential conflict of interest.

Copyright © 2021 Li, Hao, Jin, Wang and Liu. This is an open-access article distributed under the terms of the Creative Commons Attribution License (CC BY). The use, distribution or reproduction in other forums is permitted, provided the original author(s) and the copyright owner(s) are credited and that the original publication in this journal is cited, in accordance with accepted academic practice. No use, distribution or reproduction is permitted which does not comply with these terms.

frontiers in Materials

ORIGINAL RESEARCH
published: 18 February 2021
doi: 10.3389/fmats.2020.611568

Insight Into the Strengthening Mechanism of the Al-Induced Cross-Linked Calcium Aluminosilicate Hydrate Gel: A Molecular Dynamics Study

Gaozhan Zhang[1], *Yang Li*[2], *Jun Yang*[3]*, *Qingjun Ding*[4] *and Daosheng Sun*[5]

[1]Advanced Building Materials Key Laboratory of Anhui Province, School of Materials and Chemical Engineering, Anhui Jianzhu University, Hefei, China, [2]School of Materials and Chemical Engineering, Anhui Jianzhu University, Hefei, China, [3]Advanced Building Materials Key Laboratory of Anhui Province, School of Materials and Chemical Engineering, Anhui Jianzhu University, Hefei, China, [4]School of Materials Science and Engineering, Wuhan University of TechnologyWuhan, China, [5]Advanced Building Materials Key Laboratory of Anhui Province, School of Materials and Chemical Engineering, Anhui Jianzhu University, Hefei, China

OPEN ACCESS

Edited by:
Dongshuai Hou,
Qingdao University of Technology, China

Reviewed by:
Youyong Li,
Soochow University, China
Shuai Zhou,
Chongqing University, China

***Correspondence:**
Jun Yang
jyang017@126.com

Specialty section:
This article was submitted to Computational Materials Science, a section of the journal Frontiers in Materials

Received: 29 September 2020
Accepted: 28 December 2020
Published: 18 February 2021

Citation:
Zhang G, Li Y, Yang J, Ding Q and Sun D (2021) Insight Into the Strengthening Mechanism of the Al-Induced Cross-Linked Calcium Aluminosilicate Hydrate Gel: A Molecular Dynamics Study. Front. Mater. 7:611568. doi: 10.3389/fmats.2020.611568

Understanding and controlling the mechanical properties of calcium aluminosilicate hydrate (C-A-S-H) gel is essential to the performance improvement of cementing materials. This study characterizes the mechanical properties and failure mechanism of cross-linked C-A-S-H that have Al/Si ratios ranging from 0 to 0.20 by employing the reactive molecular dynamics simulation. In these constructed C-A-S-H models, the Al-induced cross-linking effect on the aluminosilicate chains is well reproduced. With the incorporation of aluminate species, layered C-S-H structure gradually transforms into three-dimensional C-A-S-H. The uniaxial tensile tests show that Al-induced cross-links significantly increase the cohesive force and stiffness of C-A-S-H along both ***y***- and ***z***-directions. In the C-A-S-H model with the Al/Si ratio equal to 0.2, in which all the bridging sites are cross-linked, the toughness along y-direction significantly improves the interlayer mechanical properties compared to those within the layers. The deformation mechanism of the C-A-S-H structure is also studied. Results show that the depolymerization of the calcium aluminosilicate skeleton is the main route to uptake the loading energy. Both the increase of ***y***- and ***z***-directional strength of the structure can be related to the increasing polymerization of aluminosilicate chains along that direction. This demonstrates the important role of aluminosilicate chains in resisting the external tensile loading. Besides, during the failure process in C-A-S-H elongation, the hydrolysis reactions of calcium silicate skeleton are caused by the coupling effect of loading and interlayer water "attack." While the Al-O-Si bond breakage results from the protonation of bridging oxygen atom, the hydrolytic reaction of Si-O-Si is initiated by five-coordinate silicon formation. Both pathways weaken the bridging bond and thus result in the breakage of T-O-Si, where T is Al or Si.

Keywords: Al-induced cross-linking, calcium aluminosilicate hydrate, mechanical properties, strengthening mechanism, reactive molecular dynamics

INTRODUCTION

Cement manufacture is estimated to produce approximately 6–8% of the yearly man-made global CO_2 emissions (Mir and Nehme, 2017). Moreover, due to the increasing demand for concrete materials, this part of carbon emission is still increasing (Scrivener, 2008). In order to lower the environmental impact of the construction industry, people have used industrial wastes or byproducts to develop alternative binders (Mikulčić et al., 2016). The wide usage of some supplementary cementitious materials (SCMs), including fly ash (FA) and blast furnace slag (BFS) (Lothenbach et al., 2011), has not only reduced CO_2 emission (Sethy et al., 2016) (Huntzinger and Eatmon, 2009) but also prepared blended cement pastes that exhibit better performance than pure cement paste in some aspects, such as resistance in sulfate attack (Juenger et al., 2011) and alkali-aggregate reaction (ASR) (Shehata and Thomas, 2002; Duchesne and Bérubé, 1994). The Portland cement (PC) production results in about 0.85 tonnes/tonne of CO_2 emission (Feiz et al., 2015), while the CO_2 emissions by FA and BFS production are only 1/94 and 1/43 of the amount CO_2 emitted during cement manufacture, respectively (Chen et al., 2010).

High-volume SCM blended cement is often richer in Si and Al element than the PC (Lothenbach et al., 2011). This changes the stoichiometry of calcium silicate hydrate (C-S-H) gel, the main hydration product of cement-based materials. The Ca/Si ratio of the C-S-H gel is lowered and aluminum is incorporated into its structure (Lothenbach et al., 2011), leading to the formation of calcium aluminosilicate hydrate (C-A-S-H). Since C-A-S-H gel is the phase that gives strength to the hardened cement blend, it is necessary to study its mechanical properties. One of the cases is the mechanical properties of cross-linked C-A-S-H. C-S-H is structurally similar to tobermorite (Hamid, 1981; Merlino et al., 2001), which has principal layers composed of pseudooctahedrally coordinated calcium sheets sandwiched on both sides by silicate chains in the form of "drierkette." In the interlayer regions, there are water molecules and calcium ions that connect the adjacent main layers. Hence, the C-S-H structure is weak in the interlayer direction (Hou et al., 2014b). When aluminum is included in the C-S-H structure, it resides on the silicate chains and heals the broken silicate chains. In these chains, Al occupancy in the bridging position is preferred over the pairing position (Manzano et al., 2009a; Pegado et al., 2014). The branched (alumino)silicate chains are more easily formed in the C-A-S-H gel than in the C-S-H gel (Myers et al., 2015; Bernal et al., 2013; Myers et al., 2013). It is found that calcium-poor and aluminum-rich cementitious environment and high temperature (up to 80°C) can promote the cross-linked C-A-S-H formation. Structurally, the branch chains bridge the neighboring principal layers with covalent bonds, which improve the interlayer interaction in the C-A-S-H structure. This was experimentally proved by recent studies from (Geng et al., 2017a; Geng et al., 2017b). They have investigated the compressibility of the crystal lattice of both non-cross- and cross-linked C-(A-)S-H under hydrostatic pressure, utilizing the synchrotron radiation-based high-pressure X-ray diffraction (XRD) technique. The results showed that the stiffness of non-cross-linked C-A-S-H is lower in the z-axis than in the xy-plane (the readers can see the stacked main layers along z-direction for C-A-S-H molecular structure in **Figure 1A**), and the cross-links can stiffen the C-A-S-H gel along the interlayer direction. However, the strengthening mechanism of cross-links remains not fully understood, owing to the experimental limit in accessing smaller length scales.

This article aims to study the mechanical properties of cross-linked C-A-S-H gel through molecular dynamics (MD) simulation. MD can give insight into the properties of materials at the molecular scale level and provide a complementary understanding of the experimental findings. Its wide application in the C-S-H studies renders the research length scale down to nanometers. The mechanical properties of mineral analogues of C-S-H, tobermorite and jennite, were calculated and the results match well with experimental data (Shahsavari et al., 2009) (Manzano et al., 2009b; Murray et al., 2010). Pellenq (Pellenq et al., 2009) proposed a "realistic C-S-H model" of the Ca/Si ratio of 1.7, which can accurately predict the experimentally obtained structure and strength properties (Allen et al., 2007; Constantinides and Ulm, 2007; Ulm et al., 2007). After that, the C-S-H model with various Ca/Si ratios was also constructed (Abdolhosseini Qomi et al., 2014) (Hou et al., 2015b) and its mechanical properties were in good agreement with the experimental results. The C-A-S-H (Ca/Si ratio = 1.7) with various Al/Ca ratios was also simulated by (Qomi et al., 2012) and (Hou et al., 2015a). The results show that the aluminum substitution for interlayer calcium improves the polymerization of aluminosilicate chains as well as the mechanical properties of C-A-S-H. Based on the MD simulation, cement/aggregate/fiber interface characterization (Zhou et al., 2019) and aggregate radiation failure (Zhou and Ju, 2020) were also investigated. The above studies provided an excellent basis for the implementation of our work.

In this article, the mechanical response and constitutive relationships of C-A-S-H with different cross-linking degrees are investigated by simulating uniaxial tension. Note that the branch structure in our constructed model is different from those in Qomi's (Qomi et al., 2012) and Hou's model (Hou et al., 2015a). In our models, cross-links occurred through the bond formation between the bridging silicate and aluminate sites in aluminosilicate chains of two adjacent primary layers, where the bridging sites can only bind to each other by pairs. This cross-linking mode is more related to the existing C-A-S-H structure models (Manzano et al., 2009a) (Pegado et al., 2014) and can characterize the mechanical responses more accurately. Relying on the ability to couple chemical reaction with the mechanical response provided by ReaxFF (Duin et al., 2001), the morphology transformation and hydrolytic reactions of calcium aluminosilicate skeleton in the C-A-S-H model during its structural deformation are also studied. This study can help elucidate the influence mechanisms of Al substitution on the performance of C-S-H gel and guide the design of sustainable concrete in engineering practice.

COMPUTATIONAL METHOD

Reactive Force Field

The atomic interaction within the models was defined by the reactive force field (ReaxFF). ReaxFF was initially developed to

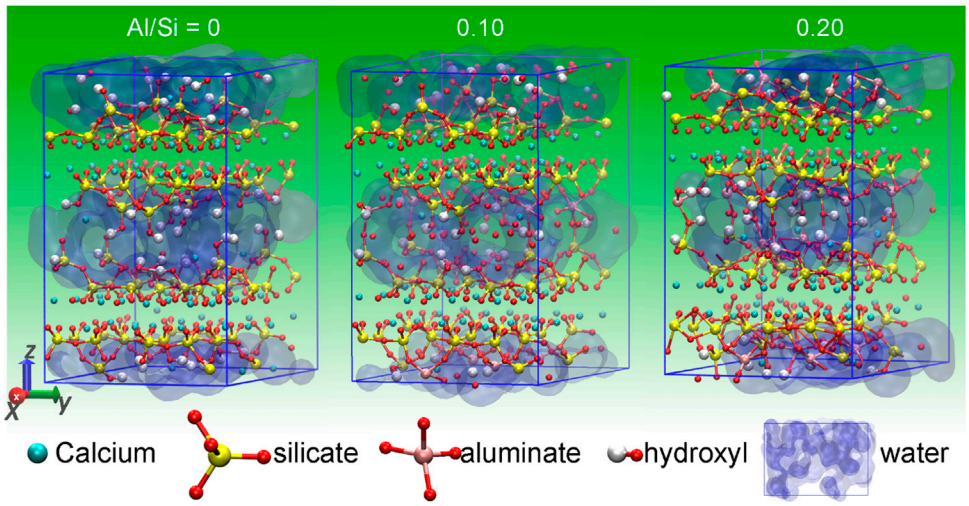

FIGURE 1 | Atomistic representation of the C-(A-)S-H models with Al/Si ratios of 0, 0.10, and 0.20.

simulate hydrocarbons (Duin et al., 2001). Since then, it has been successfully applied in many fields, including combustion, catalysis, material failure, and surface chemistry. The ReaxFF force field is equipped with the ability to describe the bond formation, bond breakage, and charge polarization (Fogarty et al., 2010), without recourse to a predefined and invariable covalent bond state. Furthermore, the bond order concept in the ReaxFF allows the energy to change smoothly during an energy-conserving simulation. Previous studies have been performed to study the Si/SiO_2 interfaces (Leroch and Wendland, 2012), dynamics of gel water in the C-S-H (Manzano et al., 2012a) (Hou et al., 2015b), and the restriction of C-S-H structure on guest ions (Hou et al., 2017). These applications demonstrate that ReaxFF can capture the structure, reactivity, and mechanical features of C-A-S-H/water interfaces with great accuracy. The ReaxFF parameters for the elements in this work were taken from previously published literature (Duin et al., 2003; Manzano, et al., 2012b; Liu et al., 2012).

Model Construction

The molecular structure of C-A-S-H is constructed using the method performed in previous simulations (Pellenq et al., 2009; Yang et al., 2018). Merlino's cross-linked 11 Å tobermorite $[Ca_{4.5}Si_6O_{16}(OH)\cdot 5H_2O]$ (Merlino et al., 2001) was utilized as the starting configuration. Firstly, a supercell containing $2 \times 2 \times 1$ crystallographic tobermorite unit cells was constructed and the interlayer water within the cells was totally removed. Then, half of the bridging silicate tetrahedra in the supercell were substituted with aluminate tetrahedra. It is worth noting that only one of the two given adjacent bridging silicate tetrahedra is substituted to avoid the negative charge repulsion of aluminate species. Secondly, bridging aluminate tetrahedra were randomly deleted to create five calcium aluminosilicate skeletons of Al/Si ratios of 0, 0.05, 0.10, 0.15, and 0.20. An equivalent amount of hydrogen atoms was added to balance the negative charges induced by Al-Si substitution. Note that the upper limit Al/Si ratio is close to the maximum experimental findings of Al/Si ratio in C-A-S-H from Faucon et al. (Faucon et al., 1999) and Sun et al. (Sun et al., 2006). And this value is also the upper limit for the C-A-S-H model following the Lowenstein rule (Lowenstein, 1954). Thirdly, the structures of anhydrous calcium aluminosilicate were relaxed at 0 K. After the relaxation, water adsorption in the dry C-A-S-H model is performed by the Grand Canonical Monte Carlo (GCMC) method in the GULP package (Gale and Rohl, 2003). Adsorbent molecules were repeatedly inserted into and deleted from the simulation system until the system reaches equilibrium with the surrounding imaginary water reservoir. The adsorption was taken place with chemical potential of water of 0 eV under 300 K. The chemical potential in GCMC method was calculated following the regulation of the CSH-FF force field (Shahsavari et al., 2011). Finally, the LAMMPS software (Plimpton, 1995) (Aktulga et al., 2012) was utilized to carry out the MD. The Verlet algorithm was used to integrate the atomic trajectories in the system, with a time step of 0.25 fs. First, 250 ps of MD run was employed under constant pressure and temperature (*NPT ensemble*) (T = 298 K and P = 1 atom) to equilibrate the system. After 250 ps of MD run, 1000 ps of MD run was performed to average the system properties.

Uniaxial Tensile Loading

Given the anisotropic mechanical behavior of C-S-H gel (Hou et al., 2014b), uniaxial tensions along three dimensions were separately performed on the C-A-S-H models.

Before the tension test, the supercell of the obtained C-A-S-H models was periodically replicated along three dimensions to create cells of the size of about $4 \times 4 \times 4$ nm^3. Note that including a massive number of atoms can ensure the simulation stability of the system and its failure mode in particular. The uniaxial tension test of the structures was set to a strain rate of 0.08 per picosecond. For the purpose of anisotropic relaxation of the system, during the tension along one direction, the target pressure in directions normal to this direction was set to zero. The stress-strain

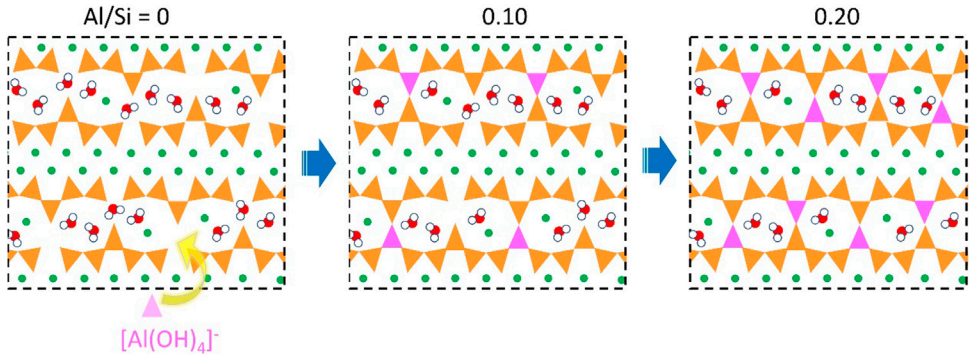

FIGURE 2 | Schematic diagram of aluminum-induced bridging effect in C-(A-)S-H, where orange and pink triangles denote silicate and aluminate tetrahedra, green circles denote calcium atoms, and red-white circles denote water molecules.

evolution curves obtained in the uniaxial tension processes are plotted to analyze the mechanical properties of C-A-S-H. In addition, configurations were recorded for every 100 steps for the analysis of failure mode.

RESULTS AND DISCUSSION

Structure of C-A-S-H Models

The obtained molecular structures of C-A-S-H models after the MD simulation are presented in **Figure 1**. For the C-S-H model (see **Figure 1A**), it can be observed that the Cas (calcium) and the Os (oxygen) atoms are bonded together to form the Cas-Os sheets, with defective "dreierketten" silicate chains flanking on each side. The negative charges of the calcium silicate layers were neutralized via the presence of interlaminar Ca^{2+} ions. In addition, there are also some water molecules in the interlaminar region. In the cross-linked C-A-S-H models (**Figures 1B,C**), aluminum in the defective bridging position of the chains not only links the broken silicate chains but also cross-links the silicate chain of the neighboring main layers. With the increase of Al/Si ratio, more aluminum atoms enter the bridging sites and cross-link the neighboring aluminosilicate chains. At the Al/Si ratio of 0.2, all bridging sites in the aluminosilicate chains are cross-linked (**Figure 1C**). In the cavities among the cross-linked aluminosilicate chains, there is zeolitic content (interlayer water molecules and Ca^{2+} ions). **Figure 2** provides a schematic diagram that describes the bridging effect of aluminum on the adjacent primary layers in C-A-S-H gel. The three 2D pictures correspond to the C-A-S-H molecular structures in **Figure 1**, respectively.

The polymerization degree of silicate tetrahedra is an important parameter that influences the mechanical response of the C-A-S-H structure. Hence, the distribution of Q^n(mAl) species in the C-A-S-H model is calculated. Q^n(mAl) represents the connectivity factor of silicate tetrahedra. The increase of ***n*** from 0 to four denotes the transformation of silicate from monomer to network structures, while ***m*** ranging from 0 to ***n*** denotes the number of neighboring aluminate species for the given silicate tetrahedron. As shown in **Figure 3A**, there are 40% of Q^1 species and 60% of Q^2 species in the Al-free C-S-H model, indicating that the silicate tetrahedra are presented in linear silicate chain structures. As aluminum gradually enters the structure, the percentages of Q^1 and Q^2 species decrease, while those of Q^2(1Al) and Q^3(1Al) increase. This suggests that silicate tetrahedra are transformed from linear to branched chain structure. As shown in **Figure 3B**, the aluminate tetrahedron heals the broken silicate chains, thereby producing two Q^2(1Al). Meanwhile, the cross-linking of the aluminate tetrahedron with the neighboring silicate chain results in a Q^3(1Al) formation.

Stress-Strain Relationship

The stress-strain relation is a common way to characterize the constitutive relationship of materials. **Figure 4** portrays the stress-strain evolution of C-A-S-H models as they are elongated along ***x***-, ***y***-, and ***z***-directions, respectively. Take the C-A-S-H model of Al/Si ratio of 0.10, for example (**Figure 4A**). With the increase of the strain along ***x***-direction, the stress firstly increases. This indicates the deformation of the C-A-S-H structure to take the tensile loading. At the strain of 0.19 Å/Å, the stress gets its maximum value of 10.66 GPa, which is the tensile strength of the structure. Then, the stress drops fast and it reduces to 4.83 GPa at the strain of 0.27 Å/Å. During this stage, cracks are formed in the C-A-S-H model and grow rapidly. After the strain of 0.27 Å/Å, the stress declines slowly until the end of the elongation process. This is because the C-A-S-H structure is destroyed after that strain level and hence cannot uptake tensile loading. The stress-strain relationship along ***y***-direction shows a ladder-like pattern (**Figure 4B**). After the initial increase, there is an increase of stress, which reaches its first maximum of 10.43 GPa at the strain of 0.13 Å/Å, followed by a rapid reduction, which is down to 6.75 GPa at the strain of 0.17 Å/Å. After the first minimum, the stress again increases and reaches a second maximum of 9.67 GPa at a strain of 0.36 Å/Å. After this strain level, the stress-strain curve turns to a monotonic decrease. The secondary increase of stress resembles the work hardening effect of the tensioned steel material (Kocks and Mecking, 2003). It is worth mentioning that the ladder-like curve in ***y***-direction presents in all the models, which suggests that the C-A-S-H structure has good plasticity along this direction. It worth noting

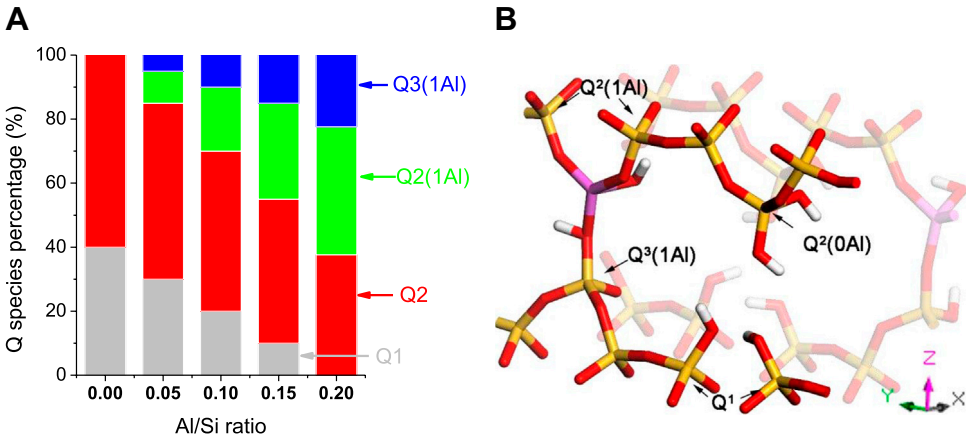

FIGURE 3 | (A) Q species distribution of the C-A-S-H models (adapted from Manzano et al., (2012b)); **(B)** atomistic representation of the Q species in the models. Yellow and red sticks denote silicate chain (Si-O); magenta and red sticks denote aluminate chain (Al-O); the green and gray spheres indicate intra- and interlayer calcium atoms; red and white ball-sticks are water molecules and hydroxyl groups.

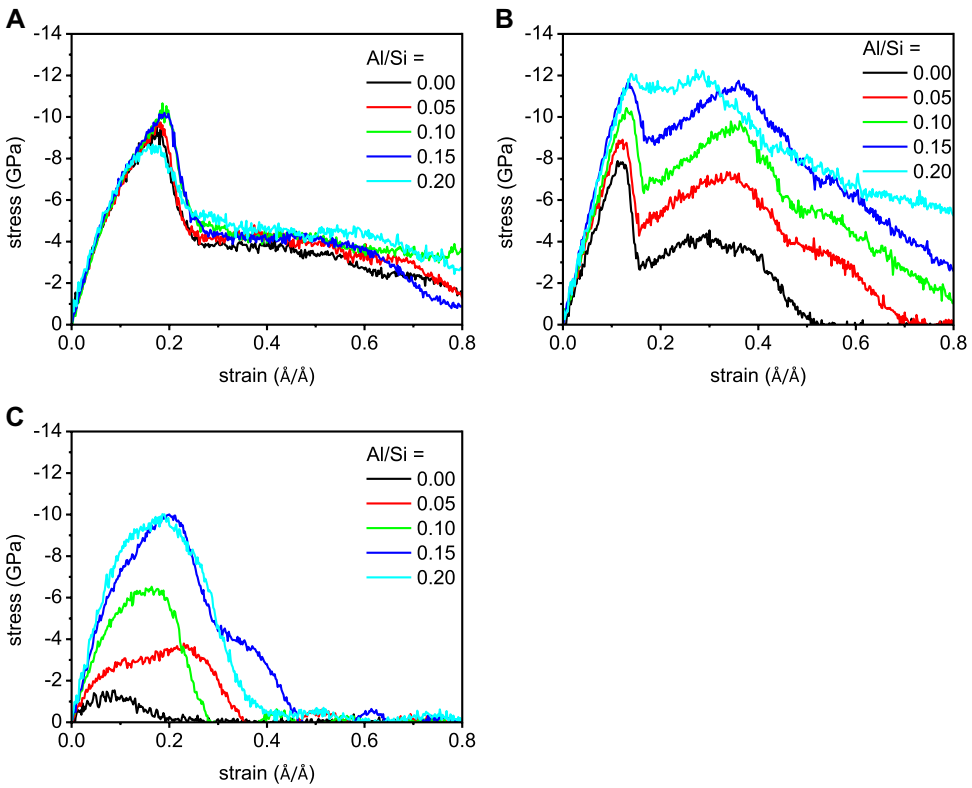

FIGURE 4 | The stress-strain relationships of the C-(A-)S-H models along **(A)** ***x*-**, **(B)** ***y*-**, and **(C)** ***z*-**directions.

that the cohesion force of C-A-S-H along *x*-direction originated from the connection between silicate chains and CaO sheets, whereas the cohesion force along y-direction originated not only from the Ca-O-Si bonds but also from the Si-O-Si bonds within silicate chains. Finally, the structural difference in *x*- and *y*-directions for C-A-S-H gel results in distinct different mechanical results. On the other hand, compared with the stress-strain relationships in ***x***- and ***y***-directions, their counterpart in ***z***-direction shows a brittle nature. As shown in **Figure 4C**, the stress increases to 6.53 GPa when the strain is 0.16 Å/Å. Then, the stress continuously decreases and gets zero at the strain of 0.28 Å/Å.

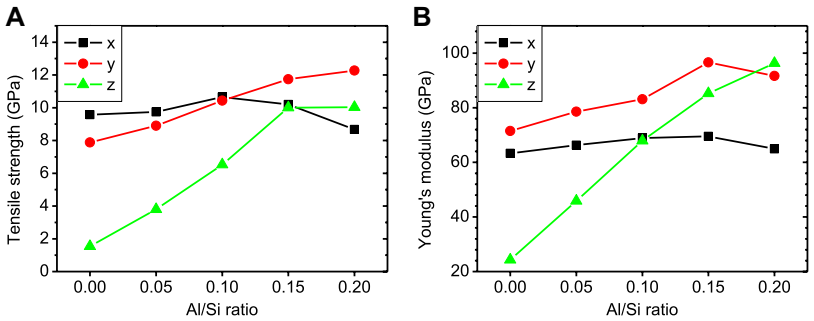

FIGURE 5 | (A) Tensile strength and **(B)** Young's modulus along three directions for C-A-S-H structures of various Al/Si ratios.

Mechanical Properties

The tensile strength and Young's modulus can more intuitionally display the evolution of mechanical properties of the structure. As shown in **Figure 5**, the ***x***- and ***y***-directional tensile strengths of the non-cross-linked C-S-H are 9.58 GPa and 7.88 GPa, respectively. But their ***z***-directional counterpart is 1.54 GPa. A similar trend can be observed in its Young's modulus. This demonstrates the mechanical feature of C-S-H gel, that is, with strong interaction in ***xy***-plane but very weak cohesion between the layers. As the Al/Si ratio increases from 0 to 0.20, the ***z***-directional tensile strength of the C-(A-)S-H displays a substantial increase from 1.54 GPa to 10.03 GPa. The Young's modulus along ***z***-direction also increases from 24.32 GPa to 96.32 GPa. This reflects that the cross-linking of aluminosilicate chains greatly improves the interlayer interaction in the C-A-S-H. Furthermore, the Al incorporation also strengthens the C-A-S-H structure along ***y***-direction. As the Al/Si ratio rises from 0 to 0.20, the tensile strength in ***y***-direction increases from 7.88 GPa to 12.27 GPa and Young's modulus increases from 71.48 GPa to 91.64 GPa. The tensile strength and Young's modulus along ***x***-direction appear to vary in relatively small ranges. With the aluminum incorporation into the structure, their values first increase and then decrease. The ***x***-directional tensile strength and Young's modulus approach their maxima at the Al/Si ratio of 0.10 and 0.15, respectively. With the cross-linking of the C-A-S-H model, the difference between interlayer strength and ***xy*** planar strength is significantly narrowed. At Al/Si ratio of 0.20, the ***z***-directional strength even compares well with the ***xy***-plane cohesion. The mechanical behavior of the C-A-S-H model transforms gradually from one featured by layered structure to one by glass-like materials. This finding is consistent with previous research (Geng et al., 2017a). They have tested the compressibility of lattice parameters of the unit cell under hydrostatic pressure. The results show that, for the non-cross-linked C-S-H, the compliance is about 3.3% per 10 GPa along the ***x***- and ***y***-directions (***a*** and ***b*** unit cell decrease by 3.3% relative to the values at atmospheric pressure at an external hydrostatic pressure of 10 GPa) and 7–11% per 10 GPa along ***z***-direction. For the cross-linked C-A-S-H sample with Al/Si ratio of 0.10, the compressibility of ***c*** parameter is largely improved (compliance ≈4% per 10 GPa) and close to that of ***a*** and ***b*** parameters, while the compressibility of a and b parameters is almost the same as that of non-cross-linked one.

Molecular Structure Evolution

In order to gain an in-depth knowledge of the underlying mechanisms of the mechanical behavior, the molecular structure evolution of C-A-S-H models under tensile loading is investigated. Since the aluminosilicate chains are essential to the loading resistance of the structure, their morphology evolution under tension process is analyzed. Furthermore, as suggested in a previous study, water molecules' intrusion will "attack" bridging bonds in the structure and weaken their bond strength (Hou et al., 2014a). This process consumes the interlayer water molecule and forms various hydroxyl groups; thus, the numbers of water molecules and hydroxyls are recorded to investigate the hydrolytic reaction during tensile loading.

Tensile Loading Along *x*-Direction

The deformed molecular structures for the C-S-H and C-A-S-H model (Al/Si = 0 and 0.20, respectively) from the strain of 0.0 Å/Å to 0.8 Å/Å during tension along ***x***-direction are shown in **Figure 6**. For the C-S-H gel (**Figure 6A**), when strain is within 0.4 Å/Å, the ionic bonds between silicate chains and principal layer Ca are prolonged to take the loading. At the strain of 0.4 Å/Å, cracks can be clearly observed in the structure. Meanwhile, the silicate chains are displaced and rotated due to the tensile loading. As a result, the arrangement of calcium silicate layers becomes disordered. As the strain increases from 0.4 Å/Å to 0.8 Å/Å, the defective regions extend rapidly and connect with one another. The C-S-H structure is fractured at the strain of 0.8 Å/Å. With respect to the C-A-S-H model (Al/Si = 0.2), the structure appears to be more rigid. As shown in **Figure 6B**, the elongation initially leads to the extending distances between silicate chains and intralayer calcium. At the strain of 0.4 Å/Å, there is a hole amid the C-A-S-H structure. However, the aluminosilicate chains around the hole appear not to be twisted and still have their linear chain structures. The calcium aluminosilicate substrate also maintains its ordered structure to some extent. With the increase of strain from 0.4 Å/Å to 0.8 Å/Å, the hole rapidly grows and causes the fracture of the C-A-S-H structure, but the layered structure remains ambiguously visible in the fractured model. This can be attributed to the highly polymerized double aluminosilicate chains that show high stiffness and less deformation under tensile loading. Overall, it can be concluded that the ***x***-directional

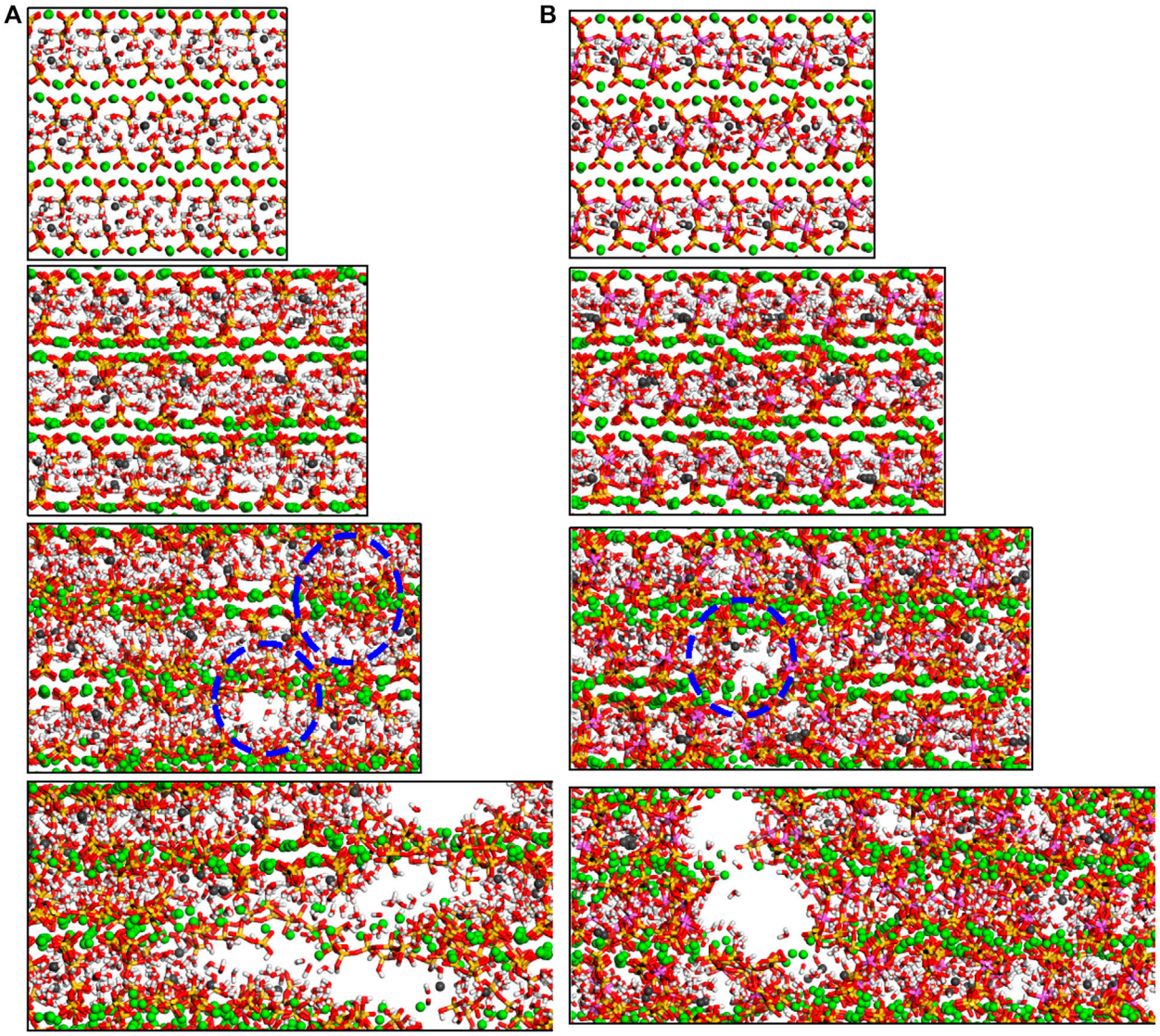

FIGURE 6 | Molecular structure evolution (view along ***y***-direction) of C-A-S-H with Al/Si ratio of **(A)** 0 and **(B)** 0.2. From top to bottom, the tensile strains along ***x***-direction are 0.0 Å/Å, 0.2 Å/Å, 0.4 Å/Å, and 0.8 Å/Å, respectively.

cohesive property originates from the ionic bonds between main layer calcium atoms and silicate clusters (Hou et al., 2014b). Al incorporation does not change the nature of interacting bonds, which can explain why the ***x***-directional strength exhibits little variation for the different models. The slight changes in tensile strength and Young's modulus may be related to the change in the rigidity of the structure.

It can be noted from **Figure 7** that there is almost no Q species variation in any of the five models, demonstrating the stability of the aluminosilicate chains during ***x***-directional elongation. The number evolution of water molecules and hydroxyl groups are shown in **Figure 8**. It can be noted that the main variation in the models is the water dissociation and Si-OH and Ca-OH formation. This corresponds to the hydrolytic reaction of Si-O-Ca bonds (Hou et al., 2015b), as depicted in **Figure 9A**. Firstly, the ionic bond between silicate tetrahedron and the main layer Ca atom is extended due to the tensile loading. The water molecule moves to silicate tetrahedron and forms a hydrogen bond with the nonbridging oxygen atom (Onb). The strong Coulomb attraction from Onb atom promotes the dissociation of water molecule to form H^+ and OH^- ions. While hydrogen ion is bonded to Onb to form Si-OH group, the remaining OH^- is coordinated to interlayer Ca^{2+} ion to form a Ca-OH group. Therefore, the water molecule dissociation screens the interaction of the silicate cluster and the Ca^{2+} ion. Moreover, in the Al-containing models, there are also some Al-OH and Al-O(H)-Si groups production, in addition to the Ca-OH and Si-OH formation. This is due to the protonation of Ob atom in Al-O-Si bonds. As portrayed in **Figure 9B**, when the aluminate tetrahedron is distorted owing to the tensile loading, two water

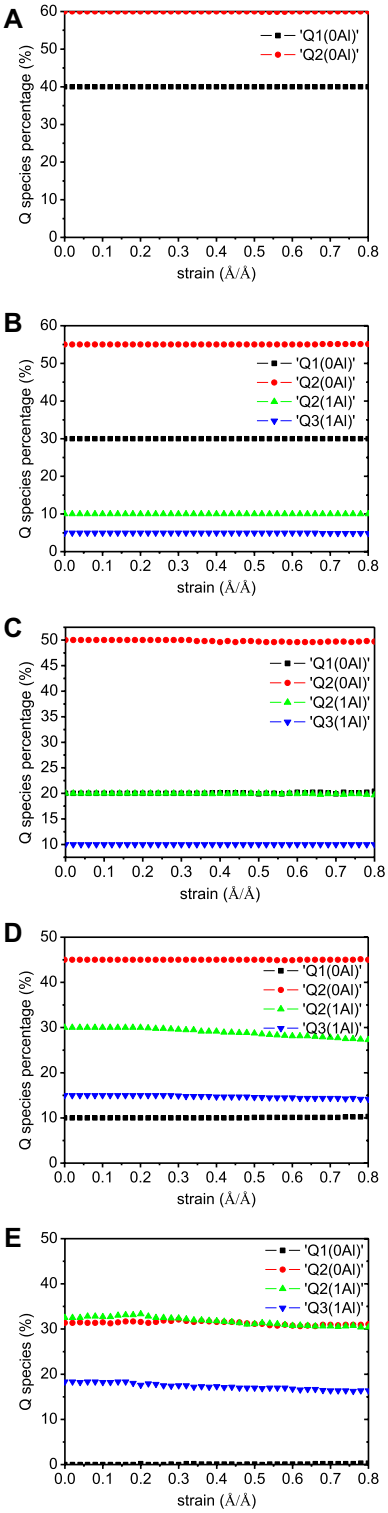

FIGURE 7 | Q species variation in C-A-S-H model under ***x*-**directional elongation. The Al/Si ratios of the model are **(A)** 0.00, **(B)** 0.05, **(C)** 0.10, **(D)** 0.15, and **(E)** 0.20.

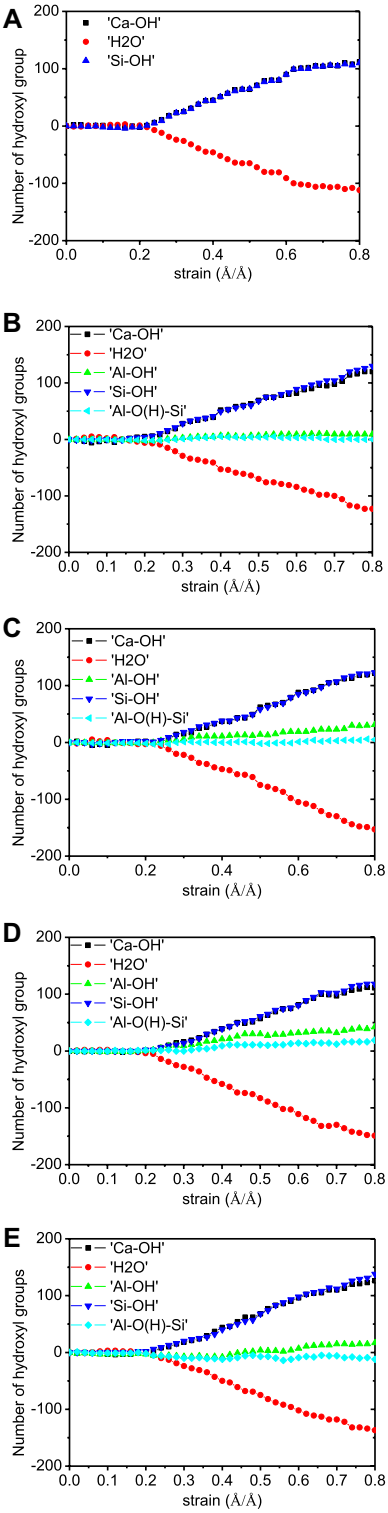

FIGURE 8 | Number evolution of Ca-OH, Si-OH, Al-OH, Al-O(H)-Si, and H_2O in C-A-S-H model during ***x*-**directional elongation. The Al/Si ratios of the model are **(A)** 0.00, **(B)** 0.05, **(C)** 0.10, **(D)** 0.15, and **(E)** 0.20.

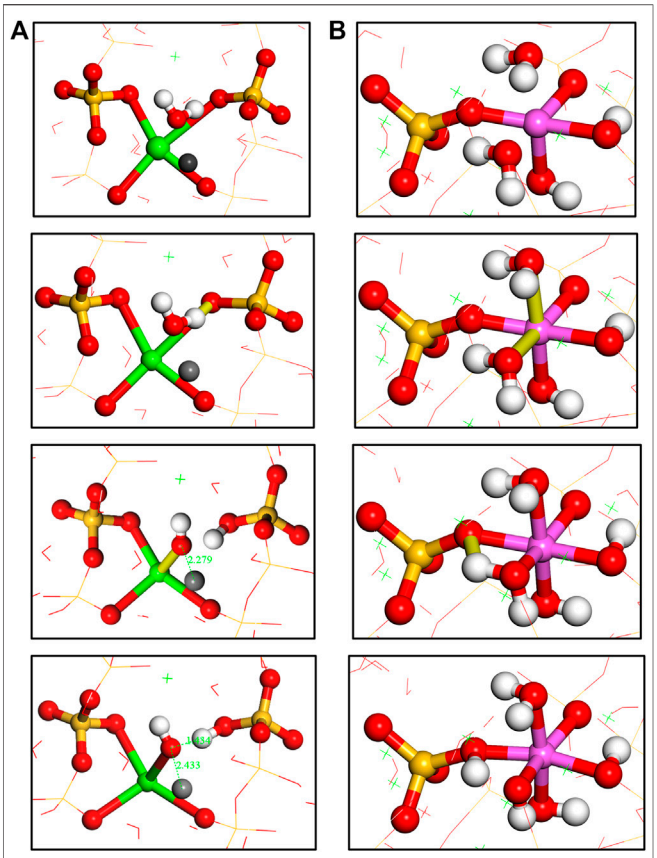

FIGURE 9 | (A) Hydrolytic reaction pathway of Si-O-Ca bond; **(B)** two water molecules association on the aluminum atom and one water molecule dissociation to form an Al-OH and Al-O(H)-Si bonds.

molecules diffuse close to the Al atom and adsorb on it. Then, one adsorbed water molecule transfers one of its hydrogen atoms to the Ob atom of the Al-O-Si bond. The water dissociation results in an Al-OH and an Al-O(H)-Si formation. It is worth noting that the Al-O(H)-Si tri-clusters are also observed in previous simulations of silicate-aluminate glasses (Benoit et al., 2001) (Cormier et al., 2000). This shows the reactivity of the Al-O-Si bond, which is different from the chemically inert Si-O-Si bond (Manzano et al., 2012a). In our work, the reactivity of Ob in Al-O-Si bonds is activated by the external loading. As proposed by Zhu et al., (2005), the energy barrier for the dissociation of water molecules can be reduced by the external loading. The loading also activates the distorted aluminate tetrahedron and leads to its transformation to octahedron. It can be noticed that hydrolytic reactions start at the strain level of about 0.2 Å/Å for all five models, which corresponds to the failure strain of C-A-S-H. The number of hydroxyls increases even at the end of the tension test, indicating the continuous hydrolytic reactions during the breakage of the C-A-S-H molecular structure.

When comparing the five models, it can be observed that the number of produced Al-OH groups first increases and then decreases with the increasing number of Al-Si substitutions. The number of Al-OH formation reaches its maximum at the Al/Si ratio of 0.15. It can be noted from **Figure 10A** that the relatively short silicate chains are easy to translate and rotate by the loading in the C-S-H model. With the increase of Al/Si ratio, aluminosilicate chains became longer and branched. These longer chains are hard to translate or rotate and are more likely to be twisted under tensile loading. Thus, the increasing Al content in the twisted chains results in more Al-OH formation. However, the polymerization of silicate/aluminate species and the formation of branch structures also stiffen the chains. At the Al/Si ratio of 0.2, the long double chains are rigid and show less extent of twist during the elongation, as illustrated in **Figure 10C**. In that situation, the number of Al-hydrolytic reactions decreases. It is widely believed that bond distortion and breakage are ways for materials to uptake external loading. Tensile test results show that Young's modulus and tensile strength of C-A-S-H also show decreases at Al/Si ratio of 0.20. Therefore, the variation in ***x***-directional mechanical properties is also correlated with the twist of aluminosilicate chains. As shown in **Figure 10**, the flexible branch chains in C-A-S-H with Al/Si ratio of 0.1 show a larger extent of twist than those of Al/Si ratio of 0 and 0.2. These chains (**Figure 10B**) play a more important role in binding together the surrounding principal layer calcium atoms.

Tensile Loading Along *y*-Direction

The structure deformation of the C-A-S-H models from strain of 0.0 Å/Å to 0.6 Å/Å during tension along ***y***-direction is presented in **Figure 11**. In the C-S-H gel (**Figure 11A**), the silicate chains are defective, limiting their ability to resist the loading. At the strain of 0.2 Å/Å, some cracks are formed in the defective silicate sites. As the strain increase, the cracks grow rapidly and connect together, until the final fracture of the model. It can be concluded that the ***y***-directional cohesion force of the model comes from the ionic bonds between silicate clusters and calcium ions. This is akin to the interaction of C-S-H along the ***x***-axis. Consequently, the Al-free C-S-H model has similar mechanical properties in ***x***- and ***y***-directions (see **Figure 5**). The mechanical properties in ***y***-direction are higher than those in ***x***-direction for the C-A-S-H model of Al/Si ratio of 0.2. This is because the prolonged aluminosilicate chains can help resist the tension. It can be noted from **Figure 11B** that the failure process of the C-A-S-H model is greatly delayed owing to the toughness of the highly polymerized aluminosilicate tetrahedra. No large cracks are observed in the C-A-S-H structure, even at the strain of 0.6 Å/Å. It is worth noting that the breakage of one bridging bond in the branch structure would not lead to the rupture of the double aluminosilicate chain. As is shown in the inset of **Figure 11B**, the neighboring chains can still resist the loading through the cross-linking connection, which can interpret the secondary increase in the stress-strain curves.

The Q species variation in the C-A-S-H during their elongation along y-direction is given in **Figure 12**. As depicted in **Figure 12A**, the proportions of Q species in the C-S-H structure are constant during the tensile process. This is consistent with the above observation that the C-S-H model is fractured across the defective sites in silicate chains. On the other hand, all the Al-containing models show a reduction of Q^2 and Q^3

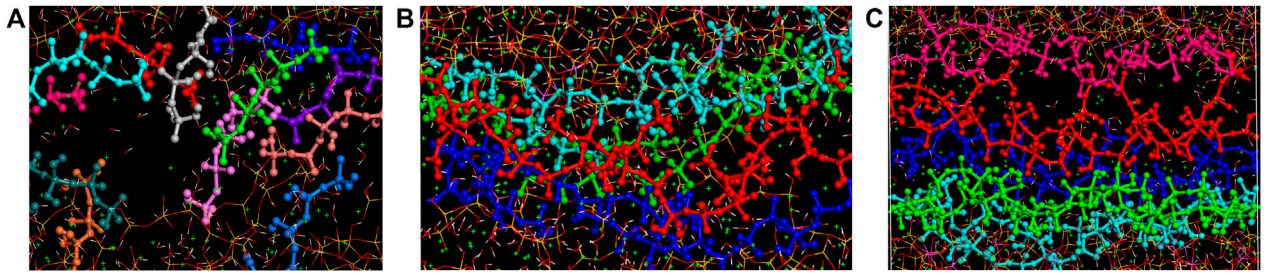

FIGURE 10 | The morphology of (alumino)silicate chains (view along ***z*-**axis) in C-A-S-H model of Al/Si ratio of **(A)** 0, **(B)** 0.10, and **(C)** 0.20 at ***x*-**directional tensile strain of 0.8 Å/Å.

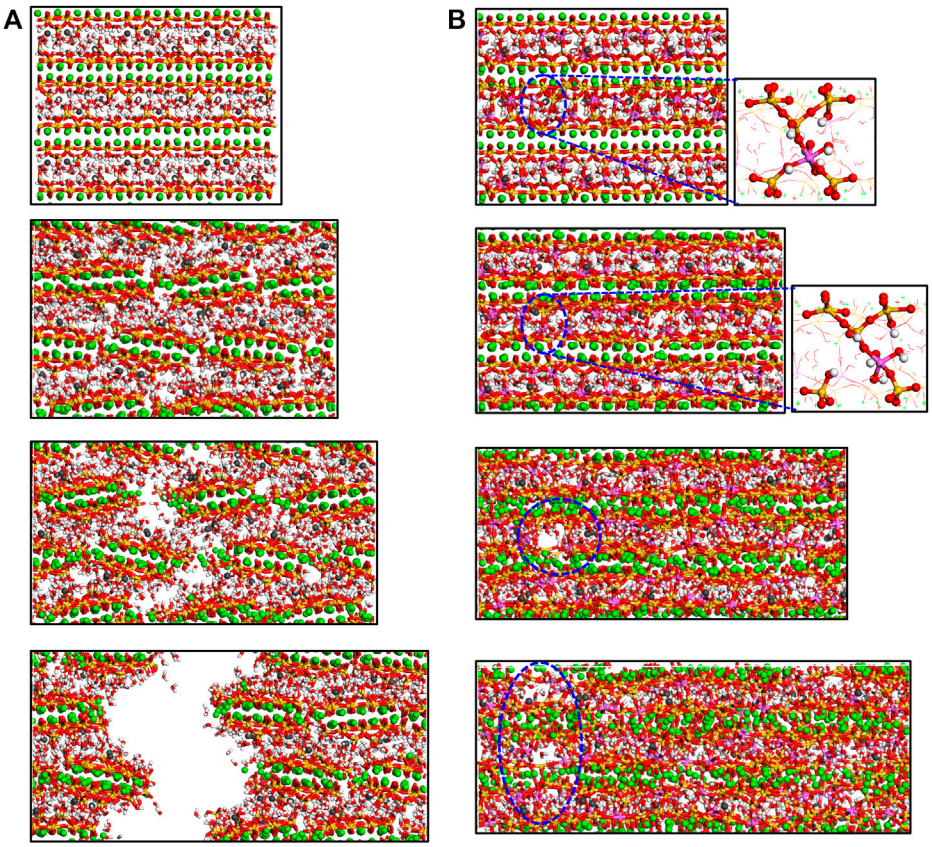

FIGURE 11 | Molecular structure evolution (view along ***x*-**direction) of C-A-S-H with Al/Si ratio of **(A)** 0 and **(B)** 0.20. From top to bottom, the tensile strains along ***z*-**direction are 0.0 Å/Å, 0.2 Å/Å, 0.4 Å/Å, and 0.6 Å/Å, respectively.

and an increase of Q^1, implying the breakage of longer chains and production of chain ends. The C-A-S-H model with Al/Si ratio of 0.1 is taken as an example to demonstrate the Q species evolution. When the strain is lower than 0.18 Å/Å, the Q species percentages remain constant. This corresponds to the extension of the aluminosilicate chains. At the strain of 0.18 Å/Å, the connections between aluminate and silicate species start to break, resulting in the reduction of $Q^2(1Al)$ and the increase of $Q^1(0Al)$. When the strain approaches 0.34 Å/Å, the siloxane bonds also begin to break, leading to the reduction of $Q^2(0Al)$ and formation of $Q^1(0Al)$. There is also a small reduction in $Q^3(1Al)$ species, suggesting a small proportion of branch structure breakage during ***y*** axial tension. After the strain of 0.7 Å/Å, the model is totally fractured and the transformation of aluminosilicate chains morphology stops. It is worth noting that the Al-O-Si bonds are broken at lower strain values than the Si-O-Si bonds, denoting that the Al-O-Si bonds are weaker than the Si-O-Si bonds. This corroborated the simulation results

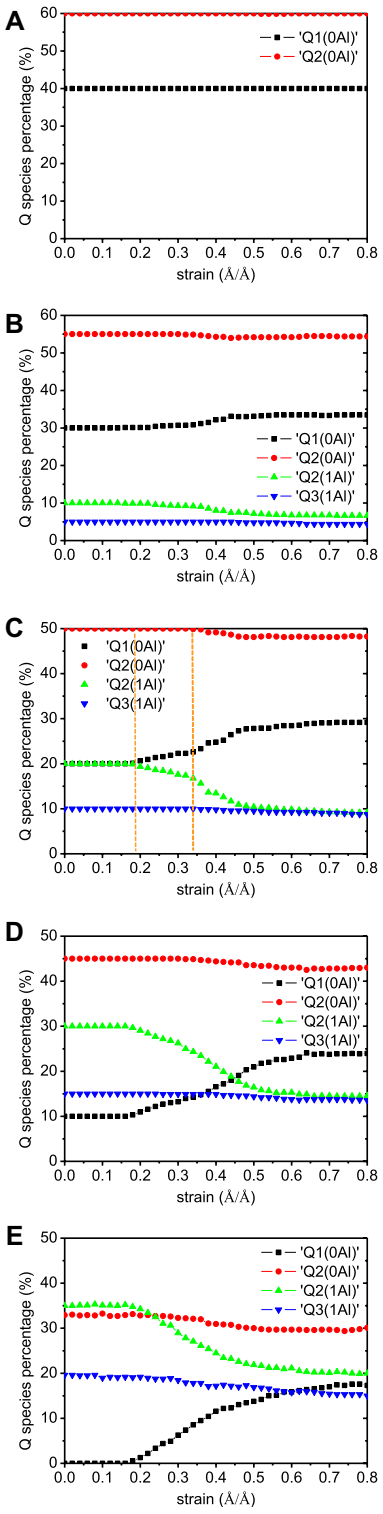

FIGURE 12 | Q species variation in C-A-S-H model under ***y***-directional elongation. The Al/Si ratios of the model are **(A)** 0.00, **(B)** 0.05, **(C)** 0.10, **(D)** 0.15, and **(E)** 0.20.

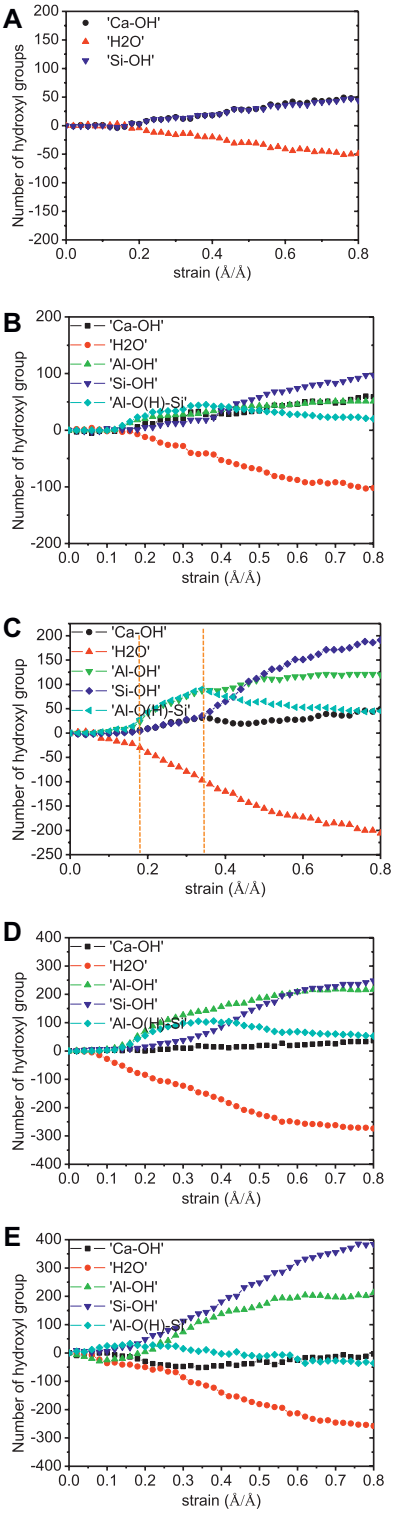

FIGURE 13 | Number evolution of Ca-OH, Si-OH, Al-OH, Al-O(H)-Si, and H_2O in C-A-S-H gel during ***y***-directional elongation. The Al/Si ratios of the model are **(A)** 0.00, **(B)** 0.05, **(C)** 0.10, **(D)** 0.15, and **(E)** 0.20.

from Qomi et al., (2012), who found that aluminosilicate chains show lower mechanical strength than silicate chains. Overall, as Al/Si ratio increases, the change of Q species content becomes more pronounced. This reflects that the longer aluminosilicate chains play more important roles in resisting the external tension.

Figure 13 shows the number of water dissociation and hydroxyls formation during the elongation process. The fracture of the C-S-H model only observes the hydrolytic reaction of Si-O-Ca ionic bonds. This is because that the presence of a large number of defective sites weakens the ability of the aluminosilicate chains to resist the loading. When the Al-incorporated models are prolonged, there are Al-OH and Al-O(H)-Si groups apart from the Ca-OH and Si-OH formation. Take the case of the C-A-S-H model of Al/Si ratio of 0.1 (see **Figure 13C**). As the strain increases from 0 Å/Å to 0.18 Å/Å (aluminosilicate chain extension stage), there are water reduction and a small amount of Al-OH and Al-O(H)-Si formation. This corresponds to the coordinate structure change of aluminum and protonation of Ob in Al-O-Si bonds (see **Figure 9B**). When the strain ranges from 0.18 Å/Å to 0.34 Å/Å, there are Si-OH, Ca-OH, Al-OH, and Al-O(H)-Si formations. This involves the breakage of both Si-O-Ca and Al-O-Si bonds. While the hydrolytic reaction of the Si-O-Ca is direct (**Figure 9A**), the breakage of Al-O-Si bond is complex, which can be described with **Eqs. 1, 2**.

$$\text{Al-O-Si} + \text{H}_2\text{O} \rightarrow \text{HO-Al-O(H)-Si} \rightarrow \text{Al-OH} + \text{Si-OH} \quad (1)$$

$$\text{Al-O-Si} + \text{H}_2\text{O} \rightarrow \text{Al-O(H)-Si} + \text{OH}^- \rightarrow \text{Al-OH} + \text{Si-OH} \quad (2)$$

It should be noted that the hydrolytic reaction of the Al-O-Si bond is a two-stage reaction. The reaction intermediates are Ca-OH, Al-OH, and Al-O(H)-Si, and the final hydrolytic reaction products are Al-OH and Si-OH. The reaction pathways are discussed in the following section. After the strain of 0.34 Å/Å, the number of Al-O(H)-Si groups drops and that of Si-OH groups increases. This is caused by the hydrolytic reaction of Al-O and Si-O bonds. Since the hydrolytic reaction of Si-O-Si only produces Si-OH groups [**Eq. 3**; Hou et al., 2015b], the number of Si-OH groups increases more rapidly at this stage.

$$\text{Si-O-Si} + \text{H}_2\text{O} \rightarrow \text{Si-OH} + \text{Si-OH} \quad (3)$$

The producing rate of Si-OH and Al-OH groups under tensile loading increases with increasing Al/Si ratio of C-A-S-H, illustrating that more aluminate/silicate bonds are broken in the cross-linked C-A-S-H model with higher Al/Si ratios. This matches well with the Q species percentages evolution, implying that the C-A-S-H is strengthened along ***y***-direction by the polymerization of aluminosilicate chains.

Tensile Loading Along *z*-Direction

The tension process of C-(A-)S-H along ***z***-direction was illustrated in Yang et al., (2018) in detail. Here, the tension failure of C-(A-)S-H along the ***z***-direction is briefly represented, in order to give a comparison between the tensile loading process along different dimensions. The molecular structure of the C-A-S-H with Al/Si ratio of 0 and 0.2 as a function of tensile strain along ***z***-direction is illustrated in **Figure 14**. It can be noted from **Figure 14A** that the calcium silicate sheets in non-cross-linked C-S-H can be easily taken apart. With increasing tensile strain, the crack is created and grown fast. When the structure is stretch-fractured, no evident deformation in calcium silicate sheets is observed. This is due to that the interlayer interacting bonds are too weak to resist the loading. On the contrary, the cross-linked C-A-S-H is stronger

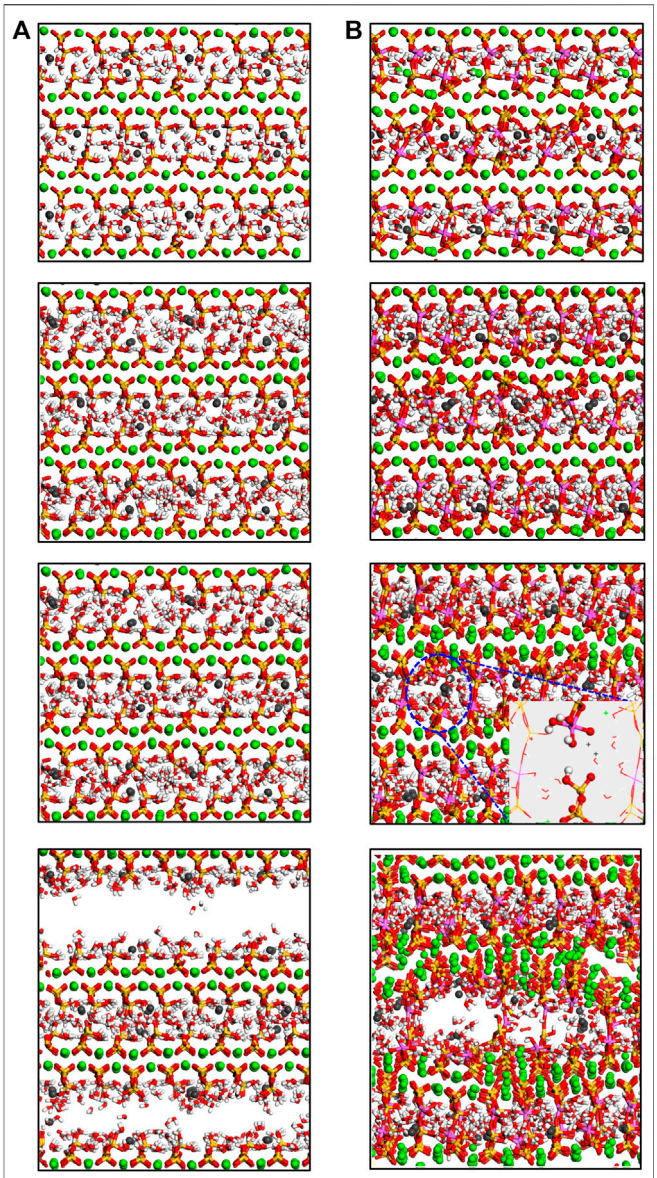

FIGURE 14 | Molecular structure evolution (view along ***y***-direction) of C-A-S-H with Al/Si ratio of **(A)** 0 and **(B)** 0.20. From top to bottom, the tensile strains along ***z***-direction are 0.0 Å/Å, 0.1 Å/Å, 0.2 Å/Å, and 0.3 Å/Å, respectively (adapted from Yang et al., (2018)).

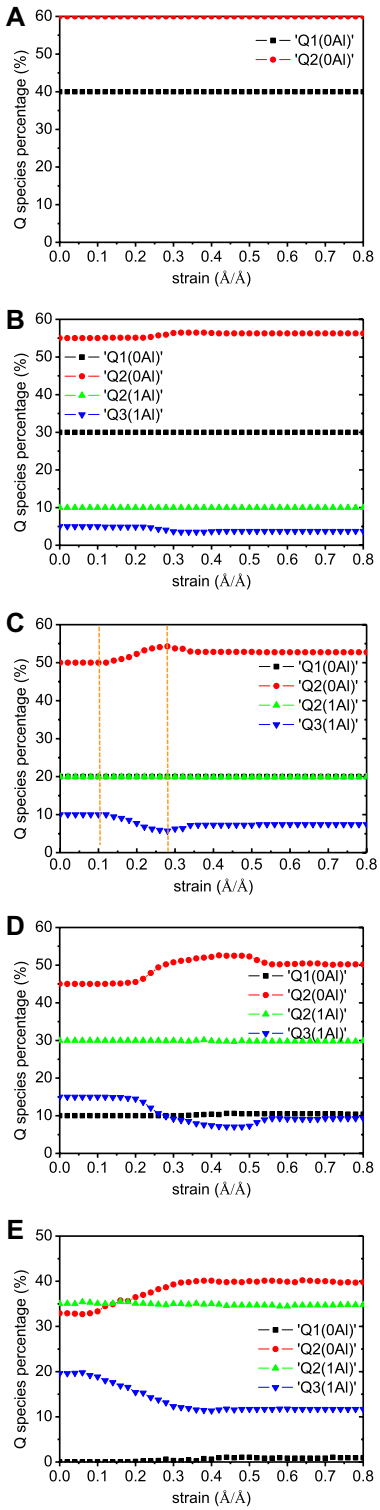

FIGURE 15 | Q species evolution of C-A-S-H model under ***z***-directional elongation. The Al/Si ratios of the model are **(A)** 0.00, **(B)** 0.05, **(C)** 0.10, **(D)** 0.15, and **(E)** 0.20 (adapted from Yang et al., (2018)).

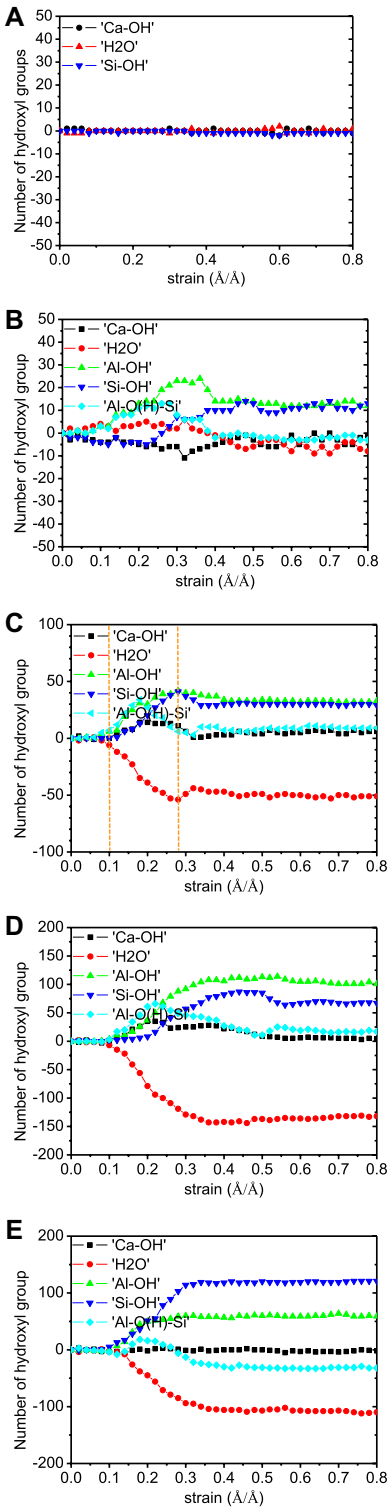

FIGURE 16 | Number of Ca-OH, Si-OH, Al-OH, Al-O(H)-Si, and H_2O evolution of C-A-S-H model under ***z***-direction elongation. The Al/Si ratios of the model are **(A)** 0.00, **(B)** 0.05, **(C)** 0.10, **(D)** 0.15, and **(E)** 0.20 (adapted from Yang et al., (2018)).

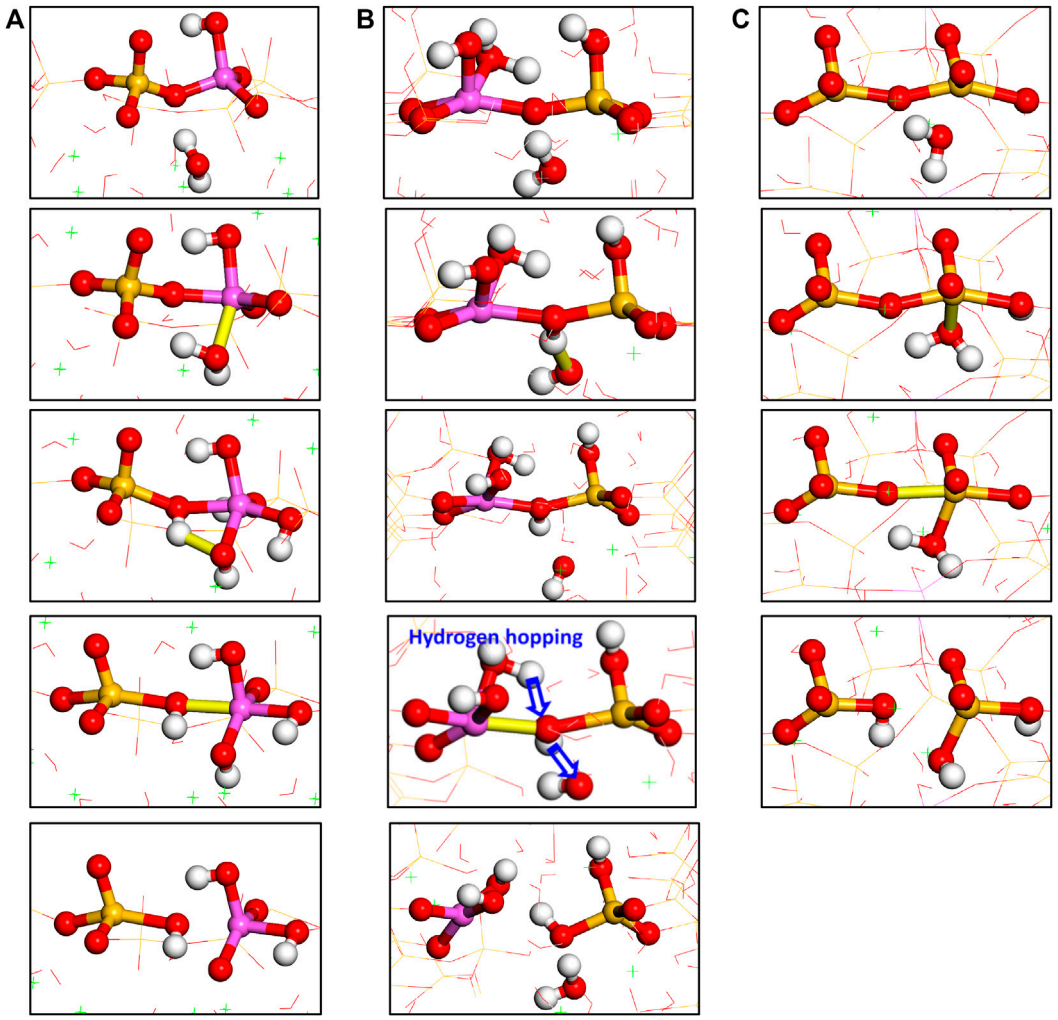

FIGURE 17 | Hydrolytic reaction pathways of Al-O-Si bonds through **(A)** Pathway 1 and **(B)** Pathway 2 (adapted from Yang et al., (2018)); **(C)** hydrolytic reaction pathway of Si-O-Si bonds.

along the interlayer direction. As shown in **Figure 14B**, the fracture of the C-A-S-H model is slighter than that of the C-S-H model at the same strain level. At the strain of 0.3 Å/Å, the model is fractured, with the calcium aluminosilicate substrate deformed and the structure turns disordered. This indicates that the principal layers act as an integral to resist the loads and deformation. Hence, the cross-linked C-A-S-H model shows higher mechanical strength than the non-cross-linked C-S-H model.

The Q species percentages evolution during the tensile loading along *z*-direction is given in **Figure 15**. Expectedly, the Q species percentages are constant during the tensile process of non-cross-linked C-S-H model (**Figure 15A**). The Q species evolution is found in the Al-substituted models and becomes more pronounced with the increase of Al/Si ratio. The main change is the decrease of Q^3(1Al) and the increase of Q^2(0Al) species, indicating the breakage of branch structures. This means that an increasing number of cross-links participated in the elongation process of the structure, thereby leading to a higher mechanical strength along *z*-direction. The number evolution of water molecules and hydroxyl groups is illustrated in **Figure 16**. There are no hydrolytic reactions in the non-cross-linked model because the elongation process involves no change in the silicate chain morphology. From another perspective, no hydrolytic reactions to take up the loading energy also denote the lower strength. In the cross-linked models, there are Al-OH and Si-OH increases and water molecules reduction, which indicates the hydrolytic reaction of Al-O-Si bonds, as described in **Eqs. 1, 2**. When comparing the five models, it can be observed that the number of hydrolytic reactions increases as the Al/Si ratio of C-A-S-H increases. This proves that the enhanced interlayer strength is correlated with the cross-links between neighboring layers.

Hydrolytic Reaction Pathways of Al-O-Si and Si-O-Si Bonds

It can be concluded that the breakage of Al-O-Si and Si-O-Si bonds in our work is the result of combined tensile loading and water "attack." This can be compared to the well-documented mechanisms found in the dissolution of aluminosilicate glasses, quartz, and feldspar, which involve the reaction of Al-O-Si and Si-O-Si under sole water "attack." The hydrolytic reaction pathways of the Al-O-Si bond are illustrated in **Figures 17A,B**. In the first pathway, the water molecule is first adsorbed on the distorted aluminate tetrahedron. Then, the water molecule dissociates into H^+ and OH^-. While the OH^- remains connected to the aluminum atom, the H^+ ion binds to the neighboring bridging oxygen atom to form an oxygen tricluster. With further increase of the strain, the Al-O bond is broken in the Al-O(H)-Si. As a result, one Si-OH group is produced. In the second pathway, the Ob atom is protonated by the hydrogen atom from the neighboring water molecule. Correspondingly, the water molecule turns into a free hydroxyl group. After the breakage of Al-O bond, the hydrogen atom in the adsorbed water molecule is transferred to the free hydroxyl to form a water molecule, as depicted in **Figure 17B**. The proton transfer resembles the "hydrogen hopping" process described by Manzano et al., (2015). The difference between the first and second hydrolytic reaction pathway is the types of reaction intermediates, which are Al-O(H)-Si and Al-OH for the first pathway but Al-O(H)-Si and Ca-OH for the second pathway. The hydrolytic reaction pathway of the Si-O-Si bond is depicted in **Figure 14C**, which is also described in Mahadevan and Garofalini (2008) (Hou et al., 2015b). Firstly, the silicate tetrahedra are distorted due to the external loading. One water molecule diffuses to the silicon atom and binds to it. Subsequently, the bridging Si-O bond in the five-coordinated silicon structure is broken, which makes the silicon atom returns to a four-coordinated structure. The adsorbed water molecule immediately gives one of its hydrogen atoms to the nonbridging oxygen atom, leading to the formation of two Si-OH groups.

According to the hydrolytic reaction pathways, the differences between Al-O-Si and Si-O-Si bonds breakage can be concluded as follows:

(1) The hydrolytic reaction of the Al-O-Si bond is a two-stage reaction, where the reaction intermediate five-/six-coordinated aluminum atom and Al-O(H)-Si groups can linger for a relatively long time until the Al-O bond breaks at high strain levels. During the Si-O-Si breakage, however, the water adsorption, Si-O bond breakage, and water dissociation almost happen simultaneously, implying the five-coordinated silicon atom and adsorbed water are thermodynamically unstable. Tsomaia (Tsomaia et al., 2003) studied the dissolution of albite crystal and glass and detected the six-coordinated Al in the surface of the samples. In those dissolution samples, the Al and Si atoms are originally tetracoordinated in aluminosilicate networks. This can corroborate our simulation results that the reaction intermediates during the breakage of the Al-O-Si bond are relatively stable. With respect to the hydrolytic reaction of the Si-O-Si bond, since most of the Si^{4+} species are four-coordinated at atmospheric pressure (Schindler and Stumm, 1987) (Bensted, 1999), it is reasonable that the five-coordinated Si is unstable. Ab initio calculations (Kubicki et al., 1996) demonstrated that the proton affinity of Si-OH is weak, which has ruled out the existence of $Si\text{-}OH_2$ at a neutral or basic solution. The flexible coordination change of the aluminum atom decreases the hydrolysis activation energy of the Al-O-Si linkages (Criscenti et al., 2005), which can help explain the lower strength of the Al-O-Si bond than that of the Si-O-Si bond.

(2) The dissolution of aluminosilicate glass, feldspar, or quartz is influenced by the environmental pH. It found that both the Si-O-Si and Al-O-Si bonds can be broken in either an acidic or alkali environment. In an acidic solution, the hydronium ion attacks the bridging site and protonates the bridging oxygen atom. This significantly weakens the bridging bonds in Si-O-Si and Si-O-Al and leads to the bonds' breakage (Xiao and Lasaga, 1994). On the other hand, in a basic environment, the hydroxyl first deprotonates the Si-OH group and turns into a water molecule. Then, the water molecule bonds to one of the silicon atoms to produce a pentacoordinated silicate species, which weakens the bridging Si-O bond and finally leads to the breakage of the Si-O-Si bond (Xiao and Lasaga, 1996). In our simulation, the protonation of bridging oxygen atom plays a role in weakening the Al-O connection, which resembles the T-O bond (T = Al or Si) attacked by hydronium ions, while the breakage of Si-O bond is facilitated by the pentacoordinated Si formation, similar to T-O bond attacked by OH^- ions. Therefore, the hydrolytic reactions of Al-O-Si and Si-O-Si bonds in our work approximately correspond to acidic dissolution and alkali dissolution, respectively. Furthermore, the low reactivity of Ob atom in Si-O-Si reduces the possibility of Si-O breakage due to proton "attack." This indicates that a higher acidic environment is needed to dissolve the Si-O-Si bond, as compared with the Al-O-Si bond (Kubicki et al., 1996).

CONCLUSION

In this work, the mechanical properties of cross-linked C-A-S-H of Al/Si ratios ranging from 0 to 0.2 were studied by MD simulating uniaxial test. Based on the ReaxFF coupled with chemical reaction and mechanical response, the failure mechanism of the C-A-S-H structure was also investigated. Several conclusions can be drawn as follows:

(1) The presence of aluminate species can heal the broken silicate clusters and cross-link the silicate chains of neighboring calcium silicate sheet. The branch structure formation significantly increases the polymerization of aluminosilicate chains, leading to the transformation from a two-to a three-dimensional C-A-S-H structure.

(2) The uniaxial tensile testing shows that, by bridging the defective silicate chains and forming branch structures, Al-induced cross-links significantly increase the tensile strength and Young's modulus of C-A-S-H structure both along ***y***- and ***z***-directions, where the latter undergoes a larger extent of increase. When all the bridging sites are cross-linked at Al/Si ratio of 0.2, the mechanical properties of the C-A-S-H structure along ***z***-direction almost match those in the ***xy***-plane.
(3) During the elongation process, the tensile loading is taken up mainly by the depolymerization of the calcium aluminosilicate skeleton, which demonstrates the backbone role of calcium aluminosilicate sheets in the C-A-S-H structure. The strengthening of the C-A-S-H structure can be achieved by the polymerization of aluminosilicate chains, which can replace weaker ionic or hydrogen bonds with stronger covalent bonds.
(4) During the failure process of the structure, the combined effect of loading and water "attack" is responsible for the bond breakage. As compared with Si-O-Si bond, the reaction intermediates during the hydrolytic reaction of the Al-O-Si bond are relatively stable, making the hydrolytic reaction process of Al-O-Si bond slower. In addition, the bridging bonds breaking in Al-O-Si and Si-O-Si are induced by different ions' "attack." While the bond breakage in Al-O-Si results from the protonation of the bridging oxygen atom, the bridging bond breakage in Si-O-Si is a consequence of the pentacoordinated silicon formation. The ions' attack weakens the bridging bond (Al-O or Si-O) and results in its rupture.

DATA AVAILABILITY STATEMENT

The original contributions presented in the study are included in the article/Supplementary Material; further inquiries can be directed to the corresponding author.

AUTHOR CONTRIBUTIONS

GZ was involved in writing of the original draft, formal analysis, and methodology. YL was involved in investigation and data curation. JY was involved in conceptualization and writing, review, and editing. QD was involved in supervision and validation. DS was involved in funding acquisition.

FUNDING

Financial support from the National Natural Science Foundation of China (Grant Nos. 51878003 and 52008002), Natural Science Research Project of Higher School of Anhui Province (Grant No. KJ2019ZD55), Excellent Young Talent Support Project of Anhui Province (Grant No. gxyqZD2019055), and Doctoral Scientific Research Startup Foundation of Anhui Jianzhu University (Grant No. 2019QDZ66) is gratefully acknowledged.

REFERENCES

Abdolhosseini Qomi, M. J., Krakowiak, K. J., Bauchy, M., Stewart, K. L., Shahsavari, R., Jagannathan, D., et al. (2014). Combinatorial molecular optimization of cement hydrates. *Nat. Commun.* 5, 4960. doi:10.1038/ncomms5960

Aktulga, H. M., Fogarty, J. C., Pandit, S. A., and Grama, A. Y. (2012). Parallel reactive molecular dynamics: numerical methods and algorithmic techniques. *Parallel Comput.* 38 (4–5), 245–259. doi:10.1016/j.parco.2011.08.005

Allen, A. J., Thomas, J. J., and Jennings, H. M. (2007). Composition and density of nanoscale calcium-silicate-hydrate in cement. *Nat. Mater.* 6 (4), 311–316. doi:10.1038/nmat1871

Benoit, M., Ispas, S., and Tuckerman, M. E. (2001). Structural properties of molten silicates from ab initio, molecular-dynamics simulations: comparison between CAO-Al2O3-SiO2, and SiO2. *Phys. Rev. B.* 64 (22), 224205. doi:10.1103/physrevb.64.224205

Bensted, J. (1999). Thaumasite – background and nature in deterioration of cements, mortars and concretes. *Cement Concr. Compos.* 21 (2), 117–121. doi:10.1016/s0958-9465(97)00076-0

Bernal, S. A., Provis, J. L., Walkley, B., Nicolas, R. S., Gehman, J. D., and Brice, D. G. (2013). Gel nanostructure in alkali-activated binders based on slag and fly ash, and effects of accelerated carbonation. *Cement Concr. Res.* 53 (2), 127–144. doi:10.1016/j.cemconres.2013.06.007

Chen, C., Habert, G., Bouzidi, Y., Jullien, A., and Ventura, A. (2010). Lca allocation procedure used as an incitative method for waste recycling: an application to mineral additions in concrete. *Resour. Conserv. Recycl.* 54 (12), 1231–1240. doi:10.1016/j.resconrec.2010.04.001

Constantinides, G., and Ulm, F.-J. (2007). The nanogranular nature of C-S-H. *J. Mech. Phys. Solid.* 55 (1), 64–90. doi:10.1016/j.jmps.2006.06.003

Cormier, L., Neuville, D. R., and Calas, G. (2000). Structure and properties of low-silica calcium aluminosilicate glasses. *J. Non-Cryst. Solids* 274 (1), 110–114. doi:10.1016/s0022-3093(00)00209-x

Criscenti, L. J., Brantley, S. L., Mueller, K. T., Tsomaia, N., and Kubicki, J. D. (2005). Theoretical and 27Al CPMAS NMR investigation of aluminum coordination changes during aluminosilicate dissolution. *Geochem. Cosmochim. Acta* 69 (9), 2205–2220. doi:10.1016/j.gca.2004.10.020

Duchesne, J., and Bérubé, M. A. (1994). Evaluation of the validity of the pore solution expression method from hardened cement pastes and mortars. *Cement Concr. Res.* 24 (3), 456–462. doi:10.1016/0008-8846(94)90132-5

Duin, V. A. C., Dasgupta, S., Lorant, F., and Goddard, W. A. (2001). Reaxff: a reactive force field for hydrocarbons. *J. Phys. Chem.* 105 (41), 9396–9409. doi:10.1021/jp004368u

Duin, V. A. C., Strachan, A., Stewman, S., Zhang, Q., Xu, X., and Goddard, W. (2003). ReaxFF SiO reactive force field for silicon and silicon oxide systems. *J. Phys. Chem.* 107 (19), 3803–3811. doi:10.1021/jp0276303

Faucon, P., Delagrave, A., Richet, C., Marchand, J. M., Zanni, H., and Zanni, H. (1999). Aluminum incorporation in calcium silicate hydrates (C–S–H) depending on their Ca/Si ratio. *J. Phys. Chem. B.* 103 (37), 7796–7802. doi:10.1021/jp990609q

Feiz, R., Ammenberg, J., Baas, L., Eklund, M., Helgstrand, A., and Marshall, R. (2015). Improving the CO2 performance of cement, part I: utilizing life-cycle assessment and key performance indicators to assess development within the cement industry. *J. Clean. Prod.* 98, 272–281. doi:10.1016/j.jclepro.2014.01.083

Fogarty, J. C., Aktulga, H. M., Grama, A. Y., van Duin, A. C., and Pandit, S. A. (2010). A reactive molecular dynamics simulation of the silica-water interface. *J. Chem. Phys.* 132 (17), 174704. doi:10.1063/1.3407433

Gale, J. D., and Rohl, A. L. (2003). The general utility lattice program (gulp). *Mol. Simulat.* 29 (5), 291–341. doi:10.1080/0892702031000104887

Geng, G., Myers, R. J., Li, J., Maboudian, R., Carraro, C., Shapiro, D. A., et al. (2017a). Aluminum-induced dreierketten chain cross-links increase the mechanical properties of nanocrystalline calcium aluminosilicate hydrate. *Sci. Rep.* 7, 44032. doi:10.1038/srep44032

Geng, G., Myers, R. J., Qomi, M. J. A., and Monteiro, P. J. M. (2017b). Densification of the interlayer spacing governs the nanomechanical properties of calcium-silicate-hydrate. *Sci. Rep.* 7 (1), 10986. doi:10.1038/s41598-017-11146-8

Hamid, S. A. (1981). The crystal structure of the 11 Ä natural tobermorite Ca2. 25 [Si3O7. 5 (OH) 1.5]· 1H2O. *Z. Kristallogr.-Cryst. Mat.* 154 (1–4), 189–198. doi:10.1524/zkri.1981.154.14.189

Hou, D., Hu, C., and Li, Z. (2017). Molecular simulation of the ions ultraconfined in the nanometer-channel of calcium silicate hydrate: hydration mechanism, dynamic properties, and influence on the cohesive strength. *Inorg. Chem.* 56 (4), 1881–1896. doi:10.1021/acs.inorgchem.6b02456

Hou, D., Li, Z., and Zhao, T. (2015a). Reactive force field simulation on polymerization and hydrolytic reactions in calcium aluminate silicate hydrate (C-A-S-H) gel: structure, dynamics and mechanical properties. *RSC Adv.* 5 (1), 448–461. doi:10.1039/c4ra10645h

Hou, D., Ma, H., Li, Z., and Jin, Z. (2014a). Molecular simulation of "hydrolytic weakening": a case study on silica. *Acta Mater.* 80, 264–277. doi:10.1016/j.actamat.2014.07.059

Hou, D., Zhao, T., Ma, H., and Li, Z. (2015b). Reactive molecular simulation on water confined in the nanopores of the calcium silicate hydrate gel: structure, reactivity, and mechanical properties. *J. Phys. Chem. C*, 119(3), 1346–1358. doi:10.1021/jp509292q

Hou, D., Zhu, Y., Lu, Y., and Li, Z. 2014b). Mechanical properties of calcium silicate hydrate (C-S-H) at nano-scale: a molecular dynamics study. *Mater. Chem. Phys.* 146 (3), 503–511. doi:10.1016/j.matchemphys.2014.04.001

Huntzinger, D. N., and Eatmon, T. D. (2009). A life-cycle assessment of Portland cement manufacturing: comparing the traditional process with alternative technologies. *J. Clean. Prod.* 17 (7), 668–675. doi:10.1016/j.jclepro.2008.04.007

Juenger, M. C. G., Winnefeld, F., Provis, J. L., and Ideker, J. H. (2011). Advances in alternative cementitious binders. *Cement Concr. Res.* 41 (12), 1232–1243. doi:10.1016/j.cemconres.2010.11.012

Kocks, U. F., and Mecking, H. (2003). Physics and phenomenology of strain hardening: the fcc case. *Prog. Mater. Sci.* 48 (3), 171–273. doi:10.1016/s0079-6425(02)00003-8

Kubicki, J. D., Blake, G. A., and Apitz, S. E. (1996). Ab initio calculations on aluminosilicate q3 species: implications for atomic structures of mineral surfaces and dissolution mechanisms of feldspars. *Am. Mineral.* 81 (7–8), 789–799. doi:10.2138/am-1996-7-801

Leroch, S., and Wendland, M. (2012). Simulation of forces between humid amorphous silica surfaces: a comparison of empirical atomistic force fields. *J. Phys. Chem. C Nanomater Interfaces* 116 (50), 26247. doi:10.1021/jp302428b

Liu, L., Jaramillo-Botero, A., Goddard, W. A., and Sun, H. (2012). Development of a reaxff reactive force field for ettringite and study of its mechanical failure modes from reactive dynamics simulations. *J. Phys. Chem.* 116 (15), 3918–3925. doi:10.1021/jp210135j

Lothenbach, B., Scrivener, K., and Hooton, R. D. (2011). Supplementary cementitious materials. *Cement Concr. Res.* 41 (12), 1244–1256. doi:10.1016/j.cemconres.2010.12.001

Lowenstein, W. (1954). The distribution of aluminum in The Tetrahedra of silicates and aluminates. *Am. Mineral.* 39, 92–96.

Mahadevan, T. S., and Garofalini, S. H. (2008). Dissociative chemisorption of water onto silica surfaces and formation of hydronium ions. *J. Phys. Chem. C.* 112 (5), 1507–1515. doi:10.1021/jp076936c

Manzano, H., Dolado, J. S., and Ayuela, A. 2009a). Aluminum incorporation to dreierketten silicate chains. *J. Phys. Chem. B.* 113 (9), 2832–2839. doi:10.1021/jp804867u

Manzano, H., Durgun, E., López-Arbeloa, I., and Grossman, J. C. (2015). Insight on tricalcium silicate hydration and dissolution mechanism from molecular simulations. *ACS Appl. Mater. Interfaces* 7 (27), 14726–14733. doi:10.1021/acsami.5b02505

Manzano, H., Moeini, S., Marinelli, F., van Duin, A. C., Ulm, F. J., and Pellenq, R. J. (2012a). Confined water dissociation in microporous defective silicates: mechanism, dipole distribution, and impact on substrate properties. *J. Am. Chem. Soc.* 134 (4), 2208–2215. doi:10.1021/ja209152n

Manzano, H., Pellenq, R. J., Ulm, F. J., Buehler, M. J., and van Duin, A. C. (2012b). Hydration of calcium oxide surface predicted by reactive force field molecular dynamics. *Langmuir* 28 (9), 4187–4197. doi:10.1021/la204338m

Manzano, H., Dolado, J. S., and Ayuela, A. (2009b). Elastic properties of the main species present in Portland cement pastes. *Acta Mater.* 57 (5), 1666–1674. doi:10.1016/j.actamat.2008.12.007

Merlino, S., Bonaccorsi, E., and Armbruster, T. (2001). The real structure of tobermorite 11 Å: normal and annomalous forms. *Eur. J. Mineral.* 13 (3), 65–80. doi:10.1127/0935-1221/2001/0013-0577

Mikulčić, H., Klemeš, J. J., Vujanović, M., Urbaniec, K., and Duić, N. (2016). Reducing greenhouse gasses emissions by fostering the deployment of alternative raw materials and energy sources in the cleaner cement manufacturing process. *J. Clean. Prod.* 136, 119–132. doi:10.1016/j.jclepro.2016.04.145

Mir, A. E., and Nehme, S. G. (2017). Utilization of industrial waste perlite powder in self-compacting concrete. *J. Clean. Prod.* 157, 507–517. doi:10.1016/j.jclepro.2017.04.103

Murray, S. J., Subramani, V. J., Selvam, R. P., and Hall, K. D. 2010). Molecular dynamics to understand the mechanical behavior of cement paste. *Transport. Res. Rec.* 2142, 75–82. doi:10.3141/2142-11

Myers, R. J., Bernal, S. A., San Nicolas, R., and Provis, J. L. (2013). Generalized structural description of calcium-sodium aluminosilicate hydrate gels: the cross-linked substituted tobermorite model. *Langmuir* 29 (17), 5294–5306. doi:10.1021/la4000473

Myers, R. J., L'Hôpital, E., Provis, J. L., and Lothenbach, B. (2015). Effect of temperature and aluminium on calcium (alumino)silicate hydrate chemistry under equilibrium conditions. *Cement Concr. Res.* 68, 83–93. doi:10.1016/j.cemconres.2014.10.015

Pegado, L., Labbez, C., and Churakov, S. V. (2014). Mechanism of aluminium incorporation into c-s-h from ab initio calculations. *J. Mater. Chem.* 2 (10), 3477–3483. doi:10.1039/c3ta14597b

Pellenq, R. J., Kushima, A., Shahsavari, R., Van Vliet, K. J., Buehler, M. J., Yip, S., et al. 2009). A realistic molecular model of cement hydrates. *Proc. Natl. Acad. Sci. U.S.A.* 106 (38), 16102–16107. doi:10.1073/pnas.0902180106

Plimpton, S. (1995). Fast parallel algorithms for short-range molecular dynamics. *J. Comput. Phys.* 117 (1), 1–19. doi:10.1006/jcph.1995.1039

Qomi, M. J., Ulm, F., and Pellenq, J. (2012). Evidence on the dual nature of aluminum in the calcium-silicate-hydrates based on atomistic simulations. *J. Am. Ceram. Soc.* 95 (3), 1128–1137. doi:10.1111/j.1551-2916.2011.05058.x

Schindler, P. W., and Stumm, W. (1987). "The surface chemistry of oxides, hydroxides, and oxide minerals," in *Aquatic surface chemistry: chemical processes at the particle-water interface*. Editor W. Stumm (New York: Wiley), 83–100.

Scrivener, K. (2008). The concrete conundrum. *Chem. World*, 62–66.

Sethy, K. P., Pasla, D., and Chandra Sahoo, U. (2016). Utilization of high volume of industrial slag in self compacting concrete. *J. Clean. Prod.* 112 (5), 581–587. doi:10.1016/j.jclepro.2015.08.039

Shahsavari, R., Pellenq, R. J., and Ulm, F. J. (2011). Empirical force fields for complex hydrated calcio-silicate layered materials. *Phys. Chem. Chem. Phys.* 13 (3), 1002–1011. doi:10.1039/c0cp00516a

Shahsavari, R., Buehler, M. J., Pellenq, R. J.-M., and Ulm, F.-J. (2009). First-principles study of elastic constants and interlayer interactions of complex hydrated oxides: case study of tobermorite and jennite. *J. Am. Ceram. Soc.* 92 (10), 2323–2330. doi:10.1111/j.1551-2916.2009.03199.x

Shehata, M. H., and Thomas, M. D. A. (2002). Use of ternary blends containing silica fume and fly ash to suppress expansion due to alkali-silica reaction in concrete. *Cement Concr. Res.* 32 (3), 341–349. doi:10.1016/s0008-8846(01)00680-9

Sun, G. K., Young, J. F., and Kirkpatrick, R. J. (2006). The role of Al in C-S-H: NMR, XRD, and compositional results for precipitated samples. *Cement Concr. Res.* 36 (1), 18–29. doi:10.1016/j.cemconres.2005.03.002

Tsomaia, N., Brantley, S. L., Hamilton, J. P., Pantano, C. G., and Mueller, K. T. (2003). NMR evidence for formation of octahedral and tetrahedral al and repolymerization of the si network during dissolution of aluminosilicate glass and crystal. *Am. Mineral.* 88 (1), 54–67. doi:10.2138/am-2003-0107

Ulm, F.-J., Vandamme, M., Bobko, C., Alberto Ortega, J., Tai, K., and Ortiz, C. (2007). Statistical indentation techniques for hydrated nanocomposites: concrete, bone, and shale. *J. Am. Ceram. Soc.* 90 (9), 2677–2692. doi:10.1111/j.1551-2916.2007.02012.x

Xiao, Y., and Lasaga, A. C. (1996). Ab initio quantum mechanical studies of the kinetics and mechanisms of quartz dissolution: OH− catalysis. *Geochem. Cosmochim. Acta* 60 (13), 2283–2295. doi:10.1016/0016-7037(96)00101-9

Xiao, Y., and Lasaga, A. C. (1994). Ab initio quantum mechanical studies of the kinetics and mechanisms of silicate dissolution: h + (h 3 o +) catalysis. *Geochem. Cosmochim. Acta* 60 (13), 2283–2295. doi:10.1016/0016-7037(96)00101-9

Yang, J., Hou, D., and Ding, Q. (2018). Structure, dynamics, and mechanical properties of cross-linked calcium aluminosilicate hydrate: a molecular

dynamics study. *ACS Sustain. Chem. Eng.* 6, 9403–9417. doi:10.1021/acssuschemeng.8b01749

Zhou, S., and Ju, J. W. (2020). The damage and healing of quartz under radiation at high temperatures. *Int. J. Damage Mech.* 29, 923–942. doi:10.1177/1056789519894547

Zhou, S., Vu-Bac, N., Arash, B., Zhu, H., and Zhuang, X. (2019). Interface characterization between polyethylene/silica in engineered cementitious composites by molecular dynamics simulation. *Molecules* 24 (8), 1497. doi:10.3390/molecules24081497

Zhu, T., Li, J., Lin, X., and Yip, S. (2005). Stress-dependent molecular pathways of silica-water reaction. *J. Mech. Phys. Solid.* 53 (7), 1597–1623. doi:10.1016/j.jmps.2005.02.002

Conflict of Interest: The authors declare that the research was conducted in the absence of any commercial or financial relationships that could be construed as a potential conflict of interest.

Copyright © 2021 Zhang, Li, Yang, Ding and Sun. This is an open-access article distributed under the terms of the Creative Commons Attribution License (CC BY). The use, distribution or reproduction in other forums is permitted, provided the original author(s) and the copyright owner(s) are credited and that the original publication in this journal is cited, in accordance with accepted academic practice. No use, distribution or reproduction is permitted which does not comply with these terms.

Advantages of publishing in Frontiers

OPEN ACCESS
Articles are free to read for greatest visibility and readership

FAST PUBLICATION
Around 90 days from submission to decision

HIGH QUALITY PEER-REVIEW
Rigorous, collaborative, and constructive peer-review

TRANSPARENT PEER-REVIEW
Editors and reviewers acknowledged by name on published articles

Frontiers
Avenue du Tribunal-Fédéral 34
1005 Lausanne | Switzerland

Visit us: www.frontiersin.org
Contact us: frontiersin.org/about/contact

REPRODUCIBILITY OF RESEARCH
Support open data and methods to enhance research reproducibility

DIGITAL PUBLISHING
Articles designed for optimal readership across devices

FOLLOW US
@frontiersin

IMPACT METRICS
Advanced article metrics track visibility across digital media

EXTENSIVE PROMOTION
Marketing and promotion of impactful research

LOOP RESEARCH NETWORK
Our network increases your article's readership